8-2019

A Comparative Study of 3d-Intercalated Transition Metal Dichalcogenides by Their Transport, Magnetic, and Electronic Properties

Deepak Sapkota
University of Tennessee, dsapkota@vols.utk.edu

A Comparative Study of 3d-Intercalated Transition Metal Dichalcogenides by Magnetic, Transport, and Electronic Properties

A Dissertation Presented for the

Doctor of Philosophy

Degree

The University of Tennessee, Knoxville

Deepak Sapkota

August 2019

Dedicated

to my beloved parents

and

to my loving wife

Acknowledgments

First of all, I would like to thank my thesis advisors Professor Norman Mannella and Professor David Mandrus for their constant guidance and supervision throughout my graduate studies. Also, I would like to express my thanks to other committee members, Professor Cristian Batista and Professor Haidong Zhou, for their support and suggestions.

I want to express my gratitude to Michael Kohler, Ling Li, and Lekh Paudel for sharing their knowledge and expertise on crystal growth techniques along with handling of the powder X-ray diffractomeer, the glove box, and the high temperature furnaces. To my lab-mates Amanda Haglund, Ganesh Pokherel, Hasitha Suriya Arachchige, Rui Xue, Candice Kinsler-Fedon, Nan Huang, and Brianna Musico for their continuous help and support. My thanks go to Randy McMillan and Doug E. Fielden for their technical support. I am also thankful to Xiaoping Wang for his help on single crystal XRD measurements in the Oak Ridge National Laboratory (ORNL). I would like to thank Jiaqiang Yan and Andrew may for their help on transport measurements.

I would like to express deep gratitude to Rumpam Mukherjee for teaching me how to use the PPMS and MPMS systems for the transport and magnetic properties measurements. To Nicholas Sirica, thank you so much for your valuable time and help on LEED and ARPES experiments.

To Federica Bondino, Igor Pis, Silvia Nappinni, and Elena Magnano in BACH of Electtra synchrotron facility, I would like to express my thanks for your help on performing core level photoemisson, X-ray absoprtion, resonant photoemission, and Soft X-ray ARPES measurements. I would like to thank Sung-Kwa Mo for his assistance on performing ARPES experiments in Advanced Light Source of Berkeley National Laboratory. I am grateful to Cristina Africh, Alberto Lodi Rizzini, and Mirko Panighel at IOM-CNR in Italy for their help

on performing the LEED and STM experiments. Also, thanks go to Maxim A. Ziatdinov for additional STM measurements in ORNL.

Special thanks to Paolo Vilmercati for his tremendous help on analyzing and interpreting the photoemission data. I am also thankful to Nirmal Ghimire for wonderful discussion on the experimental results, especially the transport and magnetic properties. Many thanks go to Alaska Subedi for his valuable suggestion on performing the DFT calculations utilizing WIEN2k.

Finally, I would like to thank my mom and dad for their endless love and belief in me. With greatest thanks to my wife, Deepshila Gautam, for your love, patience, and encouragement.

Abstract

Intercalation of transition metal dichalcogendies (TMDCs) by 3d-transition metals has been studied systematically. We mainly focus on intercalation into two host TMDCs 2H-NbS_2 and 2H-TaS_2 which are layered materials where the metal ions are in trigonal prismatic environment of chalcogens, the layers are separated by weak van der Waals force. So, foreign atoms or molecules can be inserted in between the layers of the TMDCs. The un-intercalated NbS_2 shows superconductivity below 6 K whereas TaS_2 exhibits coexistence of the superconductivity (T_c=0.8 K) with charge density wave phase (T_{CDW} =75 K). In this research, the NbS_2 is intercalated by V atom with formula unit $V_{0.3}NbS_2$, while TaS_2 by Cr with formula unit $Cr_{1/3}TaS_2$. Upon the intercalation, the electronic as well as magnetic structure of host materials are likely to be modified. It is believed that the charge transfer between the 3d-intercalant and host TMDC, specifically the d-band of Nb or Ta, just causes an increase in chemical potential without altering the band structure and shape and size of Fermi surface, also known as rigid band model. And, the local moment in magnetic ion gives rise to magnetism via RKKY interaction. In order to examine the effect of intercalation in $V_{0.3}NbS_2$ and $Cr_{1/3}TaS_2$, we investigated the magnetic, transport, and electronic properties.

In $V_{0.3}NbS_2$, which crystallizes in *P-31m* space group, we observed canted antiferromagnetic (weak ferromagnetic) magnetic ordering with majority of charge carriers as hole type. From ARPES measurements, additional bands are appeared to cross the Fermi level and shape and size of the Fermi surface are modified as compared to NbS_2. Also, V-3d states are present near the Fermi level. These findings demonstrate that the simple rigid band picture is not viable in $V_{0.3}NbS_2$ compound. Moreover, from the photon dependent ARPES measurements strong k_z dispersion is found in contrast to that of host NbS_2.

Similarly, intercalated $Cr_{1/3}TaS_2$ crystallizes in $P6_322$ space group orders ferromagnetically. Surface structure is investigated by STM, LEED, and core level photoemmission experiments. The resonant photoemmission and ARPES measurements are performed to examine the effect of charge transfer between Cr and TaS_2 layer.

Table of Contents

List of Tables

List of Figures

Chapter 1

Introduction

The 3d-intercalated transition metal dichalcogenides (TMDCs) received little attention after the chiral helical spin structure is realized in $Cr_{1/3}NbS_2$ by Moriya and Miyadi in 1982 [87]. However, following the discovery of new physics in TMDCs and its potential applications, the intercalated TMDCs are refocused for fundamental research and technological research. These materials order magnetically and are Van der Waals bonded between chalcogen layers; so they can be exfoliated and potentially used in single-layer devices such as field effect transistors. Magnetic and transport properties of few intercalated complexes have been reviewed by Friend and Yoffe [94, 95]. The magnetic exchange mechanism in the intercalated complexes is not well understood. Although, the moments are appeared to be localized to magnetic ions, there is strong interaction between the conduction electrons and local moments that has been interpreted as both RKKY [101] and itinerant exchange interactions [54, 55]. Switching the magnetic ions may tune the magnetocrystalline anisotropy and affect the metamagnetic transitions. In addition, by choosing proper transition metals in the host compound one can tune the strength of spin orbit coupling, for instance by switching the Nb-4d with the 5d element such as Ta is expected to increase the spin-orbit interaction. Aside from the magnetism, the charge transfer between the host material and intercalant species modify the electron occupation of narrow d band of host materials and can radically change its electronic and optical properties [36]. The goal of this thesis is to design and synthesis new magnetic intercalated complexes and understand the basis features of the electronic structure and the possible relations with their magnetic behavior. With this regard, we

synthesize and study two intercalated complexes $V_{0.3}NbS_2$ and $Cr_{1/3}TaS_2$ and study their magnetic, transport, and electronic properties. The structure of this thesis is as follows:

In Chapter 1 we mainly discuss an overview of this thesis providing an introduction to the TMDCs and intercalation to TMDCs with molecules or atoms, along with their interesting physical properties, followed by the motivation to study the intercalated TMDCs.

Chapter 2 and 3 mainly deal with techniques we utilized in this thesis. We give theoretical background on photoemission spectroscopy (PES) including core level PES and angle resolved PES (ARPES), X-ray absorption spectroscopy (XAS), and resonant PES (ResPES). In addition, brief discussion to the density function theory (DFT) calculations will be provided as we use WIEN2k built-in code to perform electronic structure calculations of present materials. Chapter 4 is related to the experimental setup particularly of ARES experiment and its components such as ultra high vacuum (UHV) chamber, sample manipulator, and electron analyzer. Also, the production of light sources such as He-I and II lines and synchrotron radiation source will be reviewed.

In Chapter 5, the crystal synthesis and structure of $V_{0.3}NbS_2$ has been discussed first, followed by DC/AC magnetic susceptibility, resistivity and magnetoresistance, heat capacity, and thermal conductivity data. The carrier concentration, its type, and mobility are obtained from the Hall effect measurements. Chapter 6 is focused on the electronic structure of $V_{0.3}NbS_2$ crystal. the chapter starts from surface characterization of sample by scanning tunneling microscopy (STM), low energy electron diffraction (LEED) pattern, core level PES of S-2p and V-2p, and resonant ARPES experiments. Then, bandstrucutre and density of states obtained from the DFT calculations is presented which is to be compared with ARPES spectra. Afterwards, the polarization dependent ReSPES and XAS spectra, to learn elemental sensitivity to the valence band (VB) and orbital anisotorpy, are presented. In order to check if the surface is representative of bulk, conventional ARPES and the soft X-ray ARPES results are compared. Additionally, the effect of intercalation has been investigated by comparison of ARPES and wide VB spectra of $V_{0.3}NbS_2$ with the host compound NbS_2 and another intercalated system $Cr_{1/3}NbS_2$. The orbital character of bands has been examined by the polarization dependent ARPES experiments measuring VB dispersion as well as in-plane and out-of-plane Fermi surface mapping. The dimensionality

of the sample is also inferred from out-of-plane Fermi surface mapping. The resonant as well temperature dependent ARPES results are also provided in the end of Chapter 6.

In Chapter 7, the crystal synthesis and structure, magnetic, and transport behavior of another intercalated system $Cr_{1/3}TaS_2$ will be presented. In Chapter 8, The surface of the sample is investigated by STM, LEED and core level PES, particularly of S-2p and Cr-2p core levels. Additional core levels, ResPES for Cr-L_{23} and Ta-N_3 absorption edge, and XAS results will be discussed. Also, bandstructure for $Cr_{1/3}TaS_2$ obtained from the DFT calculations which is compared with the ARPES spectra recorded at He-II photon source.

Lastly, in Chapter 9 we provide the summary of the results studying two intercalated systems $V_{0.3}NbS_2$ and $Cr_{1/3}TaS_2$. The future direction in the field of intercalation system is also offered.

1.1 Transition Metal Dichalcogenides (TMDCs)

TMDCs are layered materials with strong in-plane covalent bonds and weak van der Waals interactions between layers allowing an exfoliation into two-dimensional layers of single unit cell thickness. Although TMDCs have been studied for decades, after the discovery of graphene (in 2004 [91]), which is two dimensional allotrope of carbon atoms arranged in a honeycomb lattice, TMDCs are gaining significant interests in both fields of science and technological applications. The electron transport in graphene can correctly be explained by the relativistic Dirac equation, employing quantum electrodynamics into simple condensed matter system [92, 136]. Thus, the novel physical properties such as integer anomalous Hall effect [136] is observed even at room temperature due to large cyclotron energies for relativistic electron. Graphene is a typical example of atomically thin electrical and thermal conductor [6] with high carrier mobility [79]. These quantum phenomena may lead to applications in many fields ranging from electronic and optical devices, energy generation and storage, chemical sensors etc. Furthermore, due to mechanical and chemical stability of graphene it provides possible candidate for electronic devices in nanodimension scale. Despite the fact that it has novel physical properties and an easy access with low cost, the zero band gap bandstructure hinders the application in transistor device. The field effect

transistors (FETs) made out of the graphene can not be switched off effectively having low on/off switching ratios. However progress has been made in engineering the band gap by nanostructuring [73, 72, 47], chemical functionalization [7], and applying high electric field [137]; but these techniques add complexity and reduces carrier mobility. For this reason people are searching for alternative atomically thin 2D crystals, such candidate would be TMDCs having sizable band gap, promising new FET and optoelectronic devices. The TMDC is another class of material where the interaction of d-electrons gives rise to novel physical phenomena [134, 5].

The TMDCs are generally represented by TX_2, where T and X stand for transition metal and chalcogen atoms, respectively. Several structural polytypes of bulk TMDCs exist depending upon the stacking sequence of layers in the direction perpendicular to plane of layer. The monolayer of TMDC has three layer of atoms (X-T-X) that is chalcogen atoms in two hexagonal planes separated by a plane of transition metal atoms [123, 63], and has been found in two polytpes: 2H (H, hexagonal symmetry) and 1T (T, trigonal symmetry) phases where the metal atoms are in trigonal prismatic and octahedral enviornment of chalcogen atoms, respectively, as shown in Figure 1.1(a), the index 2(1) represents two (one) layer of TX_2. The 2H-phase corresponds to ABA stacking where the chalcogen atoms occupy the same position A and located on top of each other along perpendicular direction to layer, whereas the 1T-phase corresponds to ABC stacking [76, 97, 61]. These two polytype phases give rise to different electronic structure, particularly transition metal d band [36, 63]. Even though many TMDCs have similar structures, they cover wide range of properties from semiconductors to metals.

The best known example of TMDCs is a molybdenum disulphide (2H-MoS_2), can also be found naturally, a semiconductor with indirect bulk band gap of about 1.2 eV [35] at the Γ- point but continuously shifts to the direct band gap when thinned to monolayer, while the direct excitonic transitions at K- point remains relatively unaffected with layer number [113, 75]. The change in the bandstructure with layers is due to the effect of quantum confinement [75] and the hybridization between p_z-orbital of chalcogen and d-orbital of metal atoms [113, 71]. Remarkably the monolayer of MoS_2 emits light strongly, exhibiting an increase in luminescence quantum efficiency by more than a factor of 10^4 over the bulk

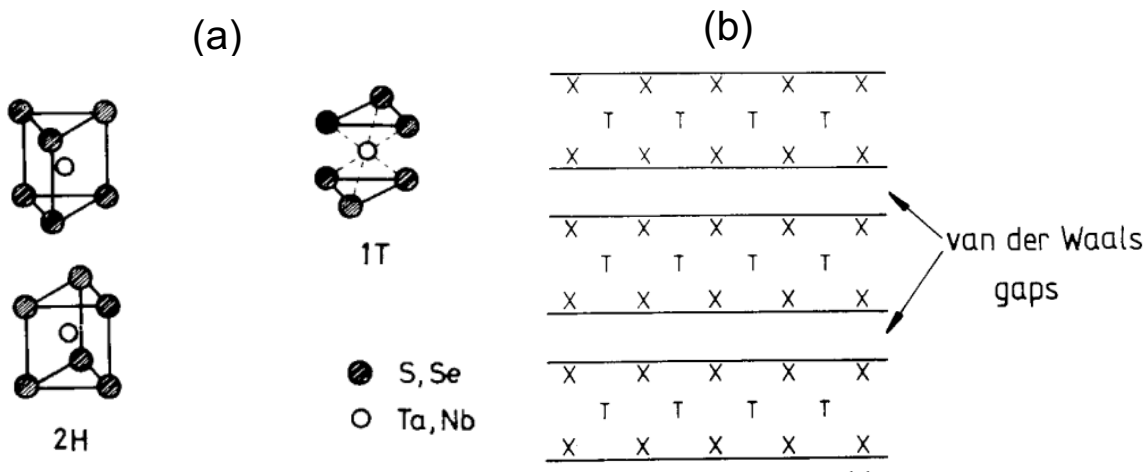

Figure 1.1: (a)2H- and 1T- polytypes of transition metal dichalcogendies. (b) Schematic representation of a TMDC, the layers are separated by weak van der Waals force. Figures from Ref. [36]

material [75]. All MoX_2 compounds are expected to undergo similar indirect-to-direct band gap transition in the monolayer scale [117]. The band gap in the range of 1-2 eV can lead to high on/off ratio, allowing more efficient control over switching and lower the power dissipation and consumption promising characteristics for active FET channel[20, 98]. It is worth to mention here another TMDC WTe_2 having interesting physical properties. WTe_2 is a semimetal exhibiting extremely large positive magnetoresistance (XMR): 13 million % at 0.53 K at magnetic field of 60 T when field is applied direction perpendicular to the layer of WTe_2, and no saturation of magnetoresistance is observed even at very high fields [3]. Highly anisotropic XMR is found in WTe_2 that is XMR reduces by 90 % when the magnetic field is applied parallel to the plane of layer.

In above paragraph we mainly discussed the Group IV TMDCs, most of them behave as semiconductors. Now we will focus on the Group V TMDCs particularly of TaX_2 and NbX_2 system; this group of TMDCs demonstrate different electronic properties than Group V TMDCs, and these compounds tend to be metallic. One intriguing property charge density wave (CDW) is common in this class of materials, CDW phase occurs due to the Fermi surface driven periodic distortion of crystal lattice. The CDW is a periodic modulation of density conduction electron inside material. First observation of CDW was reported in 1T-$TaSe_2$ [127] besides one dimensional materials. Other TMDCs such as 2H-$NbSe_2$ [128],

2H-$TaSe_2$, 1T-TaS_2 [128], 2H-TaS_2 [129] also exhibit the CDW transitions. The coexistence of superconductivity with charge density wave at low temperatures has been reported in 2H-TaS_2 and 2H-$NbSe_2$ with superconductivity transition temperature of 0.8 K [78] and 7 K [70], respectively. It has been observed that when going in series from 2H-$TaSe_2$ and 2H-TaS_2 to 2H-$NbSe_2$ and 2H-NbS_2 the ratio of in-plane and out-of-plane lattice parameter (a/c) increases, superconducting transition temperature too, while CDW transition temperature decreases dramatically [42]. Moreover, the CDW phase is absent in 2H-NbS_2, but the superconductivity exists with T_c about 6 K [46].

The physical properties of TMDCs depend largely on the ligand-field splitting of transition metal d-orbitals. In transition metal compounds, the d-levels spread into narrow energy bands, which, if partially filled, lead to metallic conductivity by d electrons. While the other s and p orbitals derived from chalcogen or metal give rise to broad energy bands: a VB comprising mainly of s- and p-orbitals of the chalcogen (bonding state) and conduction band (s and p of metals, antibonding state) [57]. According to the ligand field theory, when a system is in trigonal prismatic environment, for example Nb atom ($4d^1$) in NbS_2 or $NbSe_2$, five-fold degenerate Nb-4d state splits into singly degenerate a_1 state with symmetry d_{z^2} and two doubly degenerate e' and e'' state with symmetry $d_{x^2-y^2}$, d_{xy} and d_{xz}, d_{yz}, respectively having energy hierarchy of $e' < e'' < a_1$, depending upon degree of overlap between Nb-4d and chalcogen 3p or 4p states. On the other hand in octahedral environment of metal, d-orbitals split into higher energy state e_g with symmetry d_{z^2}, $d_{x^2-y^2}$ and lower energy state t_{2g} with symmetry d_{xy}, d_{yz}, and d_{xz}. Bandstructure obtained from the first principles DFT calculations is roughly consistent with the simplified ligand field theory as described above. For instance, in case of NbS_2 or $NbSe_2$ Nb-d_{z^2} orbitals is contributing near the Fermi level around Γ point and $d_{xy}/d_{x^2-y^2}$ orbitals at K point, an additional p_z band from the chalcogen is also present at Fermi level at the Γ point [21, 100, 62, 60, 49]. The Fermi surface calculations show two concentric cylindrical shape centered at Γ and a triangular shape at K point. The two cylinders are originated due to two formula units in unit cell of 2H-$NbSe_2$ or 2H-NbS_2. These results are corroborated by ARPES experiments [135, 14, 116, 108] as well, however in NbS_2 p_z orbital is absent [108]. k_z dispersion obtained from the ARPES experiment on $NbSe_2$ exhibits cylindrical Fermi surfaces [100], indicating very weak k_z dispersion as expected in

layer materials. The k_z dispersion of NbS_2 has not be reported yet, but it is expected to have similar behavior as of $NbSe_2$ due to isostructure and isoelectronic compound.

1.2 Intercalated TMDCs and Motivation to study Intercalated TMDCs

As we discussed above that TMDCs are layered materials where the layers are separated by weak Van der Waals bond, enabling one to insert variety of organic molecules or 3d transition metals so that the narrow d band of metal can be finely tuned [36]. The process of insertion foreign molecules or atoms into the van der Waals gap, without altering the original structure of X-T-X layer, is called intercalation. The intercalation causes profound change in electronic and magnetic properties of host compound and can be understood on the basis of charge transfer, increase in inter-layer separation, and localized magnetic moment. Thus, the intercalation can lead metal-to-semiconductor or semiconductor-to-metal and non-magnetic to magnetic transitions. It has been found that the TMDCs only form the intercalation compounds with electron donors species, intercalating with electron acceptors has not been succeeded yet [36]. Three broad categories of species such as organic molecules (typically a Lewis base), alkali metals, and 3d transition metals have been successfully intercalated. The intercalation by organic molecules and alkali metals can be found elsewhere [121, 27, 126, 37, 36], here we only focus on intercalation by 3d-transition metals as main objective of this research is based on an effect of intercalation by 3d transition metals into TMDCs, particularly in 2H-NbS_2 and 2H-TaS_2.

The intercalation of NbS_2 and TaS_2 with 3d transition metals has been a subject of interest since long range magnetic orderings exists at certain concentration of intercalant species which form an ordered superlattice [95, 94]. Both un-intercalated host compounds NbS_2 and TaS_2 belongs to hexagonal P63/mmc (194) space group and are metallic as already discussed. The intercalant species occupy the octahedral sites between the layers, while retaining the original trigonal prismatic coordination of the Nb or Ta by chalcogens, within the layers. An intercalated complex is generally represented by M_xTX_2, where M stands

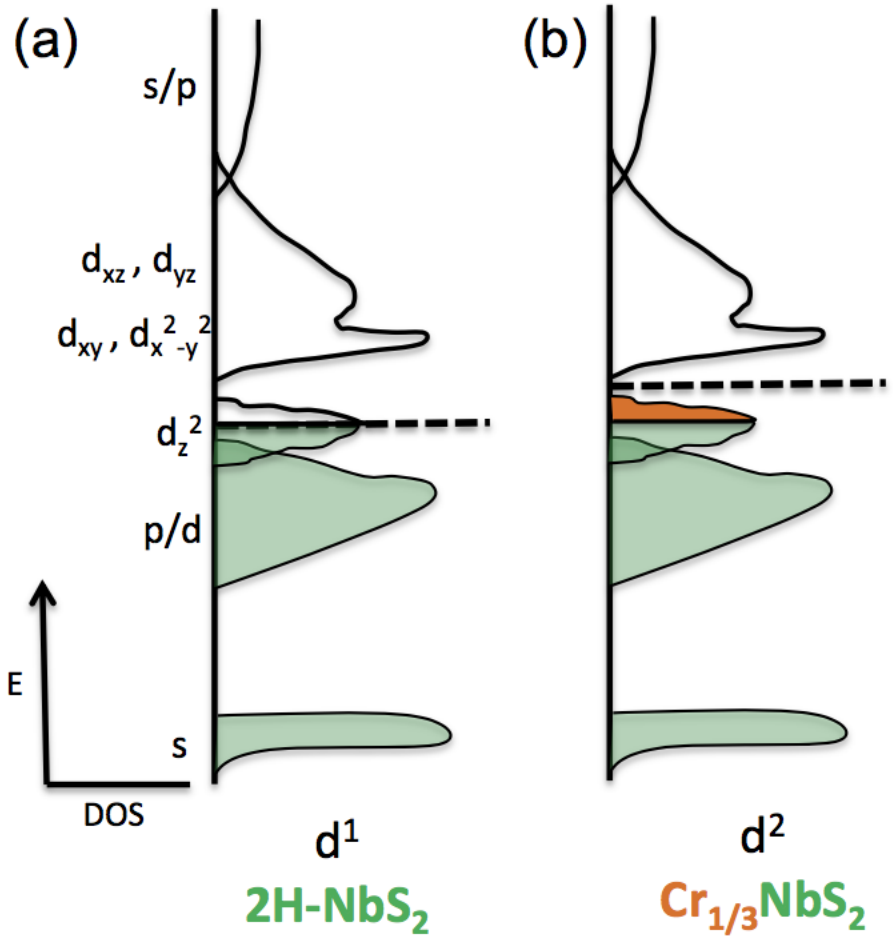

Figure 1.2: Schematic diagram of band model for the un-intercalated NbS2 and Cr-intercalated NbS_2: $Cr_{1/3}NbS_2$. Figure reproduced here from N. Sirica PhD Thesis

for 3d transition metal and x its concentration. Ordered superlatices of intercalated ions from concentration of 1/4 and 1/3 gives rise to $2a \times 2a$ and $\sqrt{3}a \times \sqrt{3}a$ superstructres, respectively, in normal state, where 'a' is in-plane lattice parameter for NbS_2 or TaS_2. In the process of intercalation the 3d transition metal donates electron to Nb or Ta d-band, resulting an oxidation states of +2 or +3 for the transition metal ions, and band filling of d sub-band increases [19]. This phenonmenon is commonly explained in terms of the rigid band model [19, 36] such that charge transfer will only raise chemical potential without altering the Fermi surface and band structure of the host materials. This common wisdom might not always be true. Moreover, the remaining electrons localized in 3d ions give rise to local magnetic moment. The simple band model for the host compound (2H-NbS_2) and intercalated system ($Cr_{1/3}NbS_2$) has been shown in Figure 1.2 (obtained from N. Sirica PhD Thesis).

A compelling example of intercalated systems is $Cr_{1/3}NbS_2$ belonging to non-centrosymmetric space group $P6_322$ with hexagonal crystal structure. Magnetic structure of this compound is well studied. The Cr-ion in $Cr_{1/3}NbS_2$ crystal is considered to be in the trivalent (+3) state and to have a localized moment forming a ferromagnetic layers perpendicular to c-axis; the magnetic transition temperature is about 127 K [84]. It has been found that this material exhibits chiral helical spin textures along c-axis with periodicity of about 48 nm [84, 87]. The helical structure, in crystals lacking inversion center, is developed from antisymmetric exchange (Dzyaloshinsky-Moriya (DM)) interaction [28, 85] between Cr atoms along c-axis. Also, from the Lorentz microscopy experiments, it has been found that upon applying small magnetic field perpendicular to c-axis the chiral helical magnetic (CHM) structure is periodically distorted and chiral soliton lattice (CSL) appears [115]. The CSL is a periodic magnetic superlattice consisting of forced ferromagnetic domain separated by 360 magnetic domain walls and it disappears above 0.230 T turning into forced ferromagnetic state [115]. Ferromagnetism in this material, and other intercalated complexes too, is believed to be interpreted in terms of Ruderman-Kittel-Kasuya-Yosida (RKKY) interaction as the intercalant species are separated by larger distance [94]: indirect exchange interaction between the localized moments via the conduction electrons. This might not be valid in case of $Cr_{1/3}NbS_2$ as Cr-d orbital which gives rise rise local spin moment (LSM) is also present

at the Fermi surface. Thus clear separation between the magnetic and itinerant degree of freedom does not occur. In other words, motion of itinerant electrons and local spin moments are influenced in a reciprocal manner and the interaction between the intinerant electrons and localized spin moment is taken only as a weak perturbation (From N. Sirica PhD Thesis). Regarding the electronic structure, it has been studied from the *Ab initio* DFT calculations [39, 15] and ARPES study [108]. It is observed that electron is transferred to 4d-band of host material and hence increases the chemical potential but additional bands contributing from the Cr atom appear at Γ and K points near the Fermi level (see Figure 6.21). The shape of the Fermi surface is more complex compare to that of host materials (see Figure 6.21) though size of pockets at Γ and K points shrinks in $Cr_{1/3}NbS_2$, representative of charge transfer to NbS_2 layer. These results contradict to the simple rigid band model. In addition, it exhibits two dimensional Fermi surface, that is very weak k_z dispersion marked difference with the DFT calculations [39]; however, it is expected that interlayer coupling enhances as the chromium atoms sits in between the layers. Additional intercalated systems such as $Ni_{1/3}NbS_2$ and $Mn_{1/3}NbS_2$ has been studied by ARPES experiments and compared the results with 2H-$NbSe_2$ [9] isostructural to 2H-NbS_2; and the authors reported non-uniform, pocket selective doping on Fermi surfaces: intercalant species causes reduction in size of pockets at K point without affecting Fermi sheets at Γ point, suggesting that simple rigid band picture has to be considered cautiously [9].

$Fe_{1/4}TaS_2$ is another 2H-TaS_2 based Fe-intercalted system. This complex has $2a \times 2a$ superstrucure of Fe ions and orders ferromagnetically below 160 K with easy axis magnetization along c-axis, contrary to the $Cr_{1/3}NbS_2$ which has easy axis along ab-plane. An extremely anisotropic magnetotransport behavior has been reported in $Fe_{1/4}TaS_2$ [88]. Below the ferromagnetic ordering temperature, a very sharp (squareness) of hysteresis loop has been observed when magnetic field is applied along c-axis with saturation magnetic moment of 4 μ_B per Fe, and the magnetoresistance is negative and drops sharply in the critical field (3.7 T); the squareness of hysteresis indicates rapid switching in magnetic moment at critical field. When the magnetic field is along ab-plane magnetization remains small and linear up to 5 T without any visible hysteresis with saturation magnetic moment of 0.25 μ_B per Fe, and the magnetoresitance becomes positive and vary quadratically with field.

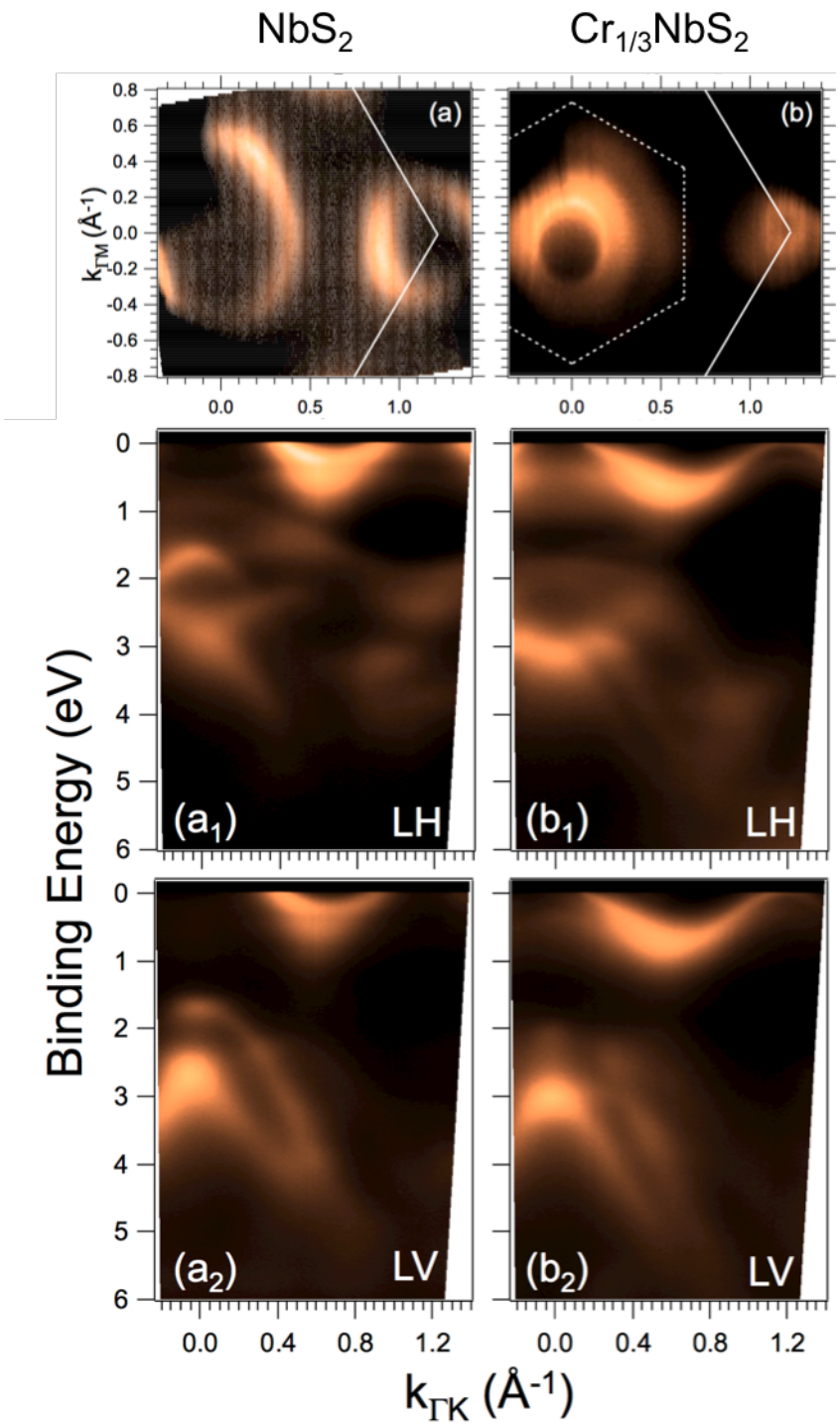

Figure 1.3: Fermi surface mappings and band dispersion for host material NbS2 (a) and intercalated complex $Cr_{1/3}NbS_2$ (b) measured along ΓK direction. Ref. [108].

Furthermore, the electronic structure of $Fe_{1/4}TaS_2$ has been studied by ARPES experiments [65]. The band dispersion obtained from the ARPES experiments matches well with the calculated band structure for 2H-TaS_2 [125, 11] with rigid sift of 0.2 eV. The magnetic interaction in this material is inferred in terms RKKY interaction [65] that is indirect exchange interaction between the localized moments in Fe ions (which are separated by large distance) via the Ta-5d conduction electrons. In order to check the validity of RKKY interaction, in-plane Fermi wavevector extracted from the ARPES experiment is used to obtain the RKKY oscillations [4] which becomes maximized at Fe-Fe distance for 2×2 superstructure, manifesting $Fe_{1/4}TaS_2$ a RKKY ferromagnet.

We presented two examples of intercalated systems $Cr_{1/3}NbS_2$ and $Fe_{1/4}TaS_2$ based on host compounds 2H-NbS_2 and 2H-TaS_2, respectively, with two different 3d-ions giving rise to distinct superstructures depending upon their concentrations. Importantly, they possess quite distinct magnetic and electronic behaviors. The former exhibits helical spin textures along c-axis and ferromagnetic easy axis lies along ab-plane, whereas the latter shows ferromagnetic orderings with magnetic easy axis perpendicular to ab-plane with sharp switching in magnetic moment at critical field due to squareness of hysteresis loop. The ferromagnetic coupling in $Fe_{1/4}TaS_2$ is interpreted on the basis of RKKY interaction but this might no be applied for $Cr_{1/3}NbS_2$. Furthermore, rigid band model could be a valid argument to describe the band structure for $Fe_{1/4}TaS_2$ but is untenable for $Cr_{1/3}NbS_2$ as well as for $Ni_{1/3}NbS_2$, and $Mn_{1/3}NbS_2$. In the light of these differences in magnetic and electronic properties by changing intercalant species, which plays more role than just injecting electrons to host materials and serving as localized magnetic moment; it is considerable to synthesize new intercalated materials by different 3d transition metals with varying their concentrations. Furthermore, this search of new materials could also lead to discovery of novel physical properties, producing potential interest to scientific community and technological application. With this regard, we studied two intercalated compounds $V_{0.3}TaS_2$ and $Cr_{1/3}TaS_2$ to develop a systematic understanding as to how the intercalant species affect the magnetic and electronic structure of host materials.

Chapter 2

Photoemission Spectroscopy

The phenomenon of photoemission was first detected by Hertz [51] in 1887, an electrode illuminated by ultraviolet radiation creates an electric sparks. In 1905, Einstein proposed the quantum nature of light to explain the experimental data of photoelectric effect: when light impinges on a sample an electron interacts with light and escapes from the sample with kinetic energy (KE) given by the following relation,

$$E_{kin} = h\nu - E_B - \phi \tag{2.1}$$

where hν is energy of photon source, E_B the binding energy (BE) of the electron, and ϕ the work function of the sample.

The momentum of the outgoing electron of mass m is determined from its kinetic energy by

$$p = \sqrt{2mE_{kin}}. \tag{2.2}$$

The representation of photoemission process in the single particle picture is shown in the Figure 2.1. The energy distribution (I(E)) of photoelectron recorded in a detector provides the density of states (N(E_B) in the solid. This is an attractive feature of the photoemission process.

With the knowledge of core-level binding energy and the elemental photoemission cross section it is relatively easy to analyze the photoemission spectrum quantitatively and determine the elemental composition of a sample. The variation in chemical environment

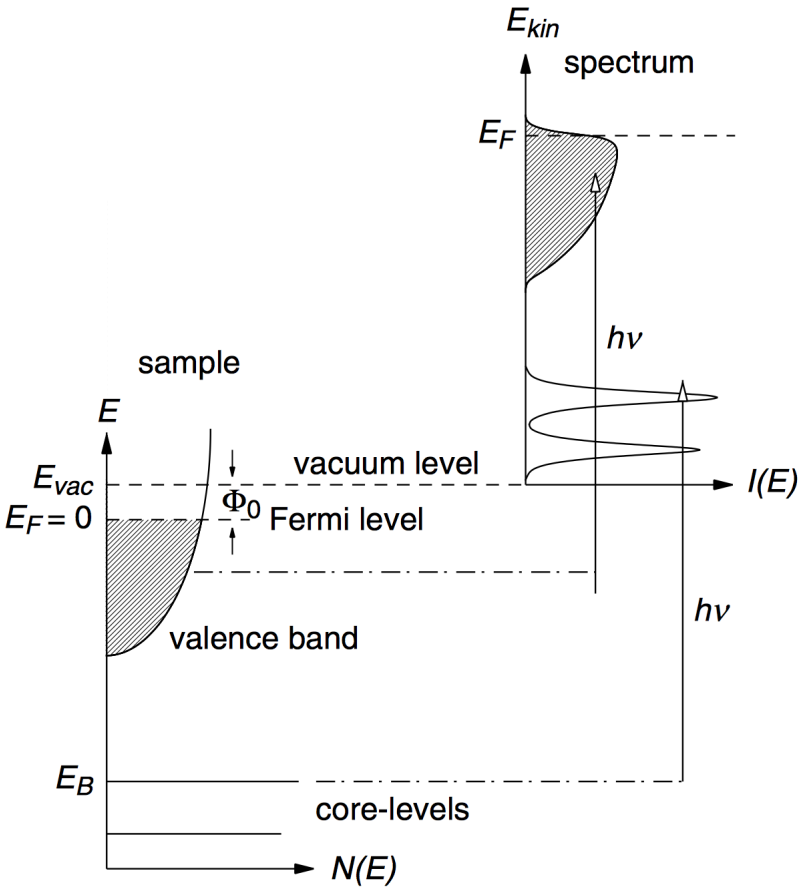

Figure 2.1: Schematic diagram of photoemission process [99]. The electron energy distribution produced by photon of energy $h\nu$ and measured as a function of kinetic energy of photoelectron.

can cause a shift in binding energy of core-level called the chemical shift. These two aspects along with the surface sensitivity make photoemission technique as an ideal tool for the chemical investigation of surfaces and thin films.

The main disadvantage of photoemission is that that it is an extreme surface sensitivity technique. So, a Ultra-High Vacuum (UHV) conditions is required to complete and experiment successfully. The requirement of UHV system is explained by the Figure 2.2, showing electron mean free path as a function of kinetic energy for selected elements, also called universal curve. The curve shows that only electrons from the very thin layer of sample involve in the photoemission process. Thus, it is necessary to have atomically clean surface if one wish to study the bulk properties of the sample. It is also important to note that even at the pressure of 10^{-9} Torr one monolayer of impurity is formed in 1000 seconds, if all the molecules or atoms impinging in a surface are stuck.

2.1 Theory of Photoemission

The photocurrent produced in photoemisison process results from the excitation of electrons from initial state to final state. The transition probability w of an electron under the influence of a time dependent perturbation Δ from initial N-electron $|\psi_i^N\rangle$ state to final state $|\psi_f^N\rangle$ is given by

$$w \propto \frac{2h}{\pi} |\langle \psi_f^N | \Delta | \psi_i^N \rangle|^2 \delta(E_f^n - E_i^n - h\nu). \tag{2.3}$$

E_i and E_f are the initial and final state energies and $h\nu$ is the photon energy. The perturbation has the form:

$$\Delta = \frac{e}{2mc}(\boldsymbol{A}.\boldsymbol{p}+\boldsymbol{p}.\boldsymbol{A}) - e\phi + \frac{e^2}{2mc^2}\boldsymbol{A}.\boldsymbol{A}, \tag{2.4}$$

where $\boldsymbol{A}$ and ϕ are vector and scalar potentials and $\boldsymbol{p} = i\hbar\nabla$ the momentum operator. The quadratic term in $\boldsymbol{A}$ can be neglected since it represents the two photon processes, and is only relevant for extremely high photon intensities. Using the commutation relation

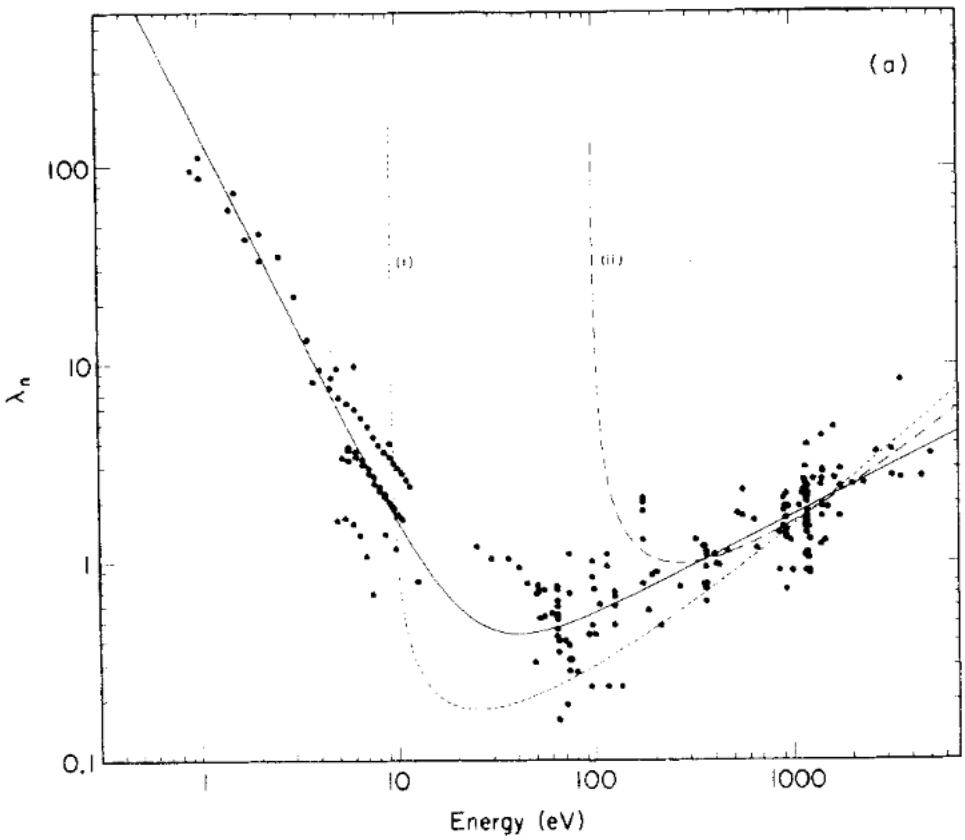

Figure 2.2: Inelastic mean free path for elements as a function of kinetic energy of photoelectron, also known as universal curve. The unit of IMFP is expressed in nm. Figure from [105]

$[\boldsymbol{A}, \boldsymbol{p}] = -i\hbar\nabla.\boldsymbol{A}$ and dipole approximation $\nabla.\boldsymbol{A} = 0$ the perturbation term becomes

$$\Delta = \frac{e}{mc}\boldsymbol{A}.\boldsymbol{p}, \tag{2.5}$$

with ϕ =0 for Coulomb gauge. It should also be noted that the dipole approximation $\nabla.\boldsymbol{A} = 0$ might not hold at the sample surface, where the electromagnetic wave may have strong spatial dependence and give rise to strong surface contributions to photoemission intensities [23].

In order to evaluate the photoemission intensity, one has to factorize the final state into the photoelectron and final N-1 particle state. The commonly used approximation is a sudden approximation. In this limit, it is assumed that removal of an electron is so fast that negligible interaction between the photoelectron and N-1 final state occurs. The N-particle final state can be expressed as

$$\psi_f^N = A\phi_f^k\psi_s^{N-1},\ E_F^N = \varepsilon_f + E_s^{N-1}, \tag{2.6}$$

where A is an operator that antisymmetrizes the wave function properly, ψ_k^f the photoelectron wavefunction with energy ε_f, and ψ_s^{N-1} the wavefunction of remaining N-1 electrons with energy E_s^{N-1}.

The initial state can also be written as:

$$\psi_i^N = A\phi_i^k\psi_i^{N-1}. \tag{2.7}$$

Then the transition matrix element in eq.(2.3) is written as

$$\langle\psi_f^N|\,\Delta\,|\psi_i^N\rangle \propto \langle\phi_f^k|\,\epsilon.\boldsymbol{p}\,|\phi_i^k\rangle\,\langle\psi_s^{N-1}|\psi_i^{N-1}\rangle\,, \tag{2.8}$$

where the spatially invariant vector potential ($A = A_0\epsilon$) is considered and its direction is defined by ϵ. The total photoemission intensity measured as a function of E_{kin} at momentum

k is the sum of transition probabilities from all initial states to all final states:

$$I(k, E_{kin}) = \sum_{f,i} w_{f,i} \propto \sum_{f,i} \frac{2h}{\pi} |\langle \phi_f^k | \epsilon.\boldsymbol{p} | \phi_i^k \rangle|^2 \sum_s |\langle \psi_s^{N-1} | \psi_i^{N-1} \rangle|^2 \delta(E_{kin} + E_s^{N-1} - E_i^N - h\nu) \tag{2.9}$$

The element $\langle \phi_f^k | \epsilon.\boldsymbol{p} | \phi_i^k \rangle = M_{f,i}$ in equation (2.9) is one electron dipole matrix element, and $|\langle \psi_s^{N-1} | \psi_i^{N-1} \rangle|^2 = |C_s|^2$ gives the probability that the removal of an electron from state i leaves the system in N-1 excited state. In non-interacting particle picture (i.e. for $s = i$) $|C_s|^2$ becomes unity and only the main peaks are contributed to the photoemission intensity. On the other hand, for strongly correlated system many of $|C_s|^2$ are non-zero, thus the main peaks for $s = i$ and satellite peaks for $s \neq i$ are observed.

The part $\sum_s |\langle \psi_s^{N-1} | \psi_i^{N-1} \rangle|^2 \delta(E_{kin} + E_s^{N-1} - E_i^N - h\nu) = A(k, h\nu)$ is one particle spectral function of hole state. Thus, the photoemission intensity has the form

$$I(k, E_{kin}) \propto \sum_{f,i} M_{f,i} A(k, h\nu). \tag{2.10}$$

The photoemission data are usually discussed in "one step" and "three-step" model. The illustration of one step and three step model is shown in Figure 2.3. In one step model, Bloch wave electron is excited into the damped final state near the surface. The damping is caused by the scattering and attenuation of electron. The one step model is more rigorous in which the photon absorption, electron removal, and electron detection should be treated as a single event. Hence the surface, vacuum and bulk have to be included in the Hamiltonian. The much simpler model which actually gives the same result as of one step model is commonly used to describe the photoemission process.

Although the three step model is purely a phenomenological approach, it has proved to be quite successful. In the three step model, the photoemission process is divided into three independent steps as follows: (1) Optical excitation of the electron in the solid. This step contains all the information about the intrinsic electronic structure of solid. (2) Transport of the electron to the surface. The transport of electron can be described in terms of electron inelastic mean free path which is proportional to the probability that the excited electron reaches to surface without an inelastic scattering (3) Escape of the electron into the vacuum.

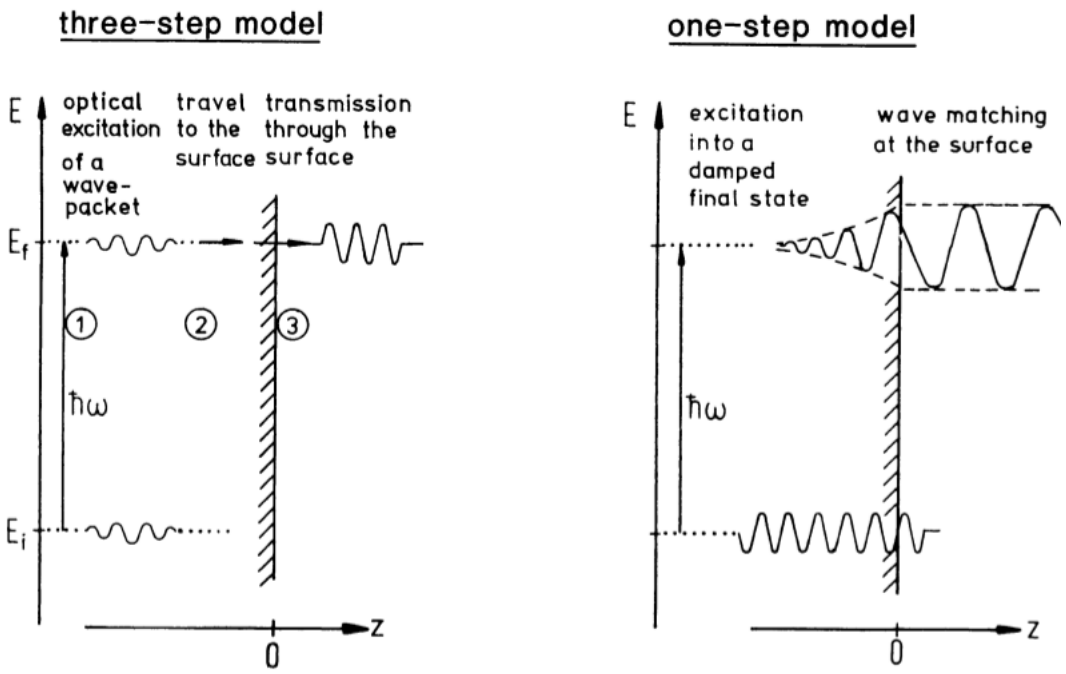

Figure 2.3: Three step and one step models of photoemission. In the three step model, electron (1) gets excited by photon (2) travels to the surface (3) escapes from the surface. In one step model, the Bloch wave electron excited into the final damped state and propagates freely into the vacuum. [56]

An electron escapes from the surface which has the component of the kinetic energy normal to the surface is sufficient to overcome the surface potential barrier (so called inner potential) and work function of the solid; the other electrons reflects back to the solid.

2.2 Core Level Photoemission

In the photoemission spectroscopy (PES) technique a photon of energy $h\nu$ liberates an electron from a system. The photoelectron can be either from the core level or from the valence level depending upon the energy of photon source used. The final state then can be viewed as one where hole has been created or a positive potential is introduced into the system. The core electrons are localized in the atomic sites and almost unchanged when the atoms condensed into the solid. On the other hand, electronic state of valence electrons are spread over the wide range and are strongly influenced by the chemical environment and the atomic species in the solid.

For N-electron system, the binding energy of photoelectron in one-electron approximation is given by [77]

$$E_B = E_f(N-1) - E_i(N), \tag{2.11}$$

where $E_i(N)$ and $E_f(N-1)$ are initial N-electron and final N-1 state energies, respectively. Each of these binding energies are approximately equal to the negative of orbital energy ϵ_k as obtained from the Koopmans' theorem utilizing the Hartree-Fock approximation. For the bound state orbital energy is negative, thus the binding energy has appropriate positive sign.

The Koopmans' theorem generally does not hold in molecules or solid because the orbital relaxation and electron correlations terms are missing in the Hartree-Fock approximation. The binding energy of k^{th} electron, when the relaxation and the correlation effects are included, can approximately be written as [29]

$$E_b(k) = -\epsilon_k - \delta_{relax} + \delta_{corr} + \delta_{relat}, \tag{2.12}$$

where δ_{relax}, δ_{corr}, and δ_{relat} are corrections for relaxations, correlations, and relativistic effects.

The core levels are believed to be unaffected by the chemical bonding, their wavefunction do not mix with the valence level responsible for bonding. But, the binding energy of the core level is extremely sensitive to the change in valence level charge distribution as bonds form. As such, when a same atom is placed in different chemical environments, the binding energy of the particular core-level is changed and is called "chemical shift". The first evidence of chemical shift has been observed in 1964 by the Hagstrom, Nordling & Siegbahn [45] in S-1s of $Na_2S_2O_3$. As an another example of chemical shift Figure 2.4 shows photoemission spectrum of C-1s from ethyl trifluroacetate, the binding energy of C-1s peak (all four peaks corresponds to C-1s) changes as the atomic species forming bonds with carbon change.

In general, the chemical shift can be explained as follows: if an atom is placed in a chemical environment where it effectively loses its charge to neighboring species, its core level will experience increase in the net Coulomb interaction which is the sum of nuclear attraction and other electron repulsion, and the binding energy increases. On the other hand, if an atom becomes more electronegative by gaining the electron from the neighboring species, the binding energy will reduce. This simple picture gives semiquantitative estimate of shift in the binding energy; the most accurate shift can be made using the Hartree-Fock approximation.

During the photoemission process, the creation of core hole leads to excitation in the remaining system. So that the core hole induces a relaxation of other electrons and thus its screening or polarization around it. The photoemission spectrum consists of the main peaks corresponding to the ground state after photoexcitation and possible satellite features representing the excited states.

The satellite feature in the core level spectra has been observed in number of transition metal compounds. The Cu-2p spectra of divalent copper compounds exhibits two satellite features corresponding to each of the two spin-orbit components ($2p_{3/2}$ and $2p_{1/2}$) (see Figure 2.5. These satellite features are due to the interaction of core-hole with the valence electrons resulting the change in potential seen by valence electrons when core hole is created. In the ground state of the halides, Cu-3d has a hole ($3d^9$ configuration), filled Cu-2p ($2p^6$), and a filled ligand shell L. The photoexication process on Cu site results two possible final states: one configuration $2p^5 3d^{10} L^{-1}$ corresponds to the main peak where a charge transfer from

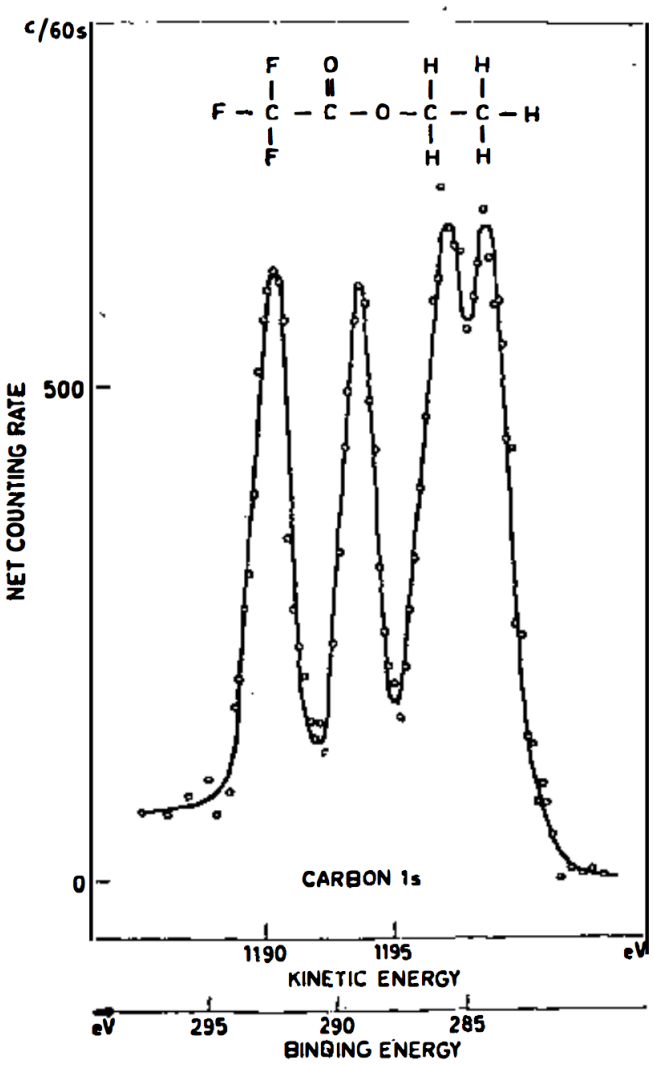

Figure 2.4: Chemical shift of carbon 1s-core level. Photoemission spectrum of C-1s electron from ethyl trifluroacetate [53].

ligand to metal atoms occurs; and another configuration $2p^5 3d^9 L$ corresponds to the the satellite structure and no correlation between ligand and the metal ion. The very similar model was proposed by Kotani and Toyozawa for metals [67]. The satellite and main peak in the unoccupied d or f shell ions (rare earth or transition metals) are caused by different screening channels. A core hole produces a positive potential and pulls the empty d (or f) state below the Fermi level creating two-hole state: one photo-hole and another the unoccupied d state. And the XPS spectrum splits into two peaks corresponding to two final states: (a) The d level is still empty though it lies below the Fermi level and it gives rise to the satellite peak, (b) The d level is filled from the ligand sp states through the hybridization and it gives rise to the the main peak; it has lower binding energy since the localized d state has higher screening effect than the delocalized sp states. The former is called the "poorly-screened state" and the latter is called "well-screened state".

Lastly, the information about the unpaired spin of valence electron and hence the magnetism in the system can be acquired from the multiplet splitting of core-level peak. The multiplet splitting in solids has been first observed by C.S. Fadley and co-workers [31, 30]. The multiplet splitting arises, upon ejection of core hole, due to the exchange interaction between the core electron to the unpaired valence electron. The exchange interaction acts only between the electrons with same spin orientations [111].

The spin parallel core electron favors energetically since the the Coulomb interaction between two electrons reduces, and corresponding core level appears in the lower binding energy site with intensity ratio of (2S+1):2S as compared to the anti-parallel orientations found at higher binding energy. The energy separation between the two peaks is given by Van Vleck's Theorem [68],

$$\Delta E_{n,s} = \frac{2S+1}{2l+1} J^l(ns, n'l'), \tag{2.13}$$

where S is the total initial state spin (initial core level spin is zero), J an atomic exchange interaction between valence subshell $n'l'$ and core-electron ns upon core-hole formation. Here the magnitude of splitting is proportional to exchange integral, hence the larger splitting will be observed for those core levels having greater spatial overlap with the valence state. It

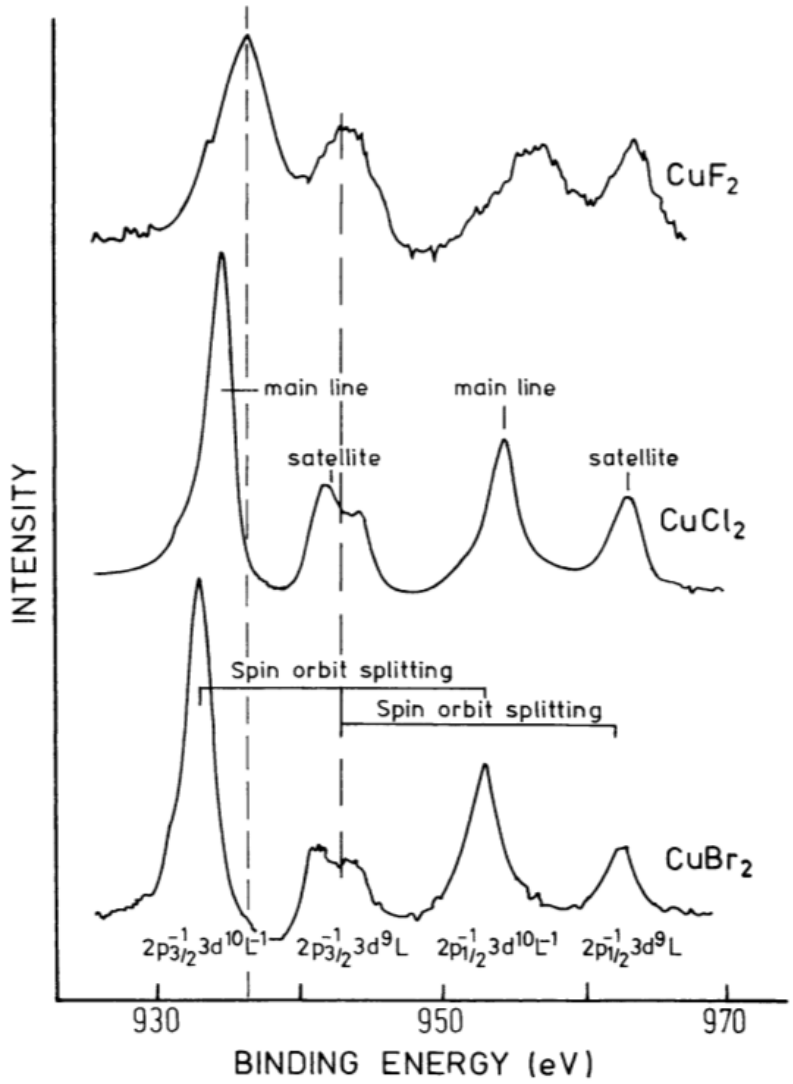

Figure 2.5: Cu-2p spectra of copper dihalides. The main peaks and satellite structures are due to the different screening channels [56, 119]. See text for more details.

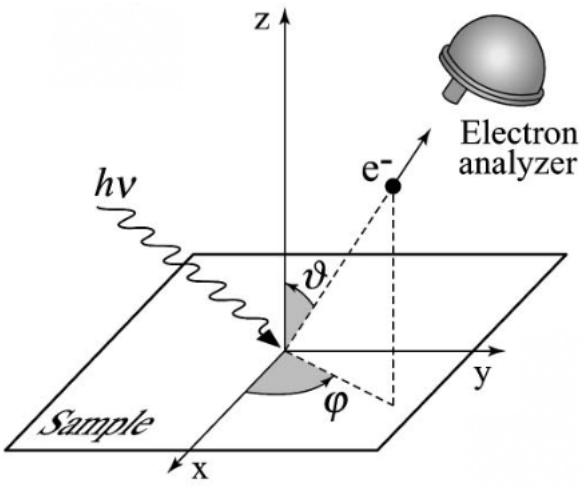

Figure 2.6: Geometrical sketch of ARPES experiment. The outgoing photoelectron emitted with polar (θ) and azimuth (ϕ) angle is detected in an electron analyzer. Ref. [23]

is to be noted that this interpretation neglects the electron correlations and approximately valid.

2.3 Angle Resolved Photoemission Spectroscopy (ARPES)

The figure 2.6 shows geometrical set up of angle resolved photoemission spectroscopy (ARPES). In ARPES, the energy of outgoing photoelectron is recorded as a function of emission angle with respect to the normal of the sample. The emission angle is directly related to the in-plane crystal momentum of initial state. Thus, it is possible to map the electronic band structure in a single crystalline sample.

The binding energy of outgoing photoelectron is obtained by the equation (2.1). And,the initial state crystal momentum parallel to the surface $k_{||}$ is conserved and related to emission angle θ by

$$p_{||} = \hbar k_{||} = \sqrt{2mE_{kin}}.\sin\theta. \tag{2.14}$$

However, the perpendicular component is not conserved due to the translational symmetry broken along normal to the sample. Hence, the crystal momentum can not be determined completely. To overcome this problem one has to make an assumption that the final state of

the photoelectron is simple plane wave. This assumption is valid only for the higher excitation energy; for lower photon energy, crystal field is relatively strong and can affect kinetic energy of the photoelectron. In this simple approximation, the perpendicular component of photoelectron is given by

$$\hbar k_{\perp} = \sqrt{2m(E_{kin}\cos^2\theta + V_0)}, \tag{2.15}$$

where V_0 is inner potential. For a system having very weak dispersion along normal to the surface (2D system), the uncertainty in $k_{\perp}$ is less relevant and the band dispersion is almost exclusively determined by the parallel component $k_{||}$.

Generally, the ARPES experiment is performed at lower photon energy ($h\nu$<100 eV). The advantage of using lower photon energy is that high momentum and energy resolutions can be achieved. Further, one can disregard the momentum of the photon. The disadvantage of working at lower photon energy source is extreme surface sensitivity and unable to probe large reciprocal space in Brillouin zone.

The ARPES is known to be one of the best tools to explain electron correlations in many body systems. The correlated electron system has been conveniently discussed by the Green's-function formalism [74, 34]. The propagation of single electron in the many-body system can be described by Green's-function [23],

$$G(\mathbf{k},\omega) = \frac{1}{\omega - \epsilon_{\mathbf{k}} - \Sigma(\mathbf{k},\omega)}, \tag{2.16}$$

where $\epsilon_{\mathbf{k}}$ is bare-band energy, ω the electron energy with respect to Fermi level, and $\Sigma(\mathbf{k},\omega) = \Sigma'(\mathbf{k},\omega) + i\Sigma"(\mathbf{k},\omega)$ electron self energy. The real and imaginary part of self energy contains all the information about the energy renormalization and lifetime, respectively of an electron. Also, the one particle spectral function can be obtained from the Green's function by the relation, $A(\mathbf{k},\omega) = -(1/\pi)\ \mathrm{Im}G(\mathbf{k},w))$ [1]

$$A(\mathbf{k},\omega) = -\frac{1}{\pi}\frac{\Sigma"(\mathbf{k},\omega)}{[\omega - \epsilon_{\mathbf{k}} - \Sigma'(\mathbf{k},\omega)]^2 + [\Sigma"(\mathbf{k},\omega]^2} \tag{2.17}$$

[1]The derivation of equations (2.17) and (2.18) can be found in Ref.[23]

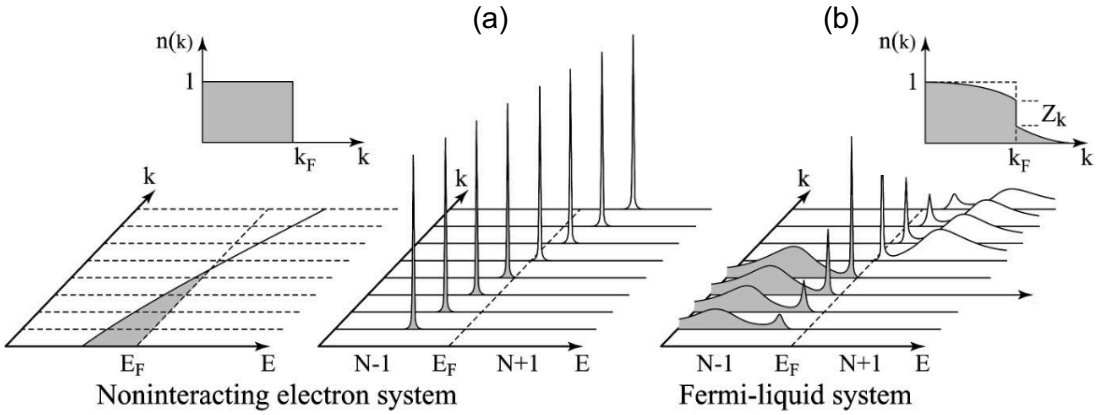

Figure 2.7: Photoemission intensity for (a) Non-interacting and (b) interacting systems. In the latter case, the main peaks along with satellite features have been observed. For each system corresponding momentum distribution (n(**k**) at ground state (T=0 K) is also shown. Ref.[23]

As the ARPES signal is proportional to the one particle spectral function by the relation,

$$I(\mathbf{k},\omega) = I_0(\mathbf{k},\nu,\mathbf{A})f(\omega)A(\mathbf{k},\omega), \tag{2.18}$$

one can extract self-energy from the experimental data which in turn gives access to the understanding of electron correlations within the many body system. Figure 2.7 shows the ARPES intensity for (a) non-correlated and (b) correlated system. In the relation (2.18), $I_0(\mathbf{k},\omega)$ is proportional to one-electron matrix element $|M_{f,i}|^2$ (see eq. (2.9) and (2.10)), Fermi function $f(\omega)$ is included since the direct photoemission probes only to the occupied states.

The matrix element $M_{f,i}$ is responsible for the dependence of photoemission data on photon energy and the polarization of photon source. The enhancement or suppression of photoemission intensity is determined by the matrix element; to have finite photoemission intensity whole integrand $M_{f,i}$ must be even function under reflection with respect to the mirror plane. (Here the scattering plane coincides with the mirror plane of the sample). The final state will have an even parity when the detector lies in the mirror plane, so $\epsilon.\boldsymbol{p}\,|\phi_i^k\rangle$ must be of even parity. Thus, the dipole operator allows one to determine the initial state within the sample, and it is even for p-polarization and odd for s-polarization light. For the

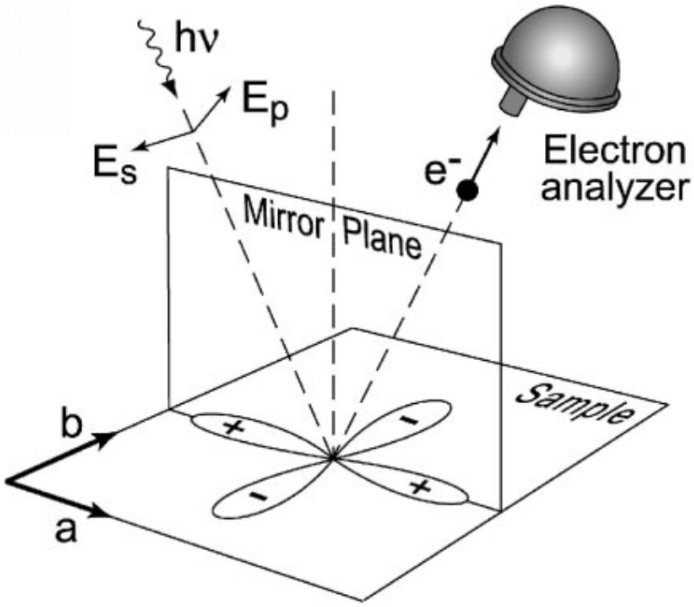

Figure 2.8: Geometrical representations of photon polarization and mirror plane. The in-plane orbital $d_{x^2-y^2}$ is symmetrized by the mirror plane. Ref.[23]

particular case shown in Figure 2.8 the whole integrand will be even parity for p-polarized light since the initial state is even parity. It is also to be noted that for p and s-geometry, the photon polarization lies in parallel and perpendicular to the scattering plane, respectively. The scattering plane is the plane where the incoming photon, outgoing photoelectron and surface normal contains.

2.3.1 Soft X-ray ARPES

One of the disadvantages of conventional ARPES, which uses the photon energy in the range of 20–100 eV, is its extreme surface sensitivity. This is observed from the universal curve of IMFP (λ) (see Figure 2.2). In order to measure bulk band-dispersion, the photon source of very low or high energies should be used. The very low photon energy can be achieved from the laser source, but it only probes to a small region near the center Brillouin zone. Thus, the high photon energy ARPES, typically in the range of 0.5–2 keV (called soft X-ray ARPES), is useful for probing bulk sensitivity.

In addition to the benefit of bulk sensitivity, surface-perpendicular momentum resolution which is obtained by uncertainty principle $\Delta k_{\perp} \approx 1/\lambda$ can be improved by the soft X-ray ARPES. Also, the final-state above about 500 eV can be considered as free electron like [32]; thus, the free-electron final state approximation is valid in case of soft X-ray ARPES. Furthermore, at sufficiently high photon energy the photoemission matrix element $M_{f,i}$ virtually reduces to the atomic cross-section, and it simplifies the interpretation of photoemission spectra in terms of valence-band spectral function [114]. Another advantage of working at high photon energies is that certain absorption edges such as L-edges of transition metals and M-edges of rare earth can be tuned, which allows resonating corresponding d- or f-states. This process can play an essential role in understanding the physics of strongly correlated system.

Despite the fact that soft X-ray ARPES has advantages as mentioned above, it also shows some serious challenges. The main challenge is the reduction in the valence band (d- and f-character) cross-section, typically 2-3 orders of magnitude, at high photon energy [133]. This has to be compensated by generating very high photon flux and the use of efficient electron detector. In case of the soft X-ray ARPES, the energy resolution (beamline plus spectrometer resolution) is in the order of tens of meV, in contrast to VUV-ARPES where it is about few meV. So, important information such as kinks in the electron dispersions relating to the quasiparticle interaction can be missing. Similarly, the momentum resolution which is related to the energy will also be worsen at high photon energy as the final state wave vector (k_f) depends on the kinetic energy of photoelectron.

The creation or annihilation of phonon is also responsible for the smearing of the momentum [59, 106] in ARPES spectrum. At high temperature and photon energy the ARPES spectra are essentially identical to the k-integrated DOS or it can be referred to the XPS limit in which the angular dependent valence band can be attributed to the X-ray photoelectron diffraction [50, 93, 40]. Considering the fact that fraction of direct transition is expected in the ARPES experiment, the effect of temperature dependent can be estimated from the photoemission Debye-Waller (DW) factor by the relation $W(T) \approx e^{(-g_n^2\langle U^2(T)\rangle)}$, where $\langle U^2(T)\rangle$ is the three dimensional mean-squared vibrational displacement at temperature T, g_n the reciprocal vector and is given by the relation, $g_n = k_f - k_i - k_{h\nu}$,

here the photon momentum $k_{h\nu}$ has been included since it is an appreciable quantity at high energy. The DW factor suggests the cryogenic experiments to limit the phononic effect. As photoelectron liberates from the system, recoil of the atom occurs hence it looses energy to the photoelectron, causing the broadening as well as the shifting of spectra.

2.4 X-ray Absorption Spectroscopy

In X-ray absorption spectroscopy (XAS), the incoming photon energy excites a core-electron into the higher unoccupied state, and the electron is recorded by some means, so XAS allows one to obtain information about the unoccupied electronic structure, particularly of valence state. Thus, for the X-ray absorption an empty final state is required, as the X-ray energy is higher than the binding energy of the core-electron the sharp increase in the absorption spectrum occurs. Traditionally, XAS is a process of measuring the intensity of X-ray before and after the X-ray passes through the thin film. But, this method is limited only for the hard X-ray as the mean absorption length is in the order of thickness of the thin film [1]. However, for the soft X-ray regime this method is problematic since it is impractical to make the free-standing thin film of thickness in the order of absorption length. Fortunately, the report in 1972 [41] suggests that electron yield from the sample is proportional to the X-ray absorption cross section, which allows one to measure soft XAS in various photoyield mode. The most commonly used photoyield modes is total electron yield (TEY) method, where all the electrons emitted from the sample are detected, independent of their energy. However, other detection modes such as fluorescence yield, partial electron yield, and ion yield has also been used; these modes will not be discussed here and can be found elsewhere [26]. Here, we only discuss the TEY method as we use this method in our experiment, which will be presented later.

In TEY mode, a detection device such as picoammeter can be used to measure the current and is amplified by the channeltron (electron multiplier) for the detectable signal. It is known that the interaction of electron with matter has much larger effect than that of photon, thus the detectable electrons are originated from the surface or few atomic layers beneath it. The mean probing depth for XAS in TEY is in the range of 3–10 nm. For

the rare earth element the probing depth lies even below this range due to the large X-ray absorption cross-section, which results small X-ray penetration depth (hence small electron escape depth). The total intensity in TEY mode has been related to the electron escape depth (λ_e) and X-ray penetration depth ($\lambda_p(\Omega)$ is given by [26]

$$I_{TEY}(\Omega) \propto \frac{\lambda_e}{\lambda_e + \lambda_p(\Omega)\sin\alpha}, \tag{2.19}$$

where α and Ω are the angle of incidence and frequency of incident X-ray, respectively. In case $\lambda_e \ll \lambda_p$, the TEY is inversely proportional to the λ_p, that is, the absorption coefficient. For the grazing incidence (α close to 0), saturation effects can occur.

Finally, an important aspect of XAS is that it provides the element specific information. In addition, with the use of linear polarization light, the anisotropy information such as molecular orientation and the lattice anisotropy can also be obtained from the XAS. The weak side is that the XAS spectra of two or more type of atoms of same element is the linear combination of all individual site which limits the usefulness of XAS for the compounds having non-equivalent atomic sites [25].

2.5 Resonant Photoemission Spectroscopy

In order to obtain elemental specific contribution to the valence band, the resonant photoemission spectroscopy (ResPES) is used [16, 83]. In ResPES measurements, the photon energy is tuned to the absorption edge of deeper core level such that the electron is excited to the lowest unoccupied state. The portion of the valence band (VB) corresponding to the resonating level is enhanced which can be extracted from the total valence band spectrum. The resonant process occurs only when the lifetime of the core hole (in the oder of femtosecond) is shorter than that of the excited state, depending upon the degree of localization of excited electron [18]. The core hole decays by the nonresonant process with no enhancement of signal in the valence band spectrum, if the excited electron delocalizes faster than the core-hole lifetime.

In the resonant process, the PES signal comprises of all the possible non-radiative decay channels. The possible non-radiative decay channels are schematically represented in the Figure 2.9. Figure 2.9 (a) and 2.9(b) represent resonant processes while 2.9 (c) represents the non-resonant process. In the first resonant process named as participator decay, an electron from VB recombines with the core hole, created upon the photoemission process, while the excited electron promoted to continuum beyond the vacuum level. This process is generally associated with ResPES event. In the second resonant process, referred to spectator decay, the excited electron remains in the same excited state and an electron from the valence band recombine with the core hole, while another electron from the VB lifted to the continuum region. The excited electron can also hop to neighboring atomic site before the core hole decays, a non-resonant decay which is generally referred as a charger transfer Auger process, where the core hole decays via normal Auger process. These two resonant channels and direct photoemission channel, both in same final states, interfere each other as such significant increase or decrease in the intensity occurs depending upon the phase of direct and resonant channels. The magnitude of the intensity modulations gives rise to the degree of localization of excited electrons to unoccupied state. Moreover, the interference of two final states gives rise asymmetry in ResPES intensity as a function of the photon energy known as "Fano line shape" [33].

The photon energy dependence of resonant photoemission can be measured in two modes: constant initial state (CIS) and constant final state (CFS) modes. In CIS mode [112, 69], the initial state energy (ionization energy) is held fixed, and the spectrum is acquired by varying the energy of incoming photon source and the kinetic energy simultaneously. Thus, the dependence of intensity modulations on the photon energy can be described by CIS mode [18] in terms of Fano profile, giving rise the time scale of the charge transfer [124]. On the other hand, in CFS mode the kinetic energy is held constant and the spectrum is recorded by varying the initial state energy and photon energy simultaneously. The cross-section of the resonance photoemission lineshape can be measured by the CIS spectrum, while CFS spectrum is related to the photon-absorption.

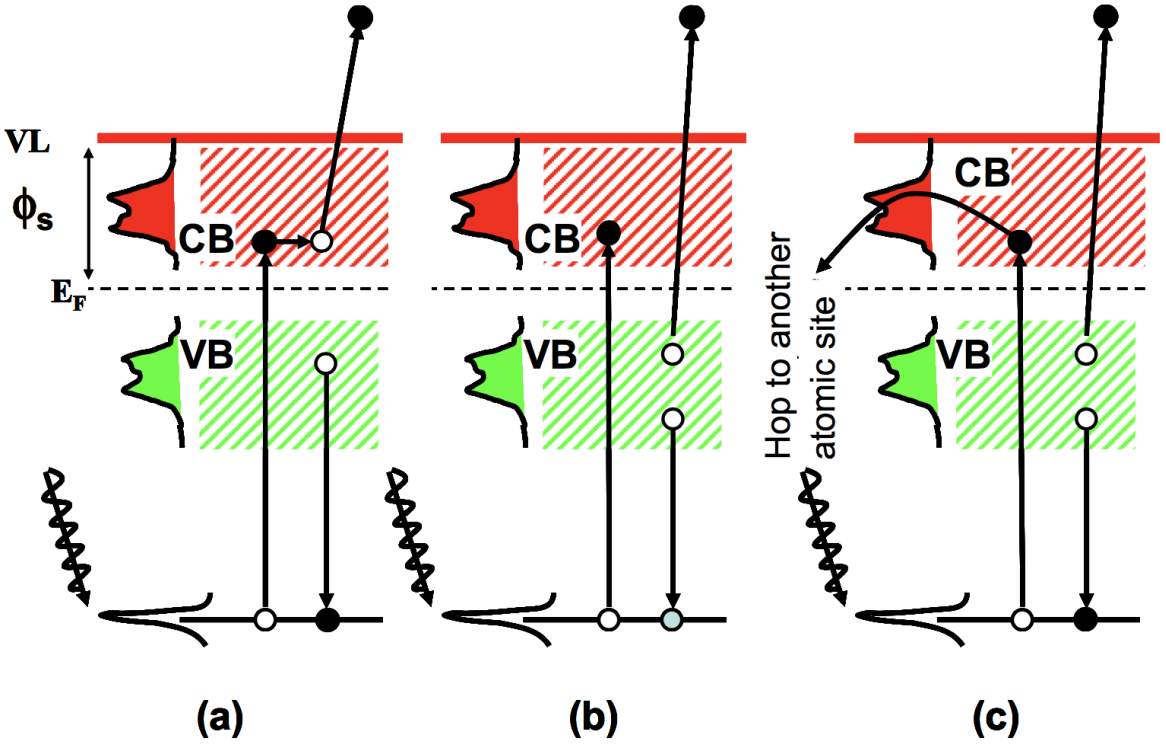

Figure 2.9: Resonant photoemission. (a) Participator decay: the excited electron in CB participates itself in decay with releasing electron from either VB or CB. (b) Spectator decay: the excited electron does not participate in decay but sits in CB while two electrons in VB participates in decay. (c) Charge transfer: he excited electron in the CB hops to neighbor atomic site and relaxation occurs via normal Auger decay. [18]

Chapter 3

Density Functional Theory

3.1 Introduction

The density functional theory (DFT) is a computational modeling which has been extensively used to investigate the electronic structure of the many body system, such as atoms, molecules, condensed phases etc., after W. Kohn and L.J. Sham in 1965 proposed a equation, based on the electron density, famously known as "Kohn-Sham equation". Their remarkable work on DFT led W. Kohn to be awarded for the Nobel prize, in chemistry, in 1998.

A simple system such as hydrogen atom or simple two-dimensional square potential can be easily solved by the Schrödinger equation. However, it is virtually impossible to solve N-body Schrödinger equation, as it contains N-independent equations and requires huge computational effort. The N-electron Schrödinger equation is given by

$$\hat{H}\Psi = \left[\sum_{i}^{N} \left(-\frac{\hbar^2}{2m_e} \bigtriangledown_i^2 \right) + \sum_{i}^{N} V(\vec{r}_i) + \sum_{i \neq j}^{N} V_{e-e}(\vec{r}_i, \vec{r}_j) \right] \Psi = E\Psi, \tag{3.1}$$

where the first term in the Hamiltonian ($\hat{H}$) is the kinetic energy, second term the potential energy from the external field due to the positively charged ions, last term is the electron-electron interaction, and E is the total energy. Here, the nuclei in molecules or solid are treated as fixed particle (Born-Oppenheimer approximation). Due to the complexity of the equation one has to make proper approximation to solve it.

There are several sophisticated methods to solve the equation (3.1). One of them is the Hartree-Fock (HF) approximation, where the wavefunction for electrons can be approximated by a single Slater determinant. The set of N-coupled equation is solved by the variational method which yield HF wavefucntion and energy. This approximation gives quite good results for the lighter atoms or molecules. However for heavier atoms or solids, the HF results is not consistent with experiment. The main drawback of HF approximation is that it neglects the electron correlations, however, it accounts the exchange interaction of electrons. To address this issue, one alternative solution is to use the DFT approach. In DFT method, one considers the electron density rather than the single particle wavefunction and it also includes the exchange and the correlations terms.

3.2 Hohenberg-Kohn Theorems

In 1961, Hohenberg and Kohn (HK) developed an approximation method to deal an inhomogeneous electron system of interacting electrons. The HK theorems can be divided into two parts: The first theorem proves the one to one mapping between the external potential and ground state electron density, while the second theorem says about the analytical form of universal functional of energy and the practical ways to obtain ground state electron densities. We briefly discuss these two theorems below, the detailed explanation can be found in the original paper by HK [52].

First Theorem:

Suppose a system of N-electron moving under the influence of external potential $v(r)$ [1], then from the postulates of quantum mechanics these quantities (N and $v(r)$) determine the ground state wave function and hence the ground state density of state; in other words, $\rho(r)$ is functional of $v(r)$. Hohenberg and Kohn proved that the opposite is also true: *the external potential $v(r)$ is uniquely determined by the corresponding ground state electron density, to within additive constant.* which can be proved as following:

[1] the external potential $v(r)$ has the form: $v(r(i)) = \sum \frac{Z_\alpha}{|r_i - r_\alpha|}$, where Z_α is the nuclear charge, r_i and r_α are the positions of electron and ion, respectively.

Let us consider two external potential $v(r)$ and $v(r')$ such that, $v(r) - v(r') = constant$, and corresponding ground state wavefunctions are ψ and ψ', respectively, giving rise to the same electron density $\rho(r)$. If the Hamiltonian and ground state energies associated with ψ and ψ' are denoted by H, H' and E, E', then one can write

$$E < E' + \int [v(r) - v(r')]\rho(r)drdr' \tag{3.2}$$

. similarly, we can also write

$$E' < E + \int [v(r') - v(r)]\rho(r)drdr' \tag{3.3}$$

. Adding (3.2) and (3.3) leads to a contradiction,

$$E + E' < E' + E. \tag{3.4}$$

Hence, $v(r)$ is a unique functional of $\rho(r)$. The external potential and the electron density determine all the ground state properties since the Hamiltonian and ground state wavefunctions are determined by them.

Second Theorem:

A universal functional of the energy, $E_v[\rho(r)]$ for a given external potential $v(r)$ can be defined in terms of density $\rho(r)$ since energy can be written as a functional of electron density, from the first theorem. For a particular potential $v(r)$ the ground state energy is determined by the global minimum value of this functional, minimization gives rise to the correct wavefunction or electron density (ground state). The ground state energy has the form

$$E = \int v(r)\rho(r)dr + F[\rho(r)] \tag{3.5}$$

The universal functional $F[\rho(r)]$ is valid for any number of particle and is independent of external potential. For the convenience, the classical long range coulomb interaction is separated from the function $F[\rho(r)]$. Then the ground state energy of inhomogeneous

electron system for the static external potential is given by

$$E = \int v(r)\rho(r)dr + \int \frac{\rho(r)n(r')}{|r'-r|}drdr' + G[\rho(r)], \tag{3.6}$$

where $G[\rho(r)]$ is another functional of density like $F[\rho(r)]$. The major complication of this equation is the determination of universal functional $G[\rho(r)]$. If $G[\rho(r)]$ were known or sufficiently simple function of density then it would be easier to determine the ground state since it only requires to minimize the electron density.

The HK theorems are very powerful as they show that the ground state density of states can be used to determine the physical properties of the system. But they do not offer a way of finding the ground state energy.

3.3 Kohn-Sham Equations

In 1965, Kohn and Sham [66] developed a simple method to solve the problem of inhomogeneous system of an interacting electrons developed by HK. The main idea is to replace a system of interacting particles by a set of non-interacting quasiparticles in an effective potential such that the non-interacting system produces same density as of the interacting system.

The ground state energy of a inhomogeneous interacting system in a static potential is given by the expression (3.6), and is minimum for the correct density $\rho(r)$. Now, the universal functional $G[\rho]$ can be written as,

$$G[\rho] = T_s[\rho] + E_{xc}[\rho], \tag{3.7}$$

where $T_s[\rho]$ is kinetic energy of non-interacting electrons of density $\rho(r)$, and $E_{xc}[\rho]$ is exchange and correlation energy of an interacting system with density $\rho(r)$. For sufficiently slowly varying density $\rho(r)$ one can, however, write

$$E_{xc}[\rho] = \int \rho(r)\epsilon_{xc}(\rho(r))dr \tag{3.8}$$

where $\epsilon_{xc}(n)$ is exchange and correlation energy per electron of a uniform electron gas of density n. Then the equation (3.6) becomes

$$E = T_s[\rho] + \int v(r)\rho(r)dr + \frac{1}{2}\int\int \frac{\rho(r)n(r')}{\mid r - r' \mid}drdr' + E_{xc}[\rho], \tag{3.9}$$

The minimization of equation (3.9) by the variational principle, implementing the condition

$$\int \delta\rho(r)dr = 0, \tag{3.10}$$

leads to

$$\int \delta\rho(r)\left\{\frac{\delta T_s[\rho]}{\delta\rho(r)} + \phi(r) + \frac{\delta E_{xc}[\rho]}{\delta\rho(r)}\right\}dr = 0, \tag{3.11}$$

where

$$\phi(r) = v(r) + \int \frac{n(r')}{\mid r - r' \mid}dr' \tag{3.12}$$

The equations (3.10) and (3.11) indicate that the non-interacting electrons moving under the influence of potential $\phi(r) + \frac{\delta E_{xc}[\rho]}{\delta\rho(r)}$ which is equivalent to the interacting system in the external potential $v(r)$ as defined by HK. The density $\rho(r)$ which satisfies these two equations, providing potential, can be simply obtained from the Schrödinger equation

$$\left\{-\frac{1}{2}\bigtriangledown^2 + \left[\phi(r) + \frac{\delta E_{xc}[\rho]}{\delta\rho(r)}\right]\right\}\psi_l(r) = \epsilon_l\psi_l(r), \tag{3.13}$$

such that

$$\rho(r) = \sum_{l=1}^{N} \mid \psi_l(r) \mid^2, \tag{3.14}$$

where N is the number of electrons (non-interacting quasiparticles). The equation (3.13) is known as famous Kohn-Sham equation. Then the total energy of the system is given by

$$E = \sum_{l=1}^{N}\epsilon_l - \frac{1}{2}\int\int \frac{\rho(r)n(r')}{|r - r'|}drdr' + E_{xc}[\rho] - \int \frac{\delta E_{xc}[\rho]}{\delta\rho(r)}dr \tag{3.15}$$

The equations (3.11)–(3.15) are commonly solved by the self-consistent method: Firstly, initial guess of $\rho(r)$ is made and then it is used to construct ϕ and $\frac{\delta E_{xc}[\rho]}{\delta\rho(r)}$, and construct a

new $\rho(r)$ from (3.13) and (3.14), the process continues until the satisfactory approximation is reached.

The biggest challenge of equation (3.15) is that the no analytical expression of exchange and correlation term ϵ_{xc} exists. Then the ϵ_{xc} has to be approximated. The number of approximations on ϵ_{xc} has been utilizing so far, here, we only discuss the local density and generalized gradient approximations.

3.4 Local Density Approximation

The local density approximation was originally proposed by Kohn and Sham and is valid for slowly varying density. In this approximation, the density is treated locally as homogeneous electron gas, and the exchange-correlation energy at each point is same, which has the form [2]:

$$E_{xc}^{LDA}[\rho] = \int \rho(r)\epsilon_{xc}^{HEG}(\rho(r))dr \tag{3.17}$$

Usually, the exchange-correlation term can be split into the exchange and the correlation terms:

$$E_{xc} = E_x + E_c \tag{3.18}$$

The exchange term is given by the Slater's formula [110], for the local density,

$$E_x = -6\left[\frac{3}{8\pi}\rho(r)\right]^{1/3}, \tag{3.19}$$

while the correlation term is calculated from the quantum Monte Carlo calculations [17].

The LDA calculations give satisfactory result for a system of low spatial varying electron density and is proven well for the structural properties of materials. However, the binding energy of molecules and the cohesive energy of solids are overestimated by the LDA approach. Furthermore, it fails to describe the magnetic and structure ordering of 3d metals, such as

[2] If the spin of the electron is taken into account it is known as local spin density approximation (LSDA) and is expressed as

$$E_{xc}^{LSDA}[\rho] = \int (\rho_\uparrow + \rho_\downarrow)\epsilon_{xc}(\rho_\uparrow, \rho_\downarrow)dr \tag{3.16}$$

iron [122]. To correct these deficiencies, an approach was developed by Perdew, Burke, and Ernzerhof in 1996 [96] which is known as the generalized gradient approximation (GGA).

3.5 Generalized Gradient Approximation

As discussed before the LDA approach is based on the homogeneous electron gas system, but the real system is different from this. The non-homogeneity of the true electron density can be addressed by including gradient of electron density, which is implemented in the GGA approximation. The exchange-correlation term for spin polarized system in GGA is expressed as,

$$E_{xc}^{GGA}[\rho] = \int \epsilon_{xc}(\rho\uparrow, \rho\downarrow, \bigtriangledown\rho_{\uparrow}, \bigtriangledown\rho_{\downarrow})dr \tag{3.20}$$

The exchange part of the functional is same as in the LDA, the gradient is only introduced into the correlation part. This functional demonstrates the improvements over the LDA predictions on ground state properties of atoms, molecules, and solids.

3.6 Augmented Plane Wave Methods

To solve Kohn-Sham equation, one has to consider an appropriate wavefunction which gives correct ground state density, and hence other properties of solid. Linear augmented plane wave (LAPW) and APW+lo, where lo stands for local orbitals, methods are extensively used to solve the Kohn-Sham equation and they predict quite satisfactory results.

In LAPW [107, 12] method, a unit cell is divided into two regions: non-overlapping atomic spheres (I) centered at atomic sites and interstitial region (II) as shown in Figure 3.1. In two regions different basis sets are used. Inside the sphere linear combination of radial functions times the spherical harmonics is used, and in the interstitial region plane wave expansion is used:

$$\phi_{kn} = \begin{cases} \sum\limits_{lm} [A_{lm,kn}\ u_l(r, E_l) + B_{lm,km}\ \dot{u}_l(r, E_l)]Y_{lm}(\hat{r}), & \vec{r} \in I; \\ \frac{1}{\sqrt{\omega}} e^{ik_n.r}, & \vec{r} \in II. \end{cases} \tag{3.21}$$

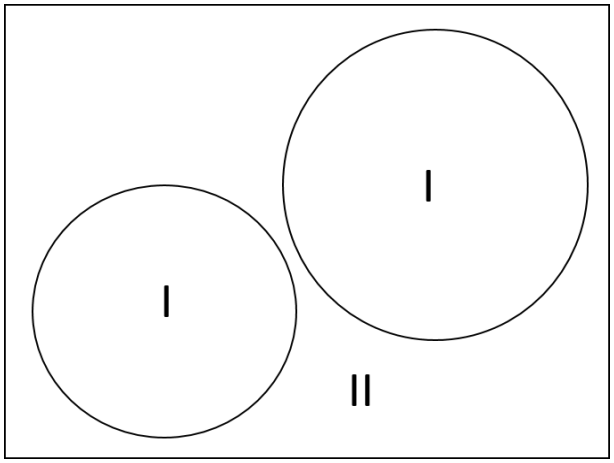

Figure 3.1: Two regions of unit cell containing two atoms, I represents the non-overlapping atomic spheres and II represents interstitial region.

where $u_l(r, E_l)$ is the radial solution of Schrödinger equation for energy E_l, $Y_{lm}(\hat{r})$ is the spherical harmonics. ω is the cell volume and $\vec{k}_n = \vec{k} + \vec{G}$, where G is reciprocal vector and k is the wave vector inside the first Brillouin zone. A_{lm} and B_{lm} are expansion coefficients and are functions of K_n.

In 2000, E. Sjöstedt et al.[109] introduced the APW+lo method, where the wave function is computed at fixed linearization energy to avoid non-linear eigenvalue,

$$\phi_{kn}^{lo} = \begin{cases} \sum\limits_{lm} [A_{lm}\ u_l(r, E_l) + B_{lm}\ \dot{u}_l(r, E_l)]Y_{lm}(\hat{r}), & \vec{r} \in I; \\ 0, & \vec{r} \in II. \end{cases} \tag{3.22}$$

where A_{lm} and B_{lm} do not depend on K_n and are determined by the condition that lo is zero at the boundary of sphere and normalized. In APW+lo method, the quantities such as the total energy, forces converges significantly faster than in LAPW with the same accuracy. So, APW+lo method is useful for the systems (f- or d- states, atoms with small sphere) which are difficult to converge.

Chapter 4

Experimental Technique for Photoemission Spectroscopy

We have utilized various techniques to successfully complete the research for this thesis. We obtained single crystal of intercalated systems by employing the chemical vapor transport method using iodine as a transport agent. The starting materials to grow crystal were stored in a glove box to prevent them from oxidation. Further, the sample mixing was also carried out inside the glove box. To synthesize the single crystals, we utilized the high temperature box and tube furnaces. In order to identify the phase of sample, we utilized the X-ray diffractometer by the Brucker Corporation. These samples are further characterized by magnetic and transport properties utilizing the Quantum Design's Magnetic properties Measurement System (MPMS) and Physical Properties Measurement System (PPMS).

Here, we mainly focus on the experimental details for the photoemission experiments as the main body of the thesis is about results obtained from the photoemission experiments.

4.1 Ultra-High Vacuum System

The photoemission experiment is carried out in the work chamber which is in Ultra-high vacuum (UHV) regime with pressure better than 10^{-11} Torr. The chamber is made up of Mu-metal so that the path of the electron is not affected by magnetic field if present in the laboratory. The UHV regime is created by the combination of varieties of pumps. It

is necessary to use the right pump depending on the pressure regime. Some pumps remove the gases and some trap or change their form. It is obvious that no single pump can take a system from the atmosphere to the UHV range. So, two or more pumps are required to use to gain this pressure. Here, we will discuss a list of pumps which are connected in photoemission spectrometer used to collect data for this thesis.

Rough or scroll pump is used initially to evacuate a vacuum system, the large volume of gas can be quickly pumped out from the work chamber with pumping speed as large as 1,000 cubic ft per minute or more. This pump brings the system into molecular regime from the laminar one, thus another pump suitable for the UHV system can be operated. Such a pump is turbomolecular pump which can be operated from steady state inlet pressure as high as 10^{-2} Torr obtained from the rough pump to below 10^{-10} Torr. And, it operates with speed to range 9,000 to 90,00 rmp. This is very clean mechanical pump that can reach to UHV regime without using traps. The turbomolecular pump is comprised of the rotating and fixed blades alternatively such that gas molecules can be pumped out by giving momentum to a desired direction with repeated strike on the moving surface. To maintain the system into lower ultimate pressure turbo pump should be backed by another smaller turbo pump which is then backed by a roughing pump.

To maintain the UHV pressure in the vacuum system for long periods of time, different kind of pumps such as titanium sublimation pump (TSP) or ion pump are used. These pumps operate differently than that mentioned earlier pumps. The TSP pump is a gas capture or the storage pump, it is often called getter pump. And, it consists of the titanium and heating sources. When the titanium is properly heated it sublimes and is deposited as a film into surrounding walls. Since the titanium is very reactive substance which easily reacts with residual gases colliding on it and changes them into solid form such as titanium hayrides, oxides, or nitrides and the pressure of the system drops. Once the titanium film becomes saturated, the titanium filament is heated to obtain fresh film on the walls of the chamber. Importantly, the operation of the pump above the normal pressure will reduce the operating life of the pump. The TSP pump is usually combined with ion pump. In the ion pump electrons are generated from cathode and are travelled towards the anode, on their way the electrons interact with the residual gas and ions are created. By applying

magnetic field electrons do not travel straight to the cathode, instead they travel in a helical path which increases the probability of colliding with the gas molecules on their way to anode. Due to the magnetic field the electron does not come easily to the anode, creating electron cloud around anode and more gas molecules are ionized. These ionized particles are accelerated towards cathode usually made up of titanium. The accelerated ions either buried into or sputtered or chipped away the cathode titanium. The sputtered titanium combines chemically with the gas to convert them into solid, which are later pumped by a pump. The ion pump are clean operating device having no moving parts or oil and can also be baked to few hundreds Celsius without damaging magnets. We can achieve the pressure better than 10^{-11} Torr with overnight bakeout of the system. The bakeout releases gas molecules stuck on the wall of the chamber. These molecules are then pumped by ion pump.

4.2 Sample Mounting and Manipulator

The sample for photoemission experiment is prepared by glueing it into a sample plate by H20E Epoxy, and on top of it a post is attached using the Torr Seal. A proper heat treatment is carried out to dry the Epoxy and Torr Seal so that the sample and the post are firmly attached to their respective positions. Then, the sample is transferred into a fast entry lock where multiple samples can also be stored in a garage, this is the only one chamber exposed to atmosphere. After pumping this chamber to the lowest possible pressure sample is moved to the preparation chamber, the base pressure for this chamber is about 10^{-9} Torr. When the preparation chamber reaches to its base pressure, the sample is finally transferred into the manipulator located in the main chamber (work chamber) where the sample is cleaved by a pincher attached to the transfer arm and valve to the preparation chamber is closed immediately. In this way very fresh surface of the sample is obtained.

The manipulator has three transitional (x,y,z) and three rotational (θ, ϕ, ω) degrees of freedom. This facilitates one to move sample from LEED to photoemission position back and forth. The LEED experiment is performed mainly to orient sample in a desired direction in BZ. Once the sample being oriented to a specific direction, it is moved back to photoemission position. The translation movements allow to focus the sample to the electron analyzer and

select the best part of the sample. The rotation degrees of freedom allows one to measure the parallel component of the momentum $k_{||}$. Three angles named polar (θ), flip (ϕ), and azimuth (ω) are responsible for k-space mapping. With the use of θ bands along k_x-direction can be recorded, aligning analyzer slit along particular direction in the BZ. The angle ϕ is used to measure the spectrum in different region by moving along k_y-direction in the BZ while orienting slit along x-direction, which allows to obtain the Fermi surface mapping of sample. Sometimes, it is also necessary to go from one to another direction in the BZ, in this case angle ω is used. As the slit lies in the mirror plane of the sample, when the sample is oriented along one direction the point in BZ lies in another direction will not contain in the mirror plane. It is to be noted that translation movements do not effect the $k_{||}$ measurements, only the count rate may be changed.

The materials of manipulator should be selected in such a way that it neither expands nor shrinks with changing temperatures, since measurements may have to be done at higher to lower temperatures. In the ARPES chamber in Mannella's lab at Joint Institute for Advanced Materials (JIAM) cold head in the manipulator is connected to the liquid nitrogen or helium Dewar through a supply line and continuously pump in the liquid by a diaphragm pump during measurement. Also, a heater is attached to the sample stage. Thus, a wide range of temperate can be achieved in the laboratory.

For a solid specimen an electrical connection is made between the sample stage and the spectrometer so that the Fermi levels of spectrometer and sample are equal which has been explained from the Figure 4.1. For a simplest case such as in metallic system it is straightforward to locate the Fermi level as it is the top most filled occupied state at absolute zero. Even in normal temperature this interpretation of Fermi level is still valid. However, for a semiconductor it is challenging to locate the Fermi level. As shown in the Figure 4.1 the vacuum level for the spectrometer need not be equal to that of sample such that electron in passing from the surface of the sample to spectrometer the electron will feel the accelerating or retarding potential of ϕ - ϕ_{spect}. Thus, the initial kinetic energy E'_{kin} of electron at the surface of the sample becomes E_{kin} inside the spectrometer,

$$E_{kin} = E'_{kin} + \phi_s - \phi_{spect} \tag{4.1}$$

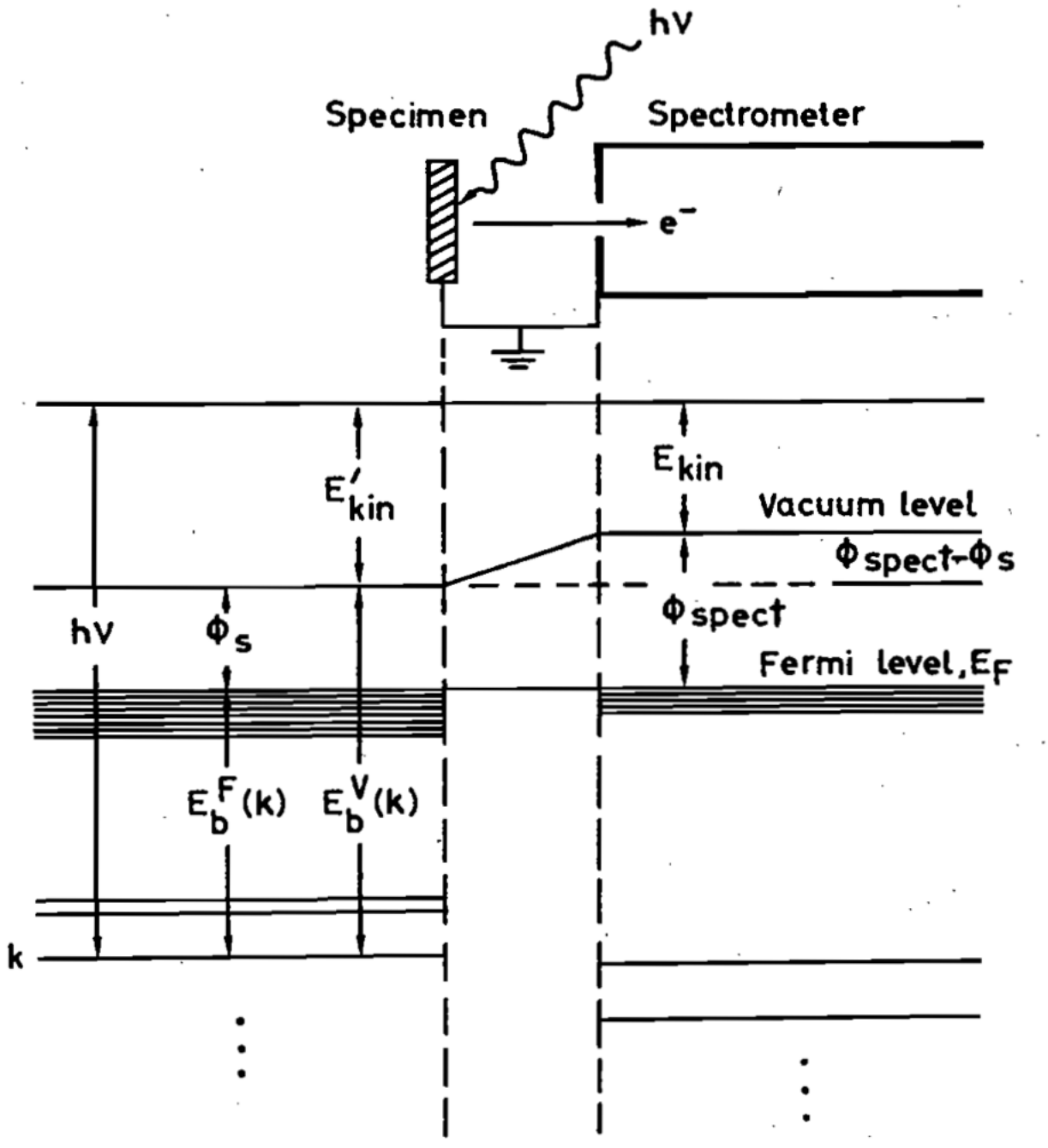

Figure 4.1: Schematic diagram of energetics for the photoemission experiments for metallic sample. The sample and spectrometers have equal Fermi level and are grounded. Ref [29]

Since the workfunction is sample dependent quantity. Thus, it is not practical to work with the workfunction of the sample. However, the work function of the spectrometer remains constant with variation of samples, so the binding energy of the metallic sample can be measured simply with reference to the identical Fermi levels of sample and spectrometer,

$$E_B^F = h\nu - E_k - \phi_{spect} = h\nu - E_k' - \phi_s, \tag{4.2}$$

where F represents the binding energy with reference to the Fermi level. Typically ϕ_{spect} are determined from the spectra recorded from the polycrystalline gold sample.

4.3 Light Sources

We used two types of radiation sources in present work which are He-based VUV radiation produced in the laboratory and the synchrotron radiation source in national laboratories. VUV radiation in the laboratory is generated from the He gas by generating VUV-microwave employing cyclotron resonance [8]. The microwave is generated by the Klystron which is powered by 300 W with frequency of 10 GHZ. Such microwave is fed to discharge region through a rectangular waveguide. In a far distance from the window, magnet poles are situated which generates magnetic field in the direction perpendicular to line of force of the electric. With the condition of the cyclotron resonance, the electrons are trapped by the magnetic field and are accelerated by microwave field to high energy encountering He atoms. The He atoms are promoted to the excited state and are then decayed by releasing multiple VUV radiation lines which are later monochromatized by a monochromator. Most of the monochromatized light are originated from the He-Iα, which is observed due to the doubly excited transition $1s2p \rightarrow 1s^2$. Another, important line is He-II α, resulting from $2p \rightarrow$1s transition. He-Iα and He-II α are centered at energies 20.21 eV and 40.81 eV, respectively.

The synchrotron radiation is generated as following: a relativistic electron circulating in a storage ring when passes through an undulator produces white radiation light called synchrotron radiation. The undulator is a straight section of the storage ring which consists of periodic structure of dipole magnets. The white light thus produced is monochromatized

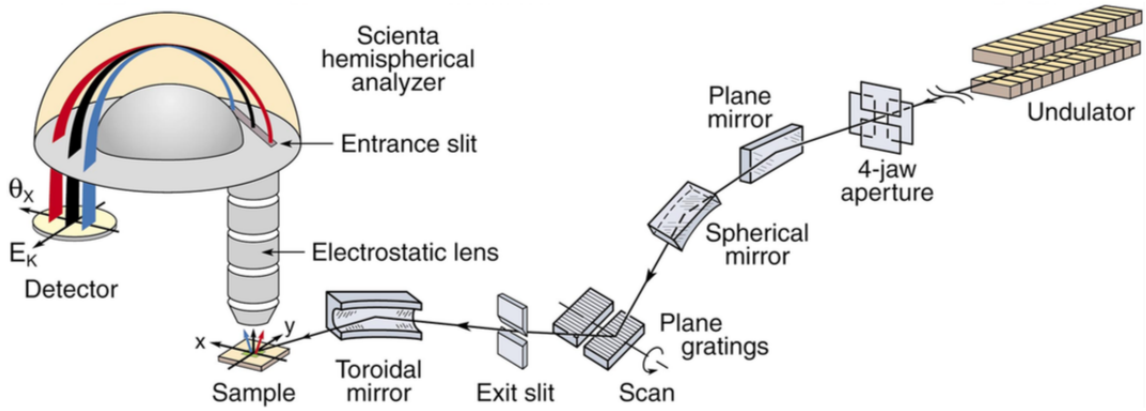

Figure 4.2: Schematic representation of the synchrotron radiation beamline. Scienta hemispherical analyzer is also shown. Ref [23]

at desired photon energy by grating monochromator which is then focused on the sample by means of some optics as depicted in the Figure 4.2. An advantage of synchrotron radiation is that wide range of photon energies from UV to X-ray regime can be achieved. In addition, it produces high flux of photons with characteristic polarization such as circular or linear polarization. In this thesis, we utilized the radiation sources of the Elettra synchrotron and Advanced Light Source in Lawrence Berkeley National Laboratory.

4.4 Electron Analyzer

An electron analyzer is mainly comprised of electrostatic lens, hemispherical analyzer, and electron detector as shown in Figure 4.2. The main body of the analyzer is hemispherical analyzer having two concentric hemispheres of outer radius R_1 and inner radius R_2. And these hemispheres are kept in a potential difference of ΔV so that only the electron having kinetic energy within the narrow range centered at $E_p = e\Delta V \frac{R_1 R_2}{(R_1 - R_2)}$ pass through the entrance slit, exits through these hemisphere and finally reaches to the detector. Where E_p is called the pass energy, the kinetic energy of electrons substantially different from the pass energy either strike to outer or inner hemisphere and will not reach to the detector.

The electrostatic lens decelerates the photoelectrons liberated from the sample to match their energy with the pass energy and focuses them to the entrance slit. The energy resolution of the of the analyzer depends on the pass energy (E_p), width of the entrance slit (w) and

the acceptance angle (α) such that $\Delta E = E_p(w/R_0 + \alpha^2/4)$, where $(R_0 = R_1 + R_2)/2$. The resolving power of the analyzer is defined by ratio of pass energy to the energy resolution $R = E_p/\Delta E = D/S$. Also, the photoemission intensity is inversely proportional to the pass energy and width of the entrance slit. So, for the better resolution it is demanded to work in low pass energy, but which yields the low photoelectron count rate.

The electrons which pass through the electrostatic lens and the hemispherical analyzer are detected in the two dimensional detector made up of two micro-channel plates (MCPs) and a phosphorus plane in series equipped with charge-coupled device (CCD) camera. The MCP is made up of million of very thin conductive glass capillaries. These capillaries act as an electron multiplier. The amplified electrons are accelerated by the screen voltage and strikes the phosphorus screen, producing light signals. These light signals are detected by the CCD camera. The intensity of light recorded in the camera is proportional to the electrons hitting the phosphorous screen which eventually proportional to the electrons pass through the plane of the exit slit, in this way the kinetic energy and the emission angle of photoelectron can be simultaneously determined.

The data in the present dissertation is obtained from the Scienta R4000 and R3000 analyzers having energy and momentum resolutions better than 3 meV and 0.1°, respectively.

Chapter 5

Crystal Structure, Magnetic, and Transport Properties of $V_{0.3}NbS_2$

5.1 Crystal Synthesis and Structure

Single crystal of $V_{0.3}NbS_2$ was synthesized by chemical vapor transport technique. Followings are the synthesis procedures. First, we prepared polycrystalline powder of $V_{0.3}NbS_2$ by heating stoichiometric ratio of V (99.80% purity), Nb (99.99 % purity), and S (99.9995 % purity) at 950°C for one week. Then, 3 grams of the finely ground polycrystalline sample and 0.5 grams of iodine were loaded into a quartz tube and sealed subsequently under vacuum. The tube is placed horizontally in a tube furnace while maintaining the temperature gradient of about 100°C ($T_{hot} = 950°C$ and $T_{cold} = 850°C$) between two ends of the tube. The polycrystalline powder transported to the colder side, due to the chemical reaction, of the tube and many single crystals were formed. Here, iodine acts as a transport agent.

The crystal structure of intercalated compound $V_{0.3}NbS_2$ is shown in Figure 5.1 and was determined from single crystal X-ray diffraction (XRD) experiment. The XRD experiment was performed in Oak Ridge National Laboratory using Rigakus single crystal diffractometer. The structural parameters obtained from the experiment are shown in Table 5.1. The $V_{0.3}NbS_2$ crystallizes in hexagonal lattice structure with centrosymmetric space group $p-31m$, having inversion center. A unit cell contains 20 number of atoms. Twelve sulfur atoms occupy the Wickoff position 6k. The six niobium atoms occupy two inequivalent

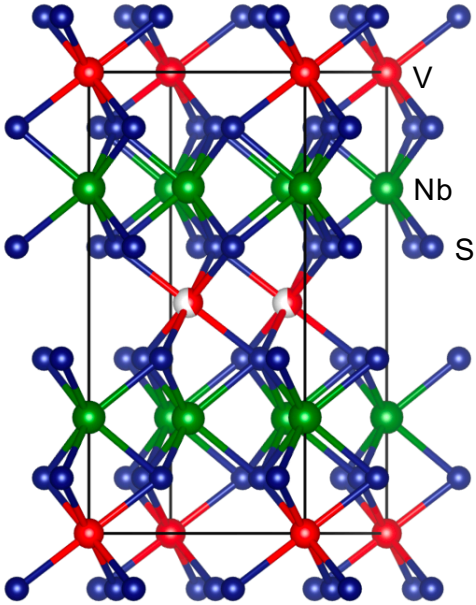

Figure 5.1: Crystal Structure of $V_{0.3}NbS_2$. Vanadium atoms at 2d site are partially occupied.

sites 2e and 4h. There are two types V atoms: V1 and V2 sitting in two inequivalent sites 2d and 1a, respectively. The vanadium atom situated at 2d site is partially occupied with occupancy value of about 0.4, whereas all other atoms have occupancy 1. The lattice parameters obtained from the XRD experiment are a = b = 5.74Å, c = 12.14Å, $\alpha = \beta =$ 90°, and $\gamma = 120°$.

In $V_{0.3}NbS_2$, each Nb atom is surrounded by six S atoms in a perfect trigonal-prismatic environment and forms layered $2H - NbS_2$, and the V-atom sits in the van der Waals gap of NbS_2 layer in octahedral hole, resulting a complete separation of two different transition metals. From the ligand field theory, trigonal crystal field splits five fold degenerate Nb-4d states into three lower energy states d_{z^2}, $d_{x^2-y^2}$, and d_{xy} and two upper energy states d_{xz} and d_{yz}. The intercalation strengthens the bonding between the NbS_2 layers with possible charge transfer from V-atom to lowest Nb 4d-state. Thus, an alternation in electronic properties of parent compound can occur upon the intercalation. Furthermore, the V-atoms which form a superstructure of periodicity $(\sqrt{3}a_0 \times \sqrt{3}a_0)R(30°)$ determine the magnetic properties of the system. Where a_0 is lattice constant of host NbS_2.

Table 5.1: $V_{0.3}NbS_2$. Atom co-ordiantes, occupancy, and Wyckoff positions in the space group *p-31m*.

atom	x	y	z	Occ.	U	Wyckoff	Sym.
Nb1	0.00000	0.00000	0.25168	1.000	0.004	2e	3.m
Nb2	0.33333	0.66667	0.24921	1.000	0.004	4h	3..
S1	0.33333	0.33333	0.12012	1.000	0.004	6k	..m
S2	0.33418	0.33418	0.37880	1.000	0.005	6k	..m
V1	0.33333	0.66667	0.50000	0.406	0.006	2d	3.2
V2	0.00000	0.00000	0.00000	1.000	0.009	1a	-3.m

5.2 M/H vs. T and M vs. H

The magnetic susceptibility (M/H) as a function of temperature is shown in Figure 5.2(a). The M/H vs. T is recorded with an application of magnetic field of 1 kOe and the field is applied along ab plane (in-plane) and c-axis (out-of plane) of the sample. In case of field along ab plane, as the temperature is reduced the M/H abruptly increases at about 50 K (critical temperature, T_C), reaches maximum value of magnetization 116.39 emu/mole at 25 K and starts to drop slowly. While the field is applied along c-axis M/H increases suddenly at T_C, an anomaly appears at about 22 K and increases almost linearly reaching maximum at 3 K. This indicates that the system is highly anisotropic with easy axis along ab plane. The maximum value of magnetization along ab plane is equivalent to 2.45% (even smaller for c-axis) of that expected for the ferromagnetic ordering. This behavior is characteristic of canted antiferromagnetism or weak ferromagnetism. The weak ferromagnetic correlations in antiferromagnetic system occurs due to the spins of neighboring ions are not exactly anti-parallel, making a small angle to each other. Hence, the moments do not cancel in the antiferromagnetically ordered state giving rise to a small net moment. The weak ferromagnetism arises from Dzyaloshinskii-Moriya interaction [86] and two possible reasons

for the weak ferromagnetism are: antisymmetric magnetic exchange, which requires the lack of inversion center between the adjacent spins, and the magnetic anisotropy associated with the sample. Such a weak ferromagntic behavior has also been reported in α-Fe_2O_3 [86], $MnCO_3$ [82], and CrF_3 [86].

Inverse M/H vs. T along in-plane and out-of-plane are shown in the inset of Figure 5.2(a). Both curves follow the Curie-Weiss (CW) behavior above 100 K. The CW fit in between 120 K and 300 K yields the Curie constant and Curie temperature of 0.92 emu $mol^{-1}K^{-1}$ per V-atom and 11 K, respectively when field is applied along ab plane, and 0.78 emu $mol^{-1}K^{-1}$ and 16 K, respectively while the field is applied along c-axis. The positive Curie-Weiss temperature indicates ferromagnetic interaction present in the system. From the Curie constants the effective magnetic moments are extracted to be 2.70 μ_B and 2.49 μ_B per V-atom along ab and perpendicular to ab plane, respectively. These values are smaller than the spin only magnetic moment for V^{+3} state which is 2.83 μ_B.

The M vs. H recorded at temperature of 5 K for field applied along both directions are shown in Figure 5.2(b). The magnetization increases rapidly at low fields and exhibits a linear behavior at higher fields without reaching saturation. Such a behavior is attributed to the canted antiferromagnetism or weak ferromagnetism, in which steep increase at low magnetic fields reflects the spontaneous magnetization and linear at high field behavior due to dominant antiferromagnetic interactions. This is further confirmed by magnetization curve recorded at various temperatures as shown in Figure 5.3 (a). The magnetization have not saturated until 5 T. And, a paramagnetic behavior is exhibited above 50 K and a clear hysteresis is observed below this temperature. It is also to be noted that for ideal antiferromagnetic interaction, magnetization varies linearly with field and passes through the zero-field. A preliminary analysis of small angle neutron scattering experiments we performed on a single crystal of $V_{0.3}NbS_2$, which yet to be published, also suggests canted antiferromagnetic orderings. The hysteresis loop for the low fields is shown in the inset of Figure 5.2(b). From the hysteresis loop, coercive field and remnant magnetization are found to be 137 Oe and 0.082 emu/g (along c-axis), respectively, while negligible coercivity is observed in the ab plane. Also, one can obtain spontaneous magnetization by extrapolation of linear part of the high-field magnetization to zero field. The spontaneous magnetization for

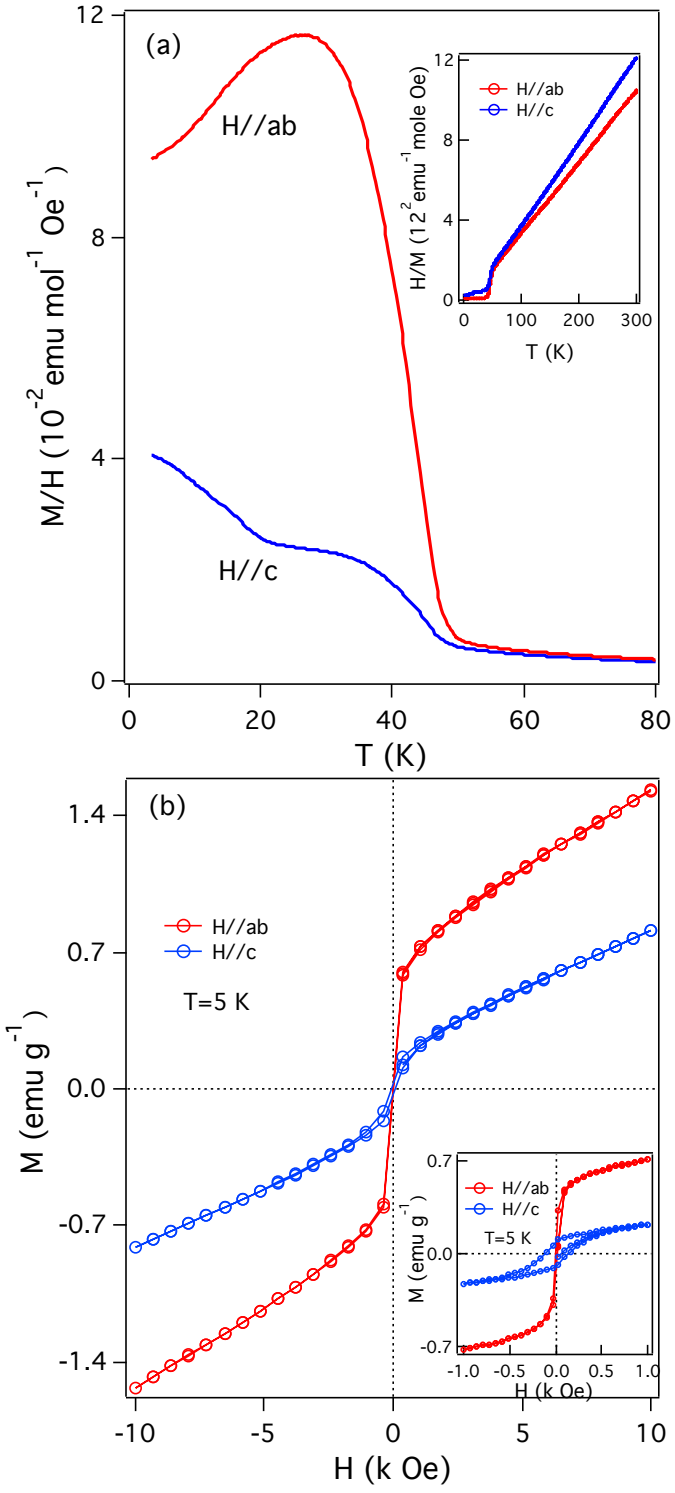

Figure 5.2: (a)M/H vs. T plot for in plane and out of plane magnetization with the application of magnetic field of 1 kOe. Inset of (a) shows H/M vs. T. Figure (b) M vs H at T= 5 K for in plane and out of plane magnetization. Zoom-in part of M-H curve is shown in inset

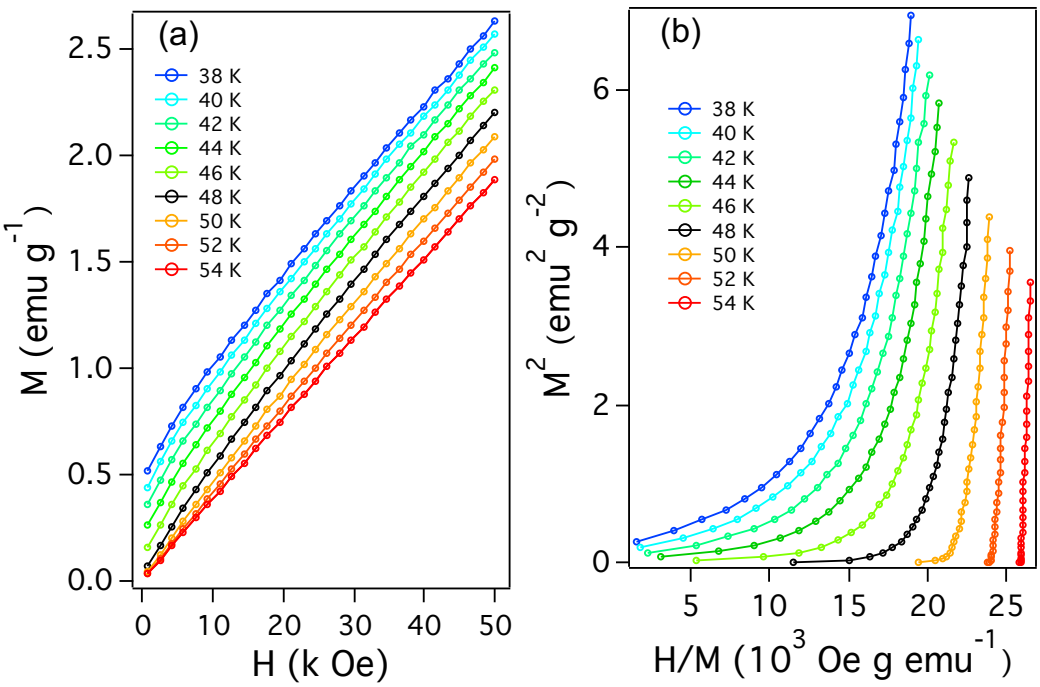

Figure 5.3: Arrot plots at various temperature.

in-plane and out-of-plane are 0.73 emu/g and 0.194 emu/g, and corresponding moments are 0.075 μ_B and 0.020 μ_B, respectively. These values of moment along with effective magnetic moments as obtained above and the behavior of M vs. H curve further confirm that $V_{0.3}NbS_2$ is highly anisotropic system with easy axis along ab plane.

5.3 AC Susceptibility

To further investigate the magnetic properties of $V_{0.3}NbS_2$ we measured the ac susceptibility as a function of temperature. In ac susceptibility, in contrast to dc measurements, ac drive magnetic field is superimposed on the dc field and the time dependent moment is obtained. So, ac susceptibility yields information about the magnetization dynamics which are not obtained in DC measurements. Here, the susceptibility is divided into the real and imaginary part, $\chi = \chi' + i\chi$", the former (χ') is in phase with the ac drive signal while the latter (χ") is out of phase.

The AC susceptibility as a function of temperature at various frequencies is shown in Figure 5.4. The measurement was performed via Quantum Design's Physical Properties

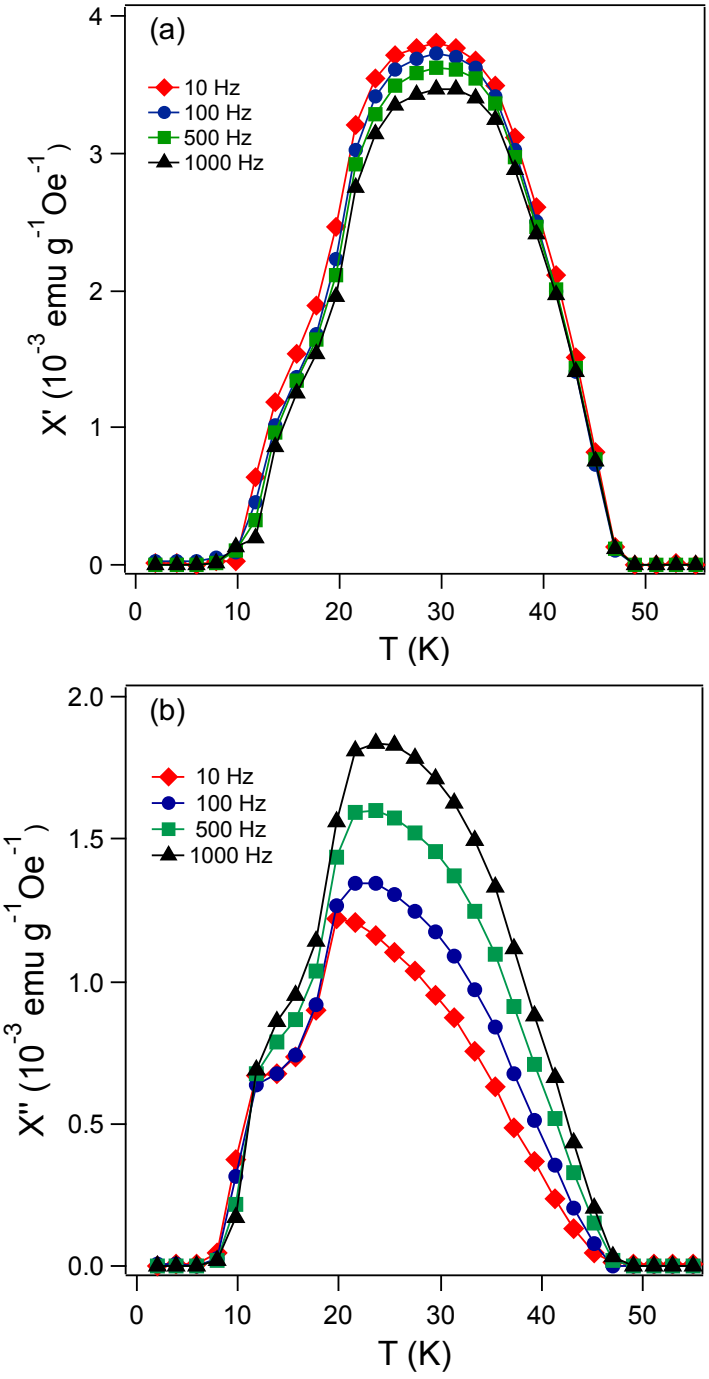

Figure 5.4: AC susceptibility at various frequency as a function of temperature. Zero DC bias field and 15 Oe of AC drive field is applied. (a) The real and (b) the imaginary components of the susceptibility.

Measurement System (PPMS). During the measurement zero dc bias field and ac driving field of 15 Oe are applied along ab plane. The upper panel in Figure 5.4 shows real and the lower shows imaginary components of the susceptibility, and both exhibit non-monotonic behavior with temperature. The real part exhibits an abrupt increase at 47 K and a broad maximum is observed which is centered at 35 K. Upon further cooling, an anomaly is observed at low temperature (around 15 K) and the susceptibility drops almost to zero at 10 K. Here, the peak temperature is independent of frequency. On the other hand, the imaginary part, which reflects the magnetic dissipation energy, shows that the peaks are appeared at lower temperatures compared to real components and are independent of the applied frequency (though a peak at 10 Hz is shifted slightly to the lower temperature). Furthermore, the height of the susceptibility peak decreases with increasing frequency for real part and opposite happens for imaginary part. Additionally, a pronounced anomaly is also observed around 11.87 K, and the susceptibility reaches almost to zero at 7 K. Remarkably, the anomaly is suppressed as the frequency is increased. The origin of anomaly at lower temperature, which are absent in case of dc measurements, is not clear yet. The independent of peaks with frequency in both the real and imaginary parts of the susceptibility attributed that the long range magnetic ordering is present in this materials ruling out the possibility of spin glass phenomenon [90]. Also, the appearance of main peaks at two different temperatures for real and imaginary parts indicates that their origin might be different. Moreover, the sudden jump in the susceptibility at 47 K confirms the weak ferromagnetism in this materials, and peak maximum followed by drop in susceptibility at low temperatures suggests the long range antiferromagntic ordering also present in the system.

5.4 Electrical Resistivity and Magnetoresistance

The electrical resistivity of $V_{0.33}NbS_2$ as a function of temperature in a range of 2–300 K measuring along ab plane is shown in Figure 5.5(a). The resistivity is recorded in Quantum Design's PPMS machine using conventional four probe technique such as gold wire and EPO-TEK H20E Epoxy are used to make contacts. The resistivity increases with increasing temperature in all the temperatures typified for the metallic system. The resistivity is

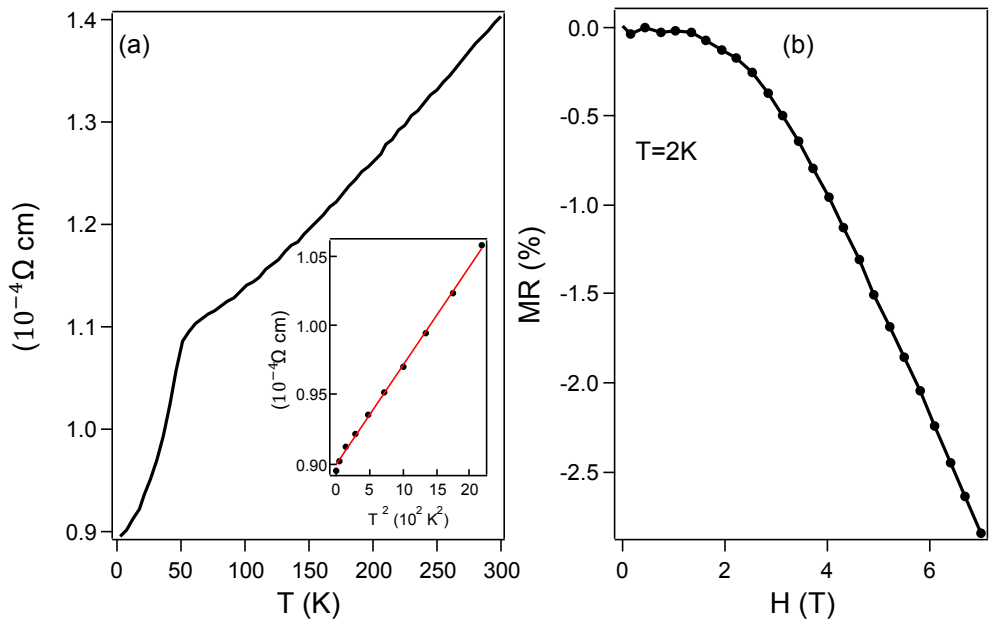

Figure 5.5: (a) Resistivity as a function of temperature, inset shows T^2 fit of ρ in the range of 2–50 K. (b) Magnetoresistance at 2 K

appreciably different than that of the host-NbS_2, that is, the superconductivity is completely suppressed, and an anomaly is observed at 50 K due the long range magnetic orderings (weak ferromagnetism) as already mentioned in the discussion of magnetic properties. The residual resistivity ratio $\rho(300\ K)/\rho(2\ K)$ is found to be 1.57. And, the room temperature resistivity is about 1.4×10^{-4} Ωcm which is about two order of magnitude smaller than the typical value for metal, for example copper has room temperature resistivity of 1.68×10^{-6} Ωcm. So, $V_{0.3}NbS_2$ can be considered as a poor metal. It is known that at low temperature region the resistivity of the conventional metal is correctly described by the famous Bloch's power law behavior: $\rho = \rho_0 + CT^5$, where the temperature independent ρ_0 is attributed to the electron scattering from impurities and crystal imperfection and T^5 contribution is originated from the electron-phonon interactions. This behavior is sometimes modified by including T^2 term such as $\rho = \rho_0 + \mathrm{bT}^2 + \mathrm{CT}^5$, here b is another constant. Remarkably, in the low temperature region (2K–46 K) the resistivity of $V_{0.33}NbS_2$ rather follows T^2 behavior: $\rho = \rho_0 + \mathrm{bT}^2$ as shown in the inset of Figure5.5(a) with negligible T^5 contribution, indicating that $V_{0.3}NbS_2$ is not a conventional metal. The values of coefficients obtained from the least square fit to the equation are $\rho_0 = 0.89 \times 10^{-4}$ Ωcm, $\mathrm{b} = 0.719 \times 10^{-6}$ ΩcmK^2. The

T^2 behavior at low temperature might be originated from the electron-electron interaction or the electron-spin wave interaction (in other words, the interaction between conduction electrons and local moments). The low temperature behavior of resistivity is a characteristic of heavy rare earth systems, but it also appears in number of transition metal compounds including 3d-intercalted transition metal dichalcogenides [95]. At higher temperatures that is above the magnetic ordering temperature, the spins are completely disordered and magnetic resistivity arises due to scattering of conduction electrons with the local moments, but this resistivity is independent of temperature. Further, the conventional electron-phonon interaction also contributes to the total resistivity at higher temperatures which gives rise to linear temperature dependence behavior in the resistivity.

The in-plane magnetoresistance ($\Delta\rho_{ab}/\rho_{ab}$) of $V_{0.3}NbS_2$ at 2 K is shown in Figure 5.5(b). The magnetic field is applied up to 7 T along the ab plane. The negative magnetoresistance is observed in all applied field with maximum value of 2.8% at 7 T. The negative magnetoresitnace can be elucidated from following: the magnetic field increases effective field acting on the localized spins and suppresses the fluctuations of the spin in space and time leading to decrease in resistivity which in turn results negative magentoresistance [130].

5.5 Hall Effect Measurements

In order to obtain information about carrier concentration and its type, we performed the Hall effect measurements. In the Hall measurements, a current is applied along one direction (here, along ab plane) and the Hall voltage is recorded in the transverse direction while magnetic field is applied perpendicular to the ab plane. From the Hall voltage, one can obtain the Hall resistivity by the relation $\rho_{xy} = V_y t/I_x$, where V_y is the Hall voltage across the sample width, I_x is the current along x-direction and t is thickness of the sample. The Hall resistivity of $V_{0.3}NbS_2$ at various temperature is shown in Figure 5.6. At all temperatures, the resistivity has positive slopes and varied linearly with the magnetic field. We have not observed anomalous Hall effect (AHE) as expected in antiferromagnetic system. The AHE is observed in ferromagnetic system where spin up and spin down charge carriers move in

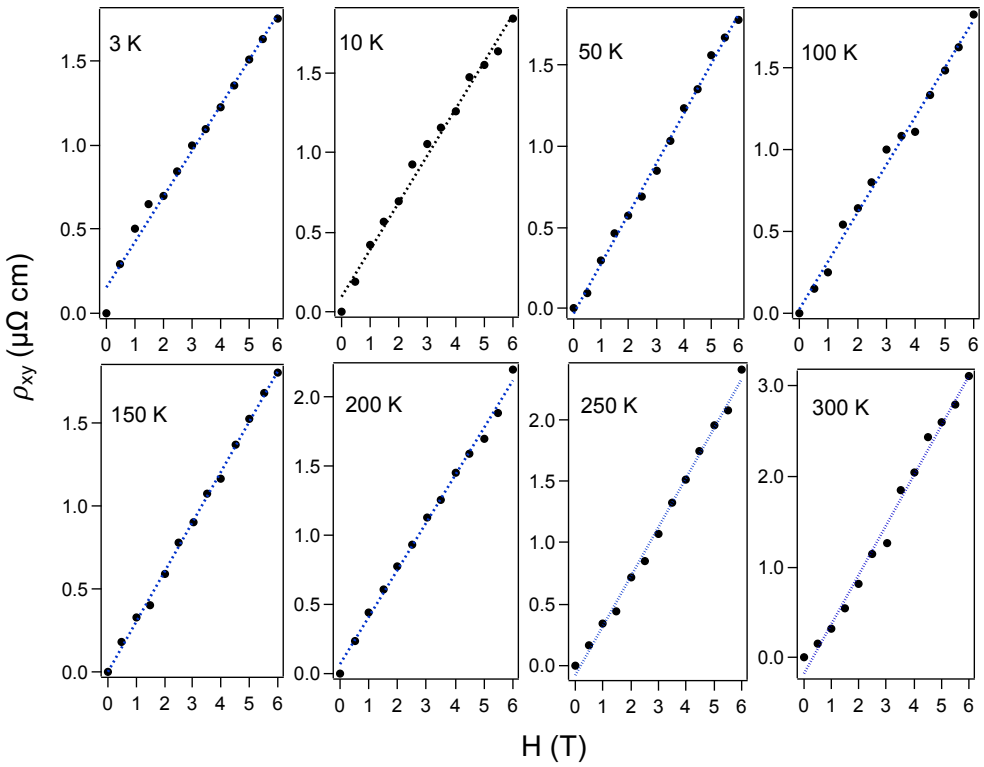

Figure 5.6: Hall resistivity at different temperature. Positive slope is observed in all temperatures, suggesting hole-like carrier.

opposite edges, upon the spin imbalance a transverse electric field is created and hence the Hall voltage.

From the slope of Hall resistivity we obtained the Hall coefficient (R_H), $\rho_{xy} = R_H B$, which is shown in Figure 5.7(b). The Hall coefficient increases with the temperature and is positive for all temperatures, implying that the majority of charge carrier is hole type. Further, from Hall coefficient one can immediately estimate the magnitude of carrier concentration by the relation $R_H = -1/ne$ in SI unit, and the carrier concentration decreases with temperature as expected for the metallic sample (see Figure 5.6(a)). The Hall coefficient is negative if the majority of charge carrier is electron while it is positive if the carrier is hole type. The magnitude of the concentration at 2 K and room temperature are 2.31×10^{21} cm^{-3} and 1.14×10^{21} cm^{-3}, respectively, these values are almost two order of magnitude smaller than those of simple metals, for example Al which has hole type concentration with room temperature value of 6.11×10^{22} cm^{-3} [64] consistent with the relatively higher resistivity

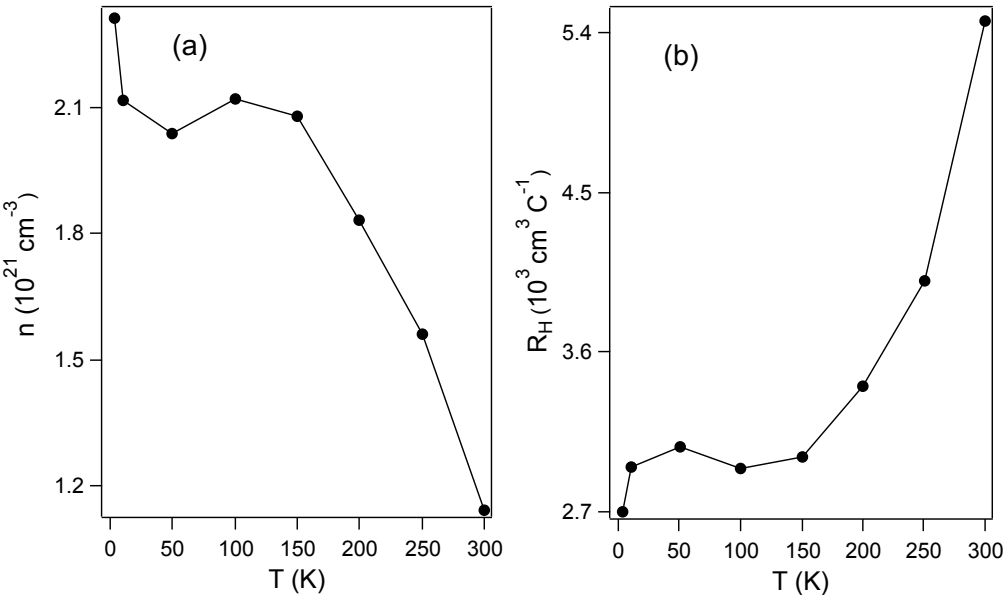

Figure 5.7: Carrier concentration and Hall coefficient obtained from the Hall resistivity data. (a) Carrier concentration has smaller value than the typical metals. (b) Positive Hall coefficients indicate charge carrier is hole type.

observed, in comparison to the typical metal. Thus, $V_{0.3}NbS_2$ can be considered as a low carrier concentration metal. The host material NbS_2 is also a hole carrier type metal with room temperature concentration of 10^{22} cm^{-3} [132]. It is interesting to compare the carrier concentration of host NbS_2 and $V_{0.3}NbS_2$ with another intercalated system $Cr_{1/3}NbS_2$ which is also a hole type metal with concentration of about 10^{20} cm^{-3} [38]. From this, we infer that vanadium atom donates electron to the NbS_2 layer, but it does not donate as much electron as Cr does to NbS_2.

5.6 Heat Capacity and Thermal Conductivity

The heat capacity of $V_{0.3}NbS_2$ recorded in PPMS as a function of temperature is shown in the Figure 5.8. The heat capacity increases with temperature and a λ-type anomaly is observed at the magnetic ordering temperature (50 K). The room temperature specific heat is about 21.5 J/(mole atom K), close to the Dulong-Petit's value $C_p = 3R \approx 24.94$J/mole K, where R is the molar gas constant. The low temperature heat capacity is fitted well with the equation $C_p = \gamma T + \beta T^3$, typical for metal, as shown in the inset of Figure 5.8(a). The first and second

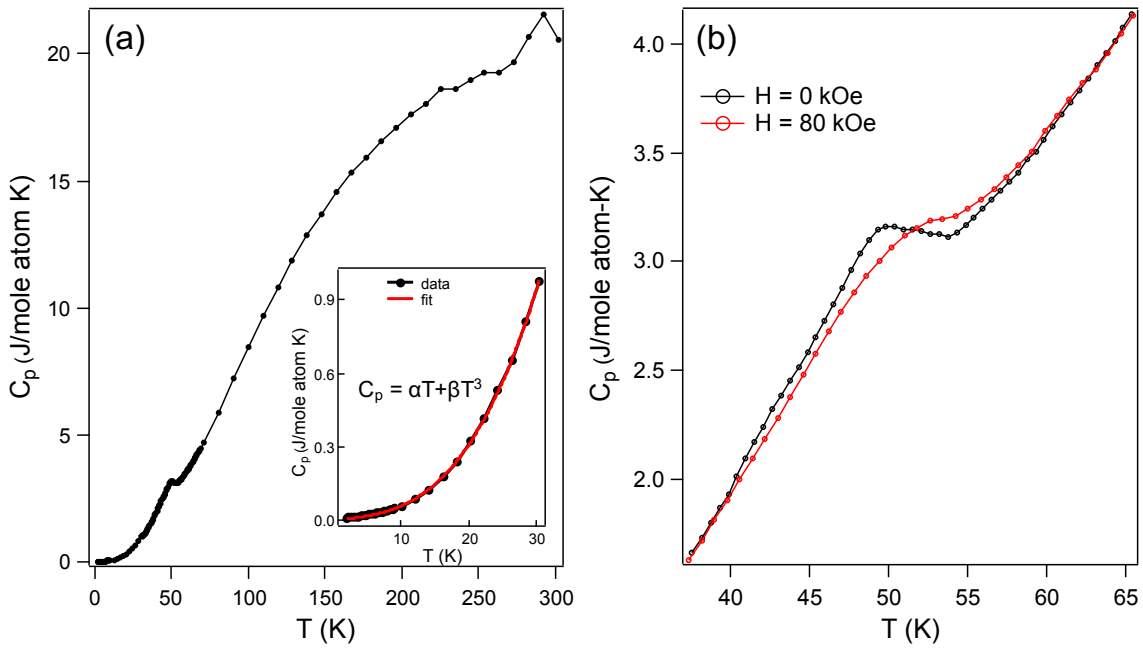

Figure 5.8: Heat capacity (C_p). (a) C_p as a function of temperature, the inset shows T^3 law fitting of C_p at low temperatures. (b) C_p vs. T at 0 kOe and 80 kOe.

terms on right side of the equation specify the electronic and phonon contributions to the heat capacity, respectively. And, the coefficients γ and β are found to be 0.27 mJ mol^{-1}K^{-1} and 0.0258 mJ mol^{-1}K^{-4}, respectively, from the least square fit to the equation. From γ we calculated the density of states at Fermi level $N(E_F)$ by relation $\mathrm{N(E_F)} = 3\gamma/\pi^2\mathrm{K_B^2}$ and the obtained value is 2.29 states (eVu.c.)$^{-1}$, where $\mathrm{K_B}$ is the Boltzmann constant. Such a one electron density $N(E_F)$ obtained from the low temperature heat capacity data may not give an accurate result since the many body effect and the magnetic effect can modify $N(E_F)$ [10], though $N(E_F)$ extracted here is close to that obtained from the first principle calculation for magnetic case which will be discussed in chapter 6. The Debye temperature $\Theta_\mathrm{D} = 422$ K is calculated using β by the relation $\theta_\mathrm{D} = (5\beta/12\mathrm{R}\pi^4)^{-1/3}$.

The heat capacity with an application of magnetic field of 8 T compared to zero field data is shown in Figure 5.8(b). Here the field is applied along c-axis of the sample and the heat capacity is recorded in the range 2–65 K. It is found that the λ- anomaly is suppressed by magnetic field. Noticeably, the heat capacity is suppressed below the magnetic ordering temperature and enhanced above the ordering temperature, when we made a comparison with zero-field heat capacity.

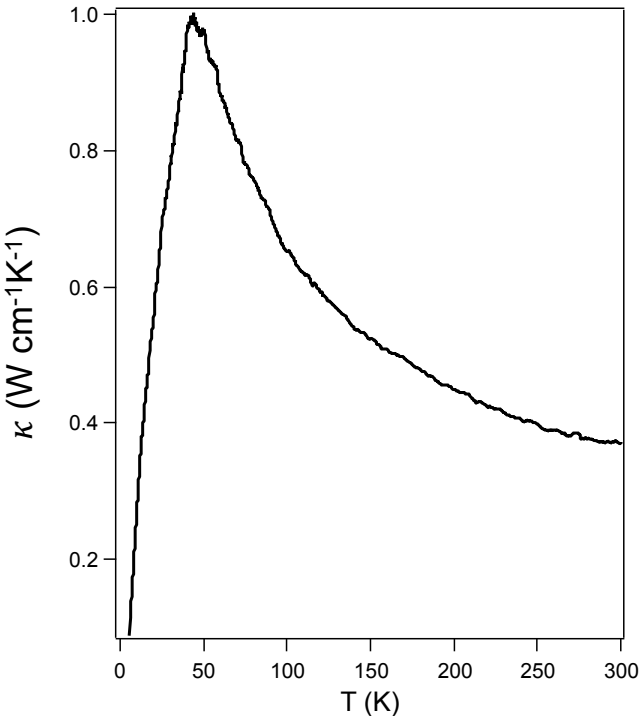

Figure 5.9: Thermal conductivity as a function of temperature. The peak is observed at the same transition temperature as seen in the heat capacity curve.

The temperature dependent thermal conductivity (κ) is shown in Figure 5.9. The κ increases with temperature and it exhibits a sharp peak just below the magnetic transition temperature and starts to decrease upon further increase in temperature. Typically, electrons and phonons are the main heat carrying entities in a metal; though, there are other possible excitations in metal such as magnons for heat transport which can be neglected because of small contributions in thermal conductivity. Thus, the thermal conductivity of a metal can generally be expressed in term of electronic and phonon contributions: $\kappa = \kappa_{\mathrm{e}} + \kappa_{\mathrm{p}}$. The electronic contribution to thermal conductivity in metal can be estimated from Widemann-Franz law: thermal conductivity of a reasonably pure metal is related to the electronic conductivity (κ_e) by the relation, $\kappa_e\rho$=LT, where ρ is the electronic resistivity, $\mathrm{L} = 2.45 \times 10^{-}8\mathrm{W}\Omega\mathrm{K}^{-2}$, T is the absolute temperature. The maximum value of electronic contribution is obtained at 46 K and is about 10.22 $\mathrm{mWcm}^{-1}\mathrm{K}^{-1}$, indicating that heat transport in the sample is due to phonons. Moreover, such a small electronic contribution is attributed from the relatively large electronic resistivity ρ; the large phonon contribution to κ is also observed in chromium-intercalted NbS_2 system [39].

Chapter 6

Electronic Structure of $V_{0.3}NbS_2$

6.1 Surface Characterization

As we discussed earlier in the Chapter 2, the quality of photoemission data depends considerably on the surface condition of the sample. So, it is extremely important to examine the surface before performing surface sensitive experiments such as photoemission or ARPES. For this reason, we first discuss the surface characterization of $V_{0.3}NbS_2$ before presenting the detailed photoemission results. The surface of the sample is investigated by the scanning tunneling microscopy (STM), low energy electron diffraction (LEED), core level photoemission spectroscopy (XPS), and angle resolved photoemission spectroscopy. In these experiments the fresh surface is obtained by cleaving the sample *in situ* in ultra high vacuum (UHV) system. In this material, the intercalant vanadium atoms are situated in the van der Waals gap between NbS2 layers. The sample cleaves through the plane of V-atoms such a way that about half of the V-atoms are likely to stay on the surface, while other half is removed by cleave. Thus, a vanadium terminated (disorder V-atoms) and sulfur terminated surface regions can be arised.

Figure 6.1(a) shows STM image to illustrate the surface morphology of the sample. The STM experiments were performed at room temperature at the 'Istituto Officina dei Materiali'(IOM) of the Italian National Research Council (CNR). The samples were cleaved and measured *in situ* in ultra high vacuum of pressure better than 10^{-10} Torr. The STM image (Figure 6.1 (a)) exhibits two main regions, one is atomically flat (at left of the image)

and another is much corrugated (at right); we assigned them as smooth and rough areas, respectively. The line scan represented by solid line in STM image (see Figure 6.1) indicates the difference in corrugation between these two regions as illustrated in Figure 6.1(b). A terrace step height of about 0.61 nm is observed, which is approximately equal to the separation distance between the NbS_2 layers along the c-axis, indicating that the sample is cleaved through the horizontal plane containing V-atoms. There are two possible cleave planes corresponding to the planes of V atoms with crystallographic positions 1a and 2d. From the line scan, an oscillation of spikes has been observed for the rough surface, while relatively smooth line profile is observed for the smooth surface.

We further investigate STM results in detail by examining atomic resolution images. The raw and filtered data for smooth region are shown in Figure 6.2(a1) and (b1), respectively. The smooth area shows the ordered periodicity of 5.75 Å which is equivalent to the lattice constant 'a' in the basal plane of $V_{0.3}NbS_2$, where the V atoms are ordered in superstructure of dimension $(\sqrt{3}a \times \sqrt{3}a)$, as compared to NbS_2. The periodicity of NbS_2 can be called by (1×1). We further observed that $(\sqrt{3} \times \sqrt{3})$ spots are not as sharp as (1×1) spots which might be due to the fact that they are originated from the position underneath the sample surface. Though the ordered vanadium atoms are located below the NbS_2 layer, the superstructure in the STM image is observed as charge transfer form V-atom to the NbS_2 layer resulting modification of local density of states [22]. The fast Fourier transform (FFT) map of Figure 6.2(a1) and (b2) are shown in Figure 6.2 (a2) and (b2). The FFT reveals the $(\sqrt{3}\times\sqrt{3})R(30^\circ)$ superstructure, consistent with the crystal structure of $V_{0.3}NbS_2$. Moreover, we do not observe any periodicity in the rough area of the sample (not shown here).

Thus, from the STM experiments, it is confirmed that the smooth surface is atomically flat and majority of vanadium atoms are removed during the process of cleave, whereas the rough surface is atomically disordered where most of the V-atoms remains but are randomly distributed.

To strengthen the STM results we performed the low energy electron diffraction (LEED) experiments. Figure 6.3 shows the LEED pattern of $V_{0.3}NbS_2$ sample. For LEED experiments, the sample is prepared by cleaving *in situ* in ultra-high vacuum of pressure better than 10^{-11} Torr. And, the measurements were performed at temperature of 77 K.

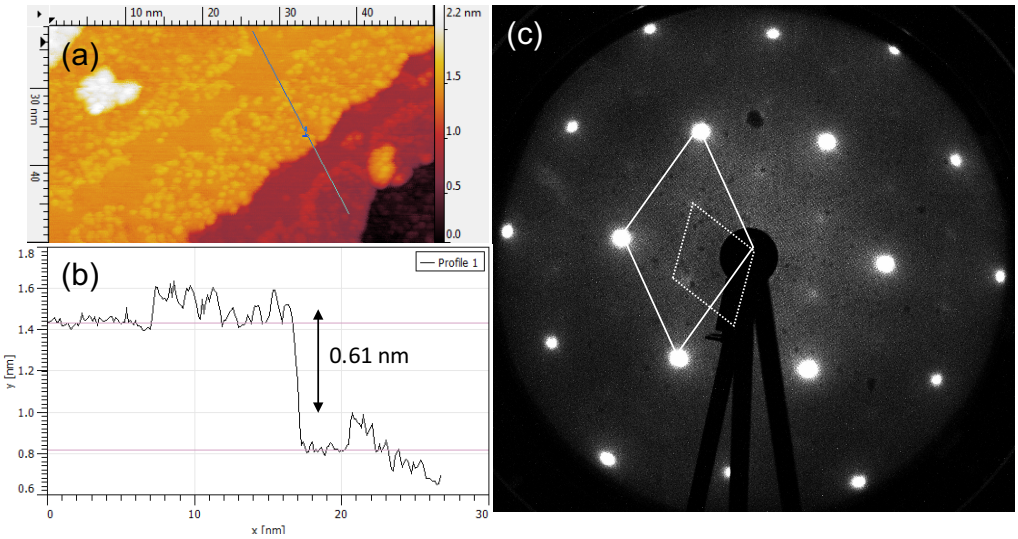

Figure 6.1: (a) Scanning tunneling microscopy image recored with negative bias voltage -1.5 V, (b) step height obtained from the line profile in (a) indicated by a line, (c) LEED image with beam energy of 171 eV, the primitive unit cells of NbS_2 (solid line) and $V_{0.3}NbS_2$ (dashed line) are indicated.

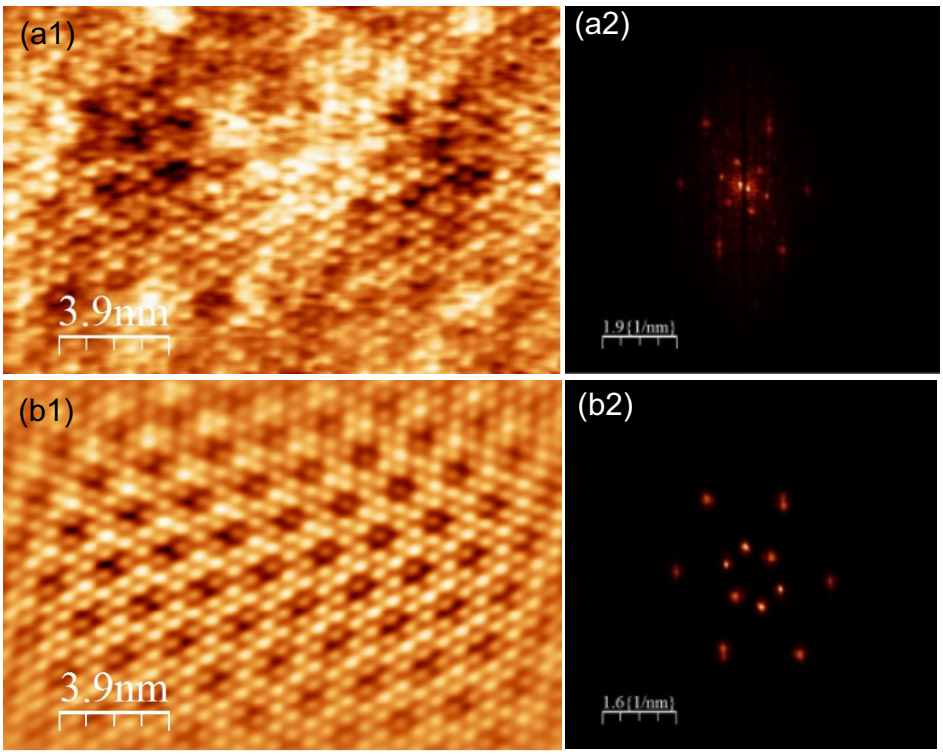

Figure 6.2: STM images (a1, b1) and corresponding fast Fourier transformations (a2, b2). (a1) is a raw STM data and (b2) is filtered image of (a1).

The data on the left panel in Figure 6.3 is measured at electron beam of energy 171 eV, while the right panel is measured at 217 eV. At beam energy of 171 eV, the LEED pattern reveals the spots originated from the parent compound NbS_2, which has lattice periodicity of (1×1). Also, very weak additional spots are also observed. As we increased the beam energy additional spots becomes brighter which is shown in 6.3(b). These additional features have a periodicity of $(\sqrt{3}\times\sqrt{3})R(30°)$, consistent with the superstructure periodicity of intercalated V-atoms. Importantly, the beam energy lower than 100 eV does not produce the ordered superstructures. The appearance of extra spots at high beam energy can be explained as following. At the low beam energy (<100 eV), the experiment is more surface sensitive and only the signals from the surface (1×1) is obtained. The surface is either vanadium-deficient (sulfur terminated) or vanadium-disordered and hence an absence of superstructure. But, at high beam energy the probing depth of the experiment increases and the signals below the NbS_2 layer can also be detected and hence the periodic superstructure. Thus, we are confirmed that the superstructure $(\sqrt{3} \times \sqrt{3})R(30°)$ is originated from the bulk of the sample and (1×1) structure is from both the bulk and surface termination with NbS_2 layer. The superstructure $(\sqrt{3} \times \sqrt{3})R(30°)$ has smaller reciprocal vectors and hence the smaller primitive unit cell in comparison to the (1×1) structure. The primitive unit cell corresponding to $(1\times\ 1)$ and $(\sqrt{3} \times \sqrt{3})$ spots are indicated by solid and dotted lines in Figure 6.1(c).

We also performed resonant ARPES, which will be discussed in more detailed later, to check if the vanadium atoms are randomly distributed or not. At the V-L_3 absorption edge, the non-dispersive feature is observed indicating that the vanadium atoms at the surface of the sample are non-periodic.

Finally, We investigated surface structure utilizing the core level spectroscopy, particularly of S-2p and V-2p core levels since the cleaving of the sample likely to expose the vanadium or sulfur terminated surfaces. We use two geometrical set up normal and grazing emissions with respect to the sample surface. The normal emission is suitable to study bulk structure whereas the grazing emission is appropriate for surface structure of the sample. All the core levels presented in this thesis were recorded in beamline for advanced dichroism (BACH) of the Elettra Synchrotron Facility in Italy.

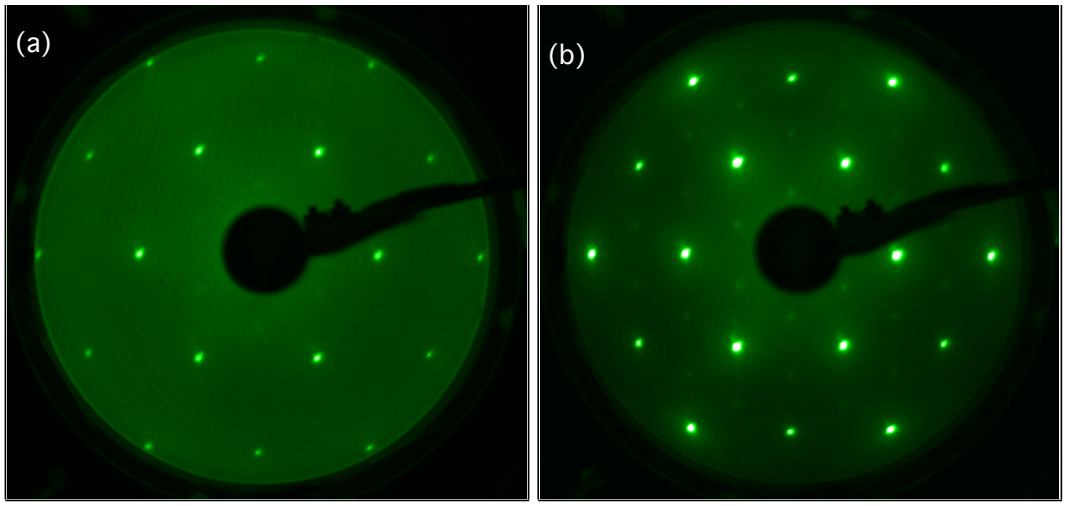

Figure 6.3: Low energy electron diffraction pattern using beam energy of (a) 171 eV and (b) 217 eV. The superstructure periodicity of $(\sqrt{3} \times \sqrt{3})R(30°)$ is more visible at high electron beam energy.

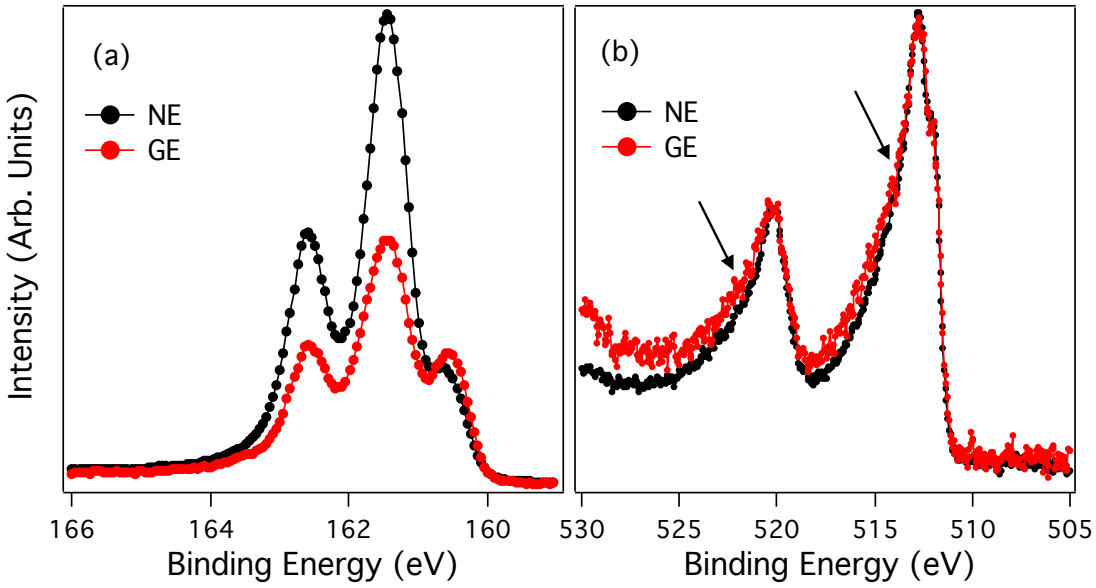

Figure 6.4: S-2p and V-2p core level at photon energy of 937 eV. (a) S-2p core level at normal and grazing emission; two sets of spin-orbit doublet are observed, corresponding to surface and bulk of the sample. (b) V-2p core level at normal and grazing emission. The surface and bulk components are not distinguished as compared to S-2p.

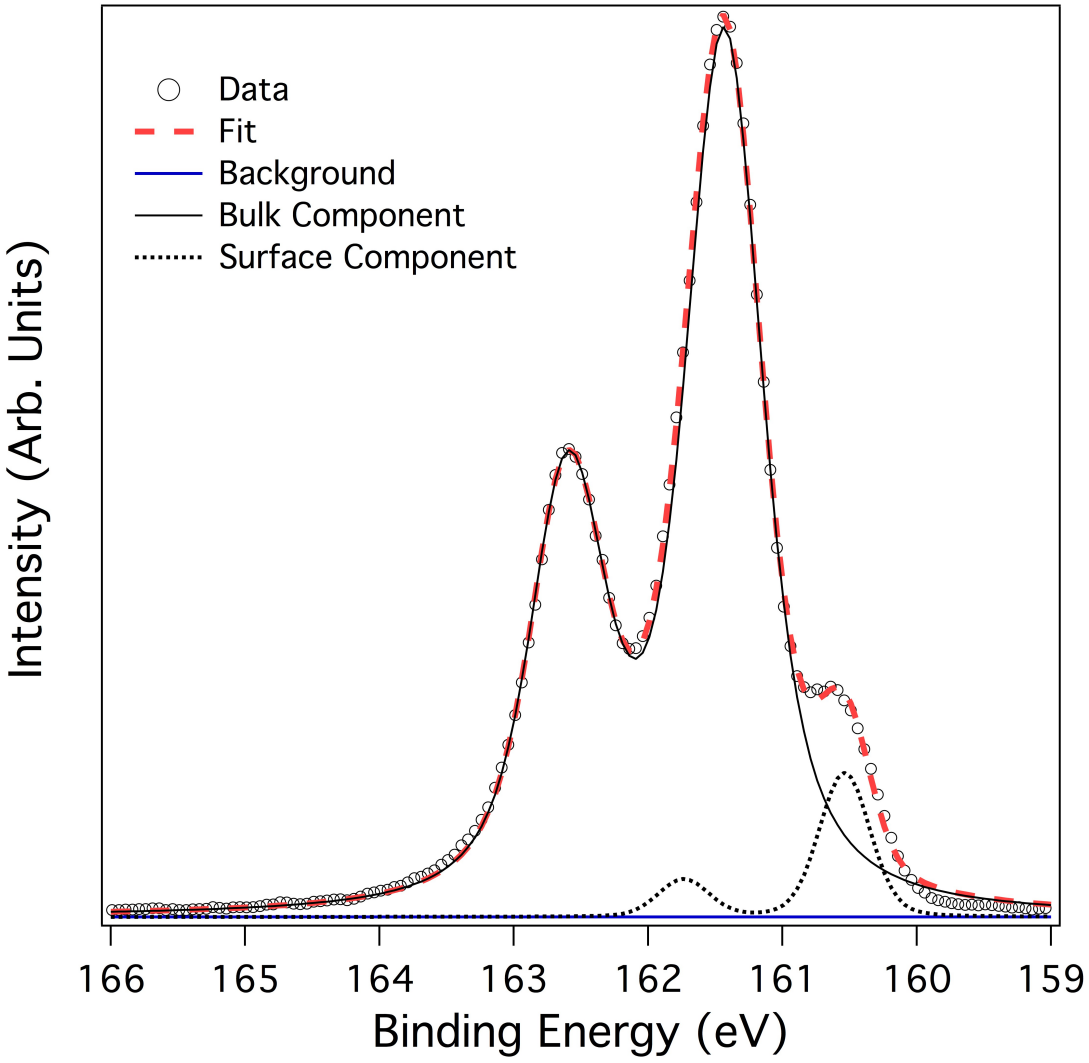

Figure 6.5: Lorentzian-Gaussian fit of S-2p spectrum recorded in the normal emission geometry. Two spin-orbit doublets are extracted associated with surface and bulk components.

The room temperature S-2p core level photoemission spectra in normal and grazing emission geometrical set-ups are shown in Figure 6.4(a). The experiments were performed with photon energy of 937 eV. Each spectrum shows mainly three structures indicating two spin-orbit doublets, S-2$p_{3/2}$ and S-2$p_{1/2}$, are present. The two doublets are obtained from the Lorentzian-Gaussian fit of the spectrum which are separated by about 0.9 eV (see Figure 6.5). In the sample cleaving process, sulfur and vanadium terminated surfaces are expected to be exposed; thus sulfur or vanadium atoms will have different chemical environments in bulk and surface of the sample. The origin of shift in energy of two doublets of S-2p is due to the different atomic coordination to sulfur at surface and bulk. The doublet in the higher binding energy is likely to be originated from the sulfur atom in the bulk of the sample, while the doublet at lower binding energy is from the surface. Moreover, the surface component of lower binding energy is evidenced from the comparison of experiments performed in two geometrical arrangements: normal and grazing emissions. The normal emission usually enhances spectrum of bulk component, while the grazing emission enhances surface component. In our data, the grazing emission exhibits increase in intensity for the component at lower binding energy than that of higher binding energy, which indicates this component is originated from the surface of the sample. Similar S-2p spectra has also been reported in intercalated systems $Cr_{1/3}NbS_2$ [108] and Fe_xNbS_2 [102]. So, the surface and bulk components are clearly distinguished in S-2p spectrum

The core level photoemission of V-2p with the normal and grazing emissions is shown in Figure 6.4. The spectra are recorded at room temperature with photon energy of 937 eV. The doublets V-2$p_{3/2}$ and 2$p_{1/2}$ are separated by binding energy of 7.7 eV, as expected. In case of V-2p core level spectrum the surface and bulk components are not clearly distinguished. However, it is expected to visible the surface component which is seen in case of S-2p since both of them are measured at the same photon energy. Further, the vanadium atoms at the surface and the bulk have different chemical environments. A weak shoulder-like structure at lower binding energy could be originated from the surface component which is not clear yet. Further, the spectra measured at normal and grazing emission set ups are not appreciably different from each other indicating that surface component to the spectrum is not discernible. In addition, we also observe two satellite features corresponding to each

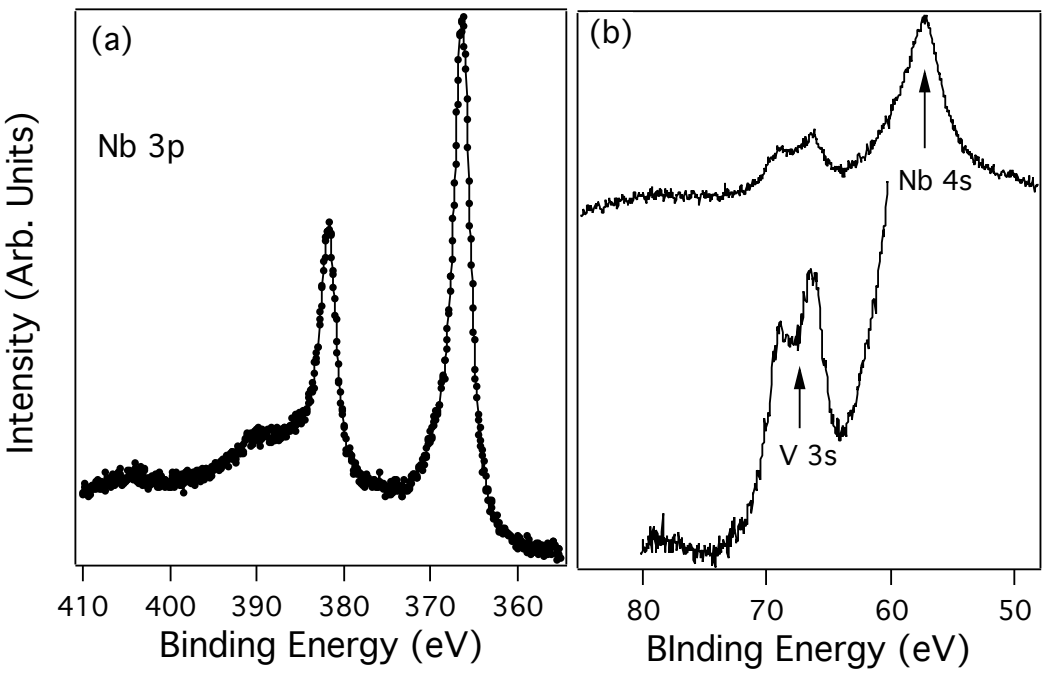

Figure 6.6: Nb-3p and V-3s core level. (a) Nb-3p core level at photon energy of 937 eV. (b) V-3s core level measured at photon energy of 495 eV shows the multiplet splitting of 3s states.

main peak at higher binding energy side marked by arrows. The satellite feature has also been observed in 2p core level of number of transition metal compounds [13] as well as the transition metal intercalated system [108, 102]. The origin of satellite is mainly due to the interaction of core hole with the valence state. There are two possible configuration upon the formation of core hole. In the first one, charge transfer from the neighboring S to the V-3d state with the configuration $2p^5 3d^5 L$ which corresponds to the main peak, where L refers to the hole formed in S-3p state. Whereas in the second case the final state has the configuration $2p^5 3d^4$ which corresponds to satellite feature, where no charge transfer from the S occurs.

Figure 6.6 shows additional core level spectra associated with the Nb-3p, V-3s, and Nb-4s. The Nb-3p spectra was recorded with the photon energy 937 eV, and it exhibits a spin-orbit doublet separated by binding energy 16.5 eV. Also, there are two structures at 404.5 eV and 389 eV which are separated by the same amount (23 eV) as the main peaks are. Similar features have also been observed at the same energy separation at high binding energy side of other core level spectra such as Nb-3d, S-2p, V-3p, and Nb-4s. These features are originated

from the plasmon excitations as expected in metallic samples. Furthermore, Nb-3p spectra does not exhibit any shoulder like feature, as seen in S-2p and V-2p spectra, associated with the main peak indicating that no surface component is present. Which further confirms that the sample is cleaved through the horizontal plane containing vanadium atoms instead of the plane of Nb atoms. The V-3s spectra were measured at photon energy of 495 eV. In the upper spectrum in Figure 6.6, the Nb-4s core level has also been indicated. We observed that the V-3s core level is split into two component and is called the multiplet splitting. The multiplet splitting arises for an atom containing unpaired electrons in the outermost shell. When a core-hole is formed two possible final states arises. If the spin of unpaired core electron has the same spin as that of unpaired d valence electron then the energy of core photoelectron reduces and the spectrum will appear in the lower binding energy, while the spins of two unpaired states are different then the spectrum appears in higher binding energy. Here, an additional structure in 3s spectrum might be due to the exchange interaction of a 3s core electron in a final state with V-3d electron in valence band. The energy separation between two states is proportional to the 3s-3d exchange integral K_{3s-3d} [120].

Thus, from the STM, LEED, and photoemission experiments, it has been confirmed that the sample is likely cleaved by the horizontal plane containing vanadium atoms. It has also been clarified that the surface of $V_{0.3}NbS_2$ consists of the S-terminated surface, which is periodic and most of V-atoms are removed during the process of cleaving, and the rough area where the V-atoms are randomly distributed and does not exhibit any periodicity. In other words, the cleaved surface has different stoichiometric ratio and periodicity than that of the bulk. This has to be carefully considered in the surface sensitive techniques such as XPS and ARPES experiments.

6.2 Electronic Structure Calculations of $V_{0.3}NbS_2$

Before discussing the experimental electronic structure of $V_{0.3}NbS_2$ by phtoemission measurements, we first provide the first principles results of the electronic calculations. The electronic structure calculations are performed with utilizing the WIEN2k package [12] which is based on density functional theory (DFT) proposed by Kohn and Sham.

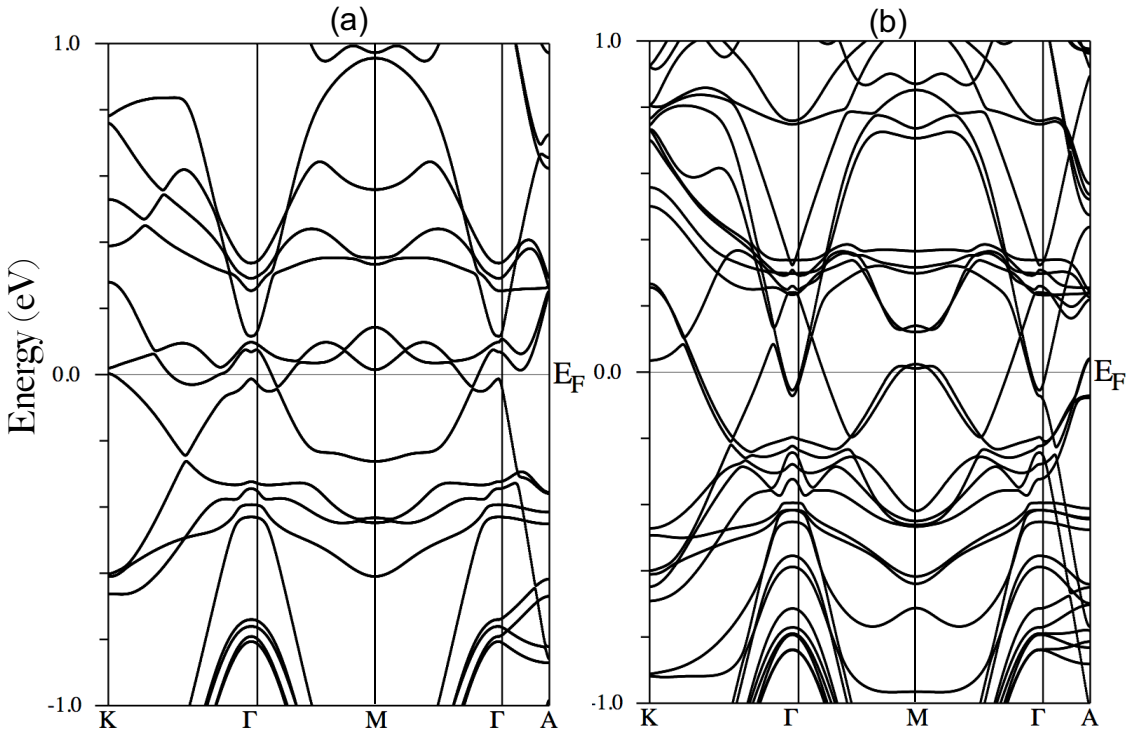

Figure 6.7: The band Structure for (a) non-magnetic and (b) antiferromagnetic states of $V_{0.3}NbS_2$ calculated along various high symmetry points.

The generalized gradient approximation of Perdew, Burke, and Ernzerhof is chosen for the exchange correlation potential. The structural parameters obtained from the single crystal XRD experiment are utilized: the muffin tin radii for Nb, S, and V are considered to be $2.49a_0$, $2.09a_0$, and $2.43a_0$, respectively, where a_0 is the Bohr's radius. And, no relaxation of structure was carried out. The basis set determined by the plane wave cut-off was specified by the value $RMT_{min}K_{max} = 7.0$, which provides a good convergence, where RMT_{min} and K_{max} denote the smallest muffin tin radius in the unit cell and the largest plane wavevector, respectively. The number of k-points in the irreducible Brillouin zone was 200. The energy separating the core and the valence states was set to -6.0 Ry.

In all DFT calculations reported here, spin-orbit coupling is considered. Further, DFT calculations for both the magnetic (antiferromagnetic) and non-magnetic states are performed, and we found that the magnetic ground state is energetically favorable over the non-magnetic case. The energy difference between the magnetic and non-magnetic state is

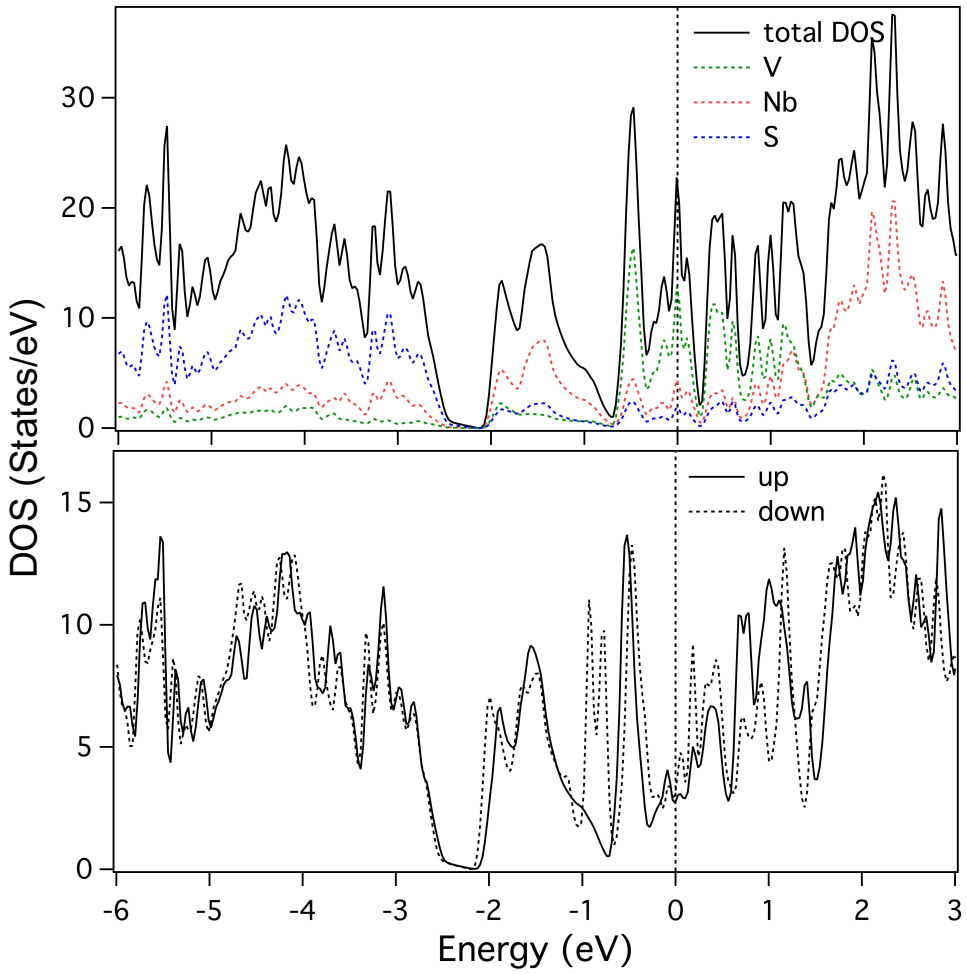

Figure 6.8: The density of states for (a) non-magnetic and (b) antiferromagnetic states. The Fermi level is located at 0 eV.

Table 6.1: Results from the first principles calculations for $V_{0.3}NbS_2$. The DOS at Fermi level and Sommerfeld's coefficients for non-magnetic (NM) and antiferromagnetic (AFM) states with spin up and down are shown.

	NM	AFM (up)	AFM (down)
DOS at E_F (States/eV)	29.19	2.60	2.89
Sommerfeld's coefficient (γ) (mJ/(mol cell K^2))	68.77	6.12	6.80

about 59 eV per unit cell. And, the calculated magnetic moment per unit cell is about 1.99 μ_B, where μ_B is the Bohr magneton.

Band structures for non-magnetic and antiferromagnetic cases along various symmetry directions are shown in Figure 6.7 (a) and 6.7 (b), respectively. The horizontal line at 0 eV represents the Fermi level. The bands in the vicinity of Fermi level are mainly dominated by V-3d and Nb-4d states; S-2p bands mainly lie in between -2 eV and -6.0 eV (not shown all bands). We also found strong k_z dispersion (see dispersion along Γ-A).

The density of states (DOS) for the non-magnetic and the magnetic states are shown in Figure 6.8 (a) and 6.8 (b), respectively. In proximity to the Fermi level (E_F), the V-3d and Nb-4d state contribute to DOS, while the broad structure in the range from -2 eV to -6 eV is originated from S-3p state, which is also evidenced from the band structure results mentioned above. The results obtained from the DOS are summarized in table 6.1. The DOS at E_F and the Sommerfeld's coefficient are larger for non-magnetic case than the magnetic case. The DOS at E_F for magnetic case is comparable to that obtained from heat capacity measurement. Further, the Figure 6.8(b) shows that DOS for spin-up and spin-down channels have slightly different shape, though they have almost equal value for Sommerfeld's coefficients and DOSs at E_F.

6.3 XAS and Resonant PES

The X-ray absorption spectra of $V_{0.3}NbS_2$ corresponding to V-$L_{2,3}$ edge is shown in Figure 6.9. Each spectra are normalized by the total photon counts. The components centered at

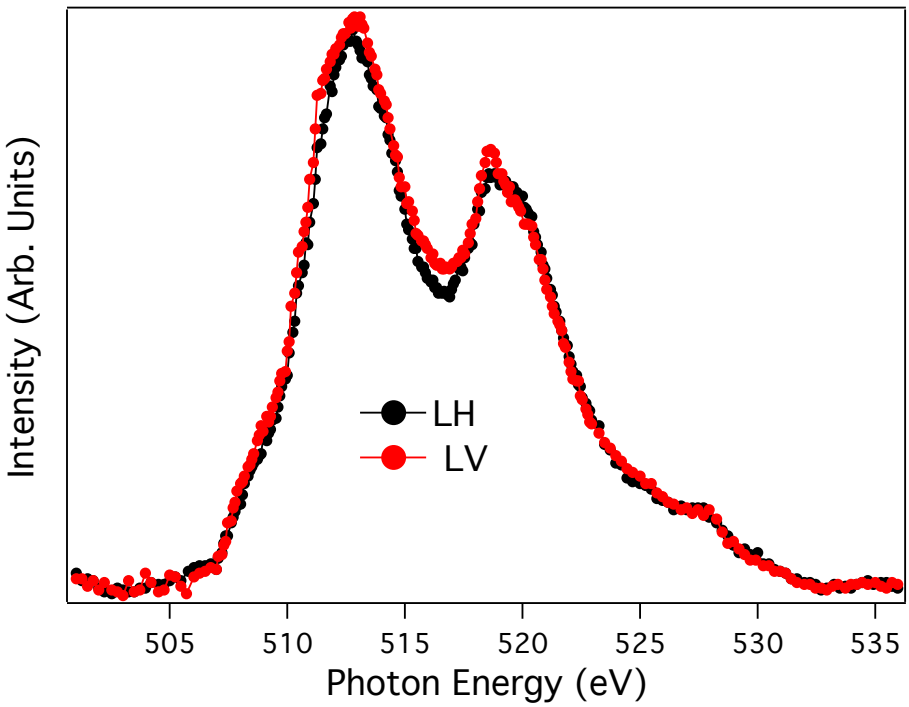

Figure 6.9: Linear dichroism. VL_{23} X-ray absorption spectroscopy for linear horizontal and linear vertical polarization of light.

512.1 eV and 519.8 eV are corresponds to L_3 ($2p_{3/2}$) and L_2 ($2p_{1/2}$) multiplets, respectively. The absorption spectra were taken by total electron yield method (TEY) as a function of photon energy. The TEY mode has been explained in detail in the Chapter 2.

The XAS spectra were recorded for two different photon polarizations: linear horizontal (LH) and linear vertical (LV) polarizations. The LH and LV are also known as π and σ polarizations, respectively. In case of the LV, the photon polarization lies completely in the sample plane, while in LH the polarization lies in both in-plane and out-of-plane of the sample. Thus, the different polarizations allows one to excite the final states having different orbital symmetries.

So, the LV polarization excites the in-plane states whereas the LH polarization excites out of plane states. No significant difference on the shape of two spectra are observed. In the L_3 component, a shoulder is present at low binding energy side for both polarizations of light, this might be originated from the randomly distributed V-atoms on the surface of the sample during the process of cleavage. Similar shoulder has also been reported in the Cr-intercalated system [108] and believed to be from disordered Cr atoms at the surface.

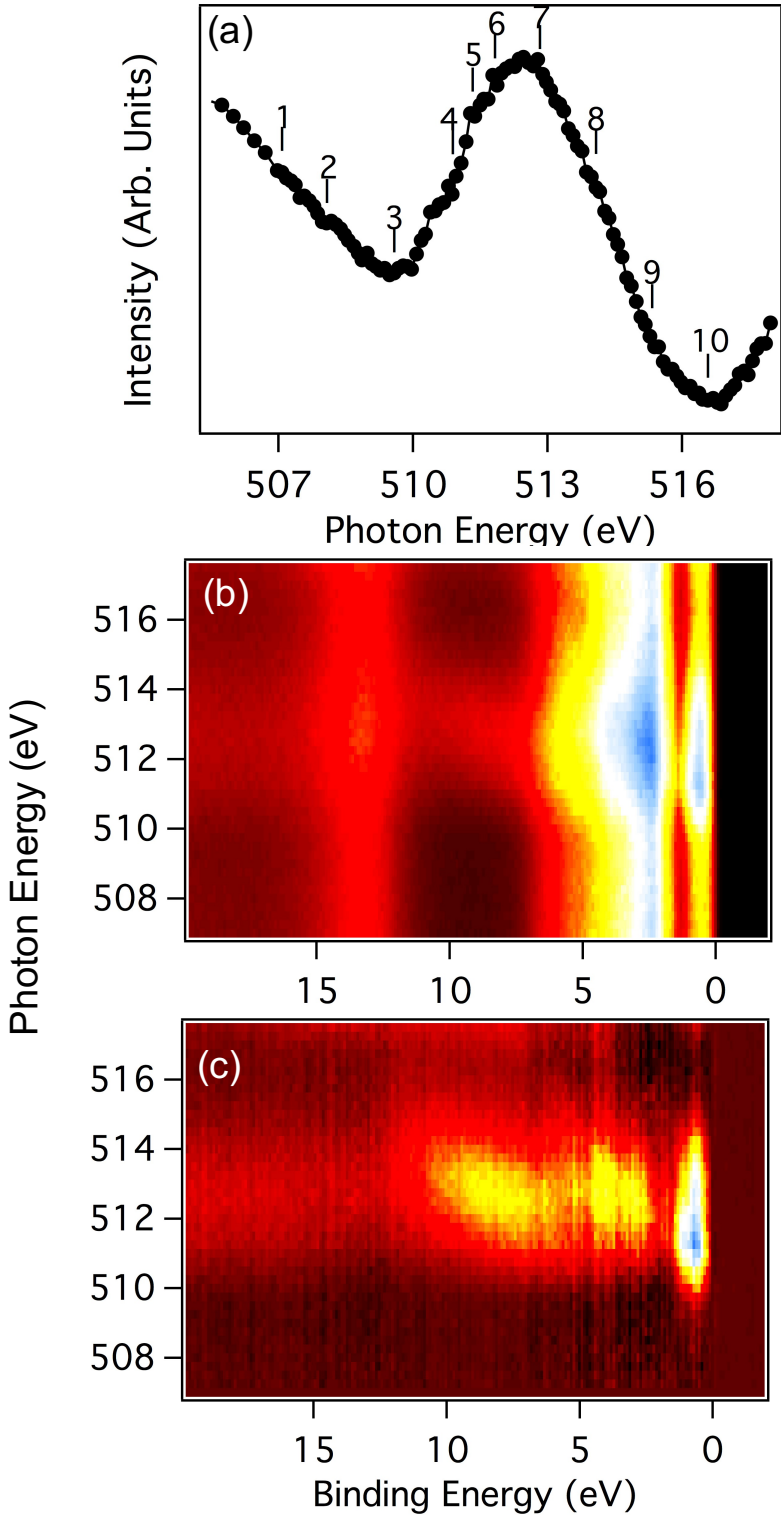

Figure 6.10: XAS and resonant photoemission spectroscopy for linear horizontal polarization. (a) V-L_3 XAS, (b) Resonant photo-emission corresponding to V-L_3 edge, (c) subtraction of off-resonant signal.

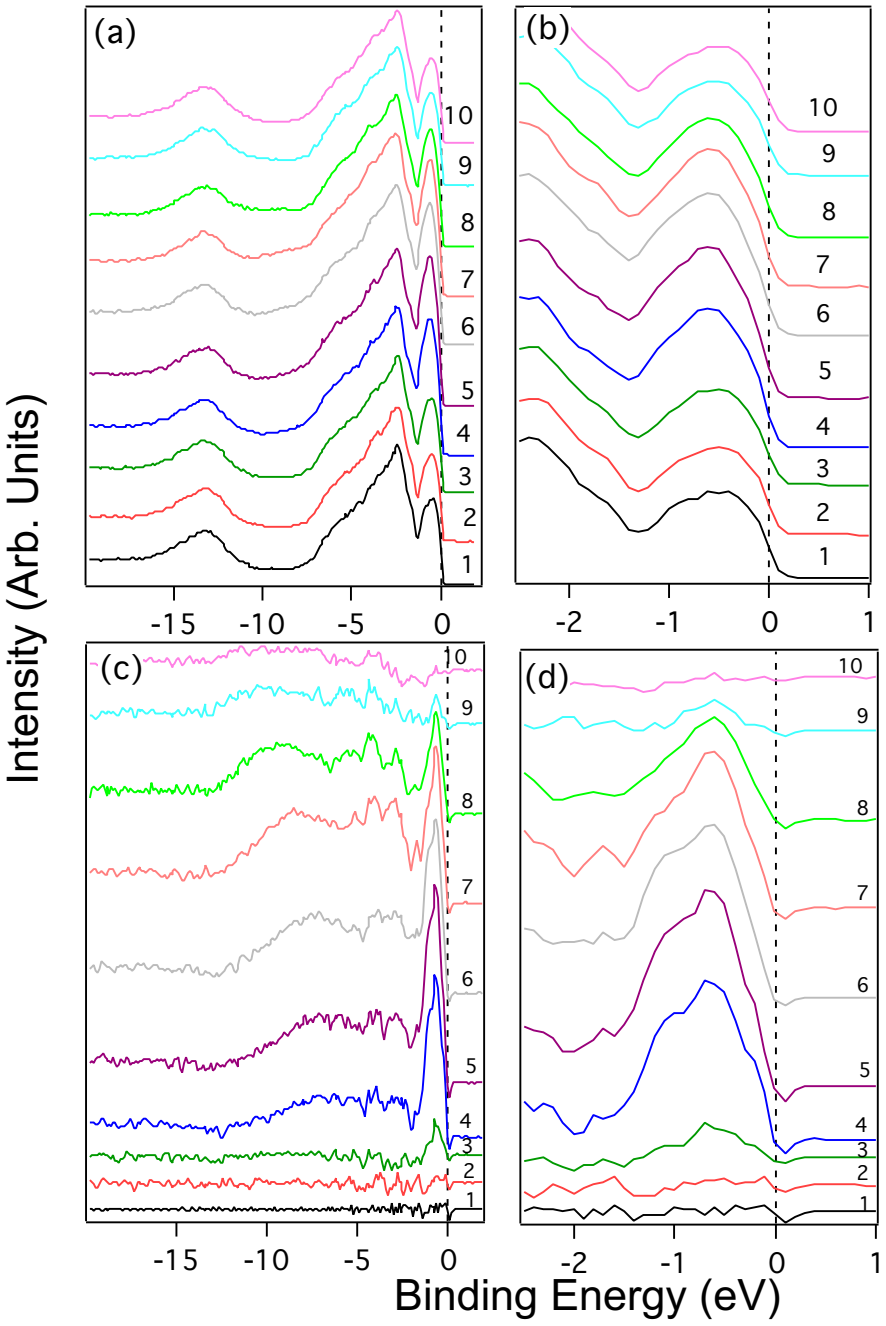

Figure 6.11: (a,c) Line profile obtained from Figure 6.10(b,c) corresponding to the photon energies as marked by numbers in Figure 6.10. (b,d) Zoom-in portion of (a,c) near Fermi level.

The shoulder in the low energy side of L_3 edge is also oberved in another intercaalted system Fe_xNbS_2 [102] sample but the origin of the shoulder has not been explained there.

The resonant photoemission (ResPeS) spectra along with the XAS spectrum corresponding to the V-L_3 absorption edge is shown in Figure 6.10 and 6.12. The resonant spectra are normalized by the total photon flux. In the ResPeS technique, the photon energy is tuned across the absorption edge of the deeper core-level and the photoelectron is excited into the unoccupied state and the region of valence band corresponding to the resonating level is enhanced and thus can be extracted from the totoal VB spectrum. Hence, this technique allows one to identify the contribution originating from the specific element in the valence band spectrum. For the ResPES experiments, we used both LH and LV polarized light in the range of 506–517 eV.

The valence spectra shown in Figure 6.10 (b) was recorded for the LH polarized light of range between 506 and 517 eV. The spectra shows mainly three structures: first in proximity to Fermi level, second at 2.4 eV, and third at 13.5 eV. First two structures are mainly originated from the V-3d and Nb-4d states, and the third structure is mainly from the S-3s state, which is also explained by the DFT calculations shown in Figure 6.8. These three features are more clearly visible in the line profile of Figure 6.11. The line profile is taken from the spectra 6.10 (b) at various photon energies marked by numbers in the XAS spectrum 6.10 (a). Figure 6.11 (b) shows the feature in proximity to Fermi level obtained from the Figure 6.11 (a). In order to check the resonant behavior in detail we subtracted the off-resonant signal from the the original spectra shown in Figure 6.10 (b). The off-resonant spectrum is taken to be at 506 eV. And, the resultant spectra (pure resonant) is shown in Figure 6.10 (c). The corresponding line profile is shown in the Figure 6.11 (c) and 6.11 (d). The pure resonant spectra demonstrated that the the spectra enhances as the photon energy matches with V-L_3 absorption edge. The states at 0.5 eV below the Fermi level is enhanced whereas the states in between 2 to 10 eV are dispersed with the photon energies (constant in kinetic energy). This dispersive features possibly originated from LVV Auger emission. The enhanced features at 0.5 eV below the Fermi level is originated from the V-sates. Since we have used LH-polarized light which mainly probes out-of-plane characters thus the enhanced component are originated from the V out-of-plane character orbital states. Similar resonant

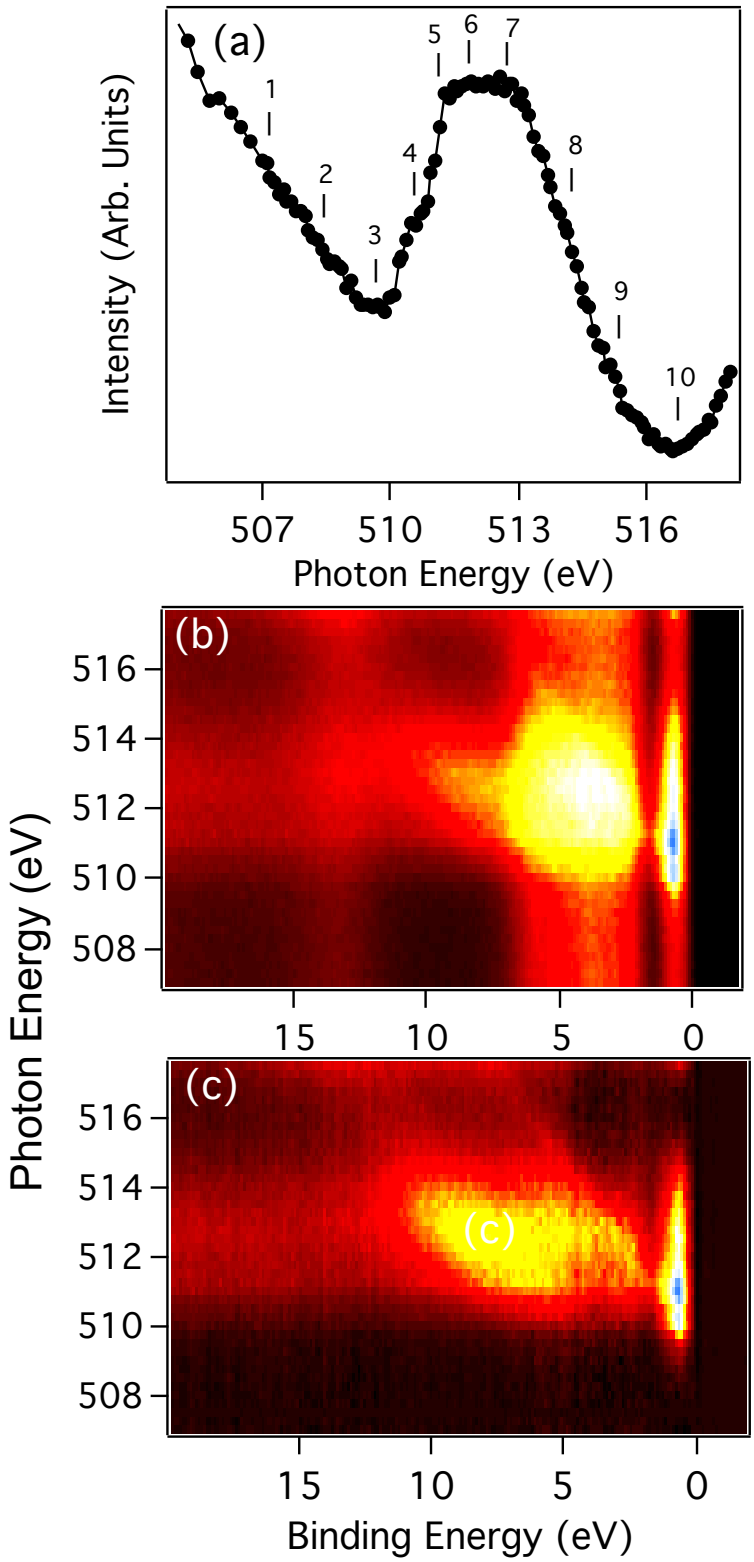

Figure 6.12: XAS along with the resonant photoemission spectra. Here the light polarization lies in the sample plane (Linear Vertical). (a) V-L_3 XAS spectroscopy, (b) Resonant photoemission corresponding to VL_3 edge. (c) Off-resonant signal is subtracted.

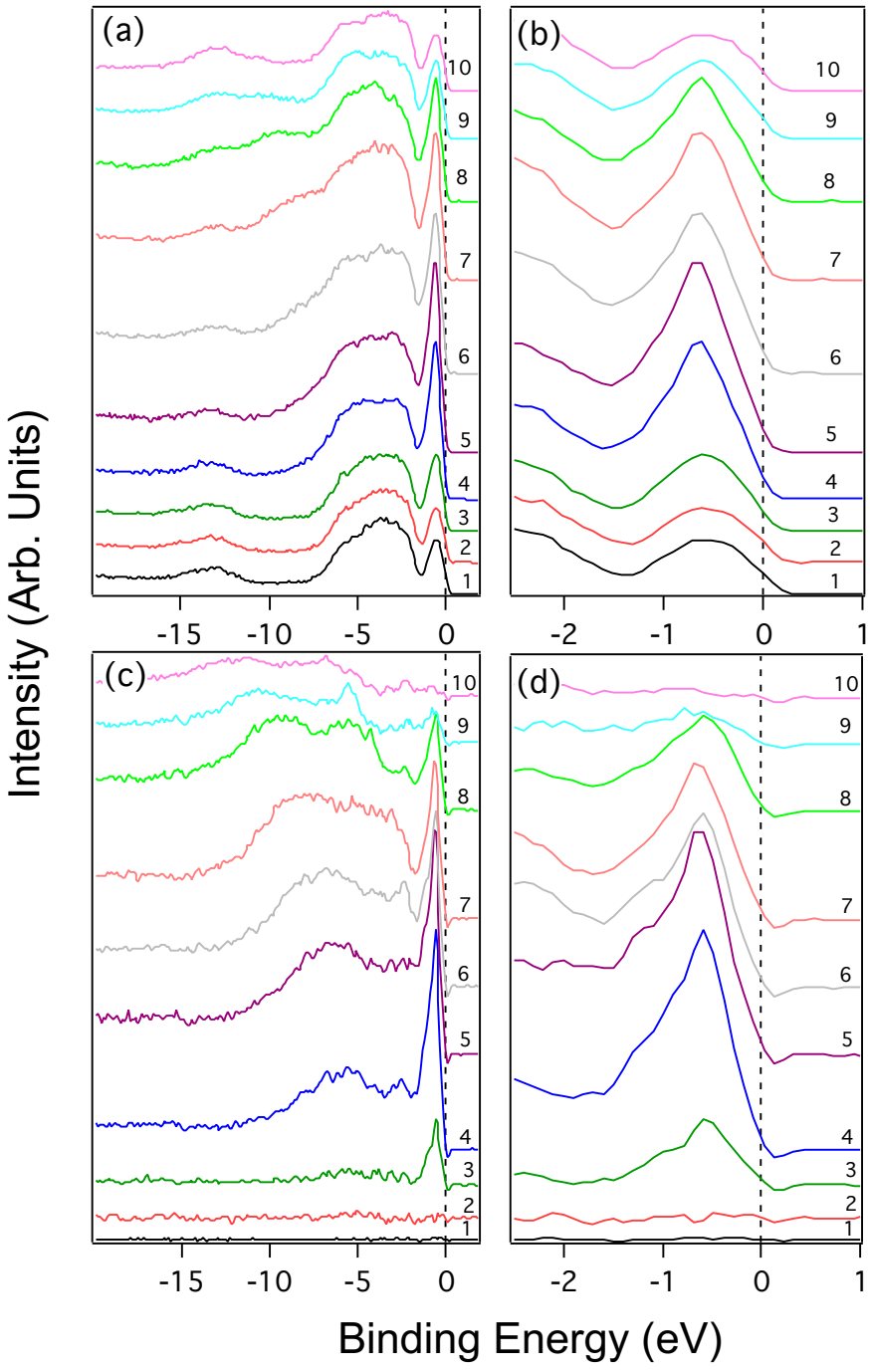

Figure 6.13: Line profiles extracted from Figure 6.12(b,c) corresponding to photon energies marked in Figure 6.12(a). (b) Zoom-in part of line profiles at Fermi energy.

PES is also reported in $Cr_{1/3}NbS_2$ sample. But, in case of $Cr_{1/3}NbS_2$ using LH-polarized light Cr-3d states are enhanced at Fermi level [N. Sirica PhD Thesis]. In other words, Cr-3d states are present just at Fermi level in $Cr_{1/3}NbS_2$,whereas V-3d states are present 0.5 eV below the Fermi level in $V_{0.3}NbS_2$, this is a marked difference between two compounds.

The Figure 6.12 (a), 6.12 (b) are XAS and ResPES for the LV polarized light. The ResPES spectra are recorded for photon energy of range 506–517 eV. As in the LH case, three main structures has also been observed in LV polarization. The off-resonant spectrum is subtracted from the spectra Figure 6.12 (b) and is shown in Figure 6.12 (c). The line profiles obtained from Figure 6.12 (b) for different photon energies as marked in XAS spectrum are shown in Figure 6.13 (a). The line profiles indicated that the first two peaks are observed at 0.6 eV and 3.6 eV. The first peak is noticeably shifted by few meV, in compare to that of LH polarized case, towards high binding energy side. Further, the second peak is observed to be more broadening in comparison to that for LH polarization and is dispersive with the photon energies originating from CVV Auger emission, as in the spectra for LH polarized case. Moreover, the subtracted spectrum shows that the state near the Fermi level (0.6 eV) is resonating as the photon energy matches with the absorption edge of V-L_3. Since the LV polarized light is used, the resonating signal are mainly from the in-plane-characters. From the polarization dependent (LH and LV) ResPES, we found that the spectral weight in the range 0.5–0.6 eV below the Fermi level consists of vanadium in-plane and out-of-plane orbital characters.

In ReSPES, the enhancement in a spectrum arises from the autoionization decay process of the type $2p^6 3d^N + h\nu \rightarrow 2p^5 3d^{N+1} \rightarrow 2p^6 3d^{N-1}\epsilon l$ which is also known as super Coster-Kronig transition [81]. The final state after the decay of this process is the same as that of the direct photoemission from the 3d-state: $2p^6 3d^N + h\nu \rightarrow 2p^6 3d^{N-1}\epsilon l$, where ϵ is energy of electron in the state $l = f, g$. Interference can occur between these two processes since both has same initial and final states. The formalism required to handle this situation was given by Fano [33], and he predicts a characteristically asymmetric peak in excitation spectra. This formalism is based on the interaction of discrete states ($p^5 3d^{N+1}$) with continuum states ($p^6 3d^{N-1}\epsilon l$). Constant initial state (CIS) spectroscopy technique can be employed to describe the enhanced spectral feature and its lineshape as explained above. In CIS technique, the

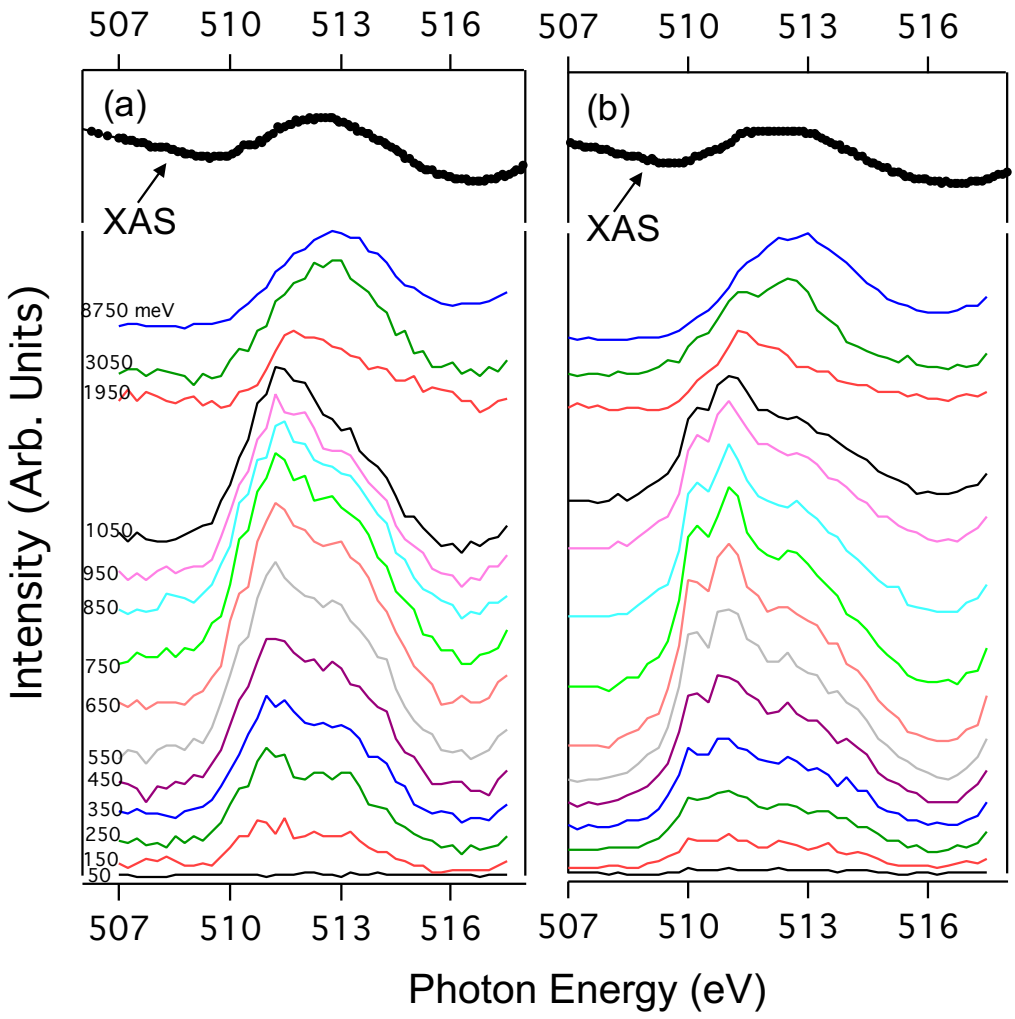

Figure 6.14: Constant initial states for linear horizontal (a) and linear vertical (b) polarization.

initial state is kept constant while the photon energy and kinetic energy is varying i.e. is $E_{kin} - h\omega$ is held fixed. In other words, the initial state is fixed while the final state is scanned. The CIS is thus mapping of the final states i.e. density of unoccupied states. The initial state is the state of the electron before irradiation whereas the final state is the unoccupied state in the conduction band to which the electron is promoted by photon.

The CIS spectra for LH and LV polarization of light is shown in Figure 6.14 (a) and 6.14 (b), respectively. The corresponding XAS spectra are also shown. For LH polarization, the CIS spectrum corresponds to 0.65 eV is strongly enhanced, while, for LV polarization the CIS spectrum at 0.75 enhances strongly. This indicates that the large density of V-3d are present near the Fermi level. As CIS spectrum are enhanced near Fermi level which demonstrated that both in-plane ($d_{x^2-y^2}$) and out-of-plane d_z^2 orbitals are present in proximity to the Fermi level. At higher initial state the line shape changes appreciably for both cases and the peak maximum is shifted towards the higher photon energy. We have not attempt to fit the CIS spectra, the spectra are expected to agree with the lineshape predicted for Fano resonance.

6.4 Conventional vs. Soft X-ray ARPES

We investigate electronic band dispersion of $V_{0.3}NbS_2$ by utilizing the conventional (VUV) as well as soft X-ray ARPES (SX-ARPES) technique. An ARPES technique for which photon source having energy less than 100 eV is known as the conventional or VUV ARPES, whereas the technique with photon energy greater than 100 eV is the soft X-ray ARPES. The conventional ARPES is a surface sensitive technique and is mostly useful to study surface state of a material. The intrinsic band dispersion and bulk sensitivity or the access to the system buried few surface layers can be achieved by SX-ARPES. However, valence band photoemission cross section decreases by few order of magnitude for SX-ARPES in comparison to the conventional VUV-ARPES. The result of experiments for VUV and SX-ARPES presented here are performed at the BACH of the Elettra Synchrotron Facility in Italy. For these experiments, we cleaved the sample at room temperature *in situ* having base pressure better than 10^{-9} Torr, and subsequently the sample was transferred to the main chamber (base pressure better than 10^{-10} Torr) where the experiment was carried out.

These data were taken when the sample is cooled to the lowest possible temperature of 41 K. Here, we have used photon source of energy of 48 eV for VUV ARPES and 218, 439, and 785 eV for SX-ARPES experiments. The estimated probing depths corresponding to photon energies 218, 439 and 785 eV are 24, 33 and 45 Å, respectively. The corresponding energy resolution for SX-ARPES are 30, 60, and 105 meV, respectively. Similarly, the energy resolution for VUV ARPES was kept at 12 meV. From the magnitude of probing depth one can tell that SX photon energies can probe the bulk structure of the material which is to be compared with the lattice parameter 12.13 Å along c-axis and $\sim$ 5-7 Å probing depth for conventional ARPES. Furthermore, we used linear vertical (LV) and linear horizontal (LH) polarized light. In case of the LV polarized light, the light polarization lies completely in the sample plane, while for LH-polarized case the light polarization has both horizontal as well as vertical component to the sample plane. For LV-polarized light we have not shown spectra for 785 eV due to very low count rate. Furthermore, we selected the photon energies for soft X-ray regime such that all probes center of the zone ($k_z = 0$) in the reduced Brillouin zone scheme utilizing inner potential determined from the photon dependent ARPES experiment.

While performing the SX-ARPES experiment data few things have to be considered over the VUV-ARPES. First of all, at higher photon energy the energy resolution of photon source and spectrometer become worse resulting overall loss in energy resolution of the experiment. The poor spectrometer resolution is due to high pass energy setup to compensate the significant loss in absorption cross section at higher photon energy. Further, momentum of photon has also to be considered at high photon energy, while making angle to k-conversion. Also, the momentum resolution worsens at higher kinetic energy since the momentum is proportional to the $E_{kin}^{1/2}$. Finally, the photoelectron matrix elements are much less sensitive to variations of the in-plane crystal momentum as the photon energy increases and it reduces to atomic cross section [114].

Our main aim to perform SX-ARPES is to check whether the conventional (VUV) ARPES is representative of bulk electronic structure of the present compound. This examination is very crucial for rest of the ARPES experiments. As the surface of the sample consists of ordered sulfur terminated region and deficient and disordered vanadium terminated region as mentioned before. Due to the advantages of the conventional ARPES, such as better

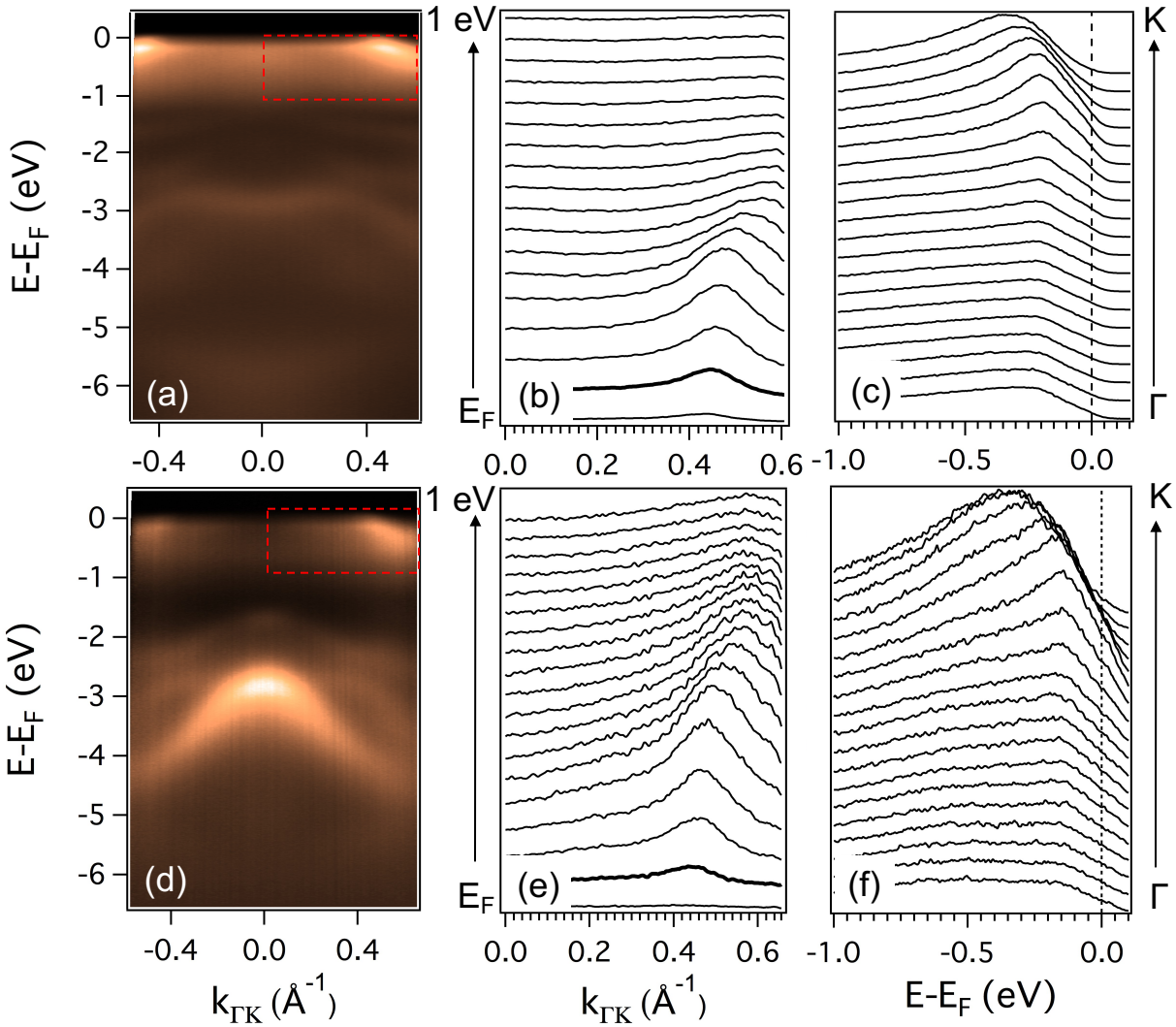

Figure 6.15: ARPES image plots for linear horizontal (a) and Linear vertical (b) polarized light. (b,e) stacked of MDCs corresponding to (a) and (d). (c,f) stacked EDC corresponding to (a) and (b). Region of the MDCs or EDCs taken are marked by dotted rectangles in the respective image plots.

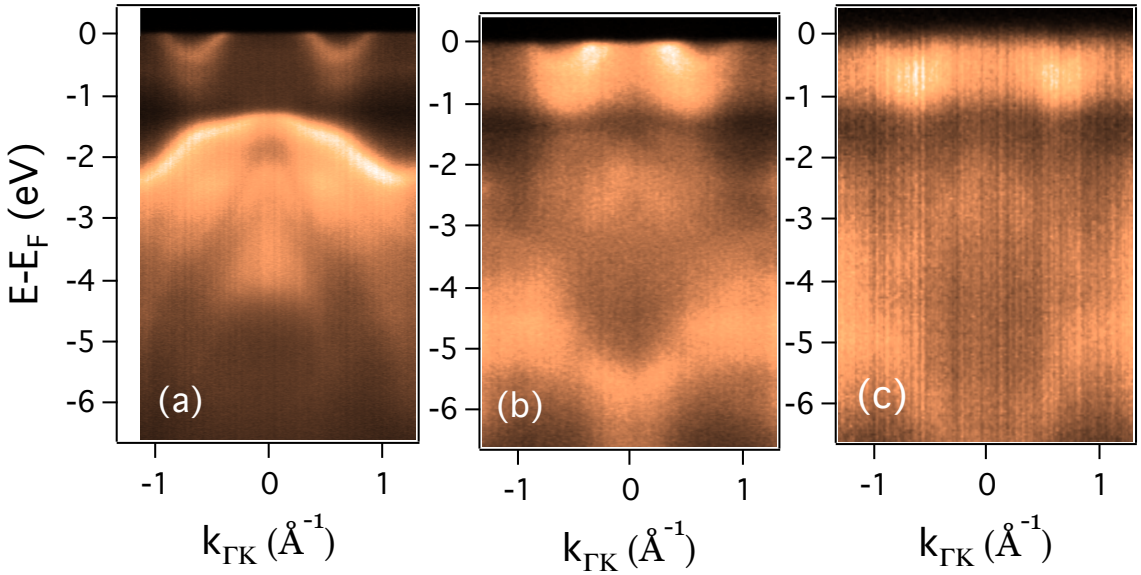

Figure 6.16: Soft X-ray ARPES for LH-polarization for at photon energies of (a) 218 eV, (b) 438 eV, and (c) 785 eV

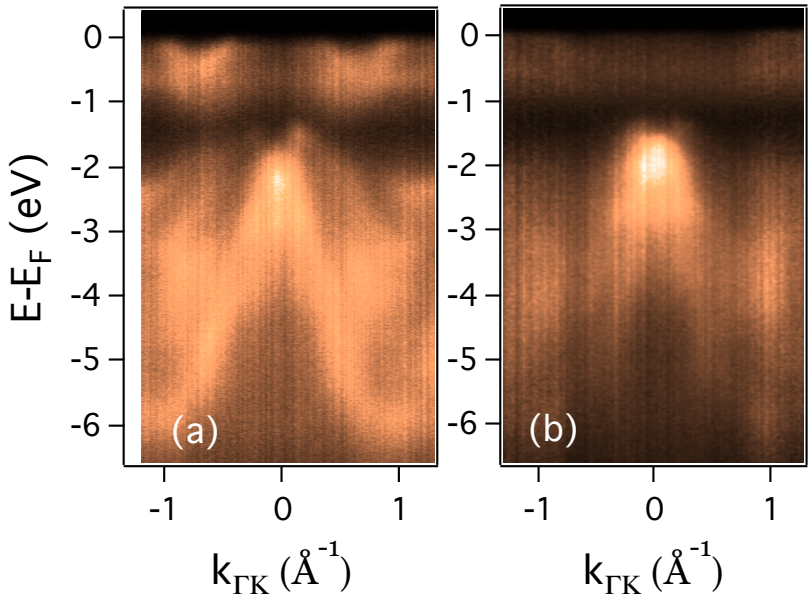

Figure 6.17: Soft X-ray ARPES for LV-polarization light for photon energies of (a) 218 eV and (b) 438 eV

energy and momentum resolution, large photo-absorption cross section, over SX-ARPES it is suitable to perform VUV-ARPES if the electronic band structure for both techniques exhibit similar spectral features. Moreover, VUV-ARPES is well suited for electronic band structure of two dimensional system.

The conventional ARPES results using photon energy of 48 eV are presented in Figure 2.6; upper panel was recorded for linear horizontal polarization whereas lower panel was recorded for linear vertical polarization. The corresponding MDC and EDC stacked are shown on the right side of each image plot. The measurements were performed when the sample is aligned along Γ-K symmetry direction. In both cases, one band crosses Fermi energy with Fermi vector of about 0.44 $\mathring{A}^{-1}$. This value is in consistent with that observed for Ni- and Mn-intercalated NbS_2 system [9]. Moreover, this Fermi point is not affected by intercalation when we compare with the parent compound NbS_2 [108]. Nevertheless, we are unable to compare the spectral features at K point with that of $Cr_{1/3}NbS_2$ and other intercalated compounds mentioned above since our experimental setup does not cover symmetry point K at this photon energy. Additionally, one band appears to be sink below the Fermi level with band minimum of about 1 eV. Furthermore, other band structures are located in the region between 1.5 to 6 eV. We have noticed that, unlike $Cr_{1/3}NbS_2$ system, k_F for α band is almost equal to the parent compound NbS_2 and the β bands centered around Γ point are absent in present compound. Thus, this intercalated system exhibits completely different electronic structure than $Cr_{1/3}NbS_2$, though it is expected that both give similar structure as both 3d transition metals donate almost equal number of charge carrier.

The SX-ARPES results for linear horizontal polarization and linear vertical polarization are shown in Figure 6.16 and 6.17, respectively. In case of LH polarization the bands in between 1.5 to 3 eV are enhanced when the photon energy of 218 eV was used. As we increased the photon energy to 438 and 785 eV, intensity of these bands reduces and band structure shows similar features as of conventional ARPES. This indicates that variation in spectral features in the ARPES spectra is not due to the variation in probing depth, rather it is due to the matrix element effect (soft X-ray regime the matrix element reduces to the atomic cross section). Furthermore, the spectral features at higher photon energies become broader along energy and momentum axis which is due to the worsening of the energy and

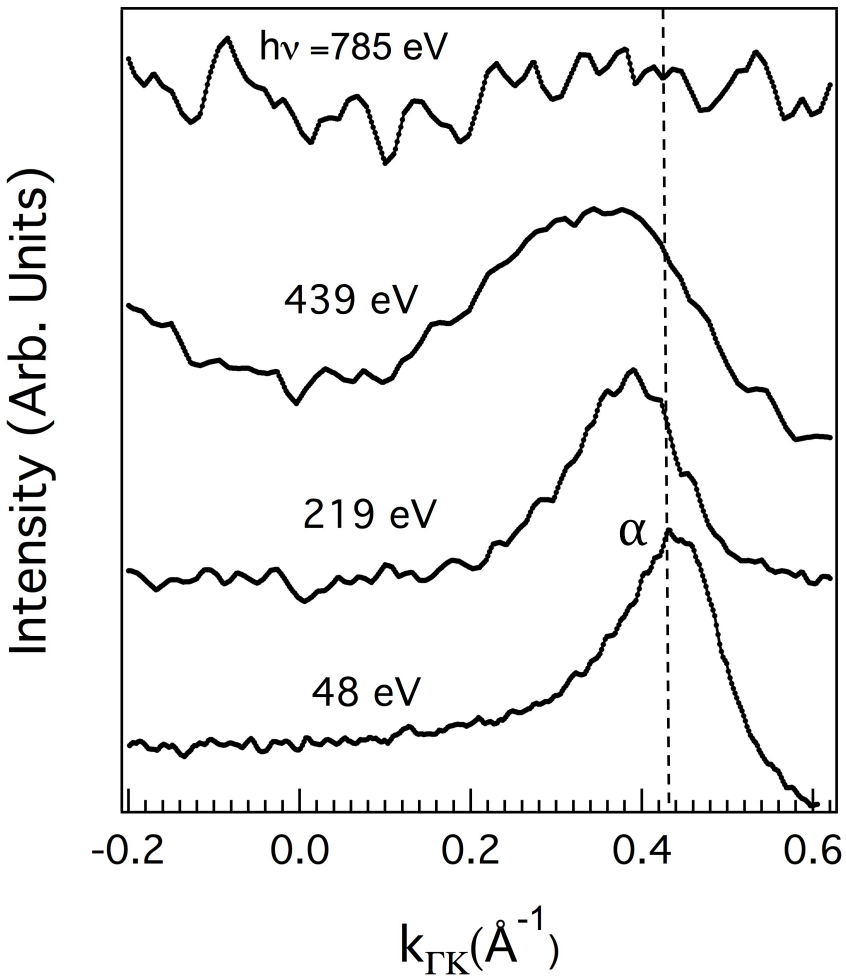

Figure 6.18: MDCs at Fermi level for the VUV and soft X-ray ARPES for the linear horizontal photon polarization.

momentum resolution. The MDCs at Fermi level corresponding to different photon energy is shown in Figure 6.18. This supports the fact that α band is present in all spectra, for 785 eV we can't resolve this band due to very low count rate. The spectral feature becomes broader due to low energy and momentum resolution at higher photon energies.

For LV-polarization SX-ARPES exhibits most of the spectral features as in VUV-ARPES. Though, the bands are not clearly resolvable for experiments performed at higher photon energies. The intensity of low lying bands is higher than that of bands close to Fermi energy. In addition, we observed completely different topology for bands lying between 2 to 5 eV for LV-polarized light than that of LH-polarized light due to the matrix element effect

Thus from the conventional and SX-ARPES, we conclude that albeit the surface of the sample is disordered and vanadium deficient, the conventional VUV-ARPES is still the representative of bulk electronic structure. In other words, the band dispersion and Fermi vector for VUV ARPES are not significantly varied with respect to the SX-ARPES.

6.5 Comparison With Parent Compound NbS_2

The Nb-3d core level photoemission spectra for the parent compound NbS_2 and intercalated system $V_{0.3}NbS_2$ is shown in Figure 6.19(a). Both the spectra are measured with the photon energy of 762 eV. The Nb-3d spectrum is obtained from Figure 9 of Ref. [108]. In addition to the spin orbit doublet $3d_{5/2}$ and $3d_{3/2}$, additional feature called satellite is also observed at high binding energy side of each main peak. The satellite features are observed in both NbS_2 and $V_{0.3}NbS_2$ samples, though it is strongly suppressed in case of the intercalated system. We haven't observed such satellite features in case of Nb-3p spectrum as shown in Figure 6.6(a), so it is confirmed that these features are not originated from the oxidation or contamination in the sample. Similar satellite structure has also been observed in $Cr_{1/3}NbS_2$ [108] , Fe_xNbS_2 [102], and $Ti_{1-x}Nb_xO_2$ [89]. The origin of the main and satellite structures is due to the two different screening channel as explained by Kotoni and Toyozawa [67]. In this condition, the potential created by core hole upon the photoexcitation is sufficient to pull the unoccupied level from the conduction band. If this unoccupied level is filled by transferring electron from the sulfur then a main peak is observed which is known as "well

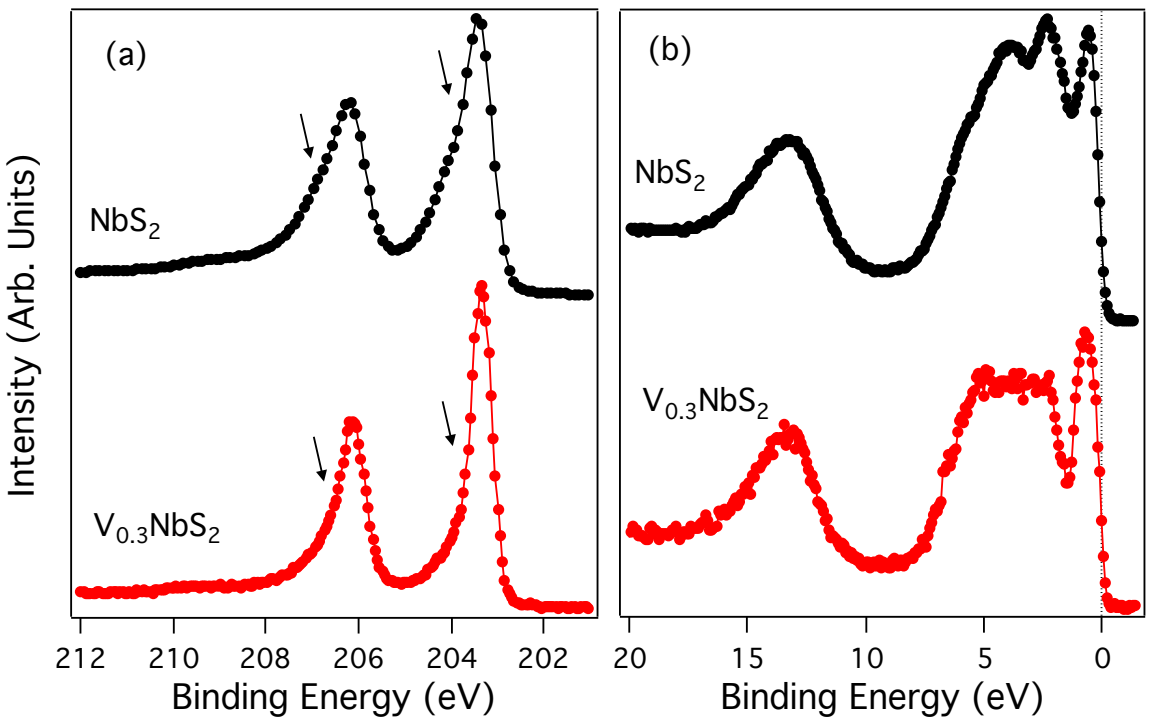

Figure 6.19: Nb-3d core level and valence band for NbS_2 and $V_{0.3}NbS_2$ at photon energy 762 eV. (a) Nb-3d core level of NbS_2 and $V_{0.3}NbS_2$. (b) valence band of NbS_2 and $V_{0.3}NbS_2$.

screened" final state as it screen well the core hole potential, whereas, if the unoccupied state remains empty then the core hole can't be screened well by valence electrons then the satellite peak observed and the final state is called "poorly screened". The width of the 3d-core level spectrum for $V_{0.3}NbS_2$ is narrower than NbS_2, indicating the charge transfer to unoccupied state which can screen well the satellite features. In this way the satellite feature is suppressed in the intercalated system, an evidence of electron transfer to Nb-4d state from V ion.

Figure 6.19(b) shows valence band spectra for NbS_2 and $V_{0.3}NbS_2$. The spectra were recorded at the photon beam of energy 762 eV. The valence band spectra for NbS_2 is obtained from the Ref.[108]. Four main structures are present in case of valence band of NbS_2, whereas three structures are present in $V_{0.3}NbS_2$. The sharp peak in proximity to Fermi level is mainly originated from an admixture of Nb-4d and V-3d states. And, this peak is slightly broader by few meV for $V_{0.3}NbS_2$ in comparison to NbS_2. The second and third peaks centered at 3.75 eV and 13.44 eV are mainly originated from S-3p and S-3s states, respectively. It is

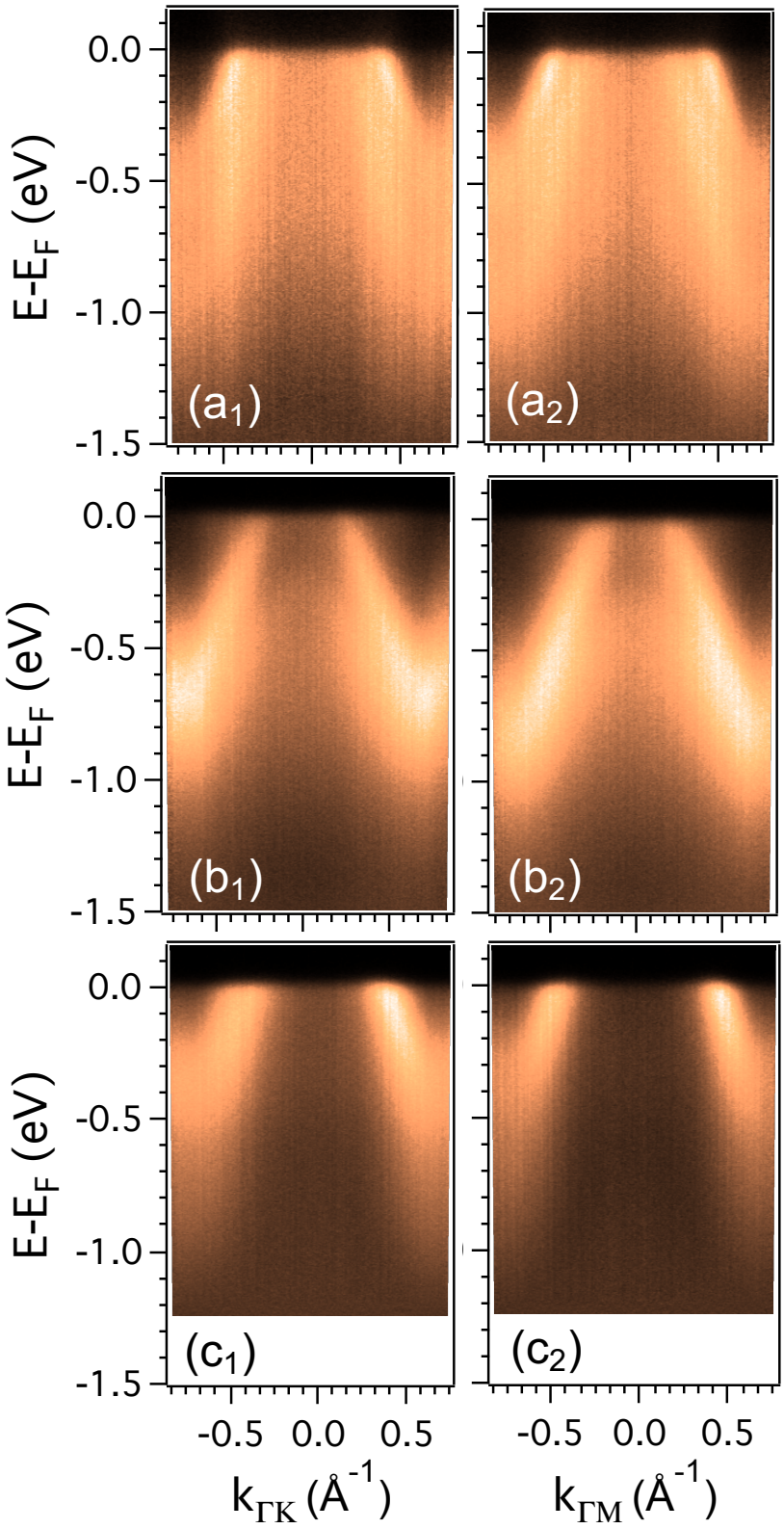

Figure 6.20: ARPES spectra for (a) NbS2, (b) Cr1/3NbS2, (c) V0.3NbS2 recorded at 140 K utilizing He-II (40.8 eV) source.

also observed that all three structures of $V_{0.3}NbS_2$ are shifted by about 150 meV to higher binding energy in compare to NbS_2, indicating the chemical potential increases upon the intercalation of V atoms. In other words, the intercalated species donate electrons to NbS_2 layers. Similar behavior is also reported in $Cr_{1/3}NbS_2$ sample [108], where main peaks are shifted by 400 meV towards higher binding energy side of the spectrum.

Comparison of ARPES spectra for three compounds NbS_2, $Cr_{1/3}NbS_2$ and $V_{0.3}NbS_2$ is shown in Figure 6.20 (a), (b), and (c), respectively. These spectra were recorded with utilizing He-II photon source (40.8 eV) at pressure better than 10^{-11} Torr. For these measurements samples were cooled to 140 K. We chose this temperature so that all lie above the magnetic transition temperature, particularly of intercalated systems. From the ARPES spectra, we observed the bands are shifted downward in case of $Cr_{1/3}NbS_2$ and $V_{0.3}NbS_2$ in compare to the parent compound. That is, a hole pocket at the Fermi level becomes smaller for the intercalated compounds, further confirming that the intercalation vanadium donates electron to the parent compound. Noticeably, vanadium intercalant injects lesser charge to the parent compound than the chromium one. The detailed experiment results for the $V_{0.3}NbS_2$ will be discussed in the subsequent sections.

6.6 Polarization Dependent of ARPES Experiment

In order to investigate orbital characters of a particular band, we performed the polarization dependent ARPES experiments. Two photon polarization σ and π were used. In σ geometry, the photon polarization lies in perpendicular to the scattering plane, whereas in π geometry it lies in the scattering plane. For these measurements, the experiments were set up such that the scattering plane lies perpendicular to the sample surface and coincides with the mirror plane of the sample. So, σ polarized light probes in-plane orbitals and π polarized light probes out-of-plane orbitals.

The polarization dependent of ARPES experiment allows one to determine the majority orbital character of each band, which is given by the symmetry of the photoelectron initial state [108, 24]. In order to have finite photoemission intensity, the whole integrand (in dipole matrix element) in the triple product of initial state, dipole operator, and the final state has

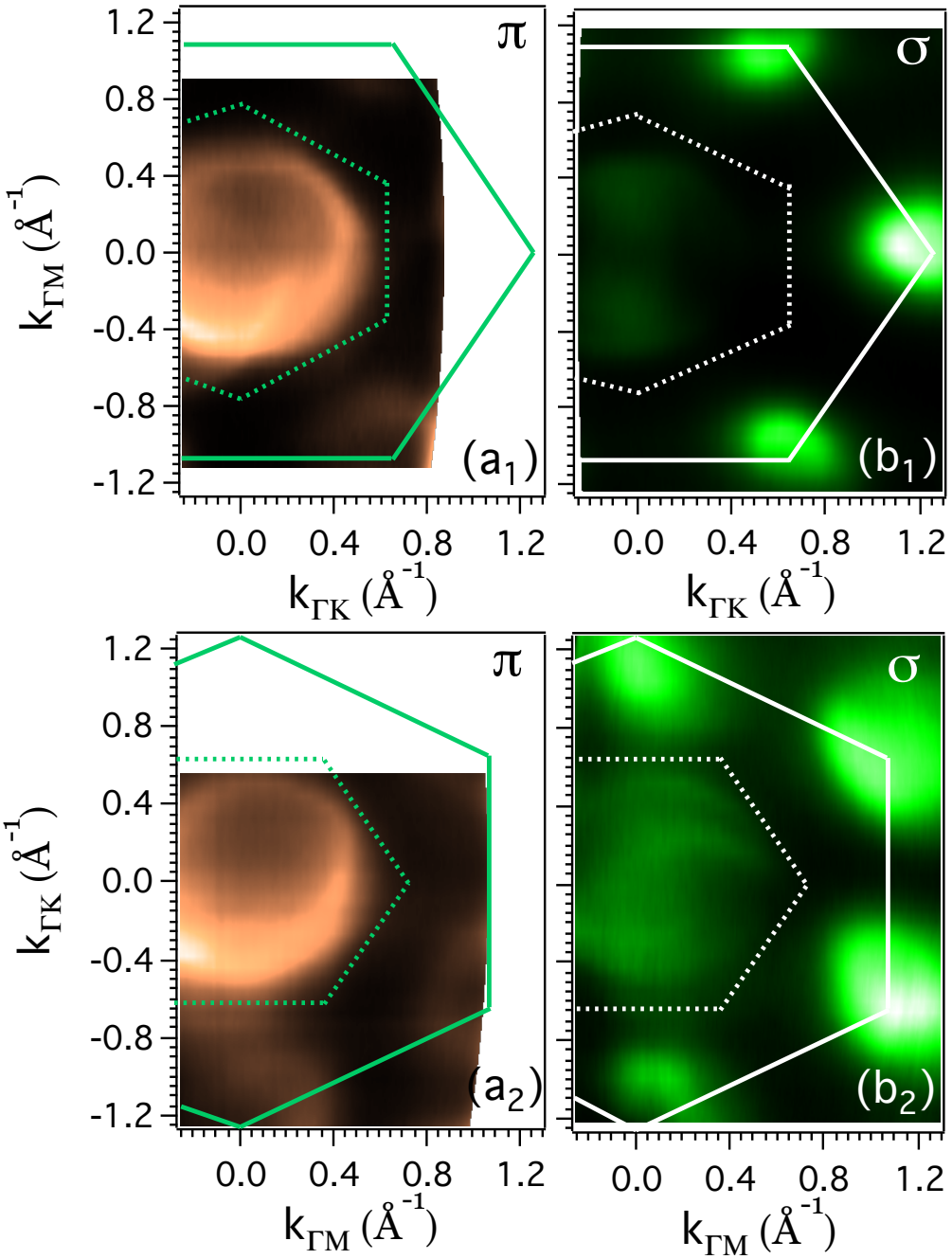

Figure 6.21: FS mapping experiments performed at photon energy of 48 eV for π (a_1, a_2) and σ (b_1, b_2) polarization of light. The directions of high symmetry points Γ-M and Γ-K are indicated in the image plots. BZs for $\sqrt{3} \times \sqrt{3}$ superstructure and 1×1 parent compound are indicated by dotted and solid lines, respectively.

to be even function under reflection with respect to the mirror plane. When the detector slit lies in the mirror plane the final state of the photoelectron wavefuntion is of even parity. For π and σ polarized light, the dipole operator is of even and odd parity, respectively. Thus, π polarized light probes the even parity initial state, while the σ polarized light probes initial state with the odd parity.

Fermi surface (FS) mapping of $V_{0.3}NbS_2$ is shown in Figure 6.21. Upper two panels are for the spectra recorded when the detector slit aligned along the ΓK direction, while the lower two panels for the slit along ΓM direction. The light polarization, σ and π, are labeled in image plots. The FS pockets at Γ and K points has nearly hexagonal and triangular cross-section, respectively as predicted by DFT calculations for parent compound NbS_2 [48]. From the FS mapping we claim that the proper Brillouin zone can not be that of $(\sqrt{3} \times \sqrt{3})$ superstructure since Γ and K point have different FS topology. It is known that K point of the BZ for parent compound is Γ point for the superstructure as these two points are separated by reciprocal lattice vector $1.26\mathring{A}^{-1}$ of $(\sqrt{3} \times \sqrt{3})$ superstructure . Thus, it is expected identical features at Γ and K point, but this is not the case. So, we consider the BZ of parent compound while analyzing the ARPES data. The intensity of spectral feature at Γ and K depends on the photon polarization. And, no spectral features are present at M point as also predicted by the DFT calculations. The intensity of bands crossing Fermi energy around Γ point is enhanced appreciably when the π- polarized light was used which indicates that these bands have even orbital characters. The intensity of these features does not change when the detector slit is aligned either along ΓK or ΓM direction. This indicates that these bands are mainly contributed from the out-of-plane orbitals. On the other hand, when the σ polarized light was used, spectral feature at K point is enhanced indicating that the bands with odd symmetry are crossing Fermi energy at this point. The symmetry of bands at K point can not be determined accurately since K point does not contain in the mirror plane when the slit is aligned along ΓM direction. The FS mapping results we obtained from experiments are in consistent with that predicted from the DFT calculations for NbS_2 [48]. The DFT predicts d_{z^2} and p_z character at the zone center (Γ point) and $d_{xy}/d_{x^2-y^2}$ character around K point. The FS mapping for the parent compound obtained from ARPES experiment has been presented in Ref [108]. In $V_{0.3}NbS_2$, the size of the

hole pockets centered around Γ and K points reduce which is in consistent that intercalant donates electron to the NbS_2 layer. The shrinkage of hole pocket has also been observed in intercalated compound $Cr_{1/3}NbS_2$. Furthermore, the shape and size of FS is significantly different than that of NbS_2 [108], particularly at the zone center, indicating that intercalant vanadium atoms not only inject electrons but also modify the electronic structure of parent compound, which is in contrast to the rigid band mechanism.

We sketched the FS for the $V_{0.3}NbS_2$ and compared with that of another intercalated compound $Cr_{1/3}NbS_2$ and host material NbS_2. These sketches are made from the MDCs at E_F shown on the right panel extracted from the Figure 6.20 and 6.25, where the high symmetry directions and the photon energies are indicated for respective materials. It has to be emphasized here that NbS_2 and $Cr_{1/3}NbS_2$ exhibit 2D k_z dispersion, so the size of the FS does not depend upon the photon energy. On the other hand, the $V_{0.3}NbS_2$ exhibits 3D like k_z dispersion (which will be discussed in another section), hence the size of the FS may depend on the photon energy. We find from the k_z dispersion of $V_{0.3}NbS_2$ that FS has smallest and largest sheets for the photon energy 40 eV and 44 eV, respectively, particularly around Γ-point. Now, we start from FS sketch of NbS_2, the outermost circular sheet around Γ point is from the α- band which has Fermi wave vector (k_F) of about 0.45 $\mathring{A}^{-1}$ as reported in the Ref [108] which is measured along ΓK direction. From the He-II light source (40.8 eV), we obtained k_F of 0.389 $\mathring{A}^{-1}$ and 0.445 $\mathring{A}^{-1}$ for the spectra recorded along ΓK and ΓM, respectively, ratio of these two quantity is equivalent to that of distance of ΓM to ΓK, thus a hexagonal like Fermi sheet can be sketched and is the 'S' band as reported in Ref [108]. FSs for $Cr_{1/3}NbS_2$ is similar to that obtained in Ref [108] except an extra hexagonal like pocket is observed for the spectra recorded at 40.8 eV (He-II). Detailed FS description of $Cr_{1/3}NbS_2$ can be found in Reference [108]. In $V_{0.3}NbS_2$, a small circular sheet is obtained while using σ polarized light of k_F 0.1 $\mathring{A}^{-1}$ measured along ΓM and ΓK direction. The smaller hexagonal sheet around Γ point is sketched from the MDCs with k_F of 0.195 $\mathring{A}^{-1}$ and 0.24 $\mathring{A}^{-1}$ when measured along ΓK and ΓM direction for He-II photon source. Similarly, the larger hexagonal hole pocket is also obtained from He-II source. The larger circle (outermost FS sheet) is observed when they are measured by π polarized light of energy 44 eV. As we mentioned earlier that 3D nature of the FS for $V_{0.3}NbS_2$ such that

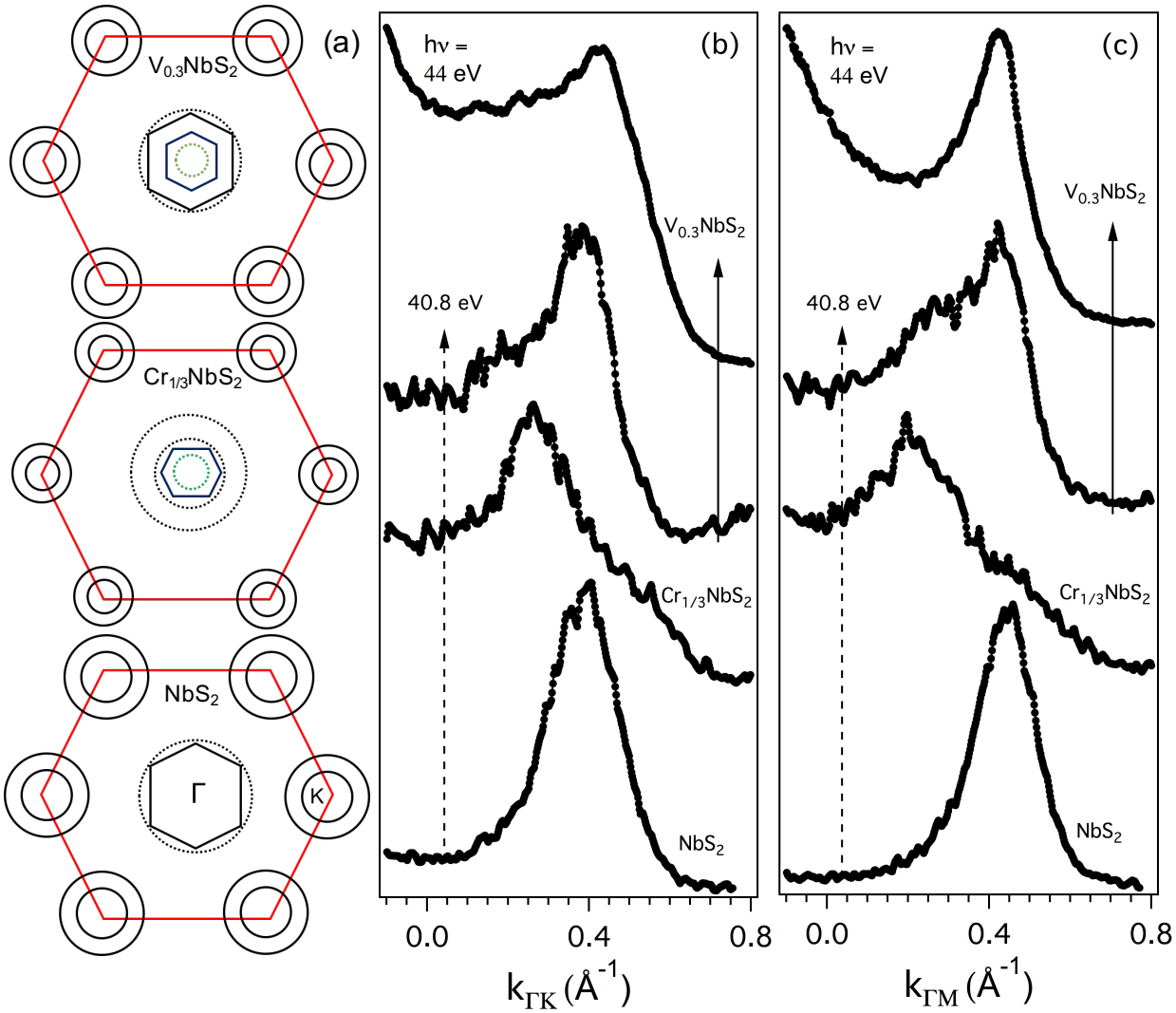

Figure 6.22: FS sketches of two intercalated compounds $V_{0.3}NbS_2$ and $Cr_{1/3}NbS_2$ compared with the parent compound NbS_2. The sketches are made from MDC at E_F shown on right panel and Ref [108]. It is noted that the size of pockets at Γ and K-point in intercalated complexes are decreased. (b) MDC at E_F extracted from the ARPES spectra 6.20 (a_1, b_1, c_1) and 6.25 (a_1) (b) MDC at E_F from the spectra 6.20 (a_2, b_2, c_2) and 6.25 (a_2)

40.8 eV photon energy gives smallest FS sheet while 44 eV gives largest one. Noticeably, the hexagonal FS sheets' corner touches the outermost circular sheet. Thus, we believe that these two are the same FS sheets: the hexagonal shape could be due to reduction in size along ΓK while it remains same along ΓM direction at photon energy of 40.8 eV. Also, two hole like pockets are observed around K-point for all three compounds and the size of pocket for both the intercalated compounds decreases at K compared to parent compound. Importantly, we found that the FS of $V_{0.3}NbS_2$ is 10% smaller than that of parent compound which is still larger than $Cr_{1/3}NbS_2$ sample indicating that V donates electron to NbS_2 but it does not donate as much electron as Cr does to NbS_2.

Figure 6.23 shows image plots of the valence band spectra covering wide energy range (up to 6 eV from the Fermi energy). The spectra were recorded using photon energy of 44 eV with π and σ polarization as labeled in the image plots. Similar spectra recorded at photon energy 48 eV are shown in Figure 6.24. Both sets of experiments are performed at temperature 17 K while keeping the energy resolution about 60 meV. The spectral features are basically the same in both sets of experiments. We will later discuss structures around Fermi energy in more detail as interesting physical properties such as magnetism, transport properties, chemical bonding etc. can be explained by inspecting the spectral weight in proximity to the Fermi energy. Bands in the energy range of 1 to 2 eV are admixture of mainly Nb-4d, and V-3d, while the bands confined between 3 to 6 eV are mainly contributed from the S-3p orbitals. It is also to be noted that out-plane orbitals such as d_{z^2} are probed when π-polarized light is used, whereas in plane orbitals like $d_{xy}/d_{x^2-y^2}$ are detected when σ-polarized light is used. Moreover, the photon energy of 44 eV corresponds to V 3p-3d absorption edge. Thus, in this photon energy V-3d bands near Fermi level most likely to be enhanced.

The ARPES spectra recorded for fine cut corresponding to wide valence band image plots: Figure 6.23 and 6.24 are shown in Figure 6.25 and 6.28, respectively. An identical experimental environment as of the wide valence band measurements were employed. Here, the better energy resolution of about 15 meV was used. The MDC and EDC stacks corresponding to Figures 6.25 and 6.28 are shown in Figure 6.26 and 6.26, and Figures 6.27 and 6.30, respectively. In case of π-polarized light of energy 44 eV along Γ-K direction

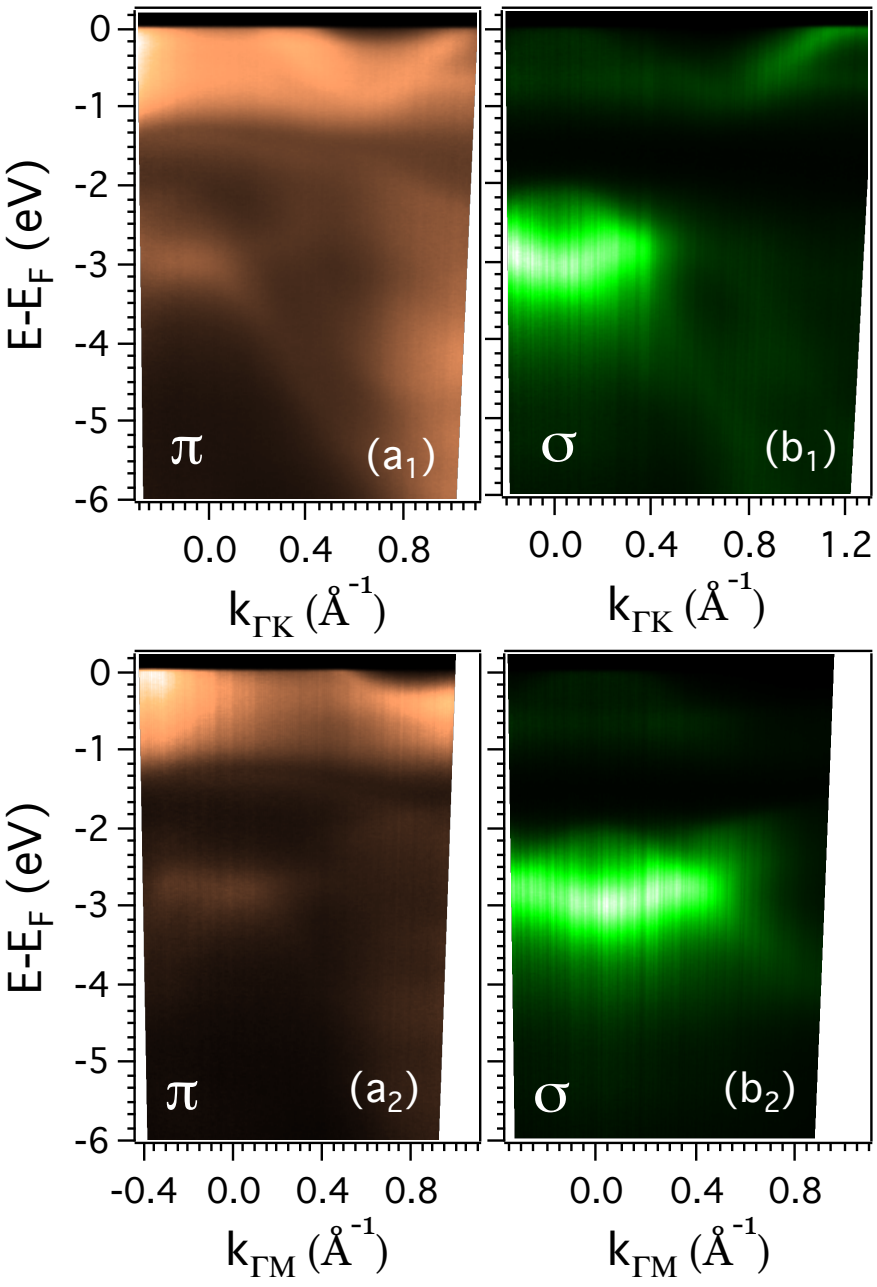

Figure 6.23: Band dispersion in the wide range of binding energy measured at photon energy 44 eV for π (a1,a2) and σ (b1,b2) polarization along ΓK (a1,b1) and ΓM (a2,b2) direction.

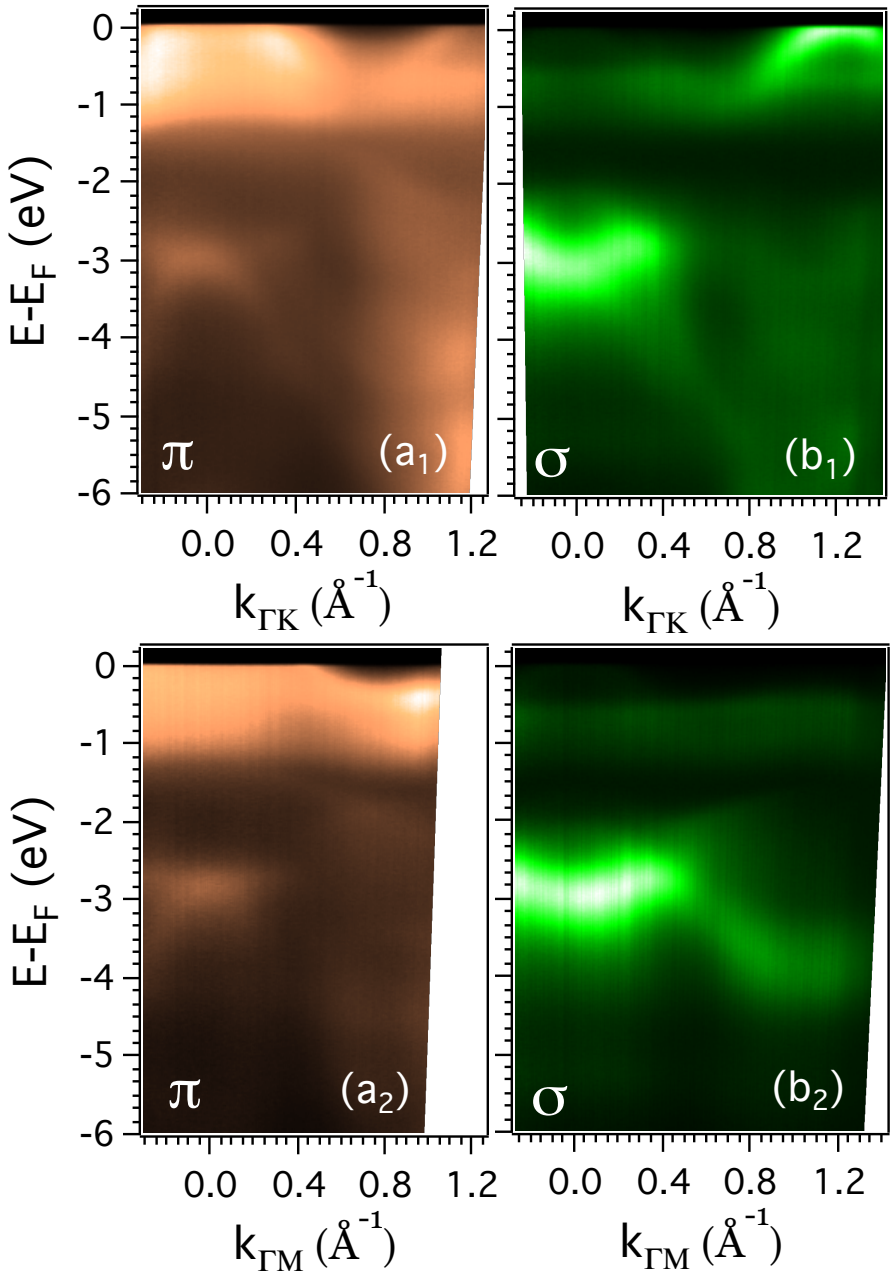

Figure 6.24: Band dispersion in the wide range of binding energy measured at photon energy 48 eV for π (a1,a2) and σ (b1,b2) polarization along Γ-K (a1,b1) and Γ-M (a2,b2) directions.

(see Figure 6.25 (a1)), we observed that two hole like bands cross the Fermi energy having Fermi vectors of 0.28 and 0.44 $\mathring{A}^{-1}$, which is more clearly discerned from the MDCs stacked in Figure 6.26 having asymmetric lineshpae. On the other hand, for σ polarized light one hole like band crosses the Fermi energy very close to Γ point with wave vector of 0.1 $\mathring{A}^{-1}$. Similarly, at K point two hole bands crosses the Fermi energy in σ polarized light. From the EDC analysis shown in 6.27 and 6.30 tells us that a non-dispersive band is located 0.7 eV below the Fermi level. Also, a dispersive band which does not cross the Fermi level confined 0.5 eV below the Fermi energy near K point as indicated in EDC stacked plot. The ARPES spectra recorded at photon energies 44 and 48 eV are essentially the same except the intensity of band near K for photon energy 48 eV are enhanced in compare to bands for 44 eV, and is also evidenced from the MDC at E_F as shown in Figure 6.31 (b), which might be due to the matrix element effect. Thus, when the sample is aligned along ΓK direction three bands near Γ and two bands near K point cross the Fermi energy. Also a non-dispersive feature is present at 0.7 eV below the Fermi level and an additional band which does not cross the Fermi energy but disperses near K point.

The lower panels in Figure 6.25 and 6.28 represent ARPES spectra when the sample is aligned along ΓM direction. From the MDC analysis, we observed that two hole-like bands cross the Fermi energy around Γ point having $k_F = 0.43$ and 0.23 $\mathring{A}^{-1}$, for π polarized light. When the light polarization is switched to σ type a band which disperses towards the Γ point crosses the Fermi level very close to Γ point with $k_F = 0.1$ $\mathring{A}^{-1}$. Additionally, a non-dispersive band lies below the Fermi level centered about 0.7 eV has been observed in both polarized light but it is more pronounced for σ-polarized light, particularly at 48 eV photon energy (see Figure 6.25 (b2)). In fact, the intensity of bands for 48 eV is higher than that of 44 eV which is due to the matrix element effect. We do not observe any band crossing the Fermi energy near M point, in consistent with the DFT calculations, which can be seen from EDC stack, as the intensity of spectral weight dramatically drops around M point in compare to Γ point.

As we discussed earlier that σ-polarized light mainly probes in-plane orbital where as π-polarized light probes out-of-plane orbital inside the sample. The band which crosses the Fermi level very close to Γ point (k_F=0.1 $\mathring{A}^{-1}$), visible in both ΓK and ΓM, can not be

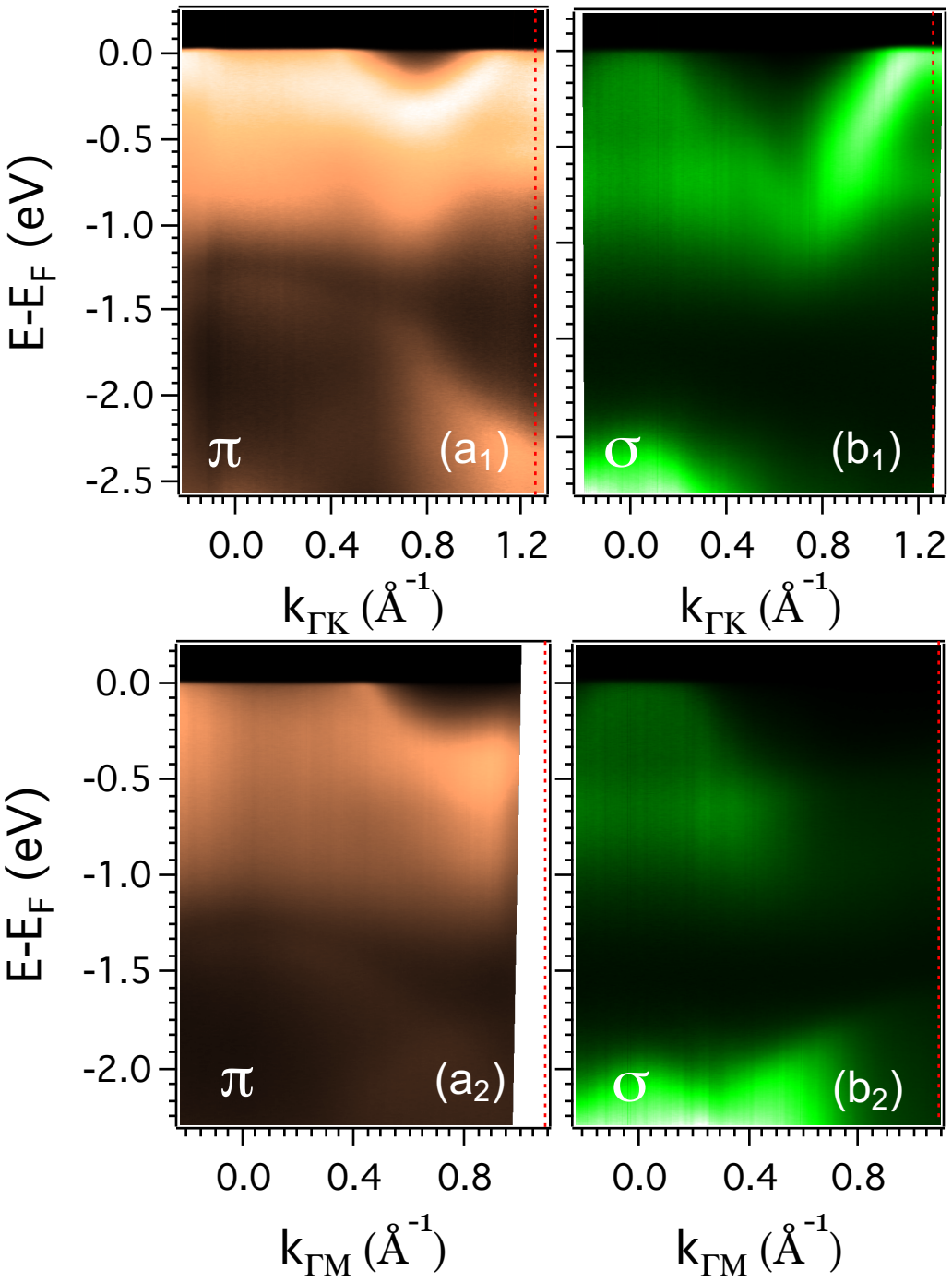

Figure 6.25: Band dispersion measured with photon energy 44 eV along high symmetry directions Γ-K (a_1 ,b_1) and Γ-M (a_2, b_2) for π (a_1, a_2) and σ (b_1, b_2) polarized light.

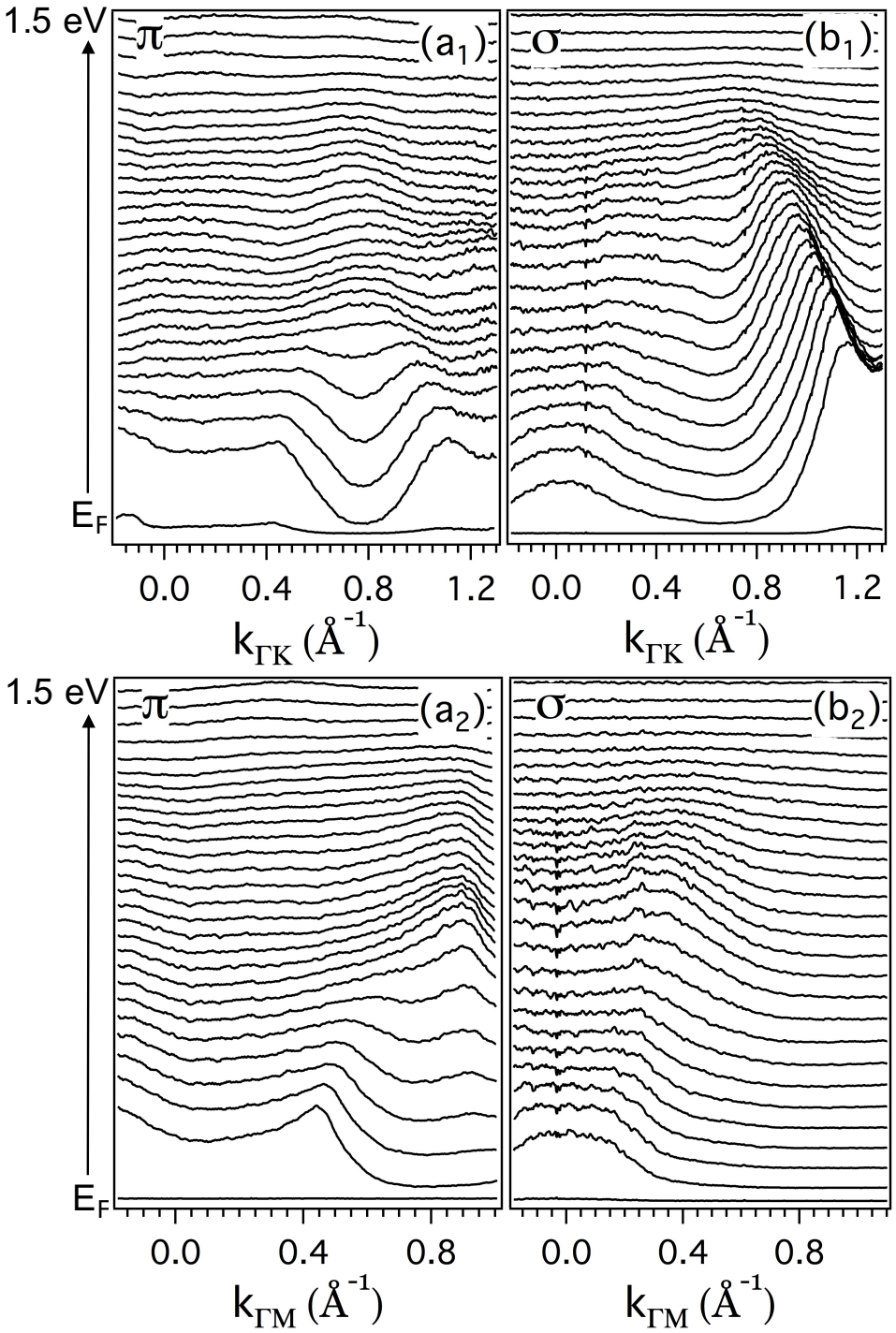

Figure 6.26: Stacked MDCs corresponding to the image plot 6.25.

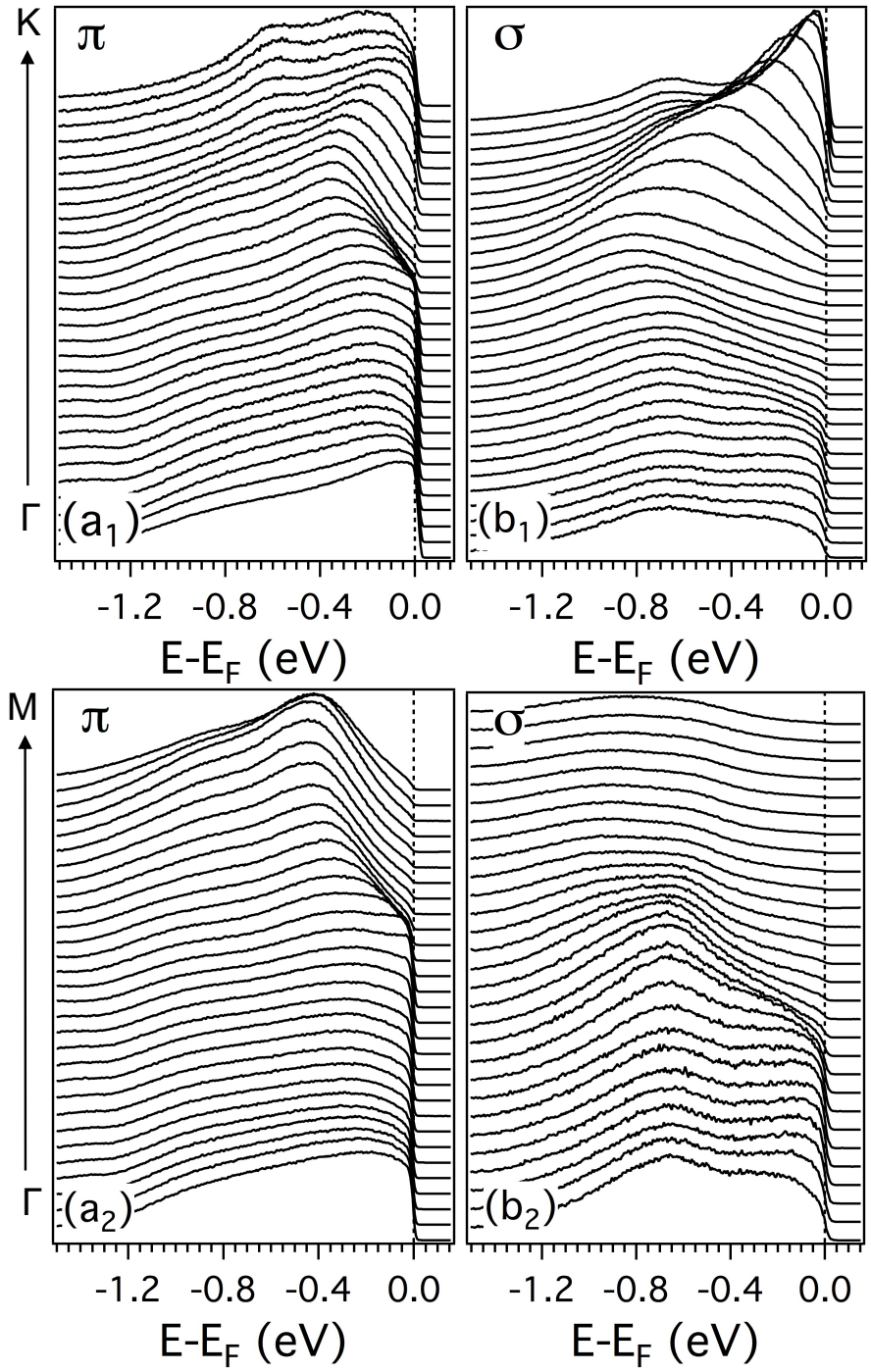

Figure 6.27: Stacked EDCs corresponding to the image plot 6.25. The Fermi level is represented vertical dotted lines at 0 eV.

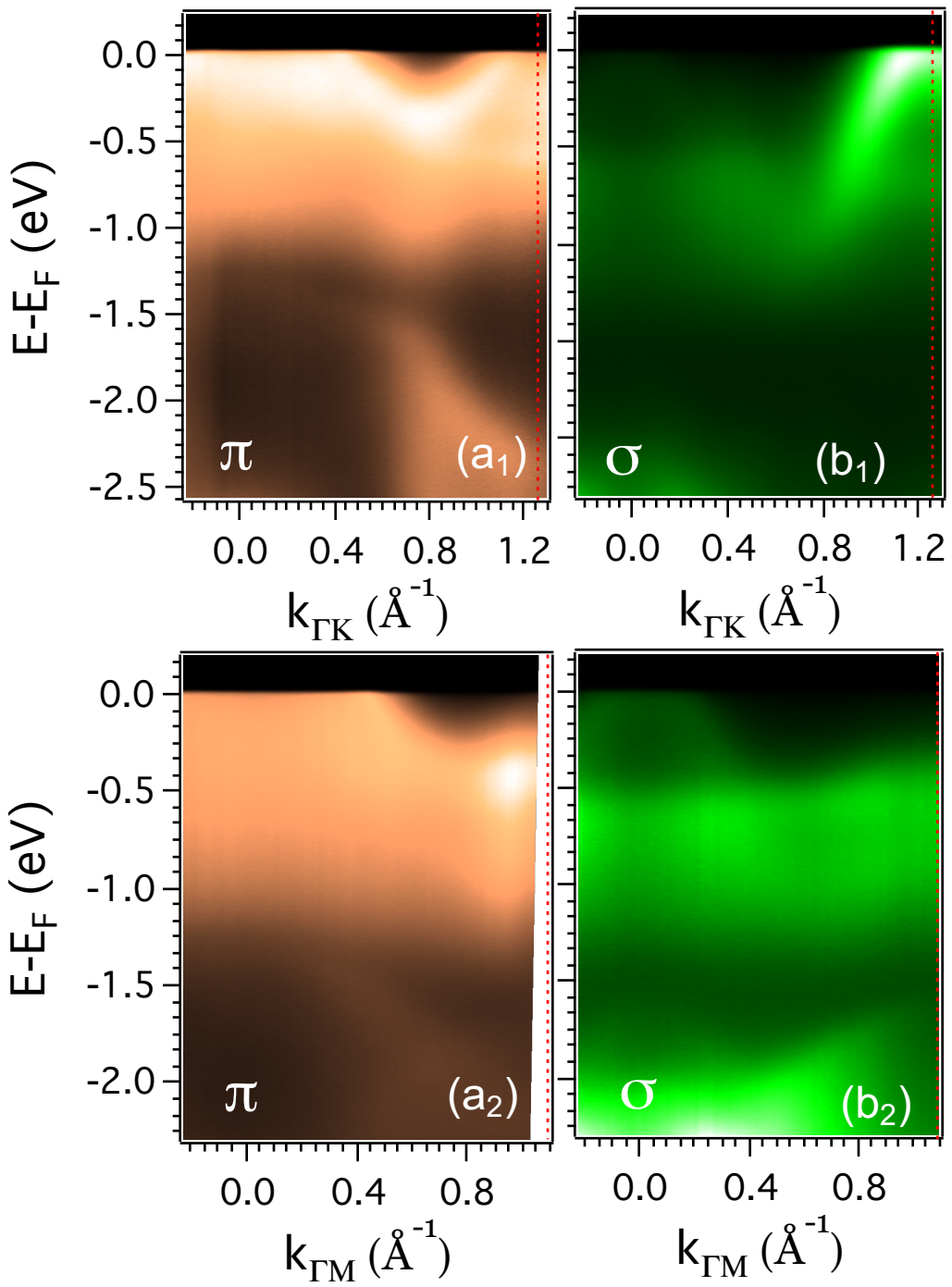

Figure 6.28: Band dispersion measured with photon energy 48 eV along high symmetry directions Γ-K (a_1, b_1) and Γ-M (a_2, b_2) for $\pi(a_1, a_2)$ and σ (b_1, b_2) polarization light.

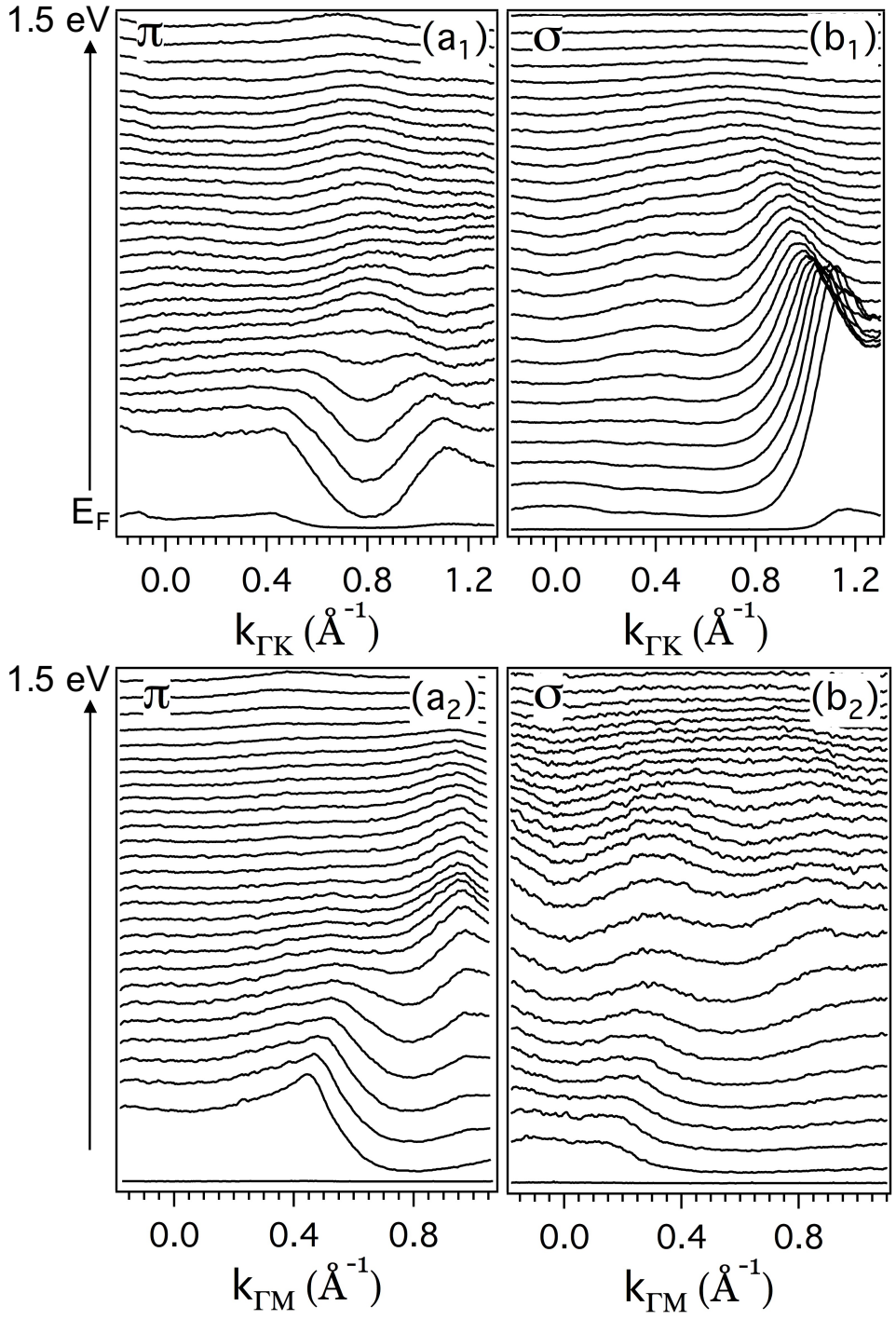

Figure 6.29: Stacked MDCs corresponding to the image plot 6.28.

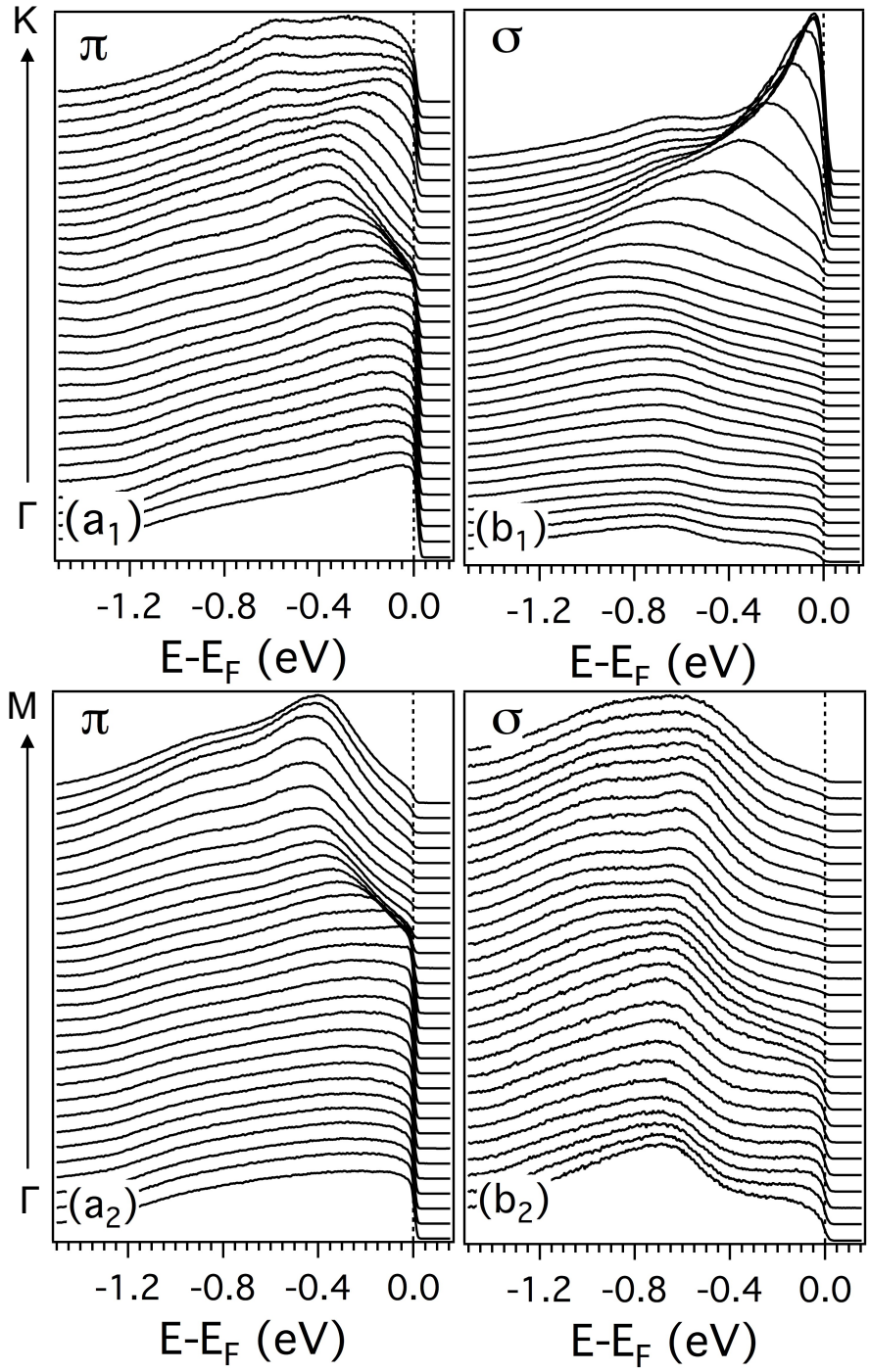

Figure 6.30: Stacked EDCs corresponding to the image plot 6.28. The Fermi level is represented by a dotted lines at 0 eV.

originated from the chalcogen p_z orbitals, in contrast to the DFT calculations for the parent compound, because these bands are observed only when the σ-polarized light is used and are absent when the π-polarized light is used. The possible origin of this band can be explained as following. It is known that K point of the BZ for parent compound is the BZ center (Γ point) for the $(\sqrt{3}\times\sqrt{3})$ superstructure, and these two points are separated by the reciprocal lattice vector of 1.26 $\mathring{A}^{-1}$ of superstructure. Thus, this band could be originated from the band at K points folds back to Γ point. This is further supported by the fact in-plane orbitals are present in both Γ and K points as σ polarized light was used. The possibility of backfolded band at Γ point has also been discussed in another intercalated system $Cr_{1/3}NbS_2$ [108].

We do not observe the bonding band in the present compound which is present about 0.2 eV below the Fermi energy in $Cr_{1/3}NbS_2$. Rather, we see broad non-dispersive features centered around 0.7 eV. These non-dispersive features are more pronounced for σ- polarized light; so these are in-plane orbitals most likely originated from V-$d_{xy}/d_{x^2-y^2}$. The photon energies we used are close to V 3p-3d absorption edge, the enhancement of the band close to Fermi energy indicates that a possible hybridization between Nb-4d and V-3d orbitals. Unlike, the δ band which is originated due to Cr-intercalant and split into δ_1 and δ_2 present near K point in $Cr_{1/3}NbS_2$ [108] is absent in $V_{0.3}NbS_2$ sample (see Figure 6.31 (b)). For the comparison of spectral features in the vicinity of Fermi energy, MDCs at Fermi energy for different photon energy and polarization are summarized in Figure 6.31.

From the polarization dependent ARPES experiments we conclude that three band crosses the Fermi level near Γ point when the sample is aligned either ΓK or ΓM direction. Two of them have orbital symmetry of d_{z^2} while one has symmetry of $d_{xy}/d_{x^2-y^2}$. The additional bands, in compare to NbS_2 band dispersion, crossing the Fermi level might not be originated from the vanadium-states as the ResPES experiments shows that the vanadium-states lie few meV below the Fermi level. The origin of these additional bands are not clear yet. On the other hand, in case of $Cr_{1/3}NbS_2$, the additional bands $\beta_{1,2}$ crossing the Fermi level are originated from the Cr-d states. This is one of the discrepancies between these two intercalated systems. Two bands cross the Fermi level around K point with orbital symmetry of $d_{xy}/d_{x^2-y^2}$. And, no band crossing the Fermi level is observed at M point as predicted by

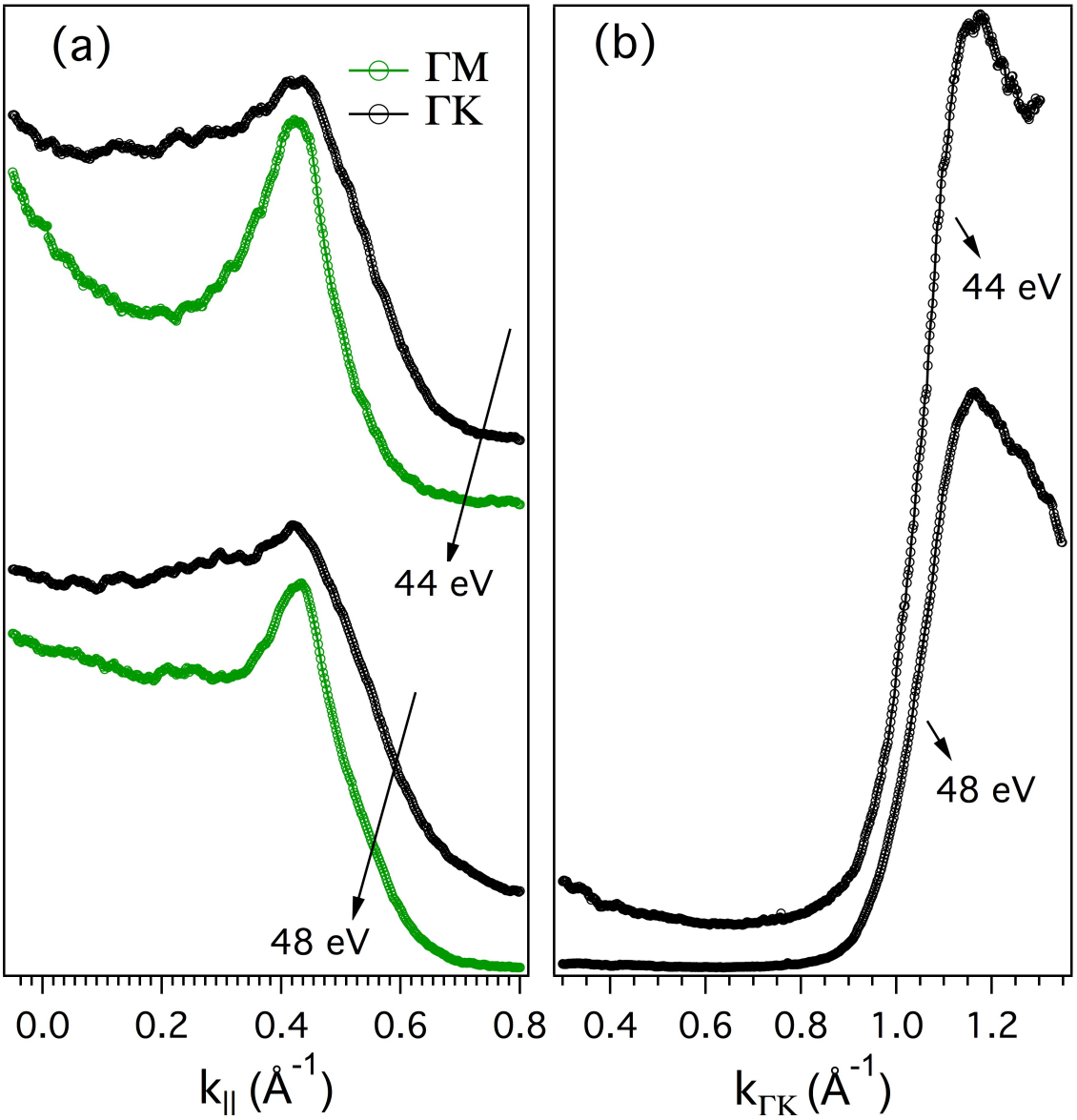

Figure 6.31: MDCs at Fermi level extracted from image plots 6.25 and 6.15.

the DFT calculations. Moreover, a non-dispersive band passes 0.7 eV below the Fermi level at Γ point. Also, an additional dispersive band around K point is observed which is confined at 0.5 eV below the Fermi level.

6.7 Resonant ARPES

Figure 6.32 shows the ARPES spectra of $V_{0.3}NbS_2$ measured utilizing the photon energies in between 506 to 515 eV, across V 2p→3d absorption threshold. These experiments are carried at BACH of Elettra synchrotron facility, Italy. Here, the light is impinging on the sample at normal emission geometrical setup. The experiments were performed at room temperature at pressure better than 10^{-10} Torr. The energy resolution was set to about 180 meV. All the spectra were normalized by bottom 50 meV of energy width. The upper spectra are recorded when LH-polarized light was used while the lower are recorded for LV-polarized light. In both cases two sets of bands, one near the Fermi energy and another in between 2 and 7 eV, are separated by a gap. And, bands are broader which is ascribed to the worsening of energy and momentum resolution at such a high photon energy.

When the LH-polarized light was used the dispersive bands are observed in all the photon energies used and bands few meV below the Fermi level are enhanced when the light energy matches with the V-L_3 absorption edge. On the other hand when LV-polarized light was used the bands are still dispersive for off-resonance regime, but when the light energy is tuned to V-L_3 absorption edge, bands near the Fermi level are enhanced but becomes non-dispersive. As mentioned earlier that LH-polarized light is sensitive to out-of-plane orbitals while LV-polarized light is sensitive to in-plane orbitals characters. The non-dispersive features could be due to the vanadium in-plane orbitals do not have enough interaction with another vanadium in-plane orbitals as they are separated by relatively large distance and atomic like non-dispersive features are observed. Another possibility of non-dispersive features could be due to the disordered vanadium atoms present at the surface of the sample, as mentioned earlier in the LEED and STM measurements. On the other hand the dispersive bands, while utilizing the LH-polarized light, observed indicates that there is a enough interaction between vanadium and niobium atoms along out-of-plane directions as niobium and vanadium atoms

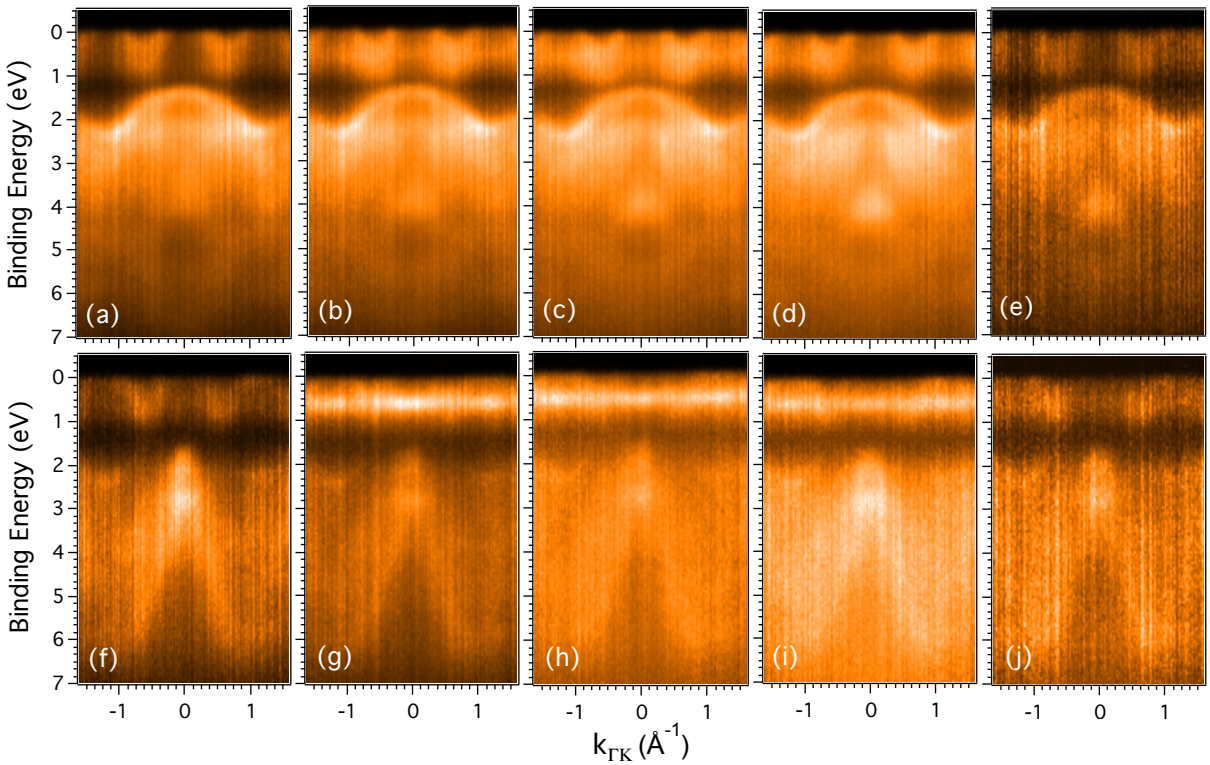

Figure 6.32: Resonant ARPES across VL_3 absorption edge with LH (a–e) and LV (f–j) polarized light. The data were recorded in resonant and off-resonant region with photon energies 506 eV (a,f), 509.6 eV (b,g), 511 eV (c,h), 512 eV (d,i), 515 eV (e,j).

are more closer than the in-plane vanadium atoms. Thus the hybridization between the V-3d and Nb-4d out-of-plane orbitals can occur and dispersive features are observed.

6.8 Photon Dependent ARPES

The photon energy dependence ARPES experiments were performed at ALS, Berkeley. These experiments are recorded at temperature 17 K with pressure better than 10^{-11} Torr. For these experiments we utilized the photon energy in the range between 40 to 65 eV to reach various k_z values in the BZ. Furthermore, we used two photon polarization σ and π, to obtain the orbital character in 3D FS, while the sample is aligned along high symmetry direction ΓM.

The ARPES spectra for selected photon energies with σ and π polarized light are shown in Figure 6.33 and 6.34, respectively. As the photon energy is increased the spectral weight at Fermi energy decreases and shifts towards high energy region in both the polarization of light. Further, the spectral weight shifts away from the center of the zone (Γ) towards M point. However, these features start to shift back to Fermi energy or Γ point at higher photon energies (after 61 eV). The enhanced spectral weight near the Fermi energy in lower photon energies could be attributed that these energies are close to V3p-3d absorption edge, resonating the V-3d bands. Importantly, non-dispersive like feature is enhanced for σ polarized light particularly for photon energies in between 49 to 61 eV. In case of π polarized light, an additional feature centered around Γ point is appeared for high photon energies, the origin of this feature is not clear yet.

The photon energy dependence of the FSs along k_z direction for σ and π polarized light are shown in Figure 6.35(a) and (b). The MDCs at Fermi energy extracted for each photon energies for π and σ polarized light are shown in Figure 6.35. These spectra were obtained by conversion of photon energy vs emission angle into k_z vs k_x. Different photon energies corresponds to different points along the c-direction in the BZ. In order to obtain the k_z dispersion, one has to determine the inner potential which is the energy from the vacuum level to the bottom of the valence band, using the periodic features along c direction. From the photon energy vs. emission angle spectra we chose two photon energies 44 and 52 eV

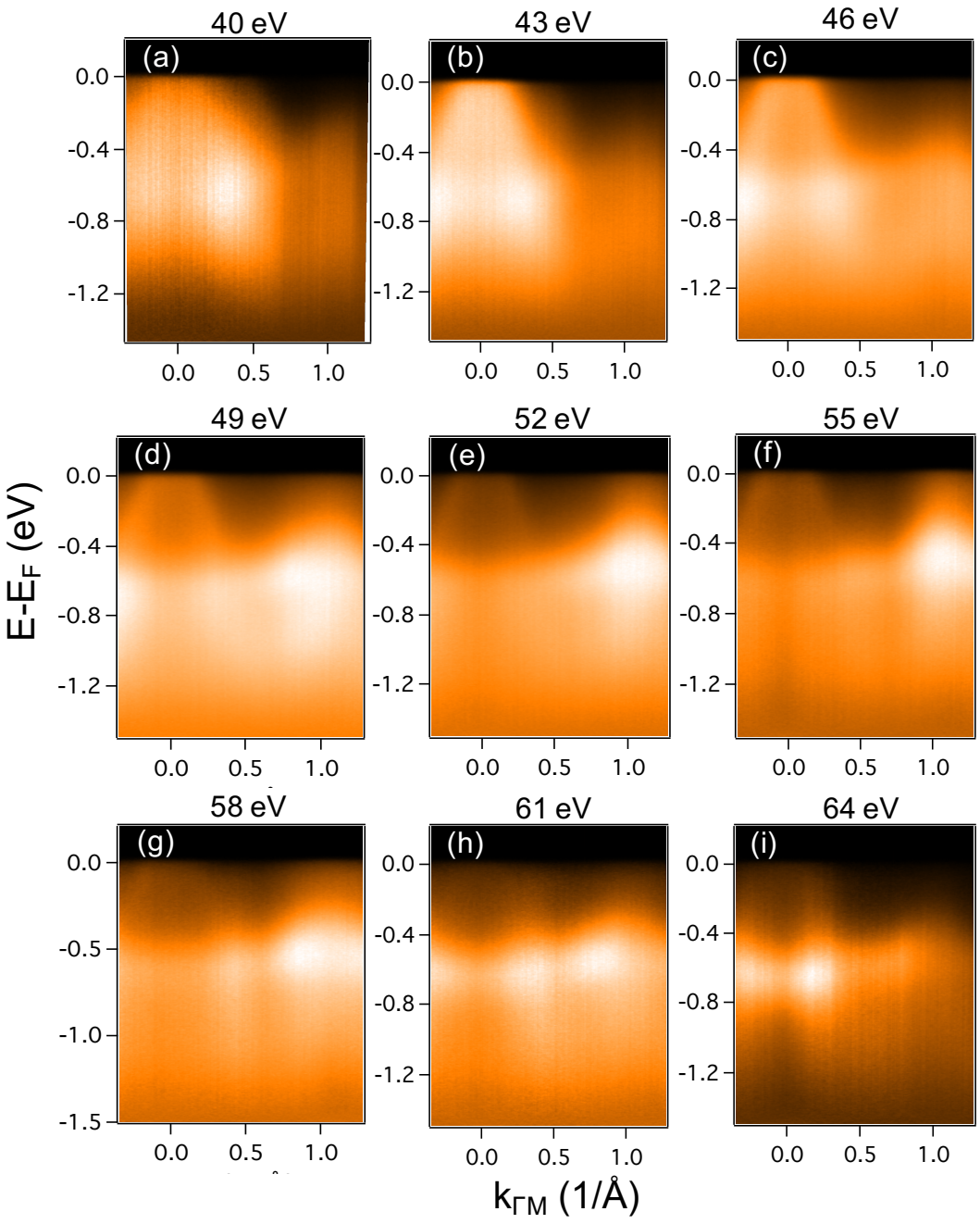

Figure 6.33: Band dispersion measured along ΓM direction at different photon energies. The σ polarized light is used for this measurement.

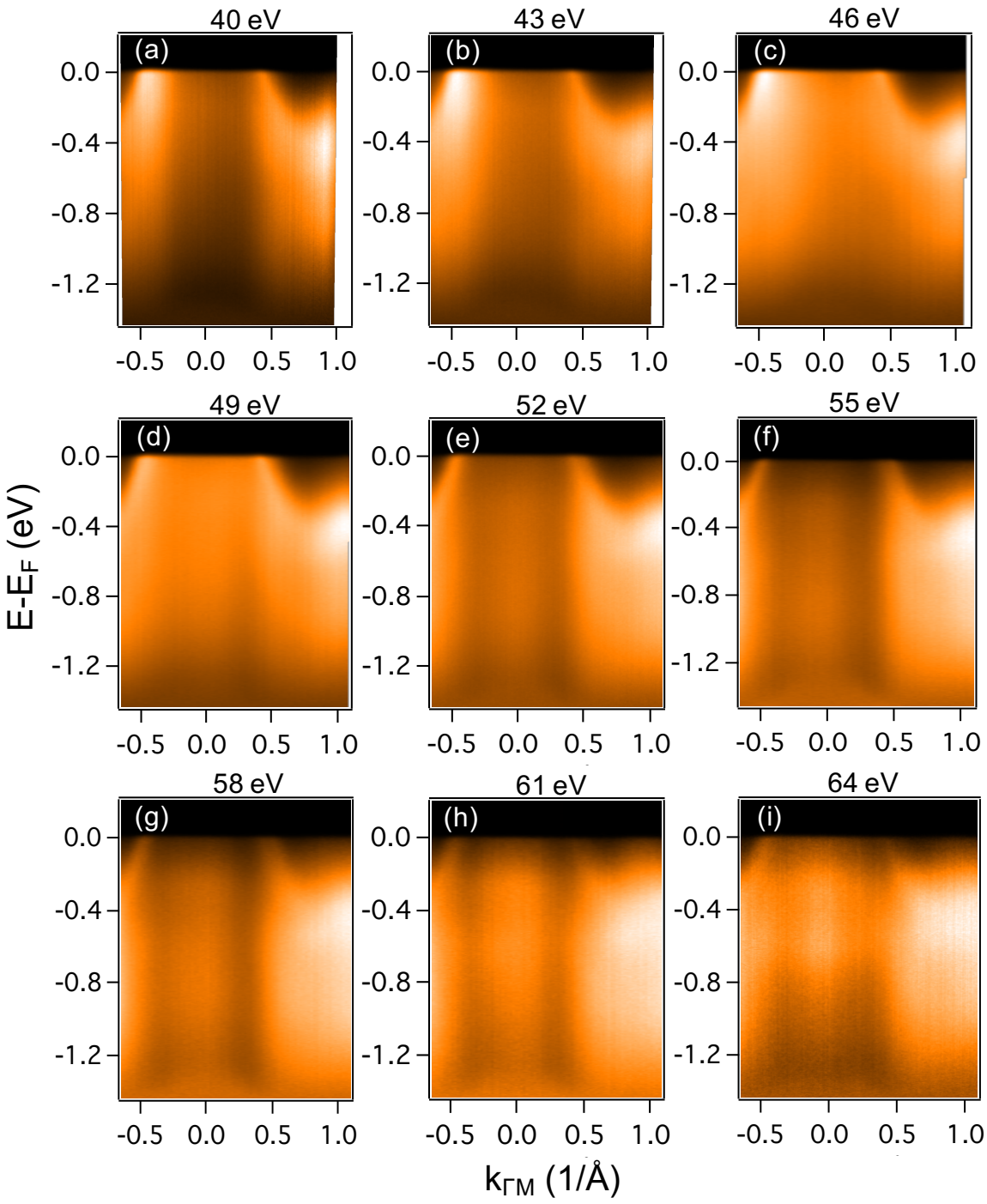

Figure 6.34: Band dispersion measured along ΓM direction at different photon energies. The π polarized light is used for this measurement.

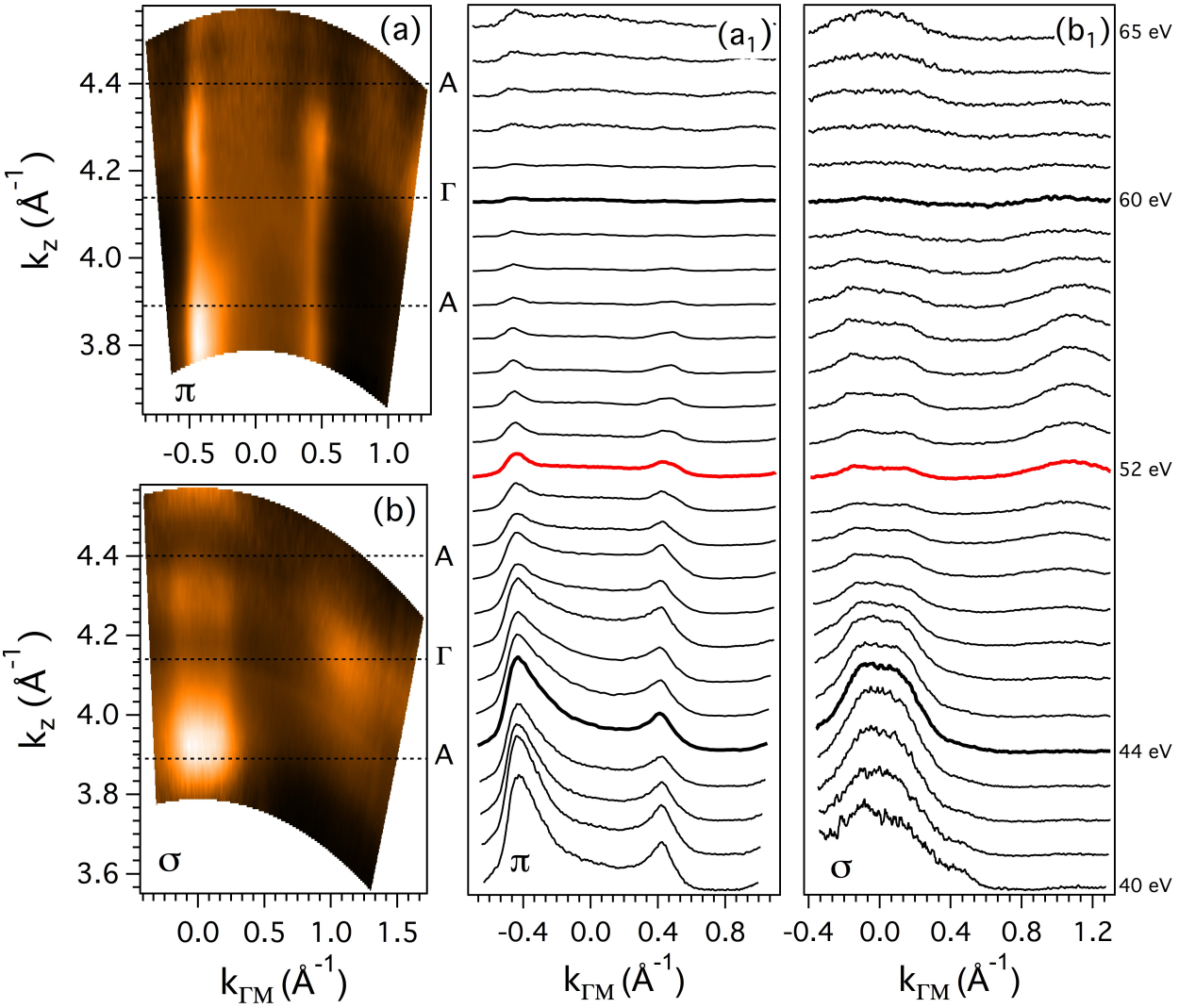

Figure 6.35: Band dispersion with variation of photon energy. (a) k_z dispersion for π-polarized light, (b) for σ- polarized light. The MDCs at E_F extracted at each photon energy (a_1) for π- and (b_1) for polarized light. The sample is aligned along the high symmetry direction ΓM.

corresponding to biggest and smallest FS as such they are representative of center (Γ point) or top (A point) in the BZ. The bold black and red curves correspond to the largest and smallest hole pockets crossing the Fermi energy. Here we chose half of the BZ. From these two photon energies we determined the inner potential to be 19.16 eV by solving two equations 2.15 for each photon energy setting the condition of normal emission ($\theta = 0$). With this inner potential, the position of high symmetry points Γ and A were determined as indicated by dotted lines in the image plots as shown in the Figure 6.35(a) and (b).

Noticeably, we observed an appearance of spectral weight around M point at higher photon energies which is due to the matrix element effect. These features are absent at low photon energies as suggested by the DFT calculations for $V_{0.3}NbS_2$ (also for NbS_2) that no bands are crossing the Fermi energy around M point. From the analysis of the image plots or the MDCs at E_F, we conclude that band dispersion appreciably depends on the polarization of light which could explain the strength and bond orientation between intercalant species and NbS_2 layers. Furthermore, the FS around the Γ point are wavy or 3D like in both polarizations of light. Thus, we are confirmed that this compound exhibits 3D Fermi surface, unlike the parent compound NbS_2 and another intercalated system $Cr_{1/3}NbS_2$ [108]. This is another discrepancy with $Cr_{1/3}NbS_2$ smaple. Furthrmore, 3D nature of Fermi surface in $V_{0.3}NbS_2$ sample suggests relatively stronger interlayer interaction compared to that for NbS_2 and $Cr_{1/3}NbS_2$. These experimental results are consistent with the DFT calculations for $V_{0.3}NbS_2$ which predicts 3D nature of electronic structure as presented earlier. Moreover, the dispersion of bands along k_z direction further suggests that our ARPES data represents the bulk electronic structure as the surface states do not disperse with the photon energy.

6.9 Temperature Dependent ARPES

The ARPES spectra recorded at various temperatures are presented in Figure 6.36. The experiments were performed *in situ* in the pressure better than 10^{-11} Torr. And, the sample was aligned along the high symmetry directions Γ-K. The π-polarized light of photon energy 48 eV was used for these experiments. An important information such as magnetism can be acquired from the temperature dependent ARPES measurements. We recorded the spectra

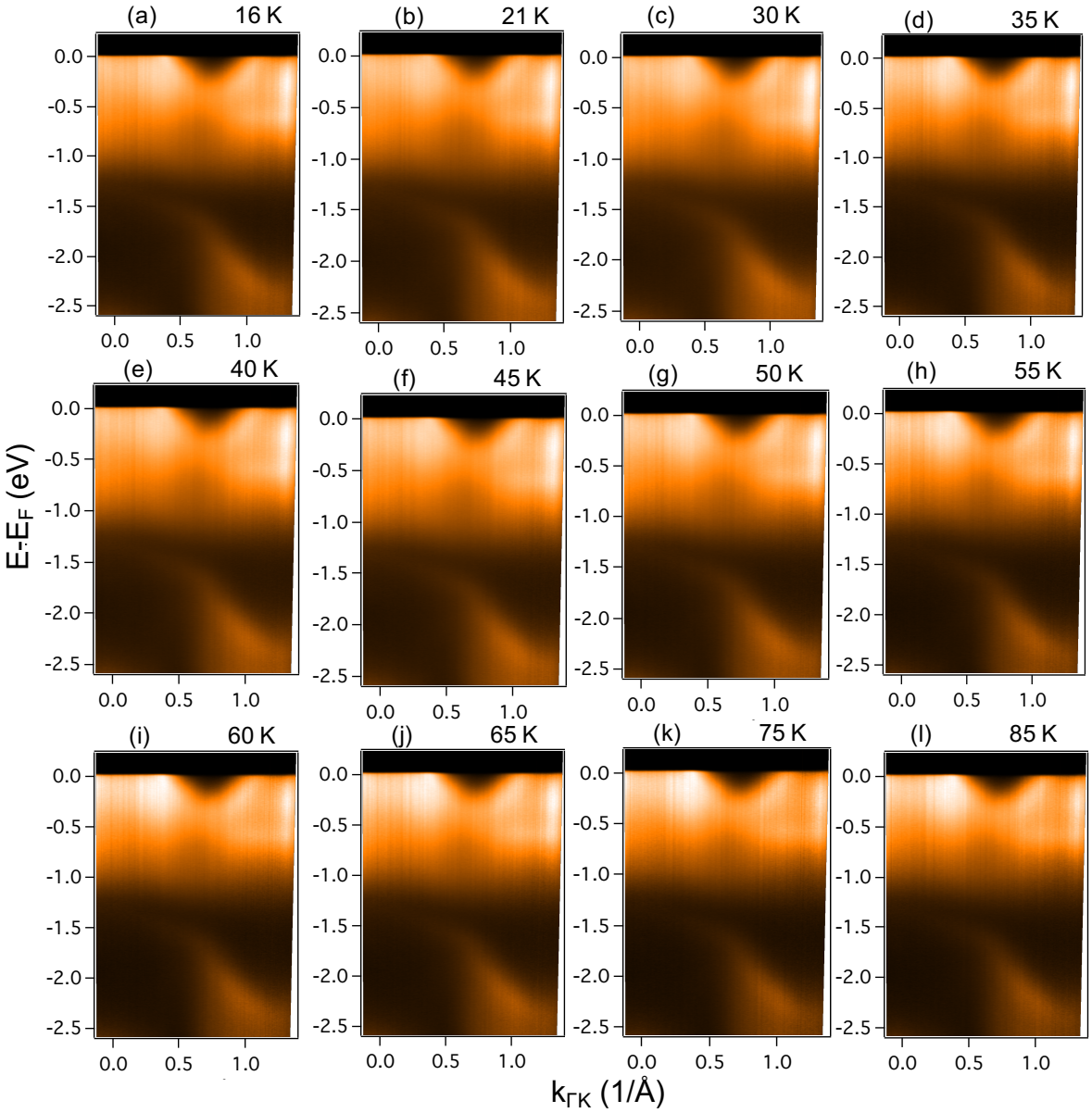

Figure 6.36: Temperature dependent band dispersion along ΓK direction measured for π polarized light of energy 48 eV.

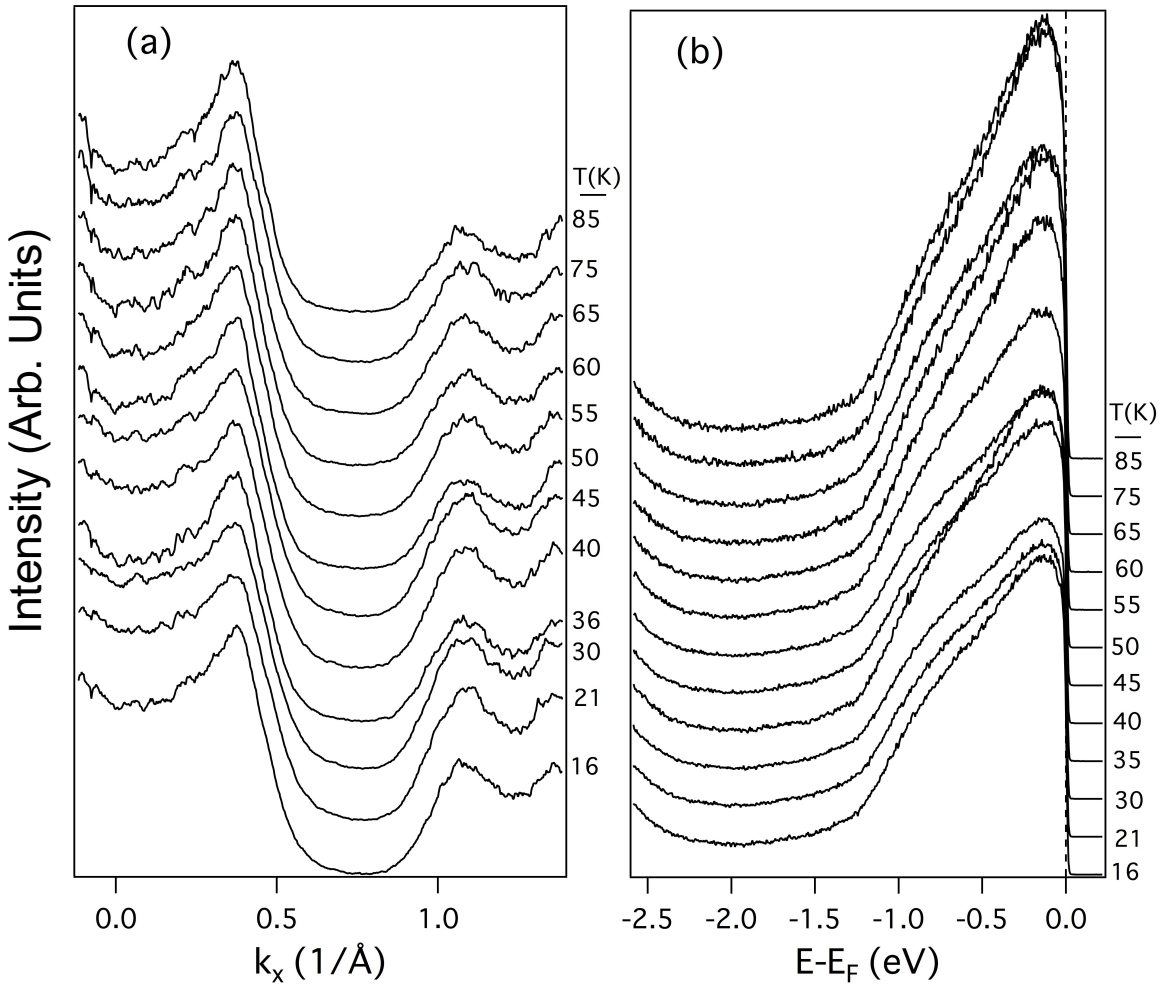

Figure 6.37: (a) MDCs at E_F corresponding to the spectra in Figure 6.36 recorded at various temperature. (b) EDCs extracted at Γ point for all temperatures from Figure 6.36.

at temperatures well above and below the magnetic transition temperature. From the image plots shown in Figure 6.36 it is hard to differentiate the spectral features for different temperatures. Thus, we have extracted the MDCs at Fermi level for each temperature associated to the spectrum shown in Figure 6.36. Also, we extracted EDCs at the normal emission that is at zone center (Γ point) for each spectrum. The MDCs at Fermi level for the spectra measured at 16 K and 85 K were compared and it is found that spectral features become broader at lower temperature (16 K) than at higher temperature (85 K). Similar behavior has also been observed in EDCs corresponding to these two spectra. This is in contrast to the general expectation of suppression of phonon-induced excitation at lower temperature causing the spectral features to be sharper. Furthermore, the Fermi wave vectors for the bands near Γ and K point do not change appreciably with the temperature. Which indicates that the carrier concentration does not vary with the temperate, in consistent with the Hall effect measurements where the carrier concentration is almost equal in this temperature range (16–85 K).

Chapter 7

Crystal Synthesis, Magnetic and Transport Properties of $Cr_{1/3}TaS_2$

7.1 Crystal Growth and Structure

Single crystal of $Cr_{1/3}TaS_2$ was synthesized by the chemical vapor transport technique. A stoichiometric ratio of high purity starting materials Cr (99.99%), Ta (99.98%), and S (99.9995%) was grounded finely inside a glove box in He-atmosphere and a pellet is made out of the powder using the cold press method. Then the pellet is sealed in a quartz tube under vacuum and heated slowly in a furnace to reach at $500°C$, after 10 hours temperature is further increased to $1000°C$ and remains at his temperature for one week and the furnace is subsequently cooled slowly to room temperature. Next, the finely ground polycrystalline powder of 3 grams obtained by above process along with 0.5 grams of iodine was loaded in another quartz tube and sealed under vacuum. The tube is kept horizontally in a tube furnace while maintaining temperature gradient of 100°C between two ends of the tube such that one end at 950°C and another at 850°C. After heating about one week most of the powder sample is transported to the cold side of the tube due to the chemical reaction and many single crystals of $Cr_{1/3}TaS_2$ were obtained. Here, iodine acts as a transport agent. Further, we investigated the XRD pattern and electron dispersive x-ray spectroscopy (EDS) of the polycryatalline powder and single crystal and noticed that resultant compound is slightly off-stoichiometric and found to be at $Cr_{0.36}TaS_2$ composition. It has been known

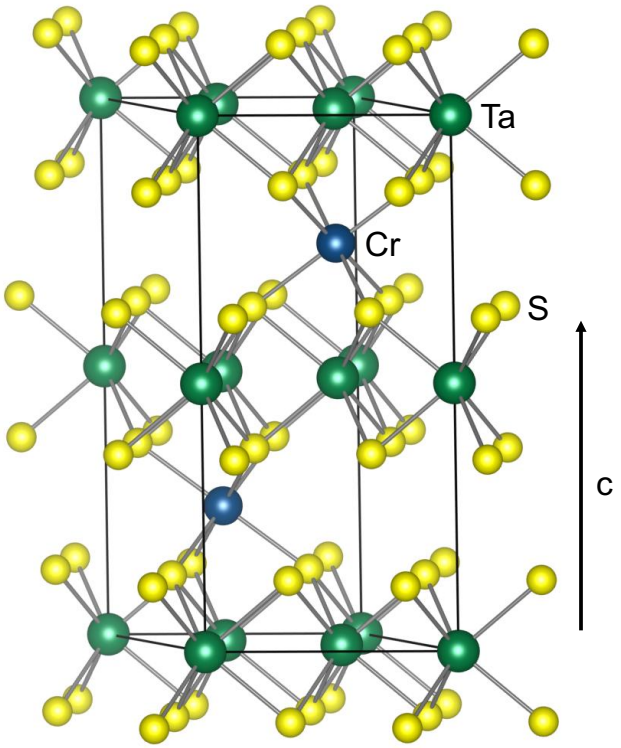

Figure 7.1: Crystal structure of $Cr_{1/3}TaS_2$ stacking along c-axis as indicated by an arrow line. Solid black lines indicate unit cell. Ta is denoted by green balls, Cr by blue, and S by yellow.

that intercalated compound M_xTX_2 does not yield exact concentration x=1/3 or 1/4, but within a differ of 10% is an acceptable limit such that the crystal structure is not appreciably modified [94]. Moreover, our LEED experiment (which will be discussed later) also confirmed that accurate concentration is 1/3, where intercalated Cr-atoms result $(\sqrt{3} \times \sqrt{3})$ (R30°) superstructure. In the following paragraph we discuss the crystal structure of $Cr_{1/3}TaS_2$.

The crystal structure of $Cr_{1/3}TaS_2$ is shown in Figure 7.1. It crystallizes in a hexagonal lattice belonging to a non-centrosymmetric space group $P6_322$, where Cr atoms sit in a octahedral hole in between the van der Waals gap formed by trigonal prismatic layers of $2H - TaS_2$. An unit cell of $Cr_{1/3}TaS_2$ contains twenty atoms: two chromium atoms occupying 2c sites, six tantalum atoms at two inequivalent positions 4f and 2a, and 12 sulfur atoms at 12i. The intercalated Cr atoms strengthens the bonding between the TaS_2 layers and can change the energy hierarchy of Ta 5d manifold orbitals which are split by the trigonal prismatic crystal field.

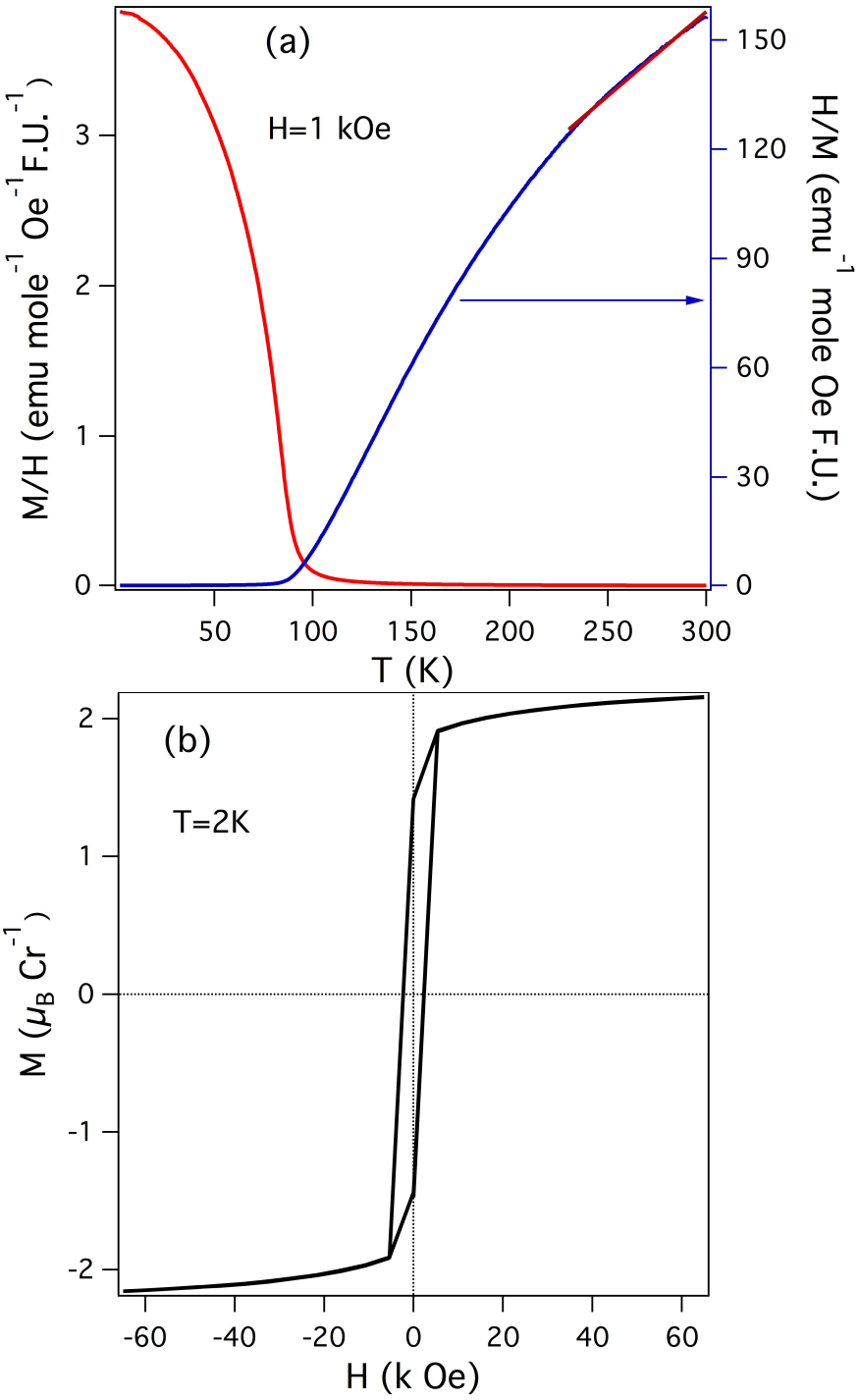

Figure 7.2: (a) M/H as a function of temperature measured at magnetic field of 1000 Oe. The H/M curve follows Curie Weiss law in the temperature range 90–200 K. (b) Magnetization as a function of magnetic field at 2 K.

7.2 M/H vs. T and M vs. H

Magnetic susceptibility (M/H) as a function of temperature is shown in Figure 7.2(a). The magnetic field of 1 kOe is applied parallel to the ab plane. The susceptibility increases with decreasing temperature and jumps around 100 K and starts to saturate at lower temperatures, signature of long-range ferromagnetic orderings. The magnetic transition temperature is smaller than that reported previously [94]. This discrepancy (besides an off-stoichiometric sample) could possibly be due to the Cr atoms randomly occupy at octahedral sites between 2H-TaS_2 layers as also reported in Ref [2]. The inverse susceptibility is shown in Figure 7.2(a) (curve in blue color). It is a non-linear function of temperature, however the Curie-Weiss law can be fitted at higher temperatures in the range of 250 to 300 K giving rise the Curie constant (C) of 0.47 emu $mol^{-1}Oe^{-1}K^{-1}$. From the Curie constant, we calculated effective paramagnetic moment to be 3.39 μ_B per Cr atom, which is smaller than the spin only moment of 3.87 μ_B per Cr for Cr^{3+} oxidation state.

The magnetization curve as a function of magnetic field recorded at 2 K is shown in Figure 7.2(b). Rapid saturation of magnetization with applied field is observed. We have determined the spontaneous magnetic moment of 1.93 μ_B at 2 K corresponding to the spontaneous magnetization which is obtained by extrapolating magnetization versus field above saturation to zero field. This moment is close to that extracted from the Figure 2(a) in Ref. [131], which was recorded at 10 K. Further, a relatively wide hysteresis loop has been observed with coercivity of 2.4 kOe and remanent magnetization which is about 73 % of spontaneous magnetization.

7.3 Electrical Resistivity and Magnetoresistance

The electrical resistivity as a function of temperature for $Cr_{1/3}TaS_2$ is shown in Figure 7.3(a). The resistivity increases with temperature in the entire temperature range, a clear indication of metallic behavior. The room temperature resistivity amounts 3.012×10^{-3} Ωcm, smaller than the typical metals such as copper which has room temperature resistivity of 1.68×10^{-6} Ωcm, which suggests low carrier density in this materials. At low temperatures,

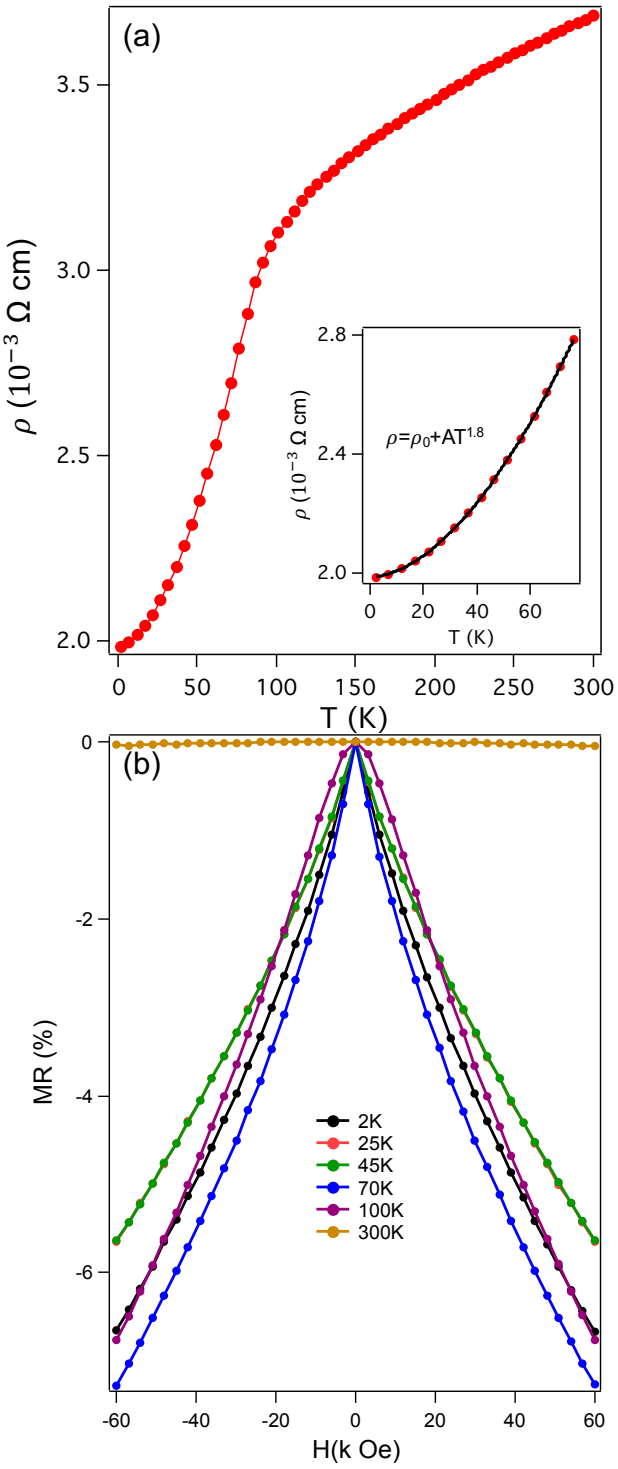

Figure 7.3: (a) Electrical resistivity of $Cr_{1/3}TaS_2$ as a function of temperature, the inset shows that resistivity correctly fits with $T^{1.8}$ power law behavior in the temperatures 2 K<T<80 K. (b) Magnetoresistance as a function of at various temperatures.

the resistivity shows the non-trivial power law behavior $\propto T^{1.8}$ which is a marked contrast to the resistivity behavior of metallic system. Usually, the resistivity of metal follows the famous Bloch's theorem: $\rho = \rho_0 + BT^5$, where the residual resistivity ρ_0 is temperature independent and related to the electron scattering from impurities and crystal imperfection and the constant B corresponds to electron-phonon interactions. Also, the low temperatures resistivity is deviated from the conventional T^2 dependent Fermi liquid behavior. The origin of unusual $T^{1.8}$–temperature dependent resistivity of present sample is not clear. This is in contrast to the T^2–dependence of resistivity in $Cr_{1/3}TaS_2$ reported by S. Parkin et al.[95]. Moreover, the marked reduction of in resistivity as it passes through the the magnetic transition temperature is due to the reduced spin scattering in the order ferromagnetic phase. Above the magnetic transition temperature, the resistivity shows the sub-linear behavior (or the resistivity saturation), opposite to the usual electron-phonon interaction which depends linearly with temperature at high temperatures. This deviation from the electron-phonon scattering might be due to the Fermi level changing with temperature in a region of small density of states. Another possibility of this saturation in resistivity might be due to compositional disorder in the sample and disorder due to the thermally excited phonons [43]. Similar results were found in several of 3d or 4d transition metal compounds [43]. Furthermore, the value of ρ_0, the prefactor of $T^{1.8}$, and RRR obtained as (ρ(300 K)/ρ(2 K)) are 2.0 mΩcm, 0.32×10^{-7} $\mu\Omega$cm/$K^{1.8}$, and 1.86, respectively. Such a relatively high value of ρ_0 and a low RRR suggests some sort of disorder present in the system possibly stemmed from the chromium intercalant. The resistivity behavior of $Cr_{1/3}TaS_2$ is markedly different than isostructural compound $Cr_{1/3}NbS_2$ [38], where the resistivity abruptly increases at magnetic transition temperature and decreases slightly at higher temperatures.

The magnetic field dependent magnetoresistance (MR), $100 \times [\rho(H) - \rho(0)/(\rho(0)]$, at various temperatures is shown in Figure 7.3. Here, the resistivity is recorded along ab plane while the magnetic field is applied perpendicular to the ab plane. The rapid decrease in the MR with the field and negative MR in all the temperatures are observed. The reduction in the resistivity can be attributed to the decrease in spin disorder scattering as the magnetic field aligns the moments along its direction. The maximum MR value of about 7.30% is observed at 2 K at maximum applied field of 60 kOe which is larger than that of $Cr_{1/3}NbS_2$

sample [38] . The magnitude of MR obtained here are in the similar range as obtained by Y. Yamashaki et. al [131]. Remarkably, the MR vs. field increases with temperature and reaches maximum in the vicinity of magnetic transition temperature and starts to decrease as it crosses this temperature.

Chapter 8

Electronic Structure of $Cr_{1/3}TaS_2$

8.1 Surface Characterization

Before the discussion of photoemission experiment, we first present the surface characterization of $Cr_{1/3}TaS_2$ sample and the first principles calculations for electronic structure.

The low energy electron diffraction (LEED) pattern for $Cr_{1/3}TaS_2$ is shown in Figure 8.1. The LEED experiment was performed at temperature 77 K using Omicron SpectaLEED equipped with a W/Th filament and a viewing angle of 102°. The fresh surface was obtained by cleaving the sample *in situ* in ultrahigh vacuum of base pressure better than 10^{-11} Torr. The electron beam of energy 201 eV is impinges on the sample surface. The sharp diffraction spots are obtained which are not significantly modified with exposure to vacuum for 24 hours, suggesting that the sample is relatively stable. In the LEED image, the bright spots are originated from the parent TaS_2 compound which have (1×1) periodicity, whereas the faint spots are originated from the intercalant Cr atoms which has periodic $(\sqrt{3} \times \sqrt{3})R(30°)$ superstructure. The observation of the superstructure periodicity confirms that this compound has Cr-concentration of 1/3 as explained by S. Parkin [94]. In k-space, the reciprocal vector for the $(\sqrt{3} \times \sqrt{3})R(30°)$ superstructure corresponding to Cr-atoms is smaller than that of (1×1) of host compound. In Figure 8.1, dotted and solid lines indicate unit cell for $(\sqrt{3} \times \sqrt{3})R(30°)$ and (1×1) periodicity, respectively. As the beam energy decreases, particularly below 100 eV, only the (1×1) spot contributed from the TaS_2 terminated surface is detected as the low beam energy probes only to the sample surface,

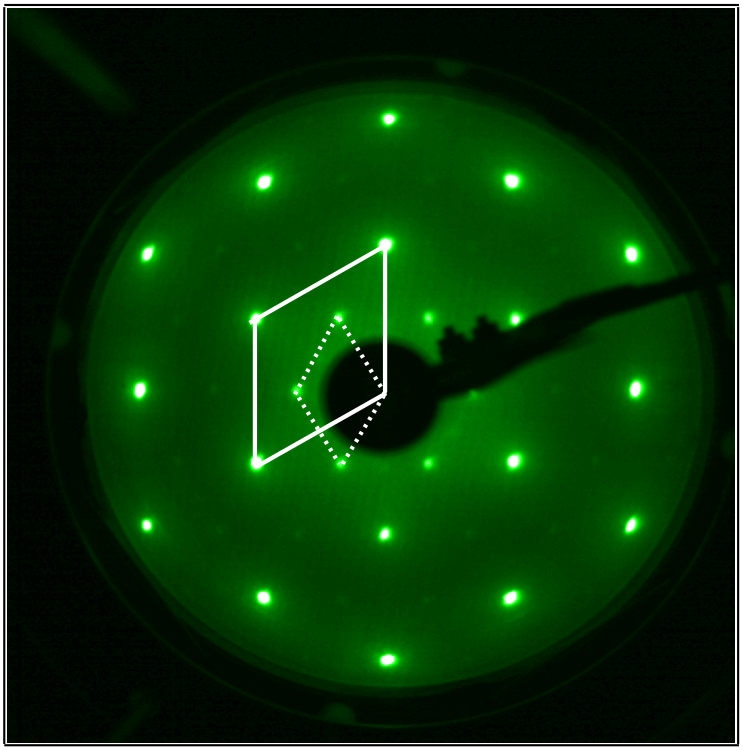

Figure 8.1: LEED image recorded with electron beam energy of 201 eV. The unit cell for the 1×1 and $(\sqrt{3} \times \sqrt{3})$ $R(30^\circ)$ are indicated by solid and dotted lines.

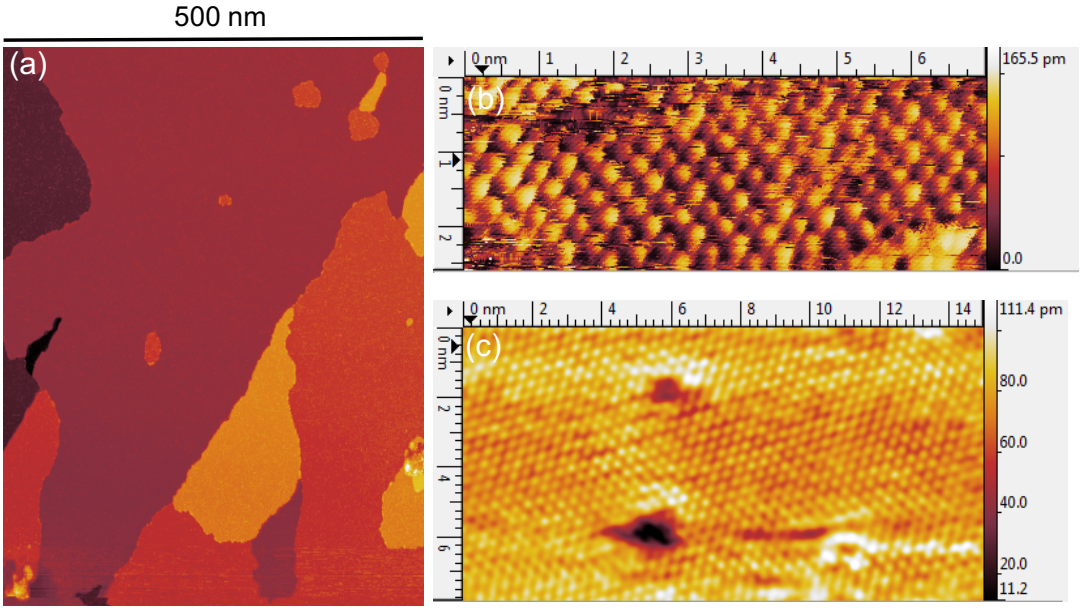

Figure 8.2: STM experiments for wide range (a) and the atomic level (b,c). The different color scheme indicates the regions corresponding to rough or smooth surface.

in contrast to high beam energy which increases the probing depth and the signal from few atomic distance beneath the surface is also detected. Thus, we assume that $(\sqrt{3}\times\sqrt{3})R(30^{\circ})$ superstructure is located well below the sample surface.

Surface of the sample is further investigated by the scanning tunnelling microscopy (STM) experiment. The STM experiments were performed at room temperature and the sample is cleaved *in situ* in UHV system of base pressure better than 10^{-10} Torr. The STM image measured in wide scale is shown in Figure 8.2. Different color scheme in the STM image represents different surface terminations such as smooth (order) TaS_2 termination or rough (disorder) Cr-terminated surfaces, similar features have also been observed in $V_{0.3}NbS_2$ as explained in Chapter 3. An atomically resolved STM images are shown in Figures 8.2(b) and (c), which has different scales. Noticeably, the atomically disordered surface does not show any periodicity in the STM image, while the ordered surface does. Furthermore, a clear hexagonal structure with an evidence of superstructure is observed which is consistent with the similar features obtained in the LEED experiments as discussed earlier.

8.2 DFT Calculations

First principles calculations of electronic structure for $Cr_{1/3}TaS_2$ is obtained by using WIEN2k package [12] which is based on the density functional theory developed by Kohn and Sham [66]. The exchange correlation potential predicted by Perdew, Burke, and Ernzerhof [96] was chosen, and no relaxation of structure was performed. The basis set determined by the plane wave cut-off was specified by the value $RMT_{min}K_{max} = 7.0$ which provides good convergence, where RMT_{min} and K_{max} denote smallest muffin tin radius in a unit cell and largest plane wavevector, respectively. The energy separation between the core and valence states are set to be -6.0 Ry. And, the number of k-points in a Brillouin zone was taken 200. The experimental structural parameters obtained by F. Hulliger et al. for $Cr_{1/3}TaS_2$ [58] have been utilized. The muffin tin radii for Cr, Ta, and S are $2.41a_0$, $2.5a_0$, and $2.08a_0$ used, respectively, where a_0 is Bohr's radius.

In our calculations, we have also included spin-orbit coupling since spin-orbit interaction is significantly large for heavier atoms like Ta. Moreover, we have performed electronic

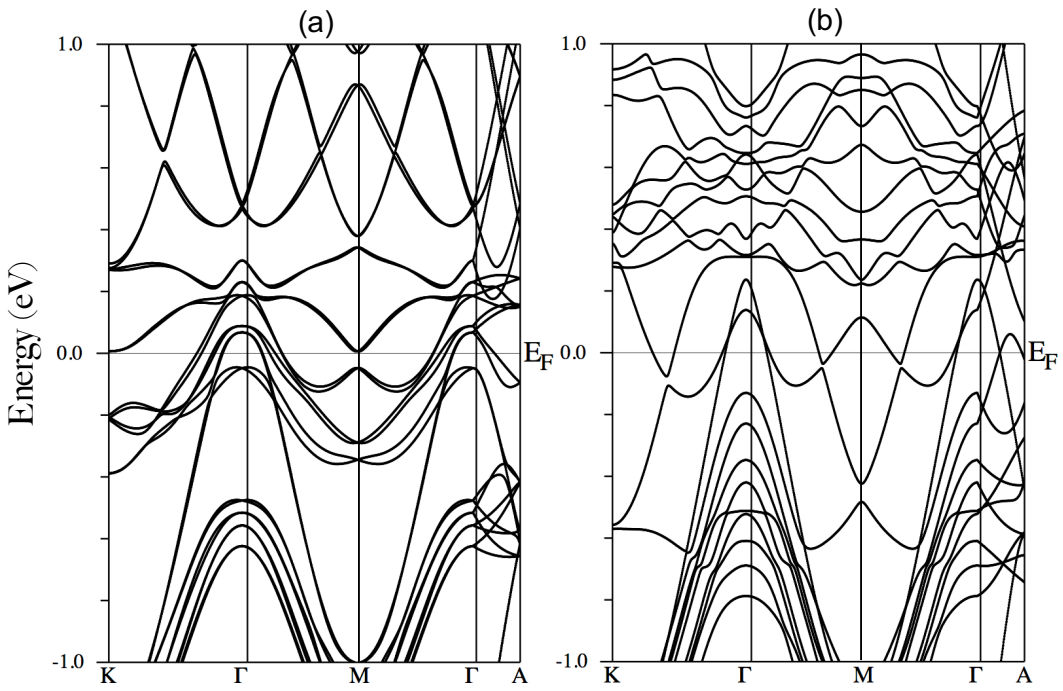

Figure 8.3: The band structure for $Cr_{1/3}TaS_2$ obtained from the first principles calculations for (a) non-magnetic and (b) magnetic states.

structure calculations for both non-magnetic and magnetic (ferromagnetic) cases. And, we found that the magnetic ground state is energetically favorable over the non-magnetic state by energy of 1.28 eV per unit cell that is 0.74 eV per Cr atom. Which supports that the long-range ferromagnetic orderings exhibited in $Cr_{1/3}TaS_2$ as observed experimentally. Also, the calculated magnetic moment per unit cell is about 6.01 μ_B or 3.0 μ_B per Cr atom which is smaller than the spin only moment 3.87 μ_B as well as effective magnetic moment 5.03 μ_B obtained from the magnetic susceptibility. This smaller value of magnetic moment in compare to that of experimental value or spin only moment is attributed to the fact that DFT calculations is mean field by nature which underestimate the spin fluctuations and generally suppresses long range magnetic ordering [80].

The band structure of $Cr_{1/3}TaS_2$ for non-magnetic state along certain symmetry lines of Brillouin zone is shown in Figure 8.3(a). E_F represents the position of Fermi level. Noticeably, each bands are split into two due to the effect of spin-orbit interaction. Many bands are crossing the Fermi level confirming the metallic system. And, a strong k_z-dispersion (see band dispersion along Γ–A direction in Figure 8.3(a) and (b)) is observed which is in contrast

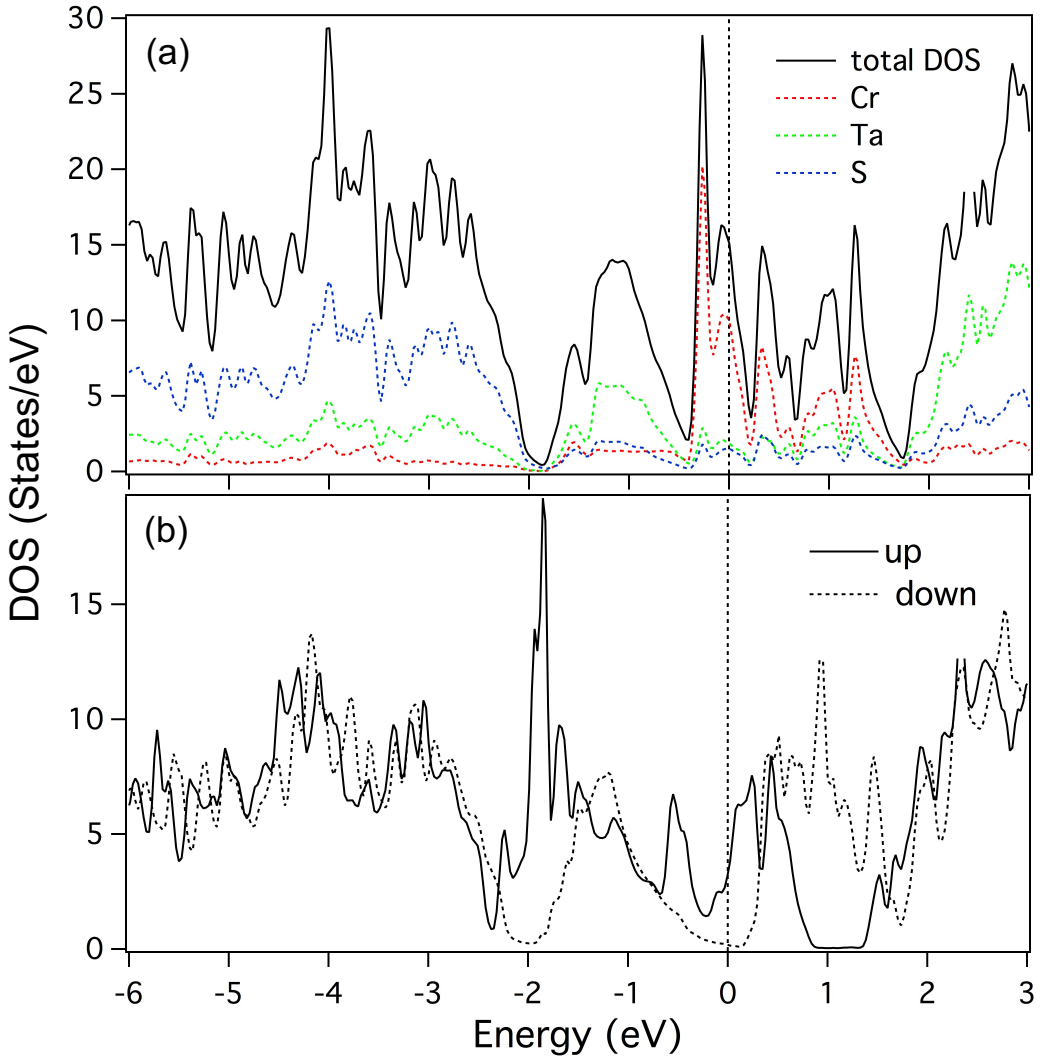

Figure 8.4: The density of states for (a) magnetic and (b) non-magnetic cases. The Fermi level is located at 0 eV.

Table 8.1: The DOS at Fermi level and Sommerfeld's coefficients for $Cr_{1/3}TaS_2$ obtained from the first principles calculation. The magnetic and non-magnetic calculations are performed.

	NM	FM (up)	FM (down)
DOS at E_F (States/eV)	16.94	3.44	0.20
Sommerfeld's coefficient (γ) (mJ/(mol cell K^2))	39.90	8.12	0.47

to the 2D-nature of band dispersion expected for the layered materials having weaker van der Waals bonding between the adjacent layers. There are ten Cr-d bands, five bands from each two Cr atoms in a unit cell of $Cr_{1/3}TaS_2$, spreading in between –0.2 eV to 1.8 eV. In Figure 8.3(a), we can see that three Cr-3d bands crosses midway between K and Γ points and confined in the valence band and seven more Cr-3d bands are located above Fermi level. And, the Ta-5d dominant bands are located in between 2 eV and 4 eV in conduction band as well as in between –0.5 to –1.5 eV in valence band. Moreover chalcogenide 3s bands are confined in between –13 eV and –14 eV (not shown in Figure). It has also to be noted that 4f-orbitals from the Ta atoms are relatively localized in atomic site and they do not contribute in Fermi surface. The band structure for the magnetic case is shown in Figure 8.3(b). In this case fewer bands are crossing the Fermi level and substantial loss in the spectral weight around Fermi level is observed in comparison to the non-magnetic case.

The density of states (DOS) calculated for non-magnetic and magnetic states are shown in Figure 8.4(a) and (b), respectively. Here, 0 eV represents the Fermi level. States near Fermi level are mainly dominated by Cr-3d atoms, Ta-5d are confined between –0.5 eV and –2 eV, and S-3p are located just below Ta-5d states. DOS at E_F and Sommerfeld's coefficient γ obtained from the calculations are listed in Table 8.1. We performed DOS calculations for both spin up and spin down channels and we noticed that the DOS at E_F are substantially reduces for both cases in compare to that of non-magnetic case. Moreover DOS at E_F for spin down shows a gap at E_F while a finite spectral weight is observed for the spin up channel, a characteristics of half metal, such a case has also been reported in another intercalated $Cr_{1/3}NbS_2$ compound.

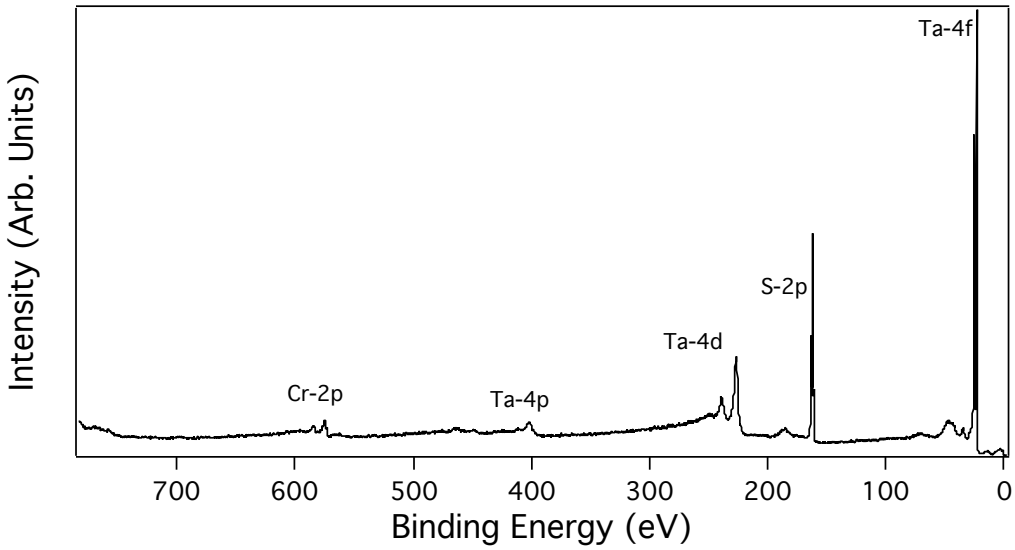

Figure 8.5: The wide range of photoemission spectra recorded with photon energy 937 eV, the number of peaks corresponding to different orbital states are identified.

8.3 Core Level Photoemission

The core level photoemission experiments were performed at BACH, Elettra in Italy. The sample is cleaved in a pressure better than 10^{-9} Torr and the experiments were performed in the analysis chamber which is in the pressure better than 4×10^{-10}. The measurements were carried at room temperature setting the energy resolution better than 0.3 eV.

First, we recorded wide scan spectrum (Figure 8.5) of $Cr_{1/3}TaS_2$ to check the quality of the sample. The wide scan covers number of core levels of Cr, Ta, and S including valence bands. The measurement was done utilizing the photon energy of 937 eV. Oxygen and carbon contamination were absent in the wide scan measurement. Further, the core levels show sharp peaks indicating the sample of good quality. Moreover, the wide scan is checked regularly, in other core level measurements too, to make sure that no contamination is appeared over the time of measurement.

The Figure 8.6(a) is representative of S-2p core level for $Cr_{1/3}TaS_2$. We used two sets of experimental geometry: normal emission (NE) and grazing emission (GE). And, photon source of energy 937 eV was used. As we previously mentioned in Chapter 6 that normal emission is more sensitive to the bulk while the grazing emission is more sensitive to the surface structure of the sample. The intensity for the core level in GE geometry reduces

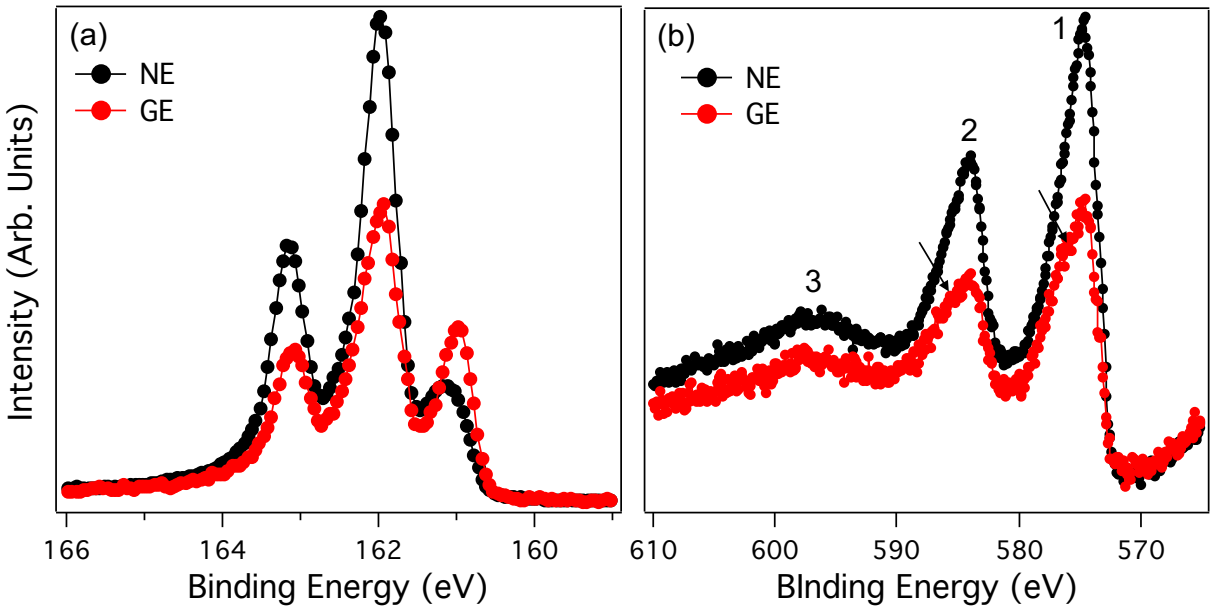

Figure 8.6: (a) S-2p and (b) Cr-2p photoemission peaks. Both spectra are recorded with photon energy of 937 eV with normal emission (NE) and grazing emission (GE) geometrical set up as indicated in the figures.

since the sampling depth is substantially decreased in this geometry. We observed S-2p core level consists of mainly three components. In fact, one pair of spin orbit doublets S-$2p_{3/2}$ and $2p_{1/2}$ are present, one corresponds to surface (lower BE peaks) and another to the bulk (higher BE peaks) of the sample. Similar surface features are also observed in $V_{0.3}NbS_2$ as reported in Chapter 6 and $Cr_{1/3}NbS_2$ [108]. The peak at the lower binding energy (in Figure 8.6(a)) is enhanced considerably when the GE geometry is employed, confirming the surface structure. The surface and bulk components arises due to the sulfur atoms at the surface and bulk have different chemical environments which causes the chemical shift to the spectrum.

The Cr-2p core level spectra using the same photon energy as used in S-2p core level experiments is shown in Figure 8.6(b). The experiments were performed in both NE and GE geometrical setups. Cr-2p spin orbit doublets $2p_{3/2}$ and $2p_{1/2}$ which are separated by 9.7 eV are observed in both the experimental setups. An additional feature, peak 3, is also observed which is about 24 eV from the main peak $2p_{3/2}$, and is a loss feature. Such loss feature is also observed at the same energy distance (24 eV) in other core level spectra we measured in this compound. This feature is assigned to a plasmon loss and is reported in $V_{0.3}NbS_2$

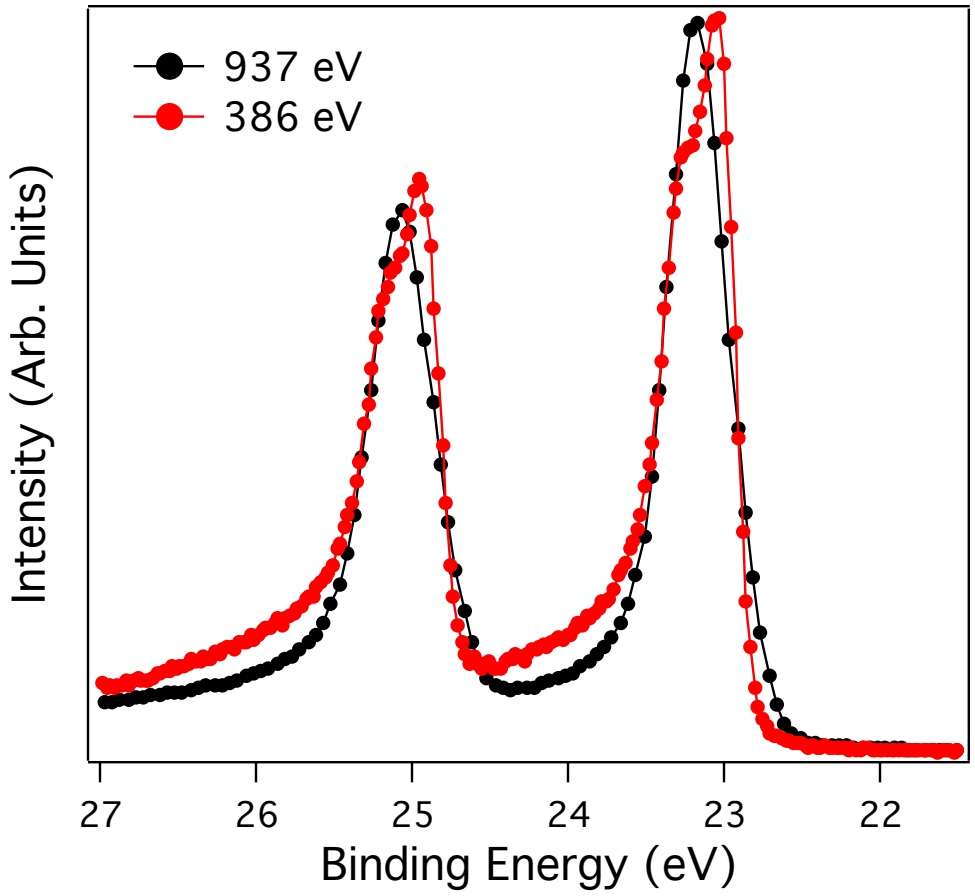

Figure 8.7: Ta-4f photoemission peak using photon energies of 937 eV and 386 eV with pass energies 100 eV and 20 eV, respectively.

in Chapter 6 and in other intercalated systems $Cr_{1/3}NbS_2$ and Fe_xNbS_2. We do not observe clear surface component in Cr-2p core level even in GE setup. Though, it is expected to have a Cr-2p surface components visible since disordered Cr atoms are present at the surface of the sample, so the Cr atoms at surface have different chemical environment than that in the bulk of the sample. But, we observe satellite features at higher binding energy associated to the main peaks 1 and 2. These satellite features arise due to the interaction of valence electrons with the core hole potential created upon the photo-excitation.

The Ta-4f core level spectrum of $Cr_{1/3}TaS_2$ recorded at room temperature is shown in Figure 8.7. We used two photon energies 937 and 386 eV with pass energies of 100 and 20 eV, respectively. And, the spectra were measured for the normal emission geometry. The spin-orbit doublet $4f_{7/2}$ and $4f_{5/2}$ are separated by energy of 1.9 eV. Each peak has shoulder like

structure in the higher binding energy side. The shoulder features are resolved when photon source of energy 386 eV is used, due to the better energy resolution as the pass energy was reduced at lower photon energy. The shoulder feature is originated from the many electron excitation as the electrons near the Fermi energy tend to screen the core-hole formation, as expected in metallic system. Such satellite features due to the many electron excitation are also reported in the parent compound 2H-TaS_2 and other intercalated 2H-TaS_2 system [104].

The Ta-4d spectrum recorded at room temperature utilizing photon energy of 937 eV is displayed in Figure 8.8(a). The spectrum exhibits a doublet $4d_{5/2}$ and $4d_{3/2}$ due to the spin orbit splitting and are separated by about 12 eV. Also, an additional features (marked by arrows) are present at higher binding energy side of the main peaks, each feature are at about 24 eV from corresponding main peak. These features are originated due to the plasmon loss excitations. The asymmetric line shape are observed in doublet peaks, which means satellite features are present associated to each main peak. The origin of the main and satellite features are described in more detail for Nb-3d core level in $V_{0.3}NbS_2$ compound in Chapter 6.

The Cr-3s core level of $Cr_{1/3}TaS_2$ measured at 937 eV is shown in Figure 8.8 (b). The spectrum displays two peaks due to the multiplet splitting of the binding energy which is a common effect in the transition metal compounds [44, 103, 118]. The multiplet splitting occurs in a transition metal atom having unpaired d-electrons in the outer shell, such that unfilled outer shell electrons interact with the 3s core electron left behind upon the photoelectron emission. If the total spin of the unpaired outer d-electrons has same spin orientation with that of 3s-core electron, energy of photoelectron decreases and a photoemission peak appears in the lower binding energy side of the spectrum, the opposite happens when they have different spin orientations that is another peak appears in higher binding side. The energy separation between two peaks is proportional to 3s-3d exchange integral K_{3s-3d} [120]. We also observed a broad feature around 95 eV indicated by an arrow, which arises due to the plasmon loss excitation as observed in Cr-2p and Ta-4d core level spectra too.

The valence band spectra for $Cr_{1/3}TaS_2$ measured with photon energies 567 and 937 eV are shown in Figure 8.8(c). The sharp peak near the Fermi energy is mainly contributed by

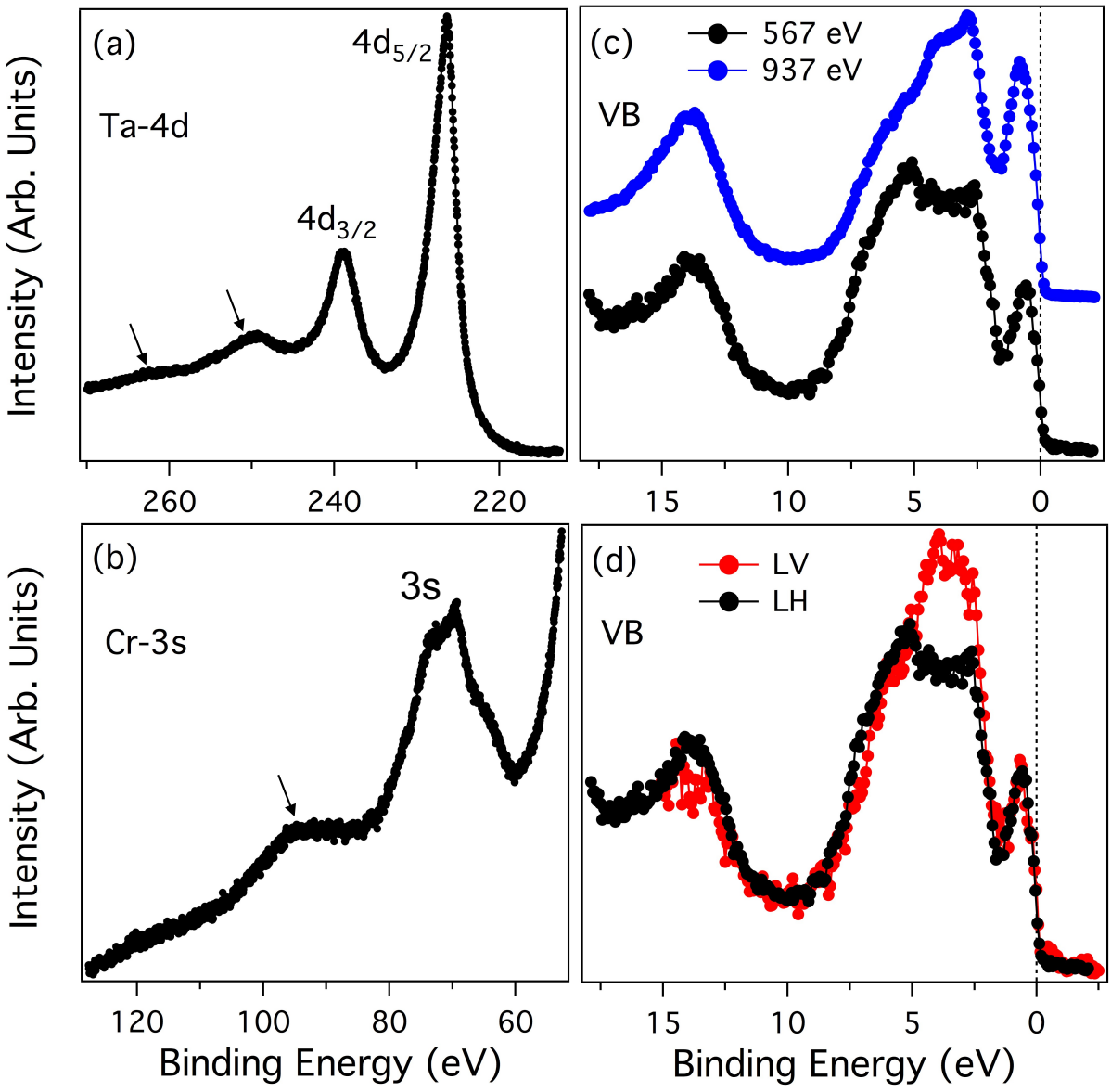

Figure 8.8: Core level and valence band spectra of $Cr_{1/3}TaS_2$. (a) Ta-4d, (b) Cr-3s core level photoemission peaks. (c) Valence band photoemission measured at photon energies 567 eV and 937 eV for σ polarized light. (d) Comparison of valence bands for σ and π polarized light of energy of 567 eV.

Ta-4d and Cr-3d orbitals, whereas broad feature (peak 2) centered around 5 eV is mainly comprised from the S-3p orbitals, and the peak centered around 15 eV is originated from the S-3s orbitals. As Ta-4f are localized well below the Fermi level at about 22 eV, so Ta-4f does not contribute to the spectral weight near the Fermi energy. The variation in peak intensity is observed at two different photon energies which is due to varying photo-absorption cross section at two energies.

The polarization dependent measurement to identify the orbital characters near the Fermi level of $Cr_{1/3}TaS_2$ are shown in Figure 8.8(d). Here, we used the LV and LH polarization of light; as mentioned before, in LV-polarized light the polarization lies completely in the plane, while for LH-polarized light has parallel and perpendicular component to the sample plane. Thus, specific orbital character can be excited using different polarization of light. We found that shape and intensity of peaks near the Fermi level and S-3s are almost equivalent for both polarization. While line shape and intensity for the middle peak, which is mainly consisted of S-3p orbitals, changes noticeably with change in photon polarization. This peak becomes more sharper and intensity is also increased, for LV-polarized light. Which is due to the intensity of in-plane orbitals such as p_x, p_y are enhanced for LV polarized which is suppressed for LH-polarized light. Moreover, the sulfur s-state is spherically symmetric, thus no change in the line shape and the intensity has been observed with change in the light polarization.

8.4 XAS and Resonant Photoemission Spectroscopy

Figure 8.9 shows XAS spectra while the photon source is tuned to Cr-L_{23} absorption edge. These spectra were recorded in BACH beamline of ELETTRA synchrotrone light source in Italy, employing the total electron yield technique. We utilized two polarization of light called LV and LH for these measurements. The peaks in XAS spectra represent transition from Cr-$2p_{1/2}$ and Cr-$2p_{3/2}$ multiplet states to lowest unoccupied state in the conduction band. Thus, the XAS also represents the unoccupied states in the valence band spectrum. We found that there is no difference between the spectra obtained by utilizing the LV- and LH-polarized light. Moreover, satellite features are observed in the lower energy side of each

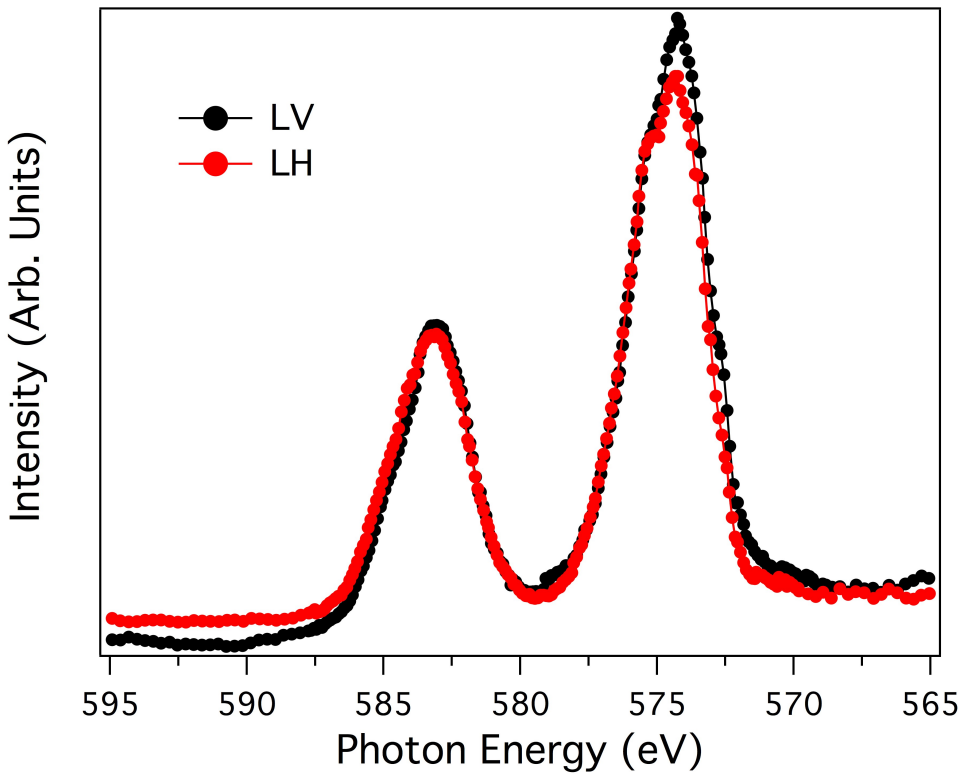

Figure 8.9: X-ray absorption spectra corresponding to Cr-L_{23} absorption edge. The LH and the LV polarized lights are used.

peak which could be originated from the disordered Cr atoms present on the surface of the sample, they may have a lower valence state compared to bulk Cr atoms.

Now, we present the result of resonant photoemission spectroscopy (ResPES) experiments performed on $Cr_{1/3}TaS_2$ sample at room temperature. These experiments were also performed in BACH beamline. In resonant photoemission experiment, photon energy is tuned across the absorption edge of deeper core level of a specific atom so that the core level electron is excited to unoccupied energy level in the conduction band. With this technique, a portion of valence band corresponding to the resonating energy levels is enhanced and hence can be extracted from the total VB structure. The ResPES is an element sensitive technique as such spectral weight in the valence band associated with the particular atom participating in resonating process can be identified. This is an advantage of ResPES over conventional photoemission spectroscopy where it is extremely difficult to resolve spectral features of specific atom in valence band.

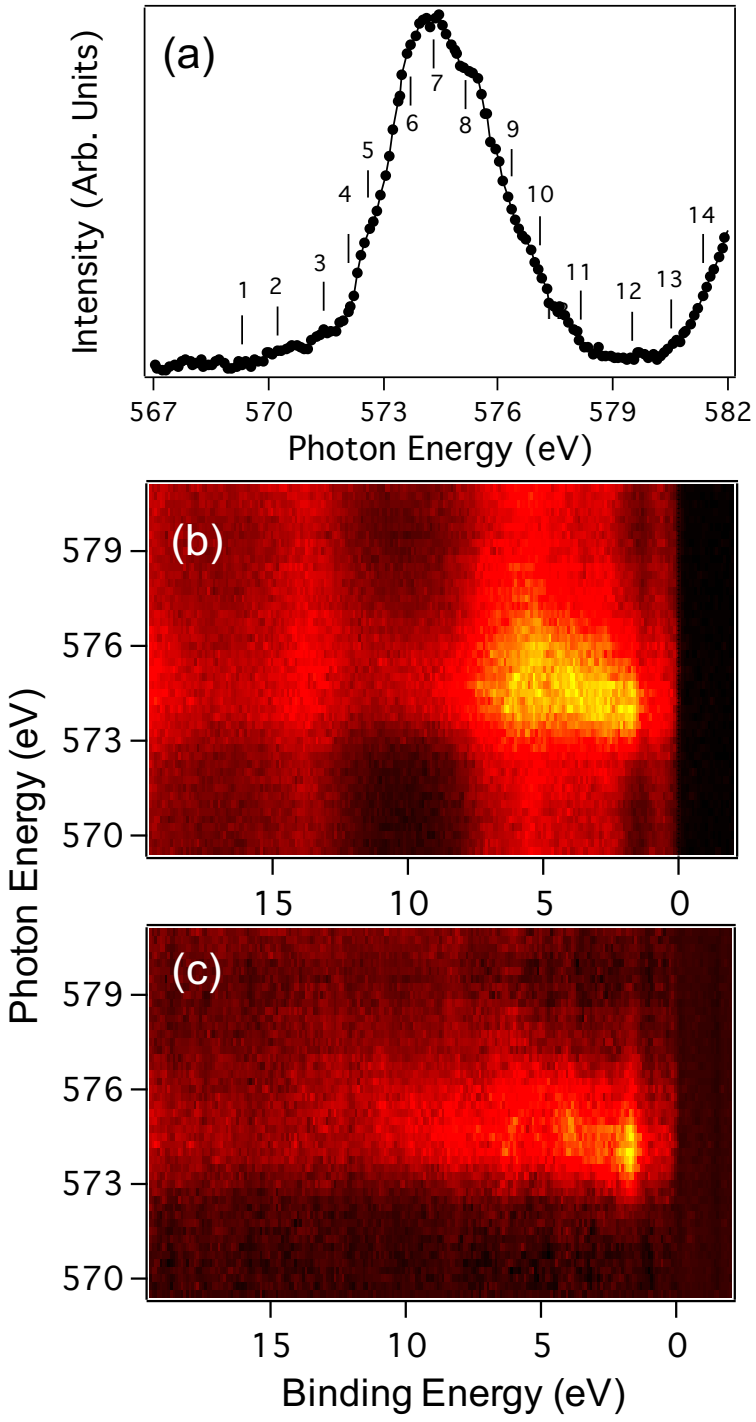

Figure 8.10: ResPES and XAS spectra measured across CrL_3 absorption edge when LH-polarized light is used. (a) Cr-L_3 XAS measured in total electron yield mode. (b) ResPES image plot. (c) ResPES image plot with off-resonant signal subtracted.

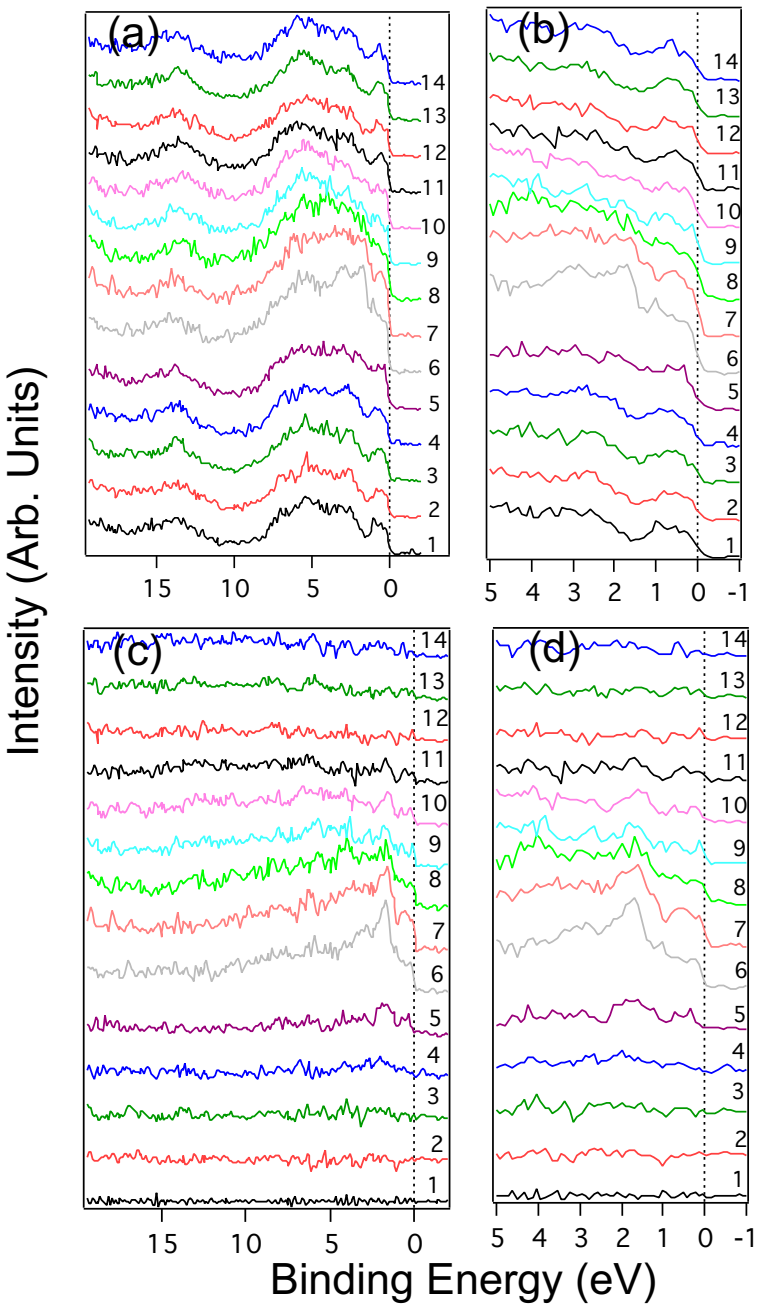

Figure 8.11: (a,c) The line profiles extracted from image plot 8.10(b,c) at photon energies marked by numbers in 8.10(a). (b,d) The line profiles in proximity to E_F obtained from (a,c).

Figure 8.10(b) shows the ResPES spectra of $Cr_{1/3}TaS_2$ obtained by scanning the photon energy from 569 to 581 eV across the Cr-L_3 absorption edge with the normal emission geometry. The corresponding XAS spectrum is shown on the top panel of the Figure. In order to observe pure resonant contribution, off-resonant signal considered at 569 eV is subtracted from the original spectrum and is shown in the Figure 8.10(c). The later spectrum shows that the several features are resonated with the photon energy. From the ResPES spectra it has been evidenced that the states very close to the Fermi level are markedly enhanced at photon energy corresponding to Cr-L_3. In addition, another feature about 1.5 eV has also been enhanced. Which is clearly visible from the line profile extracted from the image plot for the selected photon energies indicated by numbers in the XAS spectrum shown in Figure 8.10. The upper panel on the left in Figure 8.11 is the line profile corresponds to Figure 8.10(b), while the lower panel corresponds to Figure 8.10(c). The corresponding zoom-in portion of the line profiles are presented on the right side to each plot, in order to observe resonant spectra close to Fermi edge. These ResPES results elucidate that chromium states contribute to the Fermi level. Similar Cr states contributed to the Fermi level has also been reported in another intercalated system $Cr_{1/3}NbS_2$ [N. Sirica PhD Thesis]. Since we are using LH-polarized light, enhanced Cr states should have out-of-plane character.

Figure 8.12(b) shows the ResPES spectra for the photon energy scanning from 569 to 591 eV across Cr-L_3 absorption edge when the LV-polarized light was used. The corresponding XAS spectra is displayed on top panel of the Figure. The spectra in Figure 8.12(c) is obtained by subtracting the off-resonant signal (off-resonant signal is taken to be the spectrum at 569 eV photon energy). Figure 8.13(a) and (c) shows the line profiles extracted from the image plot 8.12(a) and (c), respectively. The zoom-in portion close to Fermi level is shown on right side of each plot in Figure 8.13(b) and (d). From the line profile, we observed that the spectral weight close to Fermi energy is enhanced but is pushed few meV towards the high binding energy side as compared to that of LV-polarized case. Which indicates that Cr-3d orbital, particularly, in-plane characters are also present in proximity to the Fermi level as we used LV-polarized light. Also, a portion of valence band around 1.8 eV is also markedly enhanced, possibly due to the hybridization of Cr-3d and Ta-5d in-plane orbitals.

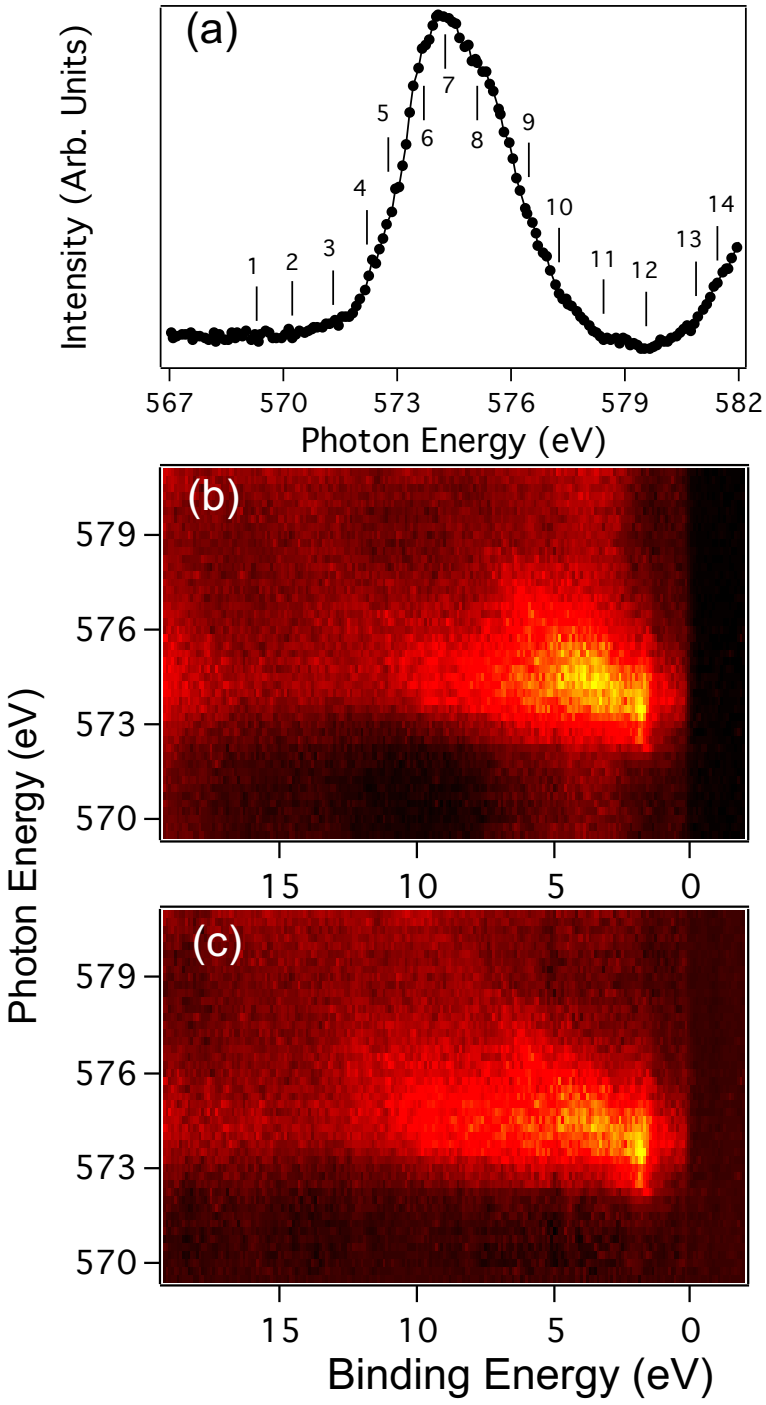

Figure 8.12: ResPES and XAS measured across CrL_3 absorption edge when LV-polarized light is used. (a) Cr-L_3 XAS measured in total electron yield mode. (b) ResPES image plot. (c) ResPES image plot with off-resonant signal subtracted.

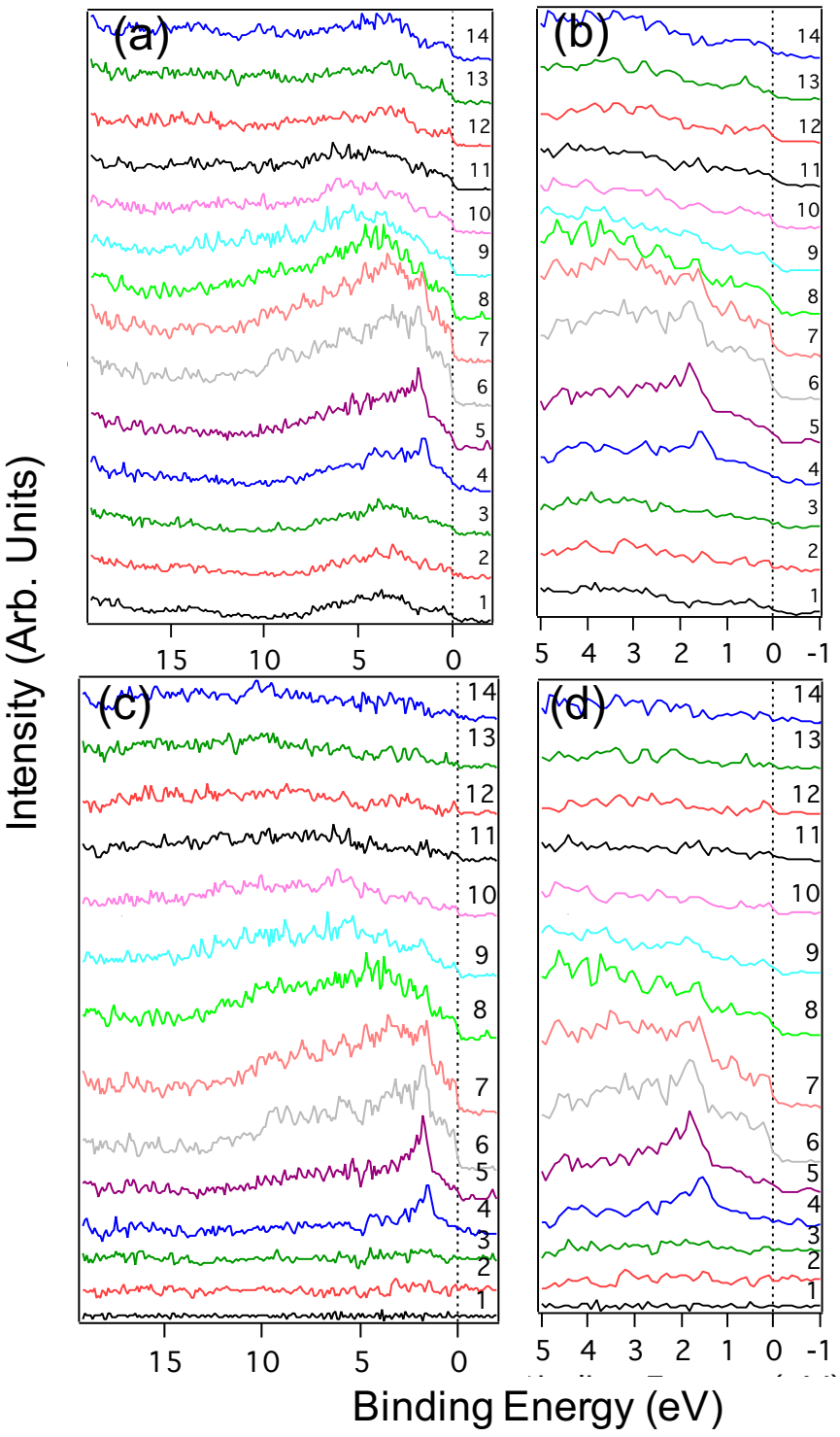

Figure 8.13: (a,c) The line profiles extracted from image plot 8.10(b,c) at photon energies marked by numbers in 8.10(a). (b,d) The line profiles in proximity to E_F obtained from (a,c).

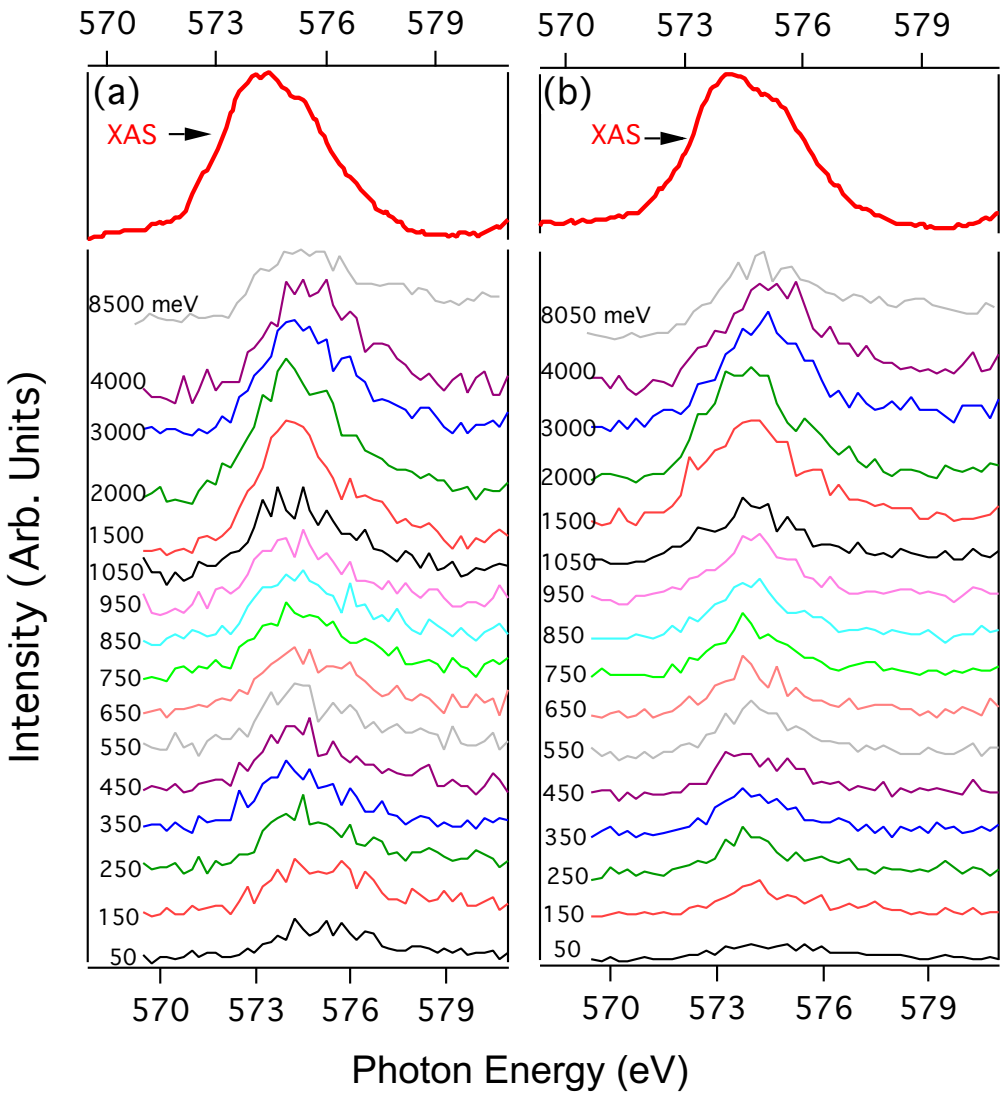

Figure 8.14: Constant initial states obtained from image plots 8.10(b) and 8.12(b). XAS is shown in thicker line (red) on the top of plot. (a) For LH and (b) for LV-polarized light.

Constant initial state (CIS) for LH and LV-polarized light obtained from the image plots 8.10(c) and 8.12(c) is displayed in Figure 8.14 (a) and (b), respectively. The corresponding XAS spectra are shown on the bold red line in each plot (see the top curve). The CIS spectrum represent the peak intensity as a function of the photon energy.

8.5 Angle Resolved Photoemission Spectroscopy on $Cr_{1/3}TaS_2$

The ARPES spectra utilizing the He-II (40.8 eV) has been shown in Figures 8.15. For these experiments, the samples were cleaved in the preparation chamber at pressure better than 10^{-10} Torr, and the sample is immediately moved to the main chamber having pressure better than 5×10^{-11} Torr where the experiments were carried out.

The condition of surface was checked regularly by measuring wide valence band in every 12 hours and we found that sample was stable over 24 hours. The samples were oriented along the high symmetry direction by LEED experiments. These ARPES experiments were measured at temperature 140 K. All the spectra presented here are normalized by the bottom 50 meV of energy range.

The ARPES results for the sample aligned along ΓK direction is shown in Figure 8.15 (a_1) and (b_1), and the corresponding EDC and MDC are shown in Figure 8.16 (a_1) and (a_2), respectively. In Figure 8.15(b_1), the spectrum was recorded such that both high symmetry points Γ and K were centered. We observed that a hole like band crosses the Fermi energy and another band is sink just below the Fermi level at Γ point. Similarly, a hole band crosses the Fermi energy at K point as well. From the EDC analysis, we observed two bands near K point such that one band sink below the Fermi level while another band crosses the Fermi energy. The ARPES spectra while the sample is oriented along ΓM are shown in Figure 8.15 (b_1) and (b_2) and corresponding MDC and EDC stacked are presented in Figure 8.16(a_2) and (b_2), respectively. As in the ΓK direction, we observed that one hole pocket cross the Fermi level near the Γ point and another band is confined below the Fermi energy around Γ point. However, near M point no bands cross the Fermi level. The ARPES spectra of

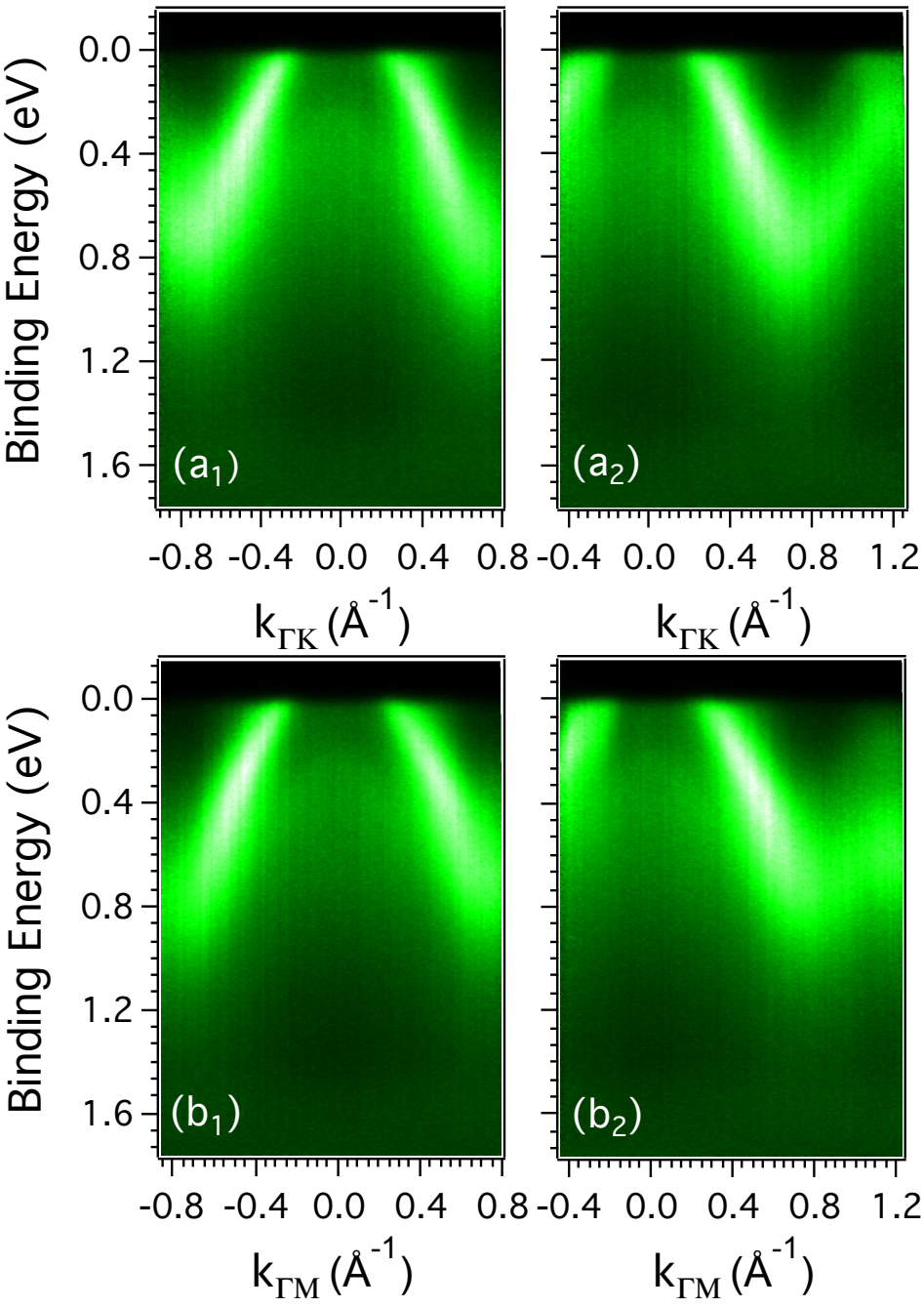

Figure 8.15: Band dispersion measured along ΓM (a_1, a_2) and ΓK (b_1 ,b_2) direction using photon source of energy 40.8 eV (He-II).

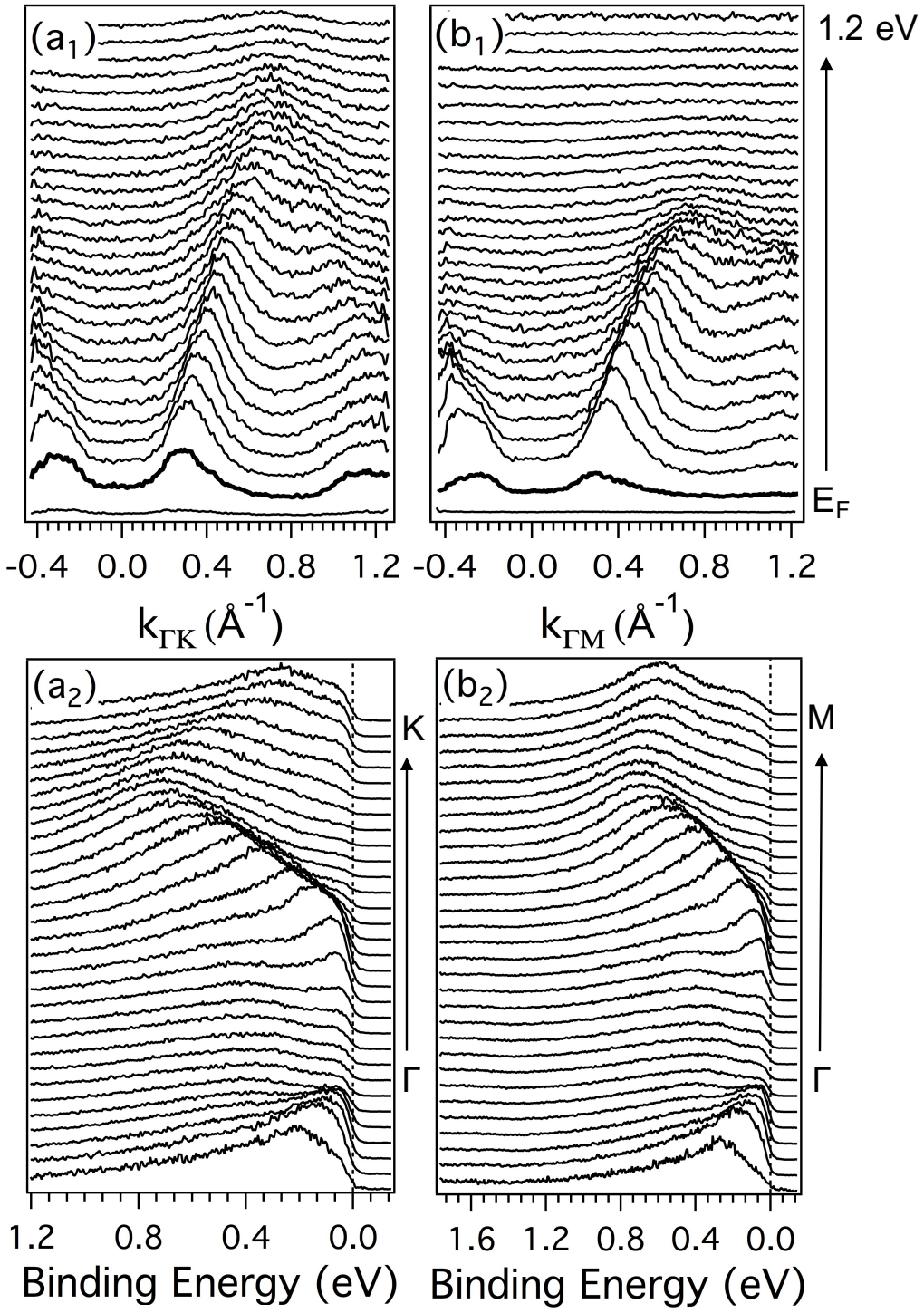

Figure 8.16: Stacked EDCs (a_1, b_1) and MDCs (b_1, b_2) corresponding to image plots 8.15 (a_2, b_2). The symbol of high symmetry points and the directions are shown.

$Cr_{1/3}TaS_2$ obtained here is similar to that of $Cr_{1/3}NbS_2$ (see Figure 6.20(b)) performed with the same experimental setup. Noticeably, in $Cr_{1/3}NbS_2$, a band located few meV below the Fermi level around Γ point is more intense in compare to that in $Cr_{1/3}TaS_2$.

Our experimental results do not agree with that the band structure obtained from the DFT calculations presented earlier. The origin of this discrepancy between the calculations and the experimental results in not clear yet. Moreover, The DFT predicts strong k_z dispersion. In order to check the band dispersion along k_z direction or 3D Fermi surface the photon energy dependent ARPES experiments has to be carried out. Furthermore the unpolarized light was used in our experiments, so we can not acquire the orbital characters of the particular band. In order to obtain these information, one has to perform the experiments in the synchrotron radiation facility which allows one to choose the range of photon energy as well as the polarization light source. Moreover, It is worthwhile to perform ARPES experiments such as Fermi surface mapping and polarization dependent band dispersion on both the parent compound TaS_2 and intercalated system $Cr_{1/3}TaS_2$ to examine the effect of the charge transfer from intercalant Cr to host TaS_2.

Chapter 9

Conclusions and Future Directions

In this thesis, we synthesized two intercalated systems $V_{0.3}NbS_2$ and $Cr_{1/3}TaS_2$ and investigated their electrical transport, magnetic, and electronic properties. We compared our findings with the host materials and a well-studied intercalated system $Cr_{1/3}NbS_2$ to inspect the effect of intercalant species to the host materials. Both the 3d-intercalant species V and Cr inject equal number of electrons to corresponding host materials and expected to have similar effect to the host.

The first intercalated system we studied was $V_{0.3}NbS_2$ grown by chemical vapor transport technique. The crystal structure had been investigated by the powder and single crystal XRD experiments and confirmed to belonging hexagonal *P-31m* space group. The resistivity shows different behavior than the host compound NbS_2: the superconductivity is completely suppressed and an anomaly appears at 50 K due to a long range magnetic orderings. The low temperatures resistivity follows the T^2 behavior, due to the interaction of conduction electron (Nb-4d) with the local moment arises from vanadium d-electrons, while the resistivity at higher temperatures (above 50 K) follows the linear behavior by usual electron-phonon scatterings. The resistivity is also appreciably different from the Cr-intercalated NbS_2 ($Cr_{1/3}NbS_2$) which shows abrupt increase at the magnetic transition temperature and decreases slightly at higher temperatures. From the Hall effect measurements of $V_{0.3}NbS_2$, we found that the resistivity exhibited positive slopes in all the temperatures the experiments performed, indicating that the majority of charge carrier is hole type. The carrier concentration obtained from the Hall coefficient is two orders of magnitude smaller

than the typical metals such as Al and it can be considered as low concentration metal. Host NbS_2 and intercalated $Cr_{1/3}NbS_2$ are also hole carrier type metals, however the carrier concentration of $V_{0.3}NbS_2$ is smaller than host NbS_2 and larger than intercalated $Cr_{1/3}NbS_2$, an evidence of electron transfer from vanadium to the host materials; but vanadium does not donate as much electrons as chromium does to NbS_2 layer. The magnetic measurements show that it is a canted antiferromagnetic system having highly anisotropic magnetic behavior with easy axis along ab plane. The DFT calculations also confirmed antiferromagnetic state favoring over the non-magnetic state by 59 eV per unit cell. And, the heat transport in this material is mainly due to the phonons as the electron contribution to it is one order of magnitude smaller than that of phonon.

We investigated the electronic structure by photoemission method which is a surface sensitive technique; thus, we first investigated the surface of the sample carefully prior to the experiments. For this, we employed the STM, LEED, and core level photoemission experiments on the sample cleaved at UHV system. The STM measurements revealed rough and smooth regions corresponding to sulfur and vanadium terminated surfaces, respectively. The rough region is non-periodic while the smooth is periodic exhibiting two ordered periodicity of (1×1) from host NbS_2 and $(\sqrt{3} \times \sqrt{3})$ from vanadium superstructure. The LEED results also show the (intense) (1×1) spots and (weak) $(\sqrt{3} \times \sqrt{3})$ as observed in the FFT of STM image. The periodicity of these two ordered states is consistent with that obtained from the single crystal XRD. The surface is further investigated by S-2p and V-2p core level photoemission experiments. The S-2p shows two spin-orbit doublets one originated from S atoms at the surface and another at the bulk of the sample (due to different chemical environment at surface and bulk). The surface component is not clearly visible in V-2p core level spectrum, though it is expected, since S-2p and V-2p core levels were recorded with same the photon energy. The non-dispersive bands observed near the Fermi level in resonant ARPES spectra performed when photon energy tuned to V-L_3 absorption edge confirmed the presence of disordered vanadium atoms at the surface of the $V_{0.3}NbS_2$ sample. Similar characteristic of surface and bulk states has also been reported in $Cr_{1/3}NbS_2$ system [108].

Though the surface of the sample is vanadium disordered or deficient, high quality ARPES spectra were observed. We chose conventional ARPES over the Soft X-ray ARPES to

investigate the band dispersion, since all the spectral features of soft X-ray ARPES is retained in the conventional (VUV) ARPES. The advantage of using the conventional to Soft X-ray ARPES is better count rate and higher momentum and energy resolutions. From ARPES measurements, it is found that all the bands in case of $V_{0.3}NbS_2$ are shifting downward with respect to that of NbS_2 meaning that electron is donated to Nb-4d states. The electron donation is also evidenced from Nb-4d core level as the satellite features are suppressed in intercalated system. The electron donation has also been confirmed in $Cr_{1/3}NbS_2$ system. The Fermi surface mapping utilizing different polarization shows that the d_{z^2} type bands at Γ and $d_{xy}/d_{x^2-y^2}$ types at K point as seen in $Cr_{1/3}NbS_2$. But the size of the pockets at Γ and K are larger than that of $Cr_{1/3}NbS_2$ but smaller than NbS_2, indicating that vanadium donates fewer electron than chromium does to NbS_2. This is consistent with the transport measurements, specifically the Hall effect measurements. Further, the shape of the Fermi surface is more complex than that of NbS_2. Also, two hole like bands of symmetry d_z^2 crossing at Γ point and two bands having symmetry $d_{xy}/d_{x^2-y^2}$ crossing at K point. A weak band of in plane character with symmetry $d_{xy}/d_{x^2-y^2}$ also crosses the Fermi level at Γ point. These findings indicate that the rigid band picture, which tells the intercalant 3d-ion only injects electrons without altering the band structure and shape of the Fermi surface, is not valid in $V_{0.3}NbS_2$. A band present at 0.2 eV below the Fermi level as presented in $Cr_{1/3}NbS_2$ has not been observed in case of $V_{0.3}NbS_2$. Also, from the resonant photoemission experiments we found that V-3d contribution confined few meV below Fermi level implying that the additional bands cross the Fermi level might not be originated from V-3d orbital state. The origin of these additional bands in comparison to NbS_2 located at the Fermi level is not clear yet. But in case of $Cr_{1/3}NbS_2$ the additional bands, namely β and δ bands are originated from Cr-3d states [108]. This is one of the discrepancies between these two intercalated systems. Further, the resonant ARPES (photon energy tuned to V-L_3 absorption edge) measurements carried out with LH polarization of light shows a strong hybridization between out-of-plane states of vanadium and niobium, resulting dispersive bands, which occurs few meV below Fermi level. However, when the LV polarized light was used, non-dispersive feature is observed indicating in-plane vanadium d-orbitals do not have strong interaction

between each other and non-dispersive atomic like band disperion observed, possibly due to large separation of vanadium atoms in the ab plane.

Here, BZ of (1×1) periodicity of host NbS2 is considered to be proper BZ to interpret our ARPES spectra. If the electronic structure of $V_{0.3}NbS_2$ were correctly described with respect ot BZ of $(\sqrt{3}\times\sqrt{3})$ superstructure, the spectral features of K would be replicated to that of Γ point since these two points are separated by the reciprocal vector of BZ for superstructure. But, we found that Γ and K points have appreciably different spectral features such as orbital characters, shape and size of the Fermi surface pockets.

DFT calculations performed on $V_{0.3}NbS_2$ show that the electronic structure is more complex than that predicted by simple rigid band shift of NbS_2 band structure. Instead, many bands arise from V-3d states are contributed in proximity to the Fermi level. Our DFT calculations does not effectively agree with with the experimental results. However, the strong k_z dispersion predicted by the calculations is also retained in the experimental result. Which is consistent with presence of out-of-plane orbitals at the Fermi level and expected to increase the interaction between the NbS_2 layers. However, in NbS_2 and $Cr_{1/3}NbS_2$ compounds it is reported to have weak k_z disperion, hence a weak interlayer coupling. In other words, the intercalation has not necessarily to be always 2D electronic structure.

Another intercalated compound we studied was $Cr_{1/3}TaS_2$, grown by CVT method, having hexagonal crystal structure as of $Cr_{1/3}NbS_2$ with non-centrosymmetric $P6_322$ space group. This material also exhibits two ordered states (1×1) from TaS_2 and $(\sqrt{3}\times\sqrt{3})$ periodicity from Cr superstructure, evidenced from the STM and LEED experiments. These periodicities are also consistent with that observed in $Cr_{1/3}NbS_2$ and $V_{0.3}NbS_2$. The $Cr_{1/3}TaS_2$ shows ferromagnetic ordering with transition temperature about 92 K. The resistivity shows the metallic behavior, saturation observed at higher temperature whereas the lower temperatures resistivity follows $T^{1.8}$ behavior. In addition, it shows the negative magnetoresistance having magnitude higher than intercalated $Cr_{1/3}NbS_2$. We also found the similar surface structure as observed in $V_{0.3}NbS_2$ and $Cr_{1/3}NbS_2$, in terms of the S-2p and Cr-2p core level spectra. In similar to $Cr_{1/3}NbS_2$, Cr-3d state is contributed to the Fermi level in $Cr_{1/3}TaS_2$ which is observed from the resonant photoemission experiments. ARPES experiments show two bands crossing at Γ and K points and a band is passed

few meV below the Fermi level. The experimental band dispersion obtained from the ARPES experiments does not agree well with our DFT calculations performed utilizing WIEN2k package. Moreover, ARPES data from the host TaS_2 is not available; so, we are unable to fully examine the effect of intercalation to electronic structure. Thus, as a future work, we propose to perform Fermi surface mapping and band dispersion utilizing different polarization for both the host TaS_2 and the intercalated $Cr_{1/3}TaS_2$ and compare the results. We also propose to perform photon dependent ARPES experiments to check the k_z dispersion which will tell degree of interlayer couplings.

In summary, we expected to have similar transport, magnetic, and electronic properties of the intercalated systems studied in this dissertation since the 3d-transition metal ions are in the same oxidation state (+3) that is they donate equal number of electrons to the host materials, but we found that their role is appreciably different to these properties. The findings acquired from this research, we hope, will establish a foundation to investigate new intercalated systems to infer the effect of intercalant species to host compounds.

Bibliography

[1] Abbate, M., Goedkoop, J., De Groot, F., Grioni, M., Fuggle, J., Hofmann, S., Petersen, H., and Sacchi, M. (1992). Probing depth of soft x-ray absorption spectroscopy measured in total-electron-yield mode. *Surface and Interface Analysis*, 18(1):65–69. 30

[2] Aksel'rud, L., Andre, Z., Kulikov, L., Takzej, G., Semenov-Kobzar, A., and Romaka, L. (1998). Tantalum and niobium disulfides intercalated with chromium and nickel. *Neorganicheskie Materialy*, 34(4):489–494. 123

[3] Ali, M. N., Xiong, J., Flynn, S., Tao, J., Gibson, Q. D., Schoop, L. M., Liang, T., Haldolaarachchige, N., Hirschberger, M., Ong, N. P., et al. (2014). Large, non-saturating magnetoresistance in wte 2. *Nature*, 514(7521):205. 5

[4] Aristov, D. (1997). Indirect rkky interaction in any dimensionality. *Physical Review B*, 55(13):8064. 12

[5] Ayari, A., Cobas, E., Ogundadegbe, O., and Fuhrer, M. S. (2007). Realization and electrical characterization of ultrathin crystals of layered transition-metal dichalcogenides. *Journal of applied physics*, 101(1):014507. 4

[6] Balandin, A. A., Ghosh, S., Bao, W., Calizo, I., Teweldebrhan, D., Miao, F., and Lau, C. N. (2008). Superior thermal conductivity of single-layer graphene. *Nano letters*, 8(3):902–907. 3

[7] Balog, R., Jørgensen, B., Nilsson, L., Andersen, M., Rienks, E., Bianchi, M., Fanetti, M., Lægsgaard, E., Baraldi, A., Lizzit, S., et al. (2010). Bandgap opening in graphene induced by patterned hydrogen adsorption. *Nature materials*, 9(4):315. 4

[8] Baltzer, P. and Karlsson, L. (1988). High-resolution extreme-ultraviolet spectrum of he between 35 and 55 ev. *Physical Review A*, 38(5):2322. 47

[9] Battaglia, C., Cercellier, H., Despont, L., Monney, C., Prester, M., Berger, H., Forró, L., Garnier, M., and Aebi, P. (2007). Non-uniform doping across the fermi surface of nbs 2 intercalates. *The European Physical Journal B*, 57(4):385–390. 10, 88

[10] Beck, P. A. and Claus, H. (1970). Density of states information from low temperature specific heat measurements. *JOURNAL OF RESEARCH OF THE NATIONAL BUREAU OF STANDARDS SECTION A-PHYSICS AND CHEMISTRY*, 74A(3):449–+. 62

[11] Blaha, P. (1991). Electronic structure and electric field gradients in 2h-tas2, litas2 and sntas2. *Journal of Physics: Condensed Matter*, 3(47):9381. 12

[12] Blaha, P., Schwarz, K., Madsen, G., Kvasnicka, D., and Luitz, J. (2001). wien2k. *An augmented plane wave+ local orbitals program for calculating crystal properties*. 40, 72, 129

[13] Bocquet, A. E., Mizokawa, T., Saitoh, T., Namatame, H., and Fujimori, A. (1992). Electronic structure of 3d-transition-metal compounds by analysis of the 2p core-level photoemission spectra. *Phys. Rev. B*, 46:3771–3784. 71

[14] Borisenko, S., Kordyuk, A., Zabolotnyy, V., Inosov, D., Evtushinsky, D., Büchner, B., Yaresko, A., Varykhalov, A., Follath, R., Eberhardt, W., et al. (2009). Two energy gaps and fermi-surface arcs in nbse 2. *Physical review letters*, 102(16):166402. 6

[15] Bornstein, A. C., Chapman, B. J., Ghimire, N. J., Mandrus, D. G., Parker, D. S., and Lee, M. (2015). Out-of-plane spin-orientation dependent magnetotransport properties in the anisotropic helimagnet cr 1/3 nbs 2. *Physical Review B*, 91(18):184401. 10

[16] Brühwiler, P., Karis, O., and Mårtensson, N. (2002). Charge-transfer dynamics studied using resonant core spectroscopies. *Reviews of Modern Physics*, 74(3):703. 31

[17] Ceperley, D. M. and Alder, B. (1980). Ground state of the electron gas by a stochastic method. *Physical Review Letters*, 45(7):566. 39

[18] Cheney, C. P., Vilmercati, P., Martin, E., Chiodi, M., Gavioli, L., Regmi, M., Eres, G., Callcott, T., Weitering, H. H., and Mannella, N. (2014). Origins of electronic band gap reduction in cr/n codoped tio 2. *Physical review letters*, 112(3):036404. xiii, 31, 32, 33

[19] Clark, W. (1976). Structural and photoemission studies of some transition metal intercalates of nbs2. *Journal of Physics C: Solid State Physics*, 9(24):L693. 9

[20] Colinge, J.-P. (2004). Multiple-gate soi mosfets. *Solid-state electronics*, 48(6):897–905. 5

[21] Corcoran, R., Meeson, P., Onuki, Y., Probst, P.-A., Springford, M., Takita, K., Harima, H., Guo, G., and Gyorffy, B. (1994). Quantum oscillations in the mixed state of the type ii superconductor 2h-nbse2. *Journal of Physics: Condensed Matter*, 6(24):4479. 6

[22] Dai, Z., Xue, Q., Gong, Y., Slough, C., and Coleman, R. (1993). Scanning-probe-microscopy studies of superlattice structures and density-wave structures in 2h-nbse 2, 2h-tase 2, and 2h-tas 2 induced by fe doping. *Physical Review B*, 48(19):14543. 65

[23] Damascelli, A., Hussain, Z., and Shen, Z.-X. (2003a). Angle-resolved photoemission studies of the cuprate superconductors. *Reviews of modern physics*, 75(2):473. xiii, 17, 25, 26, 27, 28, 48

[24] Damascelli, A., Hussain, Z., and Shen, Z.-X. (2003b). Angle-resolved photoemission studies of the cuprate superconductors. *Rev. Mod. Phys.*, 75:473–541. 93

[25] De Groot, F. (2001). High-resolution x-ray emission and x-ray absorption spectroscopy. *Chemical Reviews*, 101(6):1779–1808. 31

[26] De Groot, F. and Kotani, A. (2008). *Core level spectroscopy of solids*. CRC press. 30, 31

[27] Dines, M. B. (1975). Lithium intercalation via n-butyllithium of the layered transition metal dichalcogenides. *Materials Research Bulletin*, 10(4):287–291. 7

[28] Dzyaloshinsky, I. (1958). A thermodynamic theory of weak ferromagnetism of antiferromagnetics. *Journal of Physics and Chemistry of Solids*, 4(4):241–255. 9

[29] Fadley, C. (1978). Basic concepts of x-ray photoelectron spectroscopy. *Electron spectroscopy: theory, techniques and applications*, 2:1–156. xiii, 20, 46

[30] Fadley, C. and Shirley, D. (1970). Multiplet splitting of metal-atom electron binding energies. *Physical Review A*, 2(4):1109. 23

[31] Fadley, C., Shirley, D., Freeman, A., Bagus, P., and Mallow, J. (1969). Multiplet splitting of core-electron binding energies in transition-metal ions. *Physical Review Letters*, 23(24):1397. 23

[32] Fadley, C. S. (2012). Looking deeper: Angle-resolved photoemission with soft and hard x-rays. *Synchrotron Radiation News*, 25(5):26–31. 29

[33] Fano, U. (1961). Effects of configuration interaction on intensities and phase shifts. *Physical Review*, 124(6):1866. 32, 82

[34] Fetter, A. L. and Walecka, J. D. (2012). *Quantum theory of many-particle systems*. Courier Corporation. 26

[35] Frey, G., Elani, S., Homyonfer, M., Feldman, Y., and Tenne, R. (1998). Optical-absorption spectra of inorganic fullerenelike m s 2 (m= mo, w). *Physical Review B*, 57(11):6666. 4

[36] Friend, R. and Yoffe, A. (1987). Electronic properties of intercalation complexes of the transition metal dichalcogenides. *Advances in Physics*, 36(1):1–94. xii, 1, 4, 5, 7, 9

[37] Gamble, F. and Geballe, T. (1976). Inclusion compounds. In *Treatise on solid state chemistry*, pages 89–166. Springer. 7

[38] Ghimire, N., McGuire, M. A., Parker, D. S., Sipos, B., Tang, S., Yan, J.-Q., Sales, B. C., and Mandrus, D. (2013a). Magnetic phase transition in single crystals of the chiral helimagnet cr 1/3 nbs 2. *Physical Review B*, 87(10):104403. 61, 125, 126

[39] Ghimire, N. J., McGuire, M. A., Parker, D. S., Sipos, B., Tang, S., Yan, J.-Q., Sales, B. C., and Mandrus, D. (2013b). Magnetic phase transition in single crystals of the chiral helimagnet $cr_{1/3}nbs_2$. *Phys. Rev. B*, 87:104403. 10, 63

[40] Gray, A., Papp, C., Ueda, S., Balke, B., Yamashita, Y., Plucinski, L., Minár, J., Braun, J., Ylvisaker, E., Schneider, C., et al. (2011). Probing bulk electronic structure with hard x-ray angle-resolved photoemission. *Nature Materials*, 10(10):759. 29

[41] Gudat, W. and Kunz, C. (1972). Close similarity between photoelectric yield and photoabsorption spectra in the soft-x-ray range. *Physical Review Letters*, 29(3):169. 30

[42] Guillamón, I., Suderow, H., Vieira, S., Cario, L., Diener, P., and Rodiere, P. (2008). Superconducting density of states and vortex cores of 2h-nbs 2. *Physical review letters*, 101(16):166407. 6

[43] Gunnarsson, O., Calandra, M., and Han, J. (2003). Colloquium: Saturation of electrical resistivity. *Reviews of Modern Physics*, 75(4):1085. 125

[44] Gweon, G.-H., Park, J.-G., and Oh, S.-J. (1993). Final-state screening effect in the 3s photoemission spectra of mn and fe insulating compounds. *Physical Review B*, 48(11):7825. 136

[45] Hagström, S., Nordling, C., and Siegbahn, K. (1964). Electron spectroscopy for chemical analyses. *Physics Letters*, 9:235–236. 21

[46] Hamaue, Y. and Aoki, R. (1986). Effects of organic intercalation on lattice vibrations and superconducting properties of 2h-nbs2. *Journal of the Physical Society of Japan*, 55(4):1327–1335. 6

[47] Han, M. Y., Özyilmaz, B., Zhang, Y., and Kim, P. (2007). Energy band-gap engineering of graphene nanoribbons. *Physical review letters*, 98(20):206805. 4

[48] Heil, C., Poncé, S., Lambert, H., Schlipf, M., Margine, E. R., and Giustino, F. (2017). Origin of superconductivity and latent charge density wave in nbs 2. *Physical review letters*, 119(8):087003. 95

[49] Heil, C., Schlipf, M., and Giustino, F. (2018). Quasiparticle g w band structures and fermi surfaces of bulk and monolayer nbs 2. *Physical Review B*, 98(7):075120. 6

[50] Herman, G., Tran, T., Higashiyama, K., and Fadley, C. (1992). Valence photoelectron diffraction and direct-transition effects. *Physical review letters*, 68(8):1204. 29

[51] Hertz, H. (1887). Ueber einen einfluss des ultravioletten lichtes auf die electrische entladung. *Annalen der Physik*, 267(8):983–1000. 13

[52] Hohenberg, P. and Kohn, W. (1964). Inhomogeneous electron gas. *Phys. Rev.*, 136:B864–B871. 35

[53] Hollander, J. and Shirley, D. (1970). Chemical information from photoelectron and conversion-electron spectroscopy. *Annual review of nuclear science*, 20(1):435–466. xii, 22

[54] Hubbard, J. (1979a). The magnetism of iron. *Phys. Rev. B*, 19:2626–2636. 1

[55] Hubbard, J. (1979b). Magnetism of iron. ii. *Physical Review B*, 20(11):4584. 1

[56] Hüfner, S. (2013). *Photoelectron spectroscopy: principles and applications*. Springer Science & Business Media. xii, 19, 24

[57] Huisman, R., De Jonge, R., Haas, C., and Jellinek, F. (1971). Trigonal-prismatic coordination in solid compounds of transition metals. *Journal of Solid State Chemistry*, 3(1):56–66. 6

[58] Hulliger, F. and Pobitschka, E. (1970). On the magnetic behavior of new 2h nbs2-type derivatives. *Journal of Solid State Chemistry*, 1(2):117–119. 129

[59] Hussain, Z., Fadley, C., Kono, S., and Wagner, L. (1980). Temperature-dependent angle-resolved x-ray photoemission study of the valence bands of single-crystal tungsten: Evidence for direct transitions and phonon effects. *Physical Review B*, 22(8):3750. 29

[60] Ivanovskaya, V. V., Zobelli, A., Gloter, A., Brun, N., Serin, V., and Colliex, C. (2008). Ab initio study of bilateral doping within the mos 2-nbs 2 system. *Physical Review B*, 78(13):134104. 6

[61] Jariwala, D., Sangwan, V. K., Lauhon, L. J., Marks, T. J., and Hersam, M. C. (2014). Emerging device applications for semiconducting two-dimensional transition metal dichalcogenides. *ACS nano*, 8(2):1102–1120. 4

[62] Johannes, M., Mazin, I., and Howells, C. (2006). Fermi-surface nesting and the origin of the charge-density wave in nb se 2. *Physical Review B*, 73(20):205102. 6

[63] Kertesz, M. and Hoffmann, R. (1984). Octahedral vs. trigonal-prismatic coordination and clustering in transition-metal dichalcogenides. *Journal of the American Chemical Society*, 106(12):3453–3460. 4

[64] Kittel, C. et al. (1976). *Introduction to solid state physics*, volume 8. Wiley New York. 60

[65] Ko, K.-T., Kim, K., Kim, S. B., Kim, H.-D., Kim, J.-Y., Min, B., Park, J.-H., Chang, F.-H., Lin, H.-J., Tanaka, A., et al. (2011). Rkky ferromagnetism with ising-like spin states in intercalated fe 1/4 tas 2. *Physical review letters*, 107(24):247201. 12

[66] Kohn, W. and Sham, L. J. (1965). Self-consistent equations including exchange and correlation effects. *Physical review*, 140(4A):A1133. 37, 129

[67] Kotani, A. and Toyozawa, Y. (1974). Photoelectron spectra of core electrons in metals with an incomplete shell. *Journal of the Physical Society of Japan*, 37(4):912–919. 23, 90

[68] Kowalczyk, S., Ley, L., McFeely, F., and Shirley, D. (1975). Multiplet splitting of the manganese 2 p and 3 p levels in mn f 2 single crystals. *Physical Review B*, 11(4):1721. 23

[69] Lapeyre, G., Baer, A., Hermanson, J., Anderson, J., Knapp, J., and Gobby, P. (1974). Photoemission studies of core exciton decay in ki. *Solid State Communications*, 15(10):1601–1605. 32

[70] Lee, H., McKinzie, H., Tannhauser, D., and Wold, A. (1969). The low-temperature transport properties of nbse2. *Journal of Applied Physics*, 40(2):602–604. 6

[71] Li, T. and Galli, G. (2007). Electronic properties of mos2 nanoparticles. *The Journal of Physical Chemistry C*, 111(44):16192–16196. 4

[72] Li, X., Wang, X., Zhang, L., Lee, S., and Dai, H. (2008). Chemically derived, ultrasmooth graphene nanoribbon semiconductors. *science*, 319(5867):1229–1232. 4

[73] Lin, M.-W., Ling, C., Zhang, Y., Yoon, H. J., Cheng, M. M.-C., Agapito, L. A., Kioussis, N., Widjaja, N., and Zhou, Z. (2011). Room-temperature high on/off ratio in suspended graphene nanoribbon field-effect transistors. *Nanotechnology*, 22(26):265201. 4

[74] Mahan, G. D. (2013). *Many-particle physics*. Springer Science & Business Media. 26

[75] Mak, K. F., Lee, C., Hone, J., Shan, J., and Heinz, T. F. (2010). Atomically thin mos 2: a new direct-gap semiconductor. *Physical review letters*, 105(13):136805. 4, 5

[76] Manzeli, S., Ovchinnikov, D., Pasquier, D., Yazyev, O. V., and Kis, A. (2017). 2d transition metal dichalcogenides. *Nature Reviews Materials*, 2(8):17033. 4

[77] Martin, R. and Shirley, D. (1976). Theory of core-level photoemission correlation state spectra. *The Journal of Chemical Physics*, 64(9):3685–3689. 20

[78] Mattheiss, L. (1973). Band structures of transition-metal-dichalcogenide layer compounds. *Physical Review B*, 8(8):3719. 6

[79] Mayorov, A. S., Gorbachev, R. V., Morozov, S. V., Britnell, L., Jalil, R., Ponomarenko, L. A., Blake, P., Novoselov, K. S., Watanabe, K., Taniguchi, T., et al. (2011). Micrometer-scale ballistic transport in encapsulated graphene at room temperature. *Nano letters*, 11(6):2396–2399. 3

[80] Mazin, I., Johannes, M., Boeri, L., Koepernik, K., and Singh, D. J. (2008). Problems with reconciling density functional theory calculations with experiment in ferropnictides. *Physical Review B*, 78(8):085104. 130

[81] McGuire, E. (1972). Photoabsorption cross section of titanium to cobalt. *Journal of Physics and Chemistry of Solids*, 33(3):577–580. 82

[82] Meijer, H., Pimmelaar, L., Brouwer, S., and Van den Handel, J. (1970). Some magnetic properties of mnco3 at low field strenghts. *Physica*, 46(2):279–290. 53

[83] Menzel, D. (2008). Ultrafast charge transfer at surfaces accessed by core electron spectroscopies. *Chemical Society Reviews*, 37(10):2212–2223. 31

[84] Miyadai, T., Kikuchi, K., Kondo, H., Sakka, S., Arai, M., and Ishikawa, Y. (1983). Magnetic properties of cr1/ 3nbs2. *Journal of the Physical Society of Japan*, 52(4):1394–1401. 9

[85] Moriya, T. (1960a). Anisotropic superexchange interaction and weak ferromagnetism. *Physical Review*, 120(1):91. 9

[86] Moriya, T. (1960b). Anisotropic superexchange interaction and weak ferromagnetism. *Phys. Rev.*, 120:91–98. 52, 53

[87] Moriya, T. and Miyadai, T. (1982). Evidence for the helical spin structure due to antisymmetric exchange interaction in cr13nbs2. *Solid State Communications*, 42(3):209–212. 1, 9

[88] Morosan, E., Zandbergen, H., Li, L., Lee, M., Checkelsky, J., Heinrich, M., Siegrist, T., Ong, N. P., and Cava, R. J. (2007). Sharp switching of the magnetization in fe 1/ 4 ta s 2. *Physical Review B*, 75(10):104401. 10

[89] Morris, D., Dou, Y., Rebane, J., Mitchell, C. E. J., Egdell, R. G., Law, D. S. L., Vittadini, A., and Casarin, M. (2000). Photoemission and stm study of the electronic structure of nb-doped tio_2. *Phys. Rev. B*, 61:13445–13457. 90

[90] Mulder, C., Van Duyneveldt, A., and Mydosh, J. (1981). Susceptibility of the cu mn spin-glass: Frequency and field dependences. *Physical Review B*, 23(3):1384. 57

[91] Novoselov, K. S., Geim, A. K., Morozov, S. V., Jiang, D., Zhang, Y., Dubonos, S. V., Grigorieva, I. V., and Firsov, A. A. (2004). Electric field effect in atomically thin carbon films. *science*, 306(5696):666–669. 3

[92] Novoselov, K. S., McCann, E., Morozov, S., Falko, V. I., Katsnelson, M., Zeitler, U., Jiang, D., Schedin, F., and Geim, A. (2006). Unconventional quantum hall effect and berrys phase of 2π in bilayer graphene. *Nature physics*, 2(3):177. 3

[93] Osterwalder, J., Greber, T., Hüfner, S., and Schlapbach, L. (1990). X-ray photoelectron diffraction from a free-electron-metal valence band: Evidence for hole-state localization. *Physical review letters*, 64(22):2683. 29

[94] Parkin, S. and Friend, R. (1980a). 3 d transition-metal intercalates of the niobium and tantalum dichalcogenides. i. magnetic properties. *Philosophical Magazine B*, 41(1):65–93. 1, 7, 9, 121, 123, 127

[95] Parkin, S. and Friend, R. (1980b). 3 d transition-metal intercalates of the niobium and tantalum dichalcogenides. ii. transport properties. *Philosophical Magazine B*, 41(1):95–112. 1, 7, 59, 125

[96] Perdew, J. P., Burke, K., and Ernzerhof, M. (1996). Generalized gradient approximation made simple. *Physical review letters*, 77(18):3865. 40, 129

[97] Qian, X., Liu, J., Fu, L., and Li, J. (2014). Quantum spin hall effect in two-dimensional transition metal dichalcogenides. *Science*, 346(6215):1344–1347. 4

[98] Radisavljevic, B., Radenovic, A., Brivio, J., Giacometti, i. V., and Kis, A. (2011). Single-layer mos 2 transistors. *Nature nanotechnology*, 6(3):147. 5

[99] Reinert, F. and Hüfner, S. (2005). Photoemission spectroscopyfrom early days to recent applications. *New Journal of Physics*, 7(1):97. xii, 14

[100] Rossnagel, K., Seifarth, O., Kipp, L., Skibowski, M., Voß, D., Krüger, P., Mazur, A., and Pollmann, J. (2001). Fermi surface of 2 h- nbse 2 and its implications on the charge-density-wave mechanism. *Physical Review B*, 64(23):235119. 6

[101] Roth, L. M., Zeiger, H., and Kaplan, T. (1966). Generalization of the ruderman-kittel-kasuya-yosida interaction for nonspherical fermi surfaces. *Physical Review*, 149(2):519. 1

[102] Saitoh, Y., Kobayashi, K., Fujimori, A., Yamamura, Y., Koyano, M., Tsuji, T., and Katayama, S. (2005). Photoemission and core-level absorption spectroscopy of fexnbs2. *Journal of electron spectroscopy and related phenomena*, 144:829–832. 70, 71, 79, 90

[103] Sangaletti, L., Depero, L., Bagus, P., and Parmigiani, F. (1995). A proper anderson hamiltonian treatment of the 3s photoelectron spectra of mno, feo, coo and nio. *Chemical physics letters*, 245(4-5):463–468. 136

[104] Scarfe, J. and Hughes, H. (1989). Core-level lineshapes in photoemission from transition-metal intercalates of tas2. *Journal of Physics: Condensed Matter*, 1(38):6865. 136

[105] Seah, M. P. and Dench, W. (1979). Quantitative electron spectroscopy of surfaces: A standard data base for electron inelastic mean free paths in solids. *Surface and interface analysis*, 1(1):2–11. xii, 16

[106] Shevchik, N. (1977). Disorder effects in angle-resolved photoelectron spectroscopy. *Physical Review B*, 16(8):3428. 29

[107] Singh, D. J. (1994). Introduction to the lapw method. In *Planewaves, Pseudopotentials and the LAPW Method*, pages 35–43. Springer. 40

[108] Sirica, N., Mo, S.-K., Bondino, F., Pis, I., Nappini, S., Vilmercati, P., Yi, J., Gai, Z., Snijders, P. C., Das, P. K., Vobornik, I., Ghimire, N., Koehler, M. R., Li, L., Sapkota, D., Parker, D. S., Mandrus, D. G., and Mannella, N. (2016). Electronic structure of the chiral helimagnet and 3*d*-intercalated transition metal dichalcogenide $Cr_{1/3}Nbs_2$. *Phys. Rev. B*, 94:075141. xii, xvi, 6, 10, 11, 70, 71, 76, 88, 90, 91, 93, 95, 96, 97, 108, 116, 134, 151, 152

[109] Sjöstedt, E., Nordström, L., and Singh, D. (2000). An alternative way of linearizing the augmented plane-wave method. *Solid state communications*, 114(1):15–20. 41

[110] Slater, J. C. (1951). A simplification of the hartree-fock method. *Phys. Rev.*, 81:385–390. 39

[111] Slater, J. C. (1963). *Quantum theory of molecules and solids*, volume 1. McGraw-Hill New York. 23

[112] Smith, N. V., Thiry, P., and Petroff, Y. (1993). Photoemission linewidths and quasiparticle lifetimes. *Phys. Rev. B*, 47:15476–15481. 32

[113] Splendiani, A., Sun, L., Zhang, Y., Li, T., Kim, J., Chim, C.-Y., Galli, G., and Wang, F. (2010). Emerging photoluminescence in monolayer mos2. *Nano letters*, 10(4):1271–1275. 4

[114] Strocov, V. N., Kobayashi, M., Wang, X., Lev, L. L., Krempasky, J., Rogalev, V. V., Schmitt, T., Cancellieri, C., and Reinle-Schmitt, M. L. (2014). Soft-x-ray arpes at the

swiss light source: From 3d materials to buried interfaces and impurities. *Synchrotron Radiation News*, 27(2):31–40. 29, 85

[115] Togawa, Y., Koyama, T., Takayanagi, K., Mori, S., Kousaka, Y., Akimitsu, J., Nishihara, S., Inoue, K., Ovchinnikov, A., and Kishine, J.-i. (2012). Chiral magnetic soliton lattice on a chiral helimagnet. *Physical review letters*, 108(10):107202. 9

[116] Tonjes, W., Greanya, V., Liu, R., Olson, C., and Molinié, P. (2001). Charge-density-wave mechanism in the 2 h- nbse 2 family: Angle-resolved photoemission studies. *Physical Review B*, 63(23):235101. 6

[117] Ugeda, M. M., Bradley, A. J., Shi, S.-F., Felipe, H., Zhang, Y., Qiu, D. Y., Ruan, W., Mo, S.-K., Hussain, Z., Shen, Z.-X., et al. (2014). Giant bandgap renormalization and excitonic effects in a monolayer transition metal dichalcogenide semiconductor. *Nature materials*, 13(12):1091. 5

[118] Van Campen, D. and Klebanoff, L. (1994). Spin-resolved and high-energy-resolution xps studies of the 3s and 2s levels of metallic cobalt. *Physical Review B*, 49(3):2040. 136

[119] Van der Laan, G., Westra, C., Haas, C., and Sawatzky, G. (1981). Satellite structure in photoelectron and auger spectra of copper dihalides. *Physical Review B*, 23(9):4369. xii, 24

[120] Van Vleck, J. H. (1934). The dirac vector model in complex spectra. *Phys. Rev.*, 45:405–419. 72, 136

[121] Wan, C., Gu, X., Dang, F., Itoh, T., Wang, Y., Sasaki, H., Kondo, M., Koga, K., Yabuki, K., Snyder, G. J., et al. (2015). Flexible n-type thermoelectric materials by organic intercalation of layered transition metal dichalcogenide tis 2. *Nature materials*, 14(6):622. 7

[122] Wang, C. S., Klein, B. M., and Krakauer, H. (1985). Theory of magnetic and structural ordering in iron. *Phys. Rev. Lett.*, 54:1852–1855. 40

[123] Wang, Q. H., Kalantar-Zadeh, K., Kis, A., Coleman, J. N., and Strano, M. S. (2012). Electronics and optoelectronics of two-dimensional transition metal dichalcogenides. *Nature nanotechnology*, 7(11):699. 4

[124] Weinelt, M., Nilsson, A., Magnuson, M., Wiell, T., Wassdahl, N., Karis, O., Föhlisch, A., Mårtensson, N., Stöhr, J., and Samant, M. (1997). Resonant photoemission at the $2p$ edges of ni: Resonant raman and interference effects. *Phys. Rev. Lett.*, 78:967–970. 32

[125] Wexler, G. and Woolley, A. (1976). Fermi surfaces and band structures of the 2h metallic transition-metal dichalcogenides. *Journal of Physics C: Solid State Physics*, 9(7):1185. 12

[126] Whittingha, S. M. (2012). *Intercalation chemistry*. Elsevier. 7

[127] Wilson, J., Di Salvo, F., and Mahajan, S. (1974). Charge-density waves in metallic, layered, transition-metal dichalcogenides. *Physical review letters*, 32(16):882. 5

[128] Wilson, J. A., Di Salvo, F., and Mahajan, S. (1975). Charge-density waves and superlattices in the metallic layered transition metal dichalcogenides. *Advances in Physics*, 24(2):117–201. 5, 6

[129] Withers, R. and Wilson, J. (1986). An examination of the formation and characteristics of charge-density waves in inorganic materials with special reference to the two-and one-dimensional transition-metal chalcogenides. *Journal of Physics C: Solid State Physics*, 19(25):4809. 6

[130] Yamada, H. and Takada, S. (1972). Negative magnetoresistance of ferromagnetic metals due to spin fluctuations. *Progress of Theoretical Physics*, 48(6):1828–1848. 59

[131] Yamasaki, Y., Moriya, R., Arai, M., Masubuchi, S., Pyon, S., Tamegai, T., Ueno, K., and Machida, T. (2017). Exfoliation and van der waals heterostructure assembly of intercalated ferromagnet cr1/3tas2. *2D Materials*, 4(4):041007. 123, 126

[132] Yan, R., Khalsa, G., Schaefer, B. T., Jarjour, A., Rouvimov, S., Nowack, K. C., Xing, H. G., and Jena, D. (2018). Evolution of superconductivity in ultrathin nbs2. *arXiv preprint arXiv:1803.06097*. 61

[133] Yeh, J. and Lindau, I. (1985). Atomic subshell photoionization cross sections and asymmetry parameters: 1 z 103. *Atomic data and nuclear data tables*, 32(1):1–155. 29

[134] Yoffe, A. (2002). Low-dimensional systems: quantum size effects and electronic properties of semiconductor microcrystallites (zero-dimensional systems) and some quasi-two-dimensional systems. *Advances in Physics*, 51(2):799–890. 4

[135] Yokoya, T., Kiss, T., Chainani, A., Shin, S., Nohara, M., and Takagi, H. (2001). Fermi surface sheet-dependent superconductivity in 2h-nbse2. *Science*, 294(5551):2518–2520. 6

[136] Zhang, Y., Tan, Y.-W., Stormer, H. L., and Kim, P. (2005). Experimental observation of the quantum hall effect and berry's phase in graphene. *nature*, 438(7065):201. 3

[137] Zhang, Y., Tang, T.-T., Girit, C., Hao, Z., Martin, M. C., Zettl, A., Crommie, M. F., Shen, Y. R., and Wang, F. (2009). Direct observation of a widely tunable bandgap in bilayer graphene. *Nature*, 459(7248):820. 4

Vita

Deepak Sapkota was born and raised in Myagdi district of western Nepal. He got bachelor's and master's degrees in physics from Tribhuvan University, Kathmandu Nepal. Afterwards, in 20212, he joined the physics department at the University of Tennessee, Knoxville as a graduate student. In 2014, he started his thesis project under the supervision of Professor Norman Mannella and Professor David Mandrus. He is graduating in August of 2019 with PhD degree in physics with concentration of condensed matter physics.